Modeling Active Anisotropic Materials Undergoing Finite Deformations

BY

Yali Li

A dissertation submitted in partial fulfillment
of the requirements for the degree of
Doctor of Philosophy
(Aerospace Engineering)
in the University of Michigan
2017

Doctoral Committee:

Associate Professor Nakhiah C. Goulbourne, Chair
Professor John A. Shaw
Associate Professor Veera Sundararaghavan
Professor Alan S. Wineman

Yali Li
yalili@umich.edu
ORCID iD: 0000-0001-8665-8054

To my family

Acknowledgements

There are many people who have supported and provided me throughout this journey. I am grateful to all those who have made this work possible. First of all, I would like to thank my advisor, Prof. Nakhiah Goulbourne for her guidance and support in my study and research. I am very grateful for all the technical discussion and will be always inspired by her creativeness and incisiveness. Her reading and editing of this manuscript has greatly helped to improve the work. I would like to thank my committee members for their effort and time input on the work in this dissertation.

I sincerely thank the members of the Smart Material Research Lab in University of Michigan: Alyssa, Jacob, Riddhiman, Youngwoo, and others. I am grateful for their advices and help. Several of my fellow SMRL colleagues have been instrumental during my graduate school. I would like to express my gratitude to the staff of Aerospace engineering department for their support whenever I need it.

Lastly, I owe much thanks to my beloved family and my God for their unconditional love and support through the years. The journey would not have been possible without them.

Table of Contents

List of Figures

List of Tables

List of Appendices

Abstract

Biological and synthetic active materials have attracted a large amount of research attention over the last decade. This thesis focuses on the development of constitutive models and computational frameworks for describing the behavior of active anisotropic materials. Active anisotropic materials are defined as consisting of an isotropic matrix embedded with fibers or oriented particles that are active. In this dissertation, new constitutive formulations for active anisotropic materials undergoing finite deformations are proposed and analyzed within a generalized continuum mechanics framework. The constitutive equations have been developed for two material classes: i) natural biological muscle tissue and ii) synthetic electroactive polymers. The proposed constitutive models are successfully implemented into a finite element environment to study a range of initial boundary value problems.

In the first material class, a structure-based continuum model is proposed to capture the viscoelastic behavior due to smooth muscle tissue contractility. We employed a thick-walled model for healthy and diseased arteries to investigate the effect of active viscoelasticity on the mechanical response of the artery wall. The work focuses on the artery being overstretched on long time scales (around 1 minute), for example, during surgical events such as balloon angioplasty and stent implantation. Model results show an over fourfold increase in circumferential stresses and twofold increase in radial stresses when active viscoelasticity is considered. This suggests that

active viscoelasticity has a non-negligible effect on the artery wall stresses when longer timescales are considered.

In the second material class, a novel dielectric elastomer composite consisting of an isotropic matrix and embedded contractile fibers is proposed. Two activation modes are realized: through thickness actuation of the matrix and fiber actuation in the plane. A constitutive model is proposed to model the active anisotropic material behavior. A new user subroutine was developed for the proposed constitutive model and implemented into the commercial finite element software ABAQUS. A series of computational simulations to highlight novel deformation modes of the proposed dielectric elastomer composite are presented. The proposed composite significantly extends the actuation performance space for dielectric elastomers. Several new spatial architectures are proposed and the simulations demonstrate coordinated surface morphing through spatial activation and as a function of fiber orientation. Finally, we calculate the actuation response for complex 3D geometries, which opens the design space even further. The developed computational framework is demonstrated to be a very convenient and efficient numerical tool to study complex materials.

Chapter 1. Introduction

1.1 Modeling active anisotropic materials undergoing finite deformations

In this dissertation, new constitutive formulations for active anisotropic materials undergoing finite deformations are proposed and analyzed within a generalized continuum mechanics framework. The constitutive formulations are invariant-based and focus on multiphysics coupling in materials with embedded active fibers. The constitutive equations are developed for two material classes: i) natural biological muscle tissue and ii) synthetic electroactive polymers, which are both examples of active anisotropic materials that are also notably viscoelastic. Here, we focus on *smooth muscle tissue of the artery* as an example of a natural active material, and a novel *dielectric elastomer composite* as an example of a synthetic active material. Active contractility in natural muscle originates from chemo-mechanical coupling within the smooth muscle cell i.e. the influx of ions that trigger the motion of cyclic molecular motors. Actuation in dielectric elastomers arises from electromechanical coupling in a dielectric solid due to an applied electric field. Though the detailed coupling and mechanisms differ in these materials, the modeling framework employed is identical.

For both materials, mathematical model results are generated for simple configurations and symmetric boundary conditions, which are useful in exploring the

stress and deformation fields in a controlled way. The models are implemented into a finite element framework to solve problems with complex geometries, asymmetric boundary conditions, and (spatial) material nonlinearities. The user subroutines developed in this research are amenable to modeling a range of active anisotropic materials undergoing finite viscoelastic deformations. These computational tools provide a framework for investigating important aspects of complex material behavior. For example, in this research, the role of active contractility and geometric imperfections on the mechanical response of smooth muscle tissue is explored. For synthetic active materials, the behavior of a novel dielectric elastomer composite displaying multiple actuation modes via multiaxial activation is simulated for the first time. The role of fiber orientation and spatial architectures in enabling shape morphing with a single design is explored.

Chapter 1 is organized as follows: section 1.2 provides background knowledge on nonlinear continuum mechanics; section 1.3.1 provides an overview of smooth muscle physiology and the state of the art in modeling the arterial response; section 1.3.2 covers the basic actuation mechanism of dielectric elastomers and summarizes related work on anisotropic actuators; and section 1.4 gives a detailed outline of the dissertation.

1.2 Nonlinear continuum mechanics for modeling complex materials

In this dissertation, we define active anisotropic materials as consisting of an isotropic matrix embedded with fibers or oriented particles that are active. To date, material candidates that would fall under this class of materials are elastomers containing charged particles, electrorheological elastomers, liquid crystal elastomers, liquid crystal

polymers, and novel dielectric elastomer composites (Allen et al., 2013; Bossis et al., 2001; Göktepe and Kuhl, 2010; Holzapfel and Ogden, 2009; Rogers et al., 2010). There are also biological examples that would fall under this category of active anisotropic materials. Electromechanical coupling in muscle tissue would form part of this general group. For example, constitutive formulations have been proposed to describe cardiac muscle as an isotropic matrix containing dispersed electro-responsive fibers (Bossis et al., 2001). Muscular constructs such as the fin tissue of cuttlefish are composed of hierarchical and directed muscular hydrostats that, when electrically stimulated, enable dynamic wave propagation along the fin for fast motion and quick maneuvers (Allen et al., 2013). The wing tissue of all bat species have structural configurations consisting of active muscle fibers embedded in a collagen dominated matrix that undergo large electrically induced anisotropic deformations (Cheney et al., 2015; Cheney et al., 2014).

Elastomers are crosslinked polymers able to undergo large, reversible deformations; their use is widespread in current industrial applications as well as in new areas of research. For example, there is recent work on large stretch electroactive polymers, stretchable thin organic solar cells, actuators for soft robotics featuring embedded pneumatic networks, soft pressure sensors which intend to mimic the tactile sensing properties of skin, and various components in the construction of soft electronics like high energy storage capacitors all rely on the remarkable large-stretch properties of elastomeric materials (Fox and Goulbourne, 2008; Ilievski et al., 2011; Kaltenbrunner et al., 2012; Mannsfeld et al., 2010). Soft active materials are an emergent class of materials with multiphysics coupling such as the electric field induced actuation in dielectric elastomers (electro-mechanical coupling). The actuation response of soft active materials is reminiscent of natural muscle, such that the term synthetic muscle is

oftentimes used. Most elastomers are generally isotropic unless fillers, particles, or fibers are added.

Modeling the finite deformation behavior of soft anisotropic active solids is nontrivial. The organization of elastic fibers in a soft isotropic electroactive matrix creates mechanical anisotropy (Goulbourne, 2009). Solids containing aligned electroactive particles are mechanically isotropic in the absence of an electric field; in this case anisotropy is typically induced only upon application of an external electric field. Solids containing active fibers are both mechanically and electrically anisotropic; that is to say, the material is mechanically anisotropic when the electric field is zero, and the electromechanical coupling is anisotropic. To describe local fiber and/or particle directions (passive or active), a vector representing the material preferred direction is introduced as in Spencer (Spencer, 1965; Spencer, 2014; Spencer and Rivlin, 1962). When the fibers are passive, they are described by the directional vectors and exert influence only on the mechanical stiffness of the material. When they are active, the directional vectors couple with the electric field and hence affect the effective stiffness and deformation of the material. The amount and nature of the electromechanical coupling is strongly dependent on the orientations of the directional vectors relative to the direction and magnitude of the applied electric field. A similar concept applies for natural muscle but where the activation trigger is chemical, the coupling is chemo-mechanical and proportional to the fraction of molecular cross-bridge units.

In this dissertation, the generalized constitutive formulation for active anisotropic materials undergoing finite viscoelastic deformations is derived using a continuum mechanics framework. Mathematically, the problem is to construct the irreducible integrity bases for a scalar valued function (the free energy) that depends on

deformation gradient, the directional vectors, and the electric displacement vector. The set of invariants, also called the irreducible integrity bases, is obtained by adopting the invariant theoretical formulations previously derived by Spencer, Pipkin and Rivlin. Further constraints may come from thermodynamic considerations and/or physical restrictions. The invariants of tensors are found by satisfying material frame invariance, material symmetry, and kinematic considerations. Spencer and Rivlin obtained a finite integrity basis (invariant set) for an arbitrary number of vectors, which are denoted as skew-symmetric second order tensors and an arbitrary number of symmetric second order tensors (Pipkin and Rivlin, 1997a; Pipkin and Rivlin, 1997b; Spencer, 2014). They proved that the integrity basis under the proper orthogonal group consists only of the integrity basis for the symmetric tensors and the traces of the symmetric tensor products. They tabulated the full class of integrity bases for an arbitrary number of symmetric second order tensors, axial vectors, and polar vectors under the proper and full orthogonal groups. Pipkin and Rivlin derived the irreducible integrity bases used to obtain the constitutive equations for several physical phenomena involving electric, magnetic, and temperature gradient fields (Pipkin and Rivlin, 1997b). The invariant formulation is important because it ensures that a particular proposed model will provide physically reasonable behavior.

Nonlinear constitutive formulations for isotropic materials undergoing large deformations are covered in several seminal works (Atkin et al., 2005; Green and Rivlin, 1997; Reese and Govindjee, 1998; Simo, 1988a; Spencer, 2004; Wineman, 2009) Rajagopal and Wineman, and Dorfmann and Ogden both derived a formulation for isotropic electro-elastic materials. Their formulation consists of an invariant-based free energy function, and invariants for the isotropic electro-elastic material were introduced by

others (Dorfmann and Ogden, 2005; Dorfmann and Ogden, 2006; Rajagopal and Wineman, 1999). Bustamante developed a theoretical constitutive law for transversely isotropic electro-elastic materials, consisting of an isotropic matrix and one family of electro-active particles (Bustamante, 2009). Son proposed a constitutive formulation for anisotropic electro-elastic solids consisting of two active fiber families dispersed in an isotropic matrix (Son, 2011).

There have been numerous constitutive formulations and strain energy functions proposed for biological tissues over the last two decades. (Holzapfel et al., 2000; Humphrey, 2003; Humphrey and Canham, 2000; Humphrey and Rajagopal, 2002; Maurel et al., 1998) Invariant theoretical approaches for nonlinear elastic anisotropic continua were used by Holzapfel et al. and Gasser et al. to model passive arterial layers containing a statistical distribution of collagen fibers (Gasser et al., 2006; Holzapfel et al., 2000). Wang et al. employed an identical framework to describe tissues that have more than one varying fiber property (Wang et al., 2012). Active contractility has been modeled using a semi-phenomenological approach largely borrowed from the literature on skeletal tissue (Heidlauf and Röhrle, 2014; Heidlauf et al., 2013; Kroon, 2010; Murtada et al., 2010; Murtada et al., 2012; Oomens et al., 2003; Röhrle et al., 2008; Stålhand et al., 2008).

1.2.1 Nonlinear viscoelastic continua

Continuum approaches to model viscoelastic behavior generally fall under the integral approach or the derivative approach. For details regarding the integral approach, refer to (Coleman and Noll, 1961; Fung, 1993; Green and Rivlin, 1997; Pipkin and Rogers, 1968; Wineman, 2009). The derivative approach involves the multiplicative decomposition of the deformation gradient into elastic and inelastic parts, and is the

approach utilized in this dissertation. This concept was borrowed from elasto-plasticity theory (Lee, 1969) and applied to nonlinear viscoelastic materials by (Sidoroff, 1974). Lubliner (Lubliner, 1985) divided the free energy function into rate-independent and time dependent parts i.e. equilibrium and nonequilibrium parts. Reese and Govindjee developed a nonlinear finite viscoelasticity theory based on the decomposition of the deformation gradient (Reese and Govindjee, 1998). One important aspect in developing constitutive models in this form is the formulation of evolution equations for the internal variables. The evolution equation needs to satisfy the dissipation inequality derived from the second law of thermodynamics. For complex geometries, asymmetries, and loads, computational approaches are generally required (Simo, 1988b; Simo and Humphrey, 1998; Simo and Hughes, 2000). The derivative approach is easily implemented into a finite element framework on the basis of the well-developed finite element methods of elasto-plasticity theory.

1.3 Coupling mechanisms in active anisotropic materials

1.3.1 Smooth muscle tissue

There are countless molecular motors in muscle cells that generate axial force and contraction to enable a range of physiological functions. (Boron and Boulpaep, 2008; Brady et al., 1979; Feinberg, 2015) For example, smooth muscle cells in the artery walls contract and relax to change the volume and pressure of blood vessels, and similar functions exist in the smooth muscle cells in the airway, stomach, and intestine, etc. Cardiac muscle cells utilize and coordinate contraction of the cardiac muscle cells to pump blood from the heart to blood vessels. The force generated by skeletal muscle fibers is used to realize skeletal movement such as locomotion.

Though the detailed electro-chemo-mechanical coupling and molecular contraction mechanisms differ in these muscle tissues, their macroscopic mechanical behaviors are similar. In this dissertation, we study smooth muscle tissue in the arteries as an example of natural anisotropic active materials and propose a generalized constitutive model framework of the smooth muscle tissue. The model framework can be adapted to model other types of muscle, e.g. skeletal muscle and cardiac muscle, by tailoring the kinetic cycle.

Artery physiology is a complex interconnection of electrical, chemical, and mechanical phenomena regulated by numerous signaling pathways. At the macroscale, the artery is simply composed of three layers: a single cell layer at the lumen interface called the intima, the smooth muscle rich media layer, and an outer layer called the adventitia (see Figure 1). Smooth muscle cell membranes in various regions of the body differ in the expression of ion channels, hormone receptors, cell-signaling pathways, and other proteins that coordinate their function (Yang et al. 2003). The smooth muscle contractile unit resides in the smooth muscle cell and is composed of thin and thick filaments as shown in Figure 2. Cell contraction can be initiated by a number of physiochemical agents (e.g. hormones, drugs, neurotransmitters), mechanical stimuli, and or electrical stimuli. The contractile apparatus is based on a molecular motor characterized by cross-bridge cycling (Huxley et al., 1954i, 1954ii, Huxley, 1957, 1974, 2000, 2004, Murphy et al. 1974). The mechanism is set in motion by an increase in cytosolic calcium (Figure 2) (Fajmut et al., 2005, Hai and Murphy, 1989). The contractile force and cell stretch is proportional to the number of instantaneous cross-bridges formed by the myosin/actin complex. The contractile units in smooth muscle can produce active force at a range of lengths. Murtada et al. developed a parabolic overlap

function to describe the overlap effect of contractile units based on their understanding of the structure and sliding filament theory. Yang et al. proposed a Gaussian function to capture the overlap effect, which was adopted by (Stalhand et al., 2008, 2011) and was also used to generate our preliminary results.

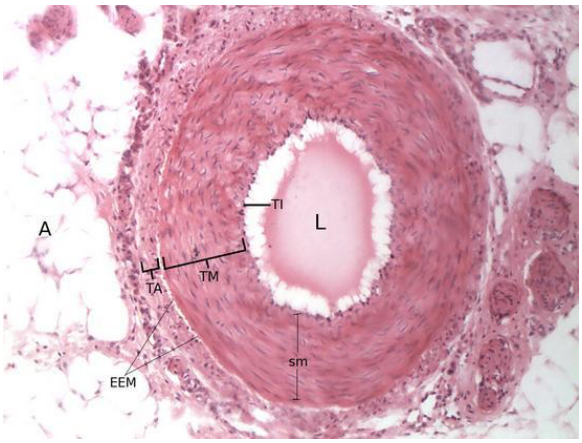

Figure 1. Muscular artery cross-section: sm-smooth muscle; TA-tunica adventitia; TM-tunica media; TI-tunica intima; L-lumen; A-adipose tissue; EEM-external elastin membrane. (the figure is taken from

http://bcrc.bio.umass.edu/bestofhistology/content/muscular-artery-100x)

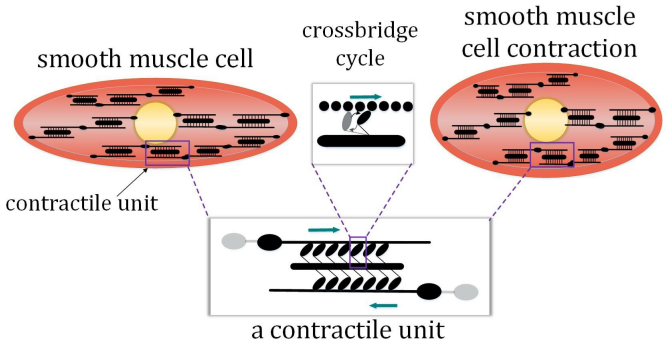

Figure 2. Schematics of the contractile unit structure and cell contraction.

Vascular tone is the degree of wall tension maintained by contraction of smooth muscle cells in the media layer relative to its maximally dilated state. As previously mentioned, smooth muscle cells contract in response to electrical, mechanical, and

chemical stimuli. Though all these stimuli are conducted through various pathways, each ultimately gives rise to an increase in cytosolic calcium concentrations $\left[Ca^{2+}\right]_i$. The calcium enters the cytosol through the sarcolemma (cell membrane) and or is released from internal calcium stores in the sarcoplasmic reticulum (SR) (Boron et al. 2009). The free calcium ions bind to calmodulin – a calcium binding protein, and forms the calcium-calmodulin complex (CaCM). This complex activates the enzyme myosin light chain kinase (MLCK), which facilitates the phosphorylation of myosin light chains by adenosine triphosphate (ATP). The contractile apparatus in the smooth muscle cell is composed of actin and myosin filaments which interact and form cross-bridges according to the well-known sliding filament theory (Figure 3). The crossbridges are responsible for generating the active force necessary for contraction. The ability to maintain a latch-state with relatively low levels of energetic demands differentiates the smooth muscle apparatus from striated muscle. Physically, this means that smooth muscle cells unlike striated muscle can maintain tension for relatively long periods of time with little energy. The cycling behavior in smooth muscle cells is also much slower and notably viscoelastic. Previous work has suggested a passive origin of the viscoelastic response from the surrounding tissues. In our work, we propose that the viscoelastic response originates from the slow cycling crossbridge mechanism within the contractile unit itself and model it accordingly (Warshaw, et al., 1990).

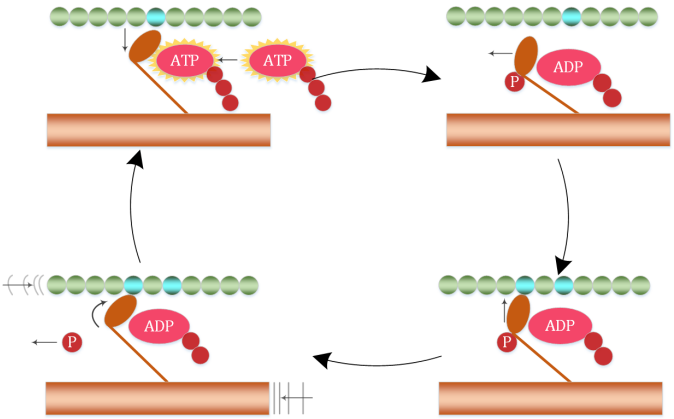

Figure 3. Schematics of the four states of cross-bridge cycling within smooth muscle cell.

Two classical experiments used to study the active properties of smooth muscle tissue are isometric and isotonic tests. (Dillon et al., 1981) The former is also referred to as the length clamp test since the total length of the specimen is held fixed during the experiment. The active stress evolution (transient characteristic) is recorded in isometric tests for certain stimuli. In isotonic tests, also referred to as load clamp tests, the load acting on the specimen is held fixed. Isometric tests are generally performed before isotonic tests so that the specimen is in a steady activated state for a certain fixed length. Isotonic tests can then be performed in which the external force is suddenly changed to another fixed value, and the amount and rate of length change are recorded. The force applied in isotonic tests is called the afterload. The increase or decrease in the specimen length immediately following application of the afterload is called the elastic recoil. The initial rate at which elastic recoil occurs is called the initial velocity (Dillon et al., 1981). The elastic recoil and the initial velocity are two main characteristics of isotonic tests.

Figure 4 (a) is a recording of the active stress developed in a K+ stimulated carotid media strip in an isometric test. Figure 4 (b) shows initial velocities following isotonic quick-release to different afterloads in isotonic tests on swine artery smooth

muscle strips. As can be seen, the time scale of the viscous effects is around 1 minute and the mechanical behavior is nonlinear. In contrast, the other two types of muscle tissue respond faster than smooth muscle tissue. The timescales of the other two types of muscle tissue are under 1 second. (Boron and Boulpaep, 2008; Jarvis and Salmons, 1991; Parmley et al., 1970; Sondergaard et al., 2010; Winters et al., 2009)

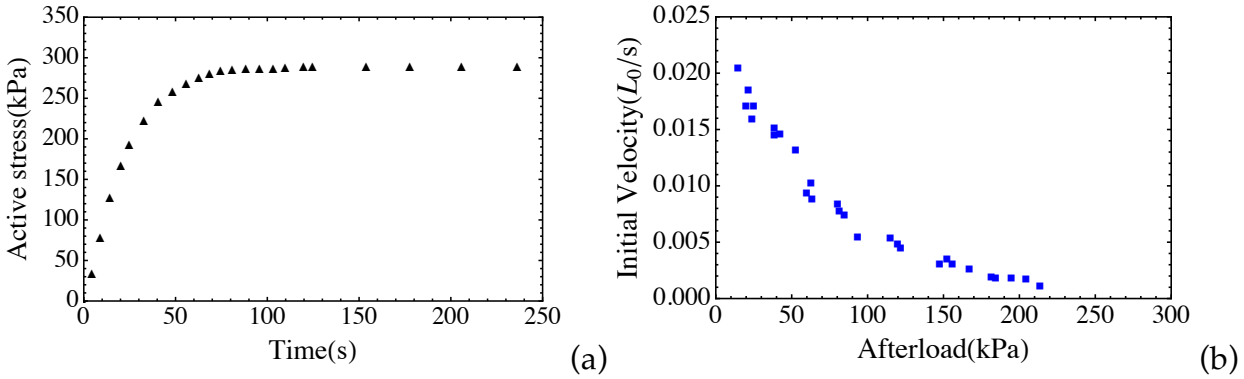

Figure 4. (a) Active stress recording in isometric tests on swine smooth muscle strips from a artery; and (b) initial velocities and afterloads recording in isotonic tests. (Experimental data is taken from (Dillon et al., 1981))

In this dissertation, a constitutive model for smooth muscle including active tone and active viscoelastic behavior is developed. We use a continuum mechanics framework to model the finite deformation behavior of the tissue following previous work by (Kroon, 2010; Murtada et al., 2010; Stålhand et al., 2008). We consider a tissue composed of two families of collagen fibers (Holzapfel et al., 2000) and represent the smooth muscle cells as a single family of fibers all embedded in a passive matrix (Spencer, 1962, 1965, 1971, 1984, Pipkin and Rivlin, 1959). A nonlinear evolution equation is introduced for the nonequilibrium part of the stress using the finite deformation viscoelastic framework of Reese and Govindjee (Reese and Govindjee, 1998). The active muscle contraction is derived from a chemical model of crossbridge cycling. We propose an active viscous part that arises from the fraction of *latch-bridges*

formed, which has the effect of slowing down the contractile unit and acting as a resistive load on the fast cycling crossbridges. We show that the constitutive model satisfies the Clausius-Duhem inequality. The model is calibrated with isometric and isotonic test data from the literature whereby a nonlinear formulation is newly introduced. A thick-walled model is employed to study the active contractility and viscoelastic effects in an artery and artery-plaque model composite. The model is then implemented into ABAQUS such that the role of geometric imperfections and active contractility for a host of conditions can be simulated and extensively studied. The results show that: i) active viscoelasticity is non-negligible during interventional events such as balloon angioplasty, and ii) we are able to establish correlations between plaque properties and overall impact on artery response. The proposed constitutive model is implemented in a new user subroutine in ABAQUS.

1.3.2 Dielectric elastomer composites

Dielectric elastomers (DEs) are an emergent class of materials with electromechanical coupling and belong to one of the two major groups in electroactive polymers. (Pelrine et al., 2000a; Pelrine et al., 2000b; Pelrine et al., 1998) Dielectric elastomers have unique characteristics such as high compliance, light weight, low cost, large actuation strain, etc. (Goulbourne et al., 2007b) DEs are considered one of the closest synthetic materials to biological muscles and are being developed for a range of applications. (Gisby et al., 2013; Goulbourne et al., 2007b; Jung et al., 2008; Koh et al., 2011; Pelrine et al., 1998) The dielectric elastomer consists of a thin dielectric layer sandwiched between two compliant electrodes. A voltage applied across the electrodes generates an electric field in the thickness direction. This results in electrostatic or Coulombic forces, which decrease film thickness and cause planar expansion of the DEs' area (see Figure 6). To

avoid extremely high voltage, the layer is generally very thin, on the order of 100 microns. Typical voltages required are around 5~10 kV for a thickness of 0.5~1 mm before prestrain (~ 250-350%) to obtain a working electric field (around 10 ~ 100 MV/m).

A large body of research has been dedicated to the development of versatile actuators using dielectric elastomers, for example planar (expander) actuators (Pelrine et al., 1998), pump-like (diaphragm) actuators (Goulbourne et al., 2007b), bending actuators (O'Brien et al., 2009), tube (spring roll) actuators (Pei et al., 2004) etc. Target DE applications include resonators (Feng et al., 2011; Zhou et al., 2014), adaptive optical elements (Shian et al., 2013), energy harvesters (Koh et al., 2011), and soft robotics (Kovacs et al., 2007) etc. The basic mechanism of planar isotropic dielectric elastomers is outlined in Figure 5, where planar expansion is most evident. In contrast to the predominant lateral expansion of dielectric elastomer sheets, the material can be configured to visibly contract by fabricating multilayered stack actuators (similar motion achieved via folded dielectric elastomer configurations or helical dielectric elastomer actuators). (Carpi et al., 2007; Carpi et al., 2005; Chuc et al., 2007)

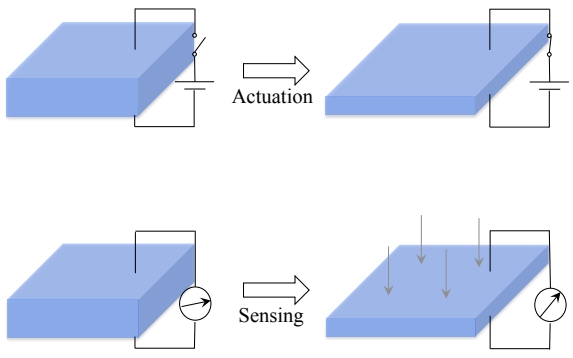

Figure 5. Principle of sensing and actuation in typical isotropic dielectric elastomers.

The main approach for modeling isotropic dielectric elastomers involves employing the general nonlinear theory of elasticity with electrostatic theory (via the principle of Maxwell stress). (Dorfmann and Ogden, 2005; Dorfmann and Ogden, 2006; Goulbourne et al., 2005; Goulbourne et al., 2007b; Rajagopal and Wineman, 1999; Suo et al., 2008; Zhao and Suo, 2008; Zhao et al., 2007) Dorfmann and Ogden provided a theoretical basis for the characterization of the nonlinear electroelastic properties of isotropic electro-sensitive materials using the invariants derived by Spencer. (Dorfmann and Ogden, 2005; Dorfmann and Ogden, 2006; Spencer, 1971) Rajagopal and Wineman provided a mathematical formulation for the study of electro-active solids (Rajagopal and Wineman, 1999). Suo et al. and Zhao et al. used a variational approach to develop a model for isotropic dielectric elastomers using material coordinates (Suo et al., 2008; Zhao and Suo, 2008; Zhao et al., 2007) Goulbourne et al. developed a method for modeling a dielectric elastomer membrane that accounts for material nonlinearities and large deformations by applying Rivlin's large elastic membrane theory. (Goulbourne et al., 2007a; Goulbourne et al., 2007b) Solutions for simple configurations (rectangular, tube, and circular membranes etc.), boundary conditions, and loading conditions have been generated using numerical approaches. Finite element formulations for isotropic and hyperelastic DEs exist but have been studied to a lesser extent. (Zhao and Suo, 2008)

Though neglected in early work, the time dependent behavior of DEs can be important (depends on the response-time of the target applications). (Pelrine et al., 2000a; Pelrine et al., 2000b; Pelrine et al., 1998; Wineman, 2009) Figure 6 (a) shows experimental data for stress relaxation tests on VHB 4910. Figure 6 (b) shows experimental data for various strain rates in VHB 4910. (Hossain et al., 2012)

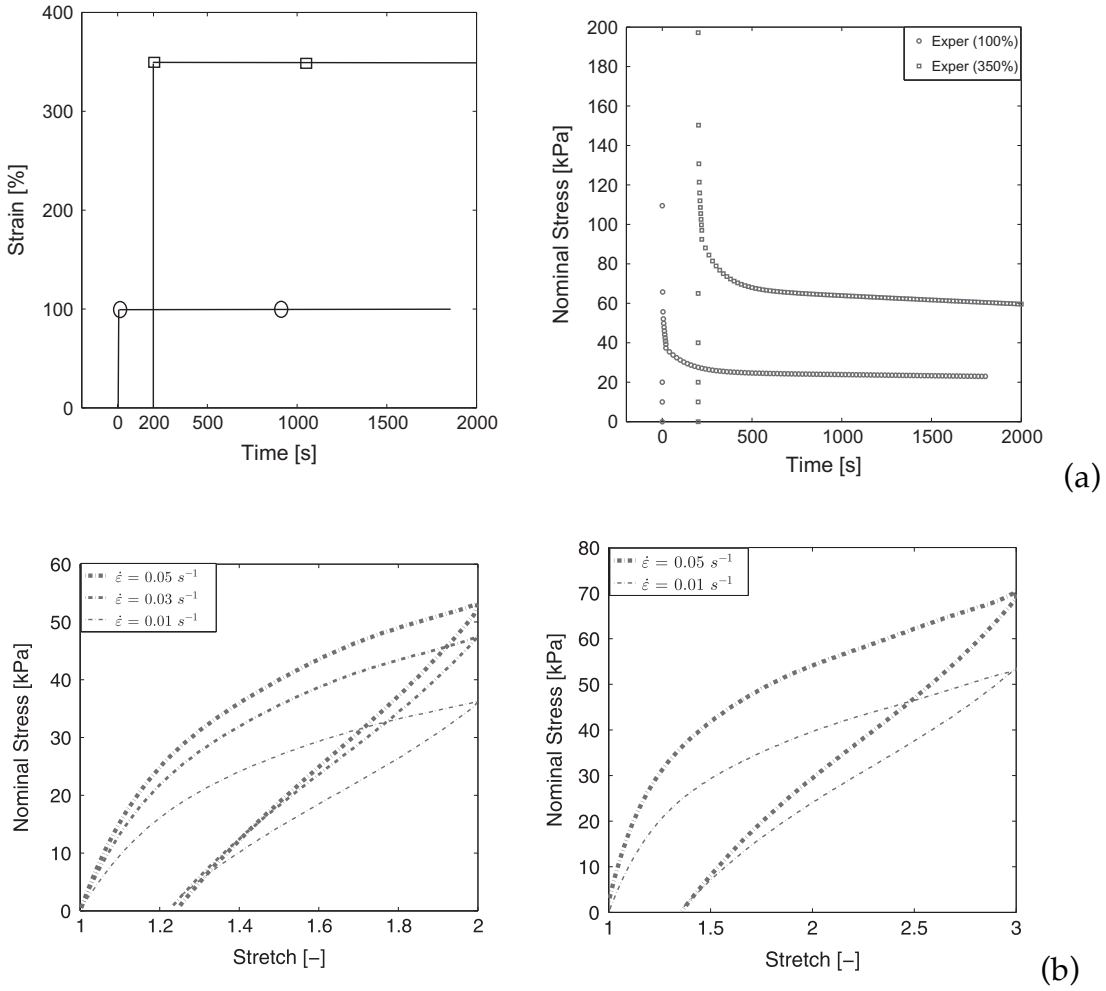

Figure 6. (a) Experimental data of stress relaxation tests on VHB 4910 at 100% and 350% strains; and (b) experimental data of loading-unloading tests at various strain rates for 100% deformation and 200 deformation on VHB 4910. (Figures are taken from (Hossain et al., 2012))

More recently, constitutive models have been developed for isotropic dielectric elastomers accounting for viscoelastic behavior. (Ask et al., 2012; Ask et al., 2015; Bortot et al., 2016; Henann et al., 2013; Hong, 2011; S. Park and D. Nguyen, 2013; Thylander et al., 2017; Wang et al., 2013a; Wang et al., 2016; Zhang et al., 2015) The mechanical part of the proposed constitutive models is based on nonlinear viscoelastic theory. Ask et al. developed phenomenological models to capture the viscous mechanical behavior by

employing a multiplicative decomposition of the deformation gradient and evolution equations using a power-law formulation. (Ask et al., 2012; Ask et al., 2015) Park and Nguyen studied viscoelastic effects on electromechanical instabilities in dielectric elastomers. Their viscous model was also based on the multiplicative decomposition of the deformation gradient; the evolution equation follows the formulation in Reese and Govindjee. (S. Park and D. Nguyen, 2013) Thylander et al. established a micromechanically motivated constitutive model for dielectric elastomers accounting the time-dependent viscous behavior using non-affine kinematics (Thylander et al., 2017). With the increased difficulty of solving the balance equations with the viscoelastic constitutive models for boundary value problems, finite element formulations are increasingly employed (Ask et al., 2015; S. Park and D. Nguyen, 2013; Thylander et al., 2017; Wang et al., 2013b; Wang et al., 2016).

Now most research to date has focused on easily fabricated isotropic dielectric elastomers. Anisotropic dielectric elastomers is a fairly unexplored area. Fiber reinforced dielectric elastomers with discrete inextensible fibers embedded in the dielectric elastomer matrix were proposed, modeled, and experimentally characterized by (Son, 2011; Son and Goulbourne, 2009) and (Shian et al., 2015). Laminated DE composite structures were theoretically proposed and studied by (Bertoldi and Gei, 2011; Rudykh et al., 2014; Siboni and Ponte Castañeda, 2016; Siboni et al., 2015). In this dissertation, a new composite architecture is proposed and explored using numerical and computational analysis tools. The active anisotropic solid consists of a family of contractile active fibers dispersed in an isotropic dielectric matrix. In the proposed dielectric elastomer composite (DEC), the fibers contract when a component of the electric field is directed along the fiber orientation. One way that the contractile units

could be realized is by arranging micron sized DEs in a stacked configuration to form a planar distribution of 1D fibers (see Figure 7 (a)). The active fibers would then contract along the fiber stack direction due to the Maxwell stress effect when an electric field is applied in the fiber direction. If the top and bottom surfaces of the homogenized composite membrane are then electroded, then a matrix dominated Maxwell stress effect would also occur (see Figure 7 (b)). In this way, multiaxial activation is realized.

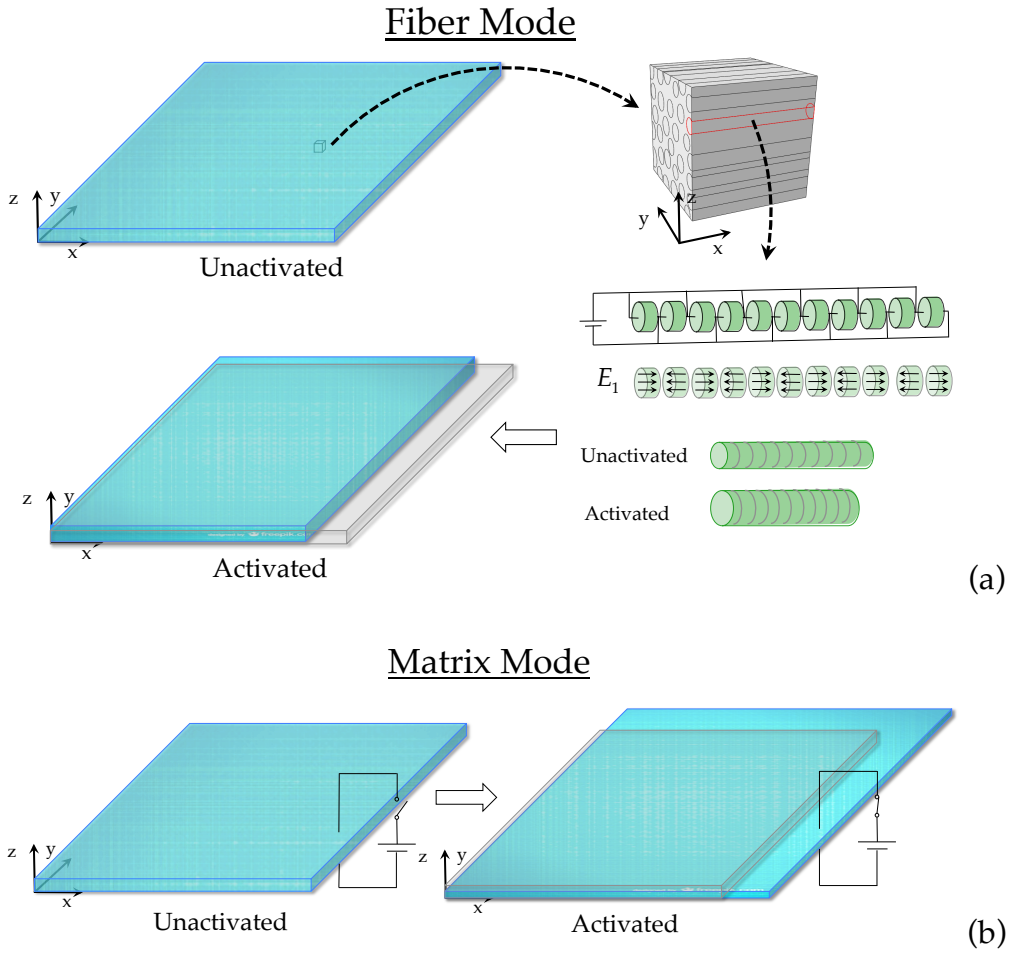

Figure 7. (a) Schematics of activation the fibers (fiber mode) in the dielectric elastomer composite, and (b) schematics of activation the matrix (matrix mode) in the dielectric elastomer composite.

In this dissertation, a new constitutive model for the proposed dielectric elastomer composite is developed. The model captures the material anisotropy and nonlinearity due to multi-axial electromechanical coupling, finite deformations, and active viscoelasticity in the fiber direction. The constitutive model is invariant-based and reminiscent of the phenomenological model for active contractility in natural muscle. Numerical solutions are generated for simple cases to explore the basic mechanisms of the proposed anisotropic solid. The model is implemented in ABAQUS via a new user subroutine to study complex geometries and composite architectures. The computational framework so developed proves to be a useful tool in simulating several novel deformation modes that cannot be achieved by existing isotropic dielectric elastomers. Specifically, the concepts of multiaxial activation and spatially distributed activation are simulated and explored for the first time. The simulations clearly point to the potential advancement and advantage of anisotropic dielectric elastomers for existing and future applications.

1.4 Thesis outline

In this dissertation, two new constitutive formulations are proposed within a continuum mechanics framework to model soft active biological and synthetic materials coupling chemical and electrical effects with mechanical effects. The model accounts for time-dependent chemo-mechanical and electro-mechanical behavior. The proposed constitutive models are successfully implemented into a finite element environment to study a range of initial boundary value problems. These numerical analysis tools provide a general framework for: i) modeling combined physiological effects in the case

of arterial segments and ii) for developing optimal synthetic architectures for dielectric elastomer composites. The outlines of the dissertation are as follows:

Chapter 2. Continuum mechanics framework. In this chapter, the continuum mechanics framework for nonlinear materials undergoing large deformations is introduced. The chapter presents the kinematics, balance laws, and invariant based strain energy functions and model formulations.

Chapter 3. Computational implementation. The general formulation for implementing constitutive models in FEM is introduced. Starting from the weak form of the equilibrium equations, the linearization and the residual form is outlined. In addition, the equivalent objective stress rates used in ABAQUS are introduced and the general form of the tangent modulus for ABAQUS user subroutines is derived.

Chapter 4. A nonlinear constitutive model for smooth muscle tissue. A structure-based continuum model is proposed to capture the active viscoelastic behavior of smooth muscle tissue. The constitutive model is based on an existing model framework and we propose a third order nonlinear evolution equation to describe the nonlinear behavior of smooth muscle contraction. Model parameters are calibrated using isometric and isotonic tests on swine carotid artery strips. The proposed model is able to capture essential characteristics of smooth muscle contraction.

Chapter 5. Numerical and computational analysis of artery stresses considering active contractility. The constitutive model in Chapter 4 for smooth muscle tissue is employed in a thick-walled model to investigate effects of smooth muscle contraction on artery stresses and quantify the role of active

viscoelasticity in the artery mechanical responses. The work focuses on the artery being overstretched on longer timescales for example during surgical events. Results are generated for a healthy two-layer artery ring and a diseased three-layer plaque-artery ring. It shows that the active viscoelastic behavior has a non-negligible effect on artery wall stresses when longer timescales are considered.

Chapter 6. A constitutive model for contractile dielectric elastomer composites. A novel dielectric elastomer composite is proposed. The new constitutive model is implemented into a finite element formulation as a user subroutine in ABAQUS. The computational formulation is verified by comparing with analytical solutions for uniaxial, biaxial, and simple shear deformations. A parameter study is conducted for three simple cases.

Chapter 7. Computational simulations of contractile dielectric elastomer composites. A series of computational simulations to highlight novel deformation modes of the proposed dielectric elastomer composite are carried out. Several new spatial architectures are proposed and the performance due to discrete activation is analyzed. Electro-hydrostatic actuation is illustrated for different membrane configurations. Relationships between spatial activation, fiber orientation, and surface morphing are shown. The actuation response for complex 3D geometries is simulated.

Chapter 8. Conclusion. The main results and findings are summarized.

Reference

Allen, J. J., Bell, G. R. R., Kuzirian, A. M., Hanlon, R. T., 2013. Cuttlefish skin papilla morphology suggests a muscular hydrostatic function for rapid changeability. Journal of Morphology 274, 645-656, doi:10.1002/jmor.20121.

Ask, A., Menzel, A., Ristinmaa, M., 2012. Phenomenological modeling of viscous electrostrictive polymers. International Journal of Non-Linear Mechanics 47, 156-165, doi:10.1016/j.ijnonlinmec.2011.03.020.
Ask, A., Menzel, A., Ristinmaa, M., 2015. Modelling of Viscoelastic Dielectric Elastomers with Deformation Dependent Electric Properties. Procedia IUTAM 12, 134-144, doi:10.1016/j.piutam.2014.12.015.
Atkin, R. J., Fox, N., Physics, 2005. An Introduction to the Theory of Elasticity. Dover Publications, Mineola, N.Y.
Bertoldi, K., Gei, M., 2011. Instabilities in multilayered soft dielectrics. Journal of the Mechanics and Physics of Solids 59, 18-42, doi:10.1016/j.jmps.2010.10.001.
Boron, W. F., Boulpaep, E., L., 2008. Medical Physiology: A Cellular and Molecular Approach by Walter F. Boron. Saunders.
Bortot, E., Denzer, R., Menzel, A., Gei, M., 2016. Analysis of viscoelastic soft dielectric elastomer generators operating in an electrical circuit. International Journal of Solids and Structures 78–79, 205-215, doi:10.1016/j.ijsolstr.2015.06.004.
Bossis, G., Abbo, C., Cutillas, S., Lacis, S., Métayer, C., 2001. Electroactive and electrostructured elastomers. International Journal of Modern Physics B 15, 564-573, doi:10.1142/S0217979201005027.
Brady, A. J., Tan, S. T., Ricchiuti, N. V., 1979. Contractile force measured in unskinned isolated adult rat heart fibres. Nature 282, 728-729.
Bustamante, R., 2009. Transversely isotropic non-linear electro-active elastomers. Acta Mechanica 206, 237, doi:10.1007/s00707-008-0092-9.
Carpi, F., Salaris, C., Rossi, D. D., 2007. Folded dielectric elastomer actuators. Smart Materials and Structures 16, S300, doi:10.1088/0964-1726/16/2/S15.
Carpi, F., Migliore, A., Serra, G., Rossi, D. D., 2005. Helical dielectric elastomer actuators. Smart Materials and Structures 14, 1210, doi:10.1088/0964-1726/14/6/014.
Cheney, J. A., Konow, N., Bearnot, A., Swartz, S. M., 2015. A wrinkle in flight: the role of elastin fibres in the mechanical behaviour of bat wing membranes. Journal of The Royal Society Interface 12, 20141286, doi:10.1098/rsif.2014.1286.
Cheney, J. A., Konow, N., Middleton, K. M., Breuer, K. S., Roberts, T. J., Giblin, E. L., Swartz, S. M., 2014. Membrane muscle function in the compliant wings of bats. Bioinspiration & Biomimetics 9, 025007, doi:10.1088/1748-3182/9/2/025007.
Chuc, N. H., Park, J. K., Thuy, D. V., Kim, H. S., Koo, J. C., Lee, Y., Nam, J.-d., Choi, H. R., 2007. Multi-stacked artificial muscle actuator based on synthetic elastomer. 2007 IEEE/RSJ International Conference on Intelligent Robots and Systems, pp. 771-776.
Coleman, B. D., Noll, W., 1961. Foundations of Linear Viscoelasticity. Reviews of Modern Physics 33, 239-249, doi:10.1103/RevModPhys.33.239.
Dillon, P. F., Aksoy, M. O., Driska, S. P., Murphy, R. A., 1981. Myosin phosphorylation and the cross-bridge cycle in arterial smooth muscle. Science 211, 495-497, doi:10.1126/science.6893872.
Dorfmann, A., Ogden, R. W., 2005. Nonlinear electroelasticity. Acta Mechanica 174, 167-183, doi:10.1007/s00707-004-0202-2.
Dorfmann, A., Ogden, R. W., 2006. Nonlinear Electroelastic Deformations. Journal of Elasticity 82, 99-127, doi:10.1007/s10659-005-9028-y.
Feinberg, A. W., 2015. Biological Soft Robotics. Annual Review of Biomedical Engineering 17, 243-265, doi:10.1146/annurev-bioeng-071114-040632.

Feng, C., Jiang, L., Lau, W. M., 2011. Dynamic characteristics of a dielectric elastomer-based microbeam resonator with small vibration amplitude. Journal of Micromechanics and Microengineering 21, 095002, doi:10.1088/0960-1317/21/9/095002.
Fox, J. W., Goulbourne, N. C., 2008. On the dynamic electromechanical loading of dielectric elastomer membranes. Journal of the Mechanics and Physics of Solids 56, 2669-2686, doi:10.1016/j.jmps.2008.03.007.
Fung, Y. C., 1993. Biomechanics: Mechanical Properties of Living Tissues, Second Edition. Springer, New York.
Gasser, T. C., Ogden, R. W., Holzapfel, G. A., 2006. Hyperelastic modelling of arterial layers with distributed collagen fibre orientations. Journal of The Royal Society Interface 3, 15-35, doi:10.1098/rsif.2005.0073.
Gisby, T. A., O'Brien, j. B. M., Anderson, I. A., 2013. Self sensing feedback for dielectric elastomer actuators. Applied Physics Letters 102, 193703, doi:10.1063/1.4805352.
Göktepe, S., Kuhl, E., 2010. Electromechanics of the heart: a unified approach to the strongly coupled excitation–contraction problem. Computational Mechanics 45, 227-243, doi:10.1007/s00466-009-0434-z.
Goulbourne, N., Mockensturm, E., Frecker, M., 2005. A Nonlinear Model for Dielectric Elastomer Membranes. Journal of Applied Mechanics 72, 899-906, doi:10.1115/1.2047597.
Goulbourne, N. C., 2009. A mathematical model for cylindrical, fiber reinforced electro-pneumatic actuators. International Journal of Solids and Structures 46, 1043-1052, doi:10.1016/j.ijsolstr.2008.10.020.
Goulbourne, N. C., Son, S., Fox, J. W., 2007a. Self-sensing McKibben actuators using dielectric elastomer sensors. Vol. 6524, pp. 652414-652414-12.
Goulbourne, N. C., Mockensturm, E. M., Frecker, M. I., 2007b. Electro-elastomers: Large deformation analysis of silicone membranes. International Journal of Solids and Structures 44, 2609-2626, doi:10.1016/j.ijsolstr.2006.08.015.
Green, A. E., Rivlin, R. S., 1997. The Mechanics of Non-Linear Materials with Memory. In: Barenblatt, G. I., Joseph, D. D., Eds.), Collected Papers of R.S. Rivlin. Springer New York, pp. 1049-1069.
Heidlauf, T., Röhrle, O., 2014. A multiscale chemo-electro-mechanical skeletal muscle model to analyze muscle contraction and force generation for different muscle fiber arrangements. Frontiers in Physiology 5, 498, doi:10.3389/fphys.2014.00498.
Heidlauf, T., xf, Hrle, O., 2013. Modeling the Chemoelectromechanical Behavior of Skeletal Muscle Using the Parallel Open-Source Software Library OpenCMISS. Computational and Mathematical Methods in Medicine 2013, e517287, doi:10.1155/2013/517287.
Henann, D. L., Chester, S. A., Bertoldi, K., 2013. Modeling of dielectric elastomers: Design of actuators and energy harvesting devices. Journal of the Mechanics and Physics of Solids 61, 2047-2066, doi:10.1016/j.jmps.2013.05.003.
Holzapfel, G. A., Ogden, R. W., 2009. Constitutive modelling of passive myocardium: a structurally based framework for material characterization. Philosophical Transactions of the Royal Society of London A: Mathematical, Physical and Engineering Sciences 367, 3445-3475, doi:10.1098/rsta.2009.0091.
Holzapfel, G. A., Gasser, T. C., Ogden, R. W., 2000. A New Constitutive Framework for Arterial Wall Mechanics and a Comparative Study of Material Models. Journal of

elasticity and the physical science of solids 61, 1-48, doi:10.1023/A:1010835316564.
Hong, W., 2011. Modeling viscoelastic dielectrics. Journal of the Mechanics and Physics of Solids 59, 637-650, doi:10.1016/j.jmps.2010.12.003.
Hossain, M., Vu, D. K., Steinmann, P., 2012. Experimental study and numerical modelling of VHB 4910 polymer. Computational Materials Science 59, 65-74, doi:10.1016/j.commatsci.2012.02.027.
Humphrey, J. D., 2003. Review Paper: Continuum biomechanics of soft biological tissues. Proceedings of the Royal Society of London A: Mathematical, Physical and Engineering Sciences 459, 3-46, doi:10.1098/rspa.2002.1060.
Humphrey, J. D., Canham, P. B., 2000. Structure, Mechanical Properties, and Mechanics of Intracranial Saccular Aneurysms. Journal of elasticity and the physical science of solids 61, 49-81, doi:10.1023/A:1010989418250.
Humphrey, J. D., Rajagopal, K. R., 2002. A constrained mixture model for growth and remodeling of soft tissues. Mathematical Models and Methods in Applied Sciences 12, 407-430, doi:10.1142/S0218202502001714.
Ilievski, F., Mazzeo, A. D., Shepherd, R. F., Chen, X., Whitesides, G. M., 2011. Soft Robotics for Chemists. Angewandte Chemie International Edition 50, 1890-1895, doi:10.1002/anie.201006464.
Jarvis, J. C., Salmons, S., 1991. An electrohydraulic apparatus for the measurement of static and dynamic properties of rabbit muscles. Journal of Applied Physiology 70, 938-941.
Jung, K., Kim, K. J., Choi, H. R., 2008. A self-sensing dielectric elastomer actuator. Sensors and Actuators A: Physical 143, 343-351, doi:10.1016/j.sna.2007.10.076.
Kaltenbrunner, M., White, M. S., Głowacki, E. D., Sekitani, T., Someya, T., Sariciftci, N. S., Bauer, S., 2012. Ultrathin and lightweight organic solar cells with high flexibility. Nature Communications 3, 770, doi:10.1038/ncomms1772.
Koh, S. J. A., Keplinger, C., Li, T., Bauer, S., Suo, Z., 2011. Dielectric Elastomer Generators: How Much Energy Can Be Converted #x003F. IEEE/ASME Transactions on Mechatronics 16, 33-41, doi:10.1109/TMECH.2010.2089635.
Kovacs, G., Lochmatter, P., Wissler, M., 2007. An arm wrestling robot driven by dielectric elastomer actuators. Smart Materials and Structures 16, S306, doi:10.1088/0964-1726/16/2/S16.
Kroon, M., 2010. A constitutive model for smooth muscle including active tone and passive viscoelastic behaviour. Mathematical Medicine and Biology 27, 129-155, doi:10.1093/imammb/dqp017.
Lee, E. H., 1969. Elastic-Plastic Deformation at Finite Strains. Journal of Applied Mechanics 36, 1-6, doi:10.1115/1.3564580.
Lubliner, J., 1985. A model of rubber viscoelasticity. Mechanics Research Communications 12, 93-99, doi:10.1016/0093-6413(85)90075-8.
Mannsfeld, S. C. B., Tee, B. C. K., Stoltenberg, R. M., Chen, C. V. H. H., Barman, S., Muir, B. V. O., Sokolov, A. N., Reese, C., Bao, Z., 2010. Highly sensitive flexible pressure sensors with microstructured rubber dielectric layers. Nature Materials 9, 859-864, doi:10.1038/nmat2834.
Maurel, W., Wu, Y., Magnenat Thalmann, N., Thalmann, D., 1998. Biomechanical Models for Soft Tissue Simulation.

Murtada, S. C., Kroon, M., Holzapfel, G. A., 2010. A calcium-driven mechanochemical model for prediction of force generation in smooth muscle. Biomechanics and Modeling in Mechanobiology 9, 749-762, doi:10.1007/s10237-010-0211-0.

Murtada, S. C., Arner, A., Holzapfel, G. A., 2012. Experiments and mechanochemical modeling of smooth muscle contraction: Significance of filament overlap. Journal of Theoretical Biology 297, 176-186, doi:10.1016/j.jtbi.2011.11.012.

O'Brien, B., McKay, T., Calius, E., Xie, S., Anderson, I., 2009. Finite element modelling of dielectric elastomer minimum energy structures. Applied Physics A 94, 507-514, doi:10.1007/s00339-008-4946-8.

Oomens, C. W. J., Maenhout, M., van Oijen, C. H., Drost, M. R., Baaijens, F. P., 2003. Finite element modelling of contracting skeletal muscle. Philosophical Transactions of the Royal Society of London. Series B, Biological Sciences 358, 1453-1460, doi:10.1098/rstb.2003.1345.

Parmley, W. W., Yeatman, L. A., Sonnenblick, E. H., 1970. Differences between isotonic and isometric force-velocity relations in cardiac and skeletal muscle. American Journal of Physiology -- Legacy Content 219, 546-550.

Pei, Q., Rosenthal, M., Stanford, S., Prahlad, H., Pelrine, R., 2004. Multiple-degrees-of-freedom electroelastomer roll actuators. Smart Materials and Structures 13, N86, doi:10.1088/0964-1726/13/5/N03.

Pelrine, R., Kornbluh, R., Pei, Q., Joseph, J., 2000a. High-Speed Electrically Actuated Elastomers with Strain Greater Than 100%. Science 287, 836-839, doi:10.1126/science.287.5454.836.

Pelrine, R., Kornbluh, R., Joseph, J., Heydt, R., Pei, Q., Chiba, S., 2000b. High-field deformation of elastomeric dielectrics for actuators. Materials Science and Engineering: C 11, 89-100, doi:10.1016/S0928-4931(00)00128-4.

Pelrine, R. E., Kornbluh, R. D., Joseph, J. P., 1998. Electrostriction of polymer dielectrics with compliant electrodes as a means of actuation. Sensors and Actuators A: Physical 64, 77-85, doi:10.1016/S0924-4247(97)01657-9.

Pipkin, A. C., Rogers, T. G., 1968. A non-linear integral representation for viscoelastic behaviour. Journal of the Mechanics and Physics of Solids 16, 59-72, doi:10.1016/0022-5096(68)90016-1.

Pipkin, A. C., Rivlin, R. S., 1997a. The Formulation of Constitutive Equations in Continuum Physics. I, 1111-1126, doi:10.1007/978-1-4612-2416-7_69.

Pipkin, A. C., Rivlin, R. S., 1997b. Electrical, Thermal and Magnetic Constitutive Equations for Deformed Isotropic Materials, 2443-2470, doi:10.1007/978-1-4612-2416-7_168.

Rajagopal, K. R., Wineman, A., 1999. A constitutive equation for non-linear electro-active solids. Acta Mechanica 135, 219-228, doi:10.1007/BF01305753.

Reese, S., Govindjee, S., 1998. A theory of finite viscoelasticity and numerical aspects. International Journal of Solids and Structures 35, 3455-3482, doi:10.1016/S0020-7683(97)00217-5.

Rogers, J. A., Someya, T., Huang, Y., 2010. Materials and Mechanics for Stretchable Electronics. Science 327, 1603-1607, doi:10.1126/science.1182383.

Röhrle, O., Davidson, J., Pullan, A., 2008. Bridging Scales: A Three-Dimensional Electromechanical Finite Element Model of Skeletal Muscle. SIAM Journal on Scientific Computing 30, 2882-2904, doi:10.1137/070691504.

Rudykh, S., Bhattacharya, K., deBotton, G., 2014. Multiscale instabilities in soft heterogeneous dielectric elastomers. Proceedings. Mathematical, Physical, and Engineering Sciences / The Royal Society 470, doi:10.1098/rspa.2013.0618.
S. Park, H., D. Nguyen, T., 2013. Viscoelastic effects on electromechanical instabilities in dielectric elastomers. Soft Matter 9, 1031-1042, doi:10.1039/C2SM27375F.
Shian, S., Diebold, R. M., Clarke, D. R., 2013. High-Speed, Compact, Adaptive Lenses Using In-Line Transparent Dielectric Elastomer Actuator Membranes. Society of Photo-Optical Instrumentation Engineers (SPIE).
Shian, S., Bertoldi, K., Clarke, D. R., 2015. Dielectric Elastomer Based "Grippers" for Soft Robotics. Advanced Materials 27, 6814-6819, doi:10.1002/adma.201503078.
Siboni, M. H., Ponte Castañeda, P., 2016. Macroscopic response of particle-reinforced elastomers subjected to prescribed torques or rotations on the particles. Journal of the Mechanics and Physics of Solids 91, 240-264, doi:10.1016/j.jmps.2016.02.028.
Siboni, M. H., Avazmohammadi, R., Castañeda, P. P., 2015. Electromechanical instabilities in fiber-constrained, dielectric-elastomer composites subjected to all-around dead-loading. Mathematics and Mechanics of Solids 20, 729-759, doi:10.1177/1081286514551501.
Sidoroff, F., 1974. Nonlinear Viscoelastic Model with an Intermediate Configuration.[UN MODELE VISCOELASTIQUE NON LINEAIRE AVEC CONFIGURATION INTERMEDIAIRE.]. Journal de Mecanique.
Simo, J. C., 1988a. A framework for finite strain elastoplasticity based on maximum plastic dissipation and the multiplicative decomposition: Part I. Continuum formulation. Computer Methods in Applied Mechanics and Engineering 66, 199-219, doi:10.1016/0045-7825(88)90076-X.
Simo, J. C., 1988b. A framework for finite strain elastoplasticity based on maximum plastic dissipation and the multiplicative decomposition. Part II: Computational aspects. Computer Methods in Applied Mechanics and Engineering 68, 1-31, doi:10.1016/0045-7825(88)90104-1.
Simo, J. C., Humphrey, J. D., 1998. Computational Inelasticity
Simo, J. C., Hughes, T. J. R., 2000. Computational Inelasticity. Springer, New York.
Son, S., 2011. Nonlinear Electromechanical Deformation of Isotropic and Anisotropic Electro-Elastic Materials.
Son, S., Goulbourne, N. C., 2009. Finite deformations of tubular dielectric elastomer sensors. Journal of Intelligent Material Systems and Structures 20, 2187-2199, doi:10.1177/1045389X09350718.
Sondergaard, C. S., Hodonsky, C. J., Khait, L., Shaw, J., Sarkar, B., Birla, R., Bove, E., Nolta, J., Si, M.-S., 2010. Human thymus mesenchymal stromal cells augment force production in self-organized cardiac tissue. The Annals of Thoracic Surgery 90, 796-803; discussion 803-804, doi:10.1016/j.athoracsur.2010.04.080.
Spencer, A. J. M., 1965. Isotropic integrity bases for vectors and second-order tensors. Archive for Rational Mechanics and Analysis 18, 51-82, doi:10.1007/BF00253982.
Spencer, A. J. M., 1971. Part III - Theory of Invariants. In: Eringen, A. C., (Ed.), Mathematics. Academic Press, pp. 239-353.
Spencer, A. J. M., 2004. Continuum Mechanics. Dover Publications, Mineola, N.Y.
Spencer, A. J. M., 2014. Continuum Theory of the Mechanics of Fibre-Reinforced Composites. Springer.

Spencer, A. J. M., Rivlin, R. S., 1962. Isotropic integrity bases for vectors and second-order tensors. Archive for Rational Mechanics and Analysis 9, 45-63, doi:10.1007/BF00253332.

Stålhand, J., Klarbring, A., Holzapfel, G. A., 2008. Smooth muscle contraction: Mechanochemical formulation for homogeneous finite strains. Progress in Biophysics and Molecular Biology 96, 465-481, doi:10.1016/j.pbiomolbio.2007.07.025.

Suo, Z., Zhao, X., Greene, W. H., 2008. A nonlinear field theory of deformable dielectrics. Journal of the Mechanics and Physics of Solids 56, 467-486, doi:10.1016/j.jmps.2007.05.021.

Thylander, S., Menzel, A., Ristinmaa, M., 2017. A non-affine electro-viscoelastic microsphere model for dielectric elastomers: Application to VHB 4910 based actuators. Journal of Intelligent Material Systems and Structures 28, 627-639, doi:10.1177/1045389X16651157.

Wang, H., Lei, M., Cai, S., 2013a. Viscoelastic deformation of a dielectric elastomer membrane subject to electromechanical loads. Journal of Applied Physics 113, 213508, doi:10.1063/1.4807911.

Wang, J., Nguyen, T. D., Park, H. S., 2013b. Electrostatically Driven Creep in Viscoelastic Dielectric Elastomers. Journal of Applied Mechanics 81, 051006-051006-5, doi:10.1115/1.4025999.

Wang, S., Decker, M., Henann, D. L., Chester, S. A., 2016. Modeling of dielectric viscoelastomers with application to electromechanical instabilities. Journal of the Mechanics and Physics of Solids 95, 213-229, doi:10.1016/j.jmps.2016.05.033.

Wang, Y., Son, S., Swartz, S. M., Goulbourne, N. C., 2012. A mixed von Mises distribution for modeling soft biological tissues with two distributed fiber properties. International Journal of Solids and Structures 49, 2914-2923, doi:10.1016/j.ijsolstr.2012.04.004.

Wineman, A., 2009. Nonlinear Viscoelastic Solids—A Review. Mathematics and Mechanics of Solids 14, 300-366, doi:10.1177/1081286509103660.

Winters, T. M., Sepulveda, G. S., Cottler, P. S., Kaufman, K. R., Lieber, R. L., Ward, S. R., 2009. Correlation Between Isometric Force and Intramuscular Pressure in Rabbit Tibialis Anterior Muscle with an Intact Anterior Compartment. Muscle & nerve 40, 79-85, doi:10.1002/mus.21298.

Zhang, J., Chen, H., Tang, L., Li, B., Sheng, J., Liu, L., 2015. Modelling of spring roll actuators based on viscoelastic dielectric elastomers. Applied Physics A 119, 825-835, doi:10.1007/s00339-015-9034-2.

Zhao, X., Suo, Z., 2008. Method to analyze programmable deformation of dielectric elastomer layers. Applied Physics Letters 93, 251902, doi:10.1063/1.3054159.

Zhao, X., Hong, W., Suo, Z., 2007. Electromechanical hysteresis and coexistent states in dielectric elastomers. Physical Review B 76, 134113, doi:10.1103/PhysRevB.76.134113.

Zhou, J., Jiang, L., Khayat, R. E., 2014. Viscoelastic effects on frequency tuning of a dielectric elastomer membrane resonator. Journal of Applied Physics 115, 124106, doi:10.1063/1.4869666.

Chapter 2. Continuum mechanics framework

2.1 Introduction

In this dissertation, the modeling of anisotropic active materials undergoing finite viscoelastic deformation is carried out using a continuum mechanics approach. The proposed constitutive models are developed using a structure informed invariant-based theory. (Pipkin and Rogers, 1968; Spencer, 1971; Spencer, 2004) Two material formulations are developed: an active anisotropic model for a smooth muscle rich arterial segment, and an active anisotropic model for a novel dielectric elastomer composite. In chapter 1, a basic overview of the characteristic features of these two materials was presented. In the case of arterial tissue, contractile units (smooth muscle cells) are uniformly and densely dispersed in an isotropic matrix along with two families of collagen fibrils. The composite is homogeneously treated as an anisotropic solid containing passive and active fibers. Upon activation, the fibers contract according to a chemo-mechanical model of the molecular motor units. The overall tissue behavior is time dependent and modeled using nonlinear viscoelastic theory, whereby a nonlinear evolution equation that captures essential features of the experimental data is proposed. In the case of the newly proposed dielectric elastomer composites, we consider a family of embedded contractile units having a preferred orientation within an isotropic dielectric elastomer matrix. The electromechanical coupling is electrostatic (the so-called Maxwell stress effect) and the composite can be activated either by contracting the fibers (in the plane) or contracting the matrix (out of plane).

In this chapter, the theoretical underpinnings of nonlinear continuum mechanics theory are summarized to establish a basis for developing the two new constitutive models. This chapter primarily serves to introduce notation and definitions used in the models. Theoretical aspects concerning the computational implementation of the models are addressed in Chapter 3. We begin with the relevant kinematic formulations in section 2.2. Multiplicative decomposition of the deformation gradients and the corresponding principal invariants for anisotropic media containing two fiber families are introduced in sections 2.3 and 2.4. Section 2.5 presents a review of the balance laws. Then strain energy functions and constitutive equations for passive media are described in section 2.6. Section 2.7 presents the two new active constitutive formulations proposed in this thesis. The constitutive relations are derived using a semi-phenomenological approach i.e. an approach which captures some structural features and is based on a discrete physical mechanism of contraction. For example, structure based models for smooth muscle contraction couple the sliding-filament theory of the actin-myosin complex within a continuum mechanics framework. (Böl et al., 2012; Kroon, 2010; Liu, 2014; Murtada and Holzapfel, 2014; Murtada et al., 2010; Murtada et al., 2012; Stålhand et al., 2008; Stålhand et al., 2011; Yang et al., 2003) The physical basis for the active components are individually derived in detail in Chapters 4 and 6. A chapter summary is provided in section 2.8.

2.2 Kinematics

2.2.1 Deformation gradient and strain tensor

In this chapter, the following notation is utilized. The dot product between two vectors is denoted by a single dot (·). The single contraction between a second order tensor and a vector or between two second order tensors is not denoted by any marker. The double

contraction operation is denoted by a double dot (:), i.e. $\mathbf{A}:\mathbf{B}=A_{ij}B_{ij}$. The tensor/outer product is denoted with the symbol ($\otimes$). Standard indicial notation is used when no corresponding tensor notation exists, and double indices imply summation from 1 to 3.

Consider an elastic solid occupying Ω_0, the undeformed fixed reference configuration, which moves to Ω, the deformed configuration. The transformation from the reference to the deformed configuration is denoted by χ such that $\mathbf{x}=\chi(\mathbf{X})\in\Omega$ for each $\mathbf{X}\in\Omega_0$. The deformation gradient $\mathbf{F}$ and Jacobian are defined as

$$\mathbf{F}=\frac{\partial\chi(\mathbf{X})}{\partial\mathbf{X}}, J=\det(\mathbf{F}), \tag{2.1}$$

with the physically-admissible convention $J>0$. Incompressible materials are subject to the constraint $J=1$.

Some important strain measures that are independent of rigid body rotations are introduced here. The right Cauchy-Green deformation tensor (in the reference configuration) is defined in terms of the deformation gradient $\mathbf{F}$ as

$$\mathbf{C}=\mathbf{F}^T\mathbf{F}. \tag{2.2}$$

Similarly, the left Cauchy-Green tensor (in the current configuration) is defined in terms of the deformation gradient $\mathbf{F}$ as

$$\mathbf{b}=\mathbf{F}\mathbf{F}^T, \tag{2.3}$$

Both right and left Cauchy-Green tensors are symmetric and positive definite, and are important strain measures in terms of material and spatial coordinates. The other two important strain measures are the Green-Lagrange strain tensor, $\mathbf{E}$, and the Euler-Almansi strain tensor, $\mathbf{e}$. They are formulated with respect to the reference and current configurations, respectively, as

$$\mathbf{E} = \frac{1}{2}\left(\mathbf{C} - \mathbf{I}\right), \tag{2.4}$$

$$\mathbf{e} = \frac{1}{2}\left(\mathbf{I} - \mathbf{b}^{-1}\right). \tag{2.5}$$

2.2.2 Time derivatives of kinematic quantities

The velocity and acceleration of a material point with respect to the reference configuration (also referred to as the material description of the velocity and acceleration fields) is obtained by taking the first and second derivatives of the motion χ with respect to time t (material time derivative) as

$$\mathbf{V}\left(\mathbf{X},t\right) = \frac{\partial \boldsymbol{\chi}\left(\mathbf{X},t\right)}{\partial t}, \mathbf{A}\left(\mathbf{X},t\right) = \frac{\partial \mathbf{V}\left(\mathbf{X},t\right)}{\partial t} = \frac{\partial^2 \boldsymbol{\chi}\left(\mathbf{X},t\right)}{\partial t^2}. \tag{2.6}$$

In the current configuration, the velocity and acceleration of a particle (also referred to as the spatial description of the velocity and acceleration fields) are denoted as $\mathbf{v}\left(\mathbf{x},t\right)$ and $\mathbf{a}\left(\mathbf{x},t\right)$. The two descriptions are transformed by using the motion, namely,

$$\mathbf{V}\left(\mathbf{X},t\right) = \mathbf{V}\left(\boldsymbol{\chi}^{-1}\left(\mathbf{x},t\right),t\right) = \mathbf{v}\left(\mathbf{x},t\right), \mathbf{A}\left(\mathbf{X},t\right) = \mathbf{A}\left(\boldsymbol{\chi}^{-1}\left(\mathbf{x},t\right),t\right) = \mathbf{a}\left(\mathbf{x},t\right). \tag{2.7}$$

They represent functions of different arguments and have the same values. The derivative of a spatial velocity field $\mathbf{v}\left(\mathbf{x},t\right)$ with respect to the spatial coordinates is defined by

$$\frac{\partial \mathbf{v}\left(\mathbf{x},t\right)}{\partial \mathbf{x}} = grad\mathbf{v}\left(\mathbf{x},t\right) = \mathbf{l}\left(\mathbf{x},t\right), \tag{2.8}$$

and the spatial field $\mathbf{l}$ is called the spatial velocity gradient. The derivative of a material velocity field $\mathbf{V}\left(\mathbf{X},t\right)$ with respect to the material coordinates is defined by

$$\frac{\partial \mathbf{V}\left(\mathbf{X},t\right)}{\partial \mathbf{X}} = Grad\mathbf{V}\left(\mathbf{X},t\right). \tag{2.9}$$

The material time derivative of the deformation gradient $\mathbf{F}$ is

$$\dot{\mathbf{F}}(\mathbf{X},t)=\frac{\partial}{\partial t}\left(\frac{\partial \boldsymbol{\chi}(\mathbf{X},t)}{\partial \mathbf{X}}\right)=\frac{\partial}{\partial \mathbf{X}}\left(\frac{\partial \boldsymbol{\chi}(\mathbf{X},t)}{\partial t}\right)=\frac{\partial \mathbf{V}(\mathbf{X},t)}{\partial \mathbf{X}}=Grad\mathbf{V}(\mathbf{X},t), \tag{2.10}$$

which is called the material velocity gradient. The relationship between the spatial and material velocity gradients is obtained through the chain rule as,

$$\mathbf{l}=\frac{\partial \mathbf{v}}{\partial \mathbf{x}}=\frac{\partial \mathbf{V}}{\partial \mathbf{X}}\frac{\partial \mathbf{X}}{\partial \mathbf{x}}=\dot{\mathbf{F}}\mathbf{F}^{-1}. \tag{2.11}$$

This concept is very useful with respect to quantities involving the derivatives of the deformation gradient such as the time derivative of the Green-Lagrange strain tensor and in deriving the objective stress rate using Lie time derivatives. Note that in general the spatial velocity gradient $\mathbf{l}$ is non-symmetric. The time derivative of the Green-Lagrange strain tensor in Eq. (2.4) is given using Eq.(2.11) as

$$\dot{\mathbf{E}}=\frac{1}{2}\left(\dot{\mathbf{F}}^{T}\mathbf{F}+\mathbf{F}^{T}\dot{\mathbf{F}}\right)=\mathbf{F}^{T}\frac{1}{2}\left(\mathbf{l}+\mathbf{l}^{T}\right)\mathbf{F}=\mathbf{F}^{T}\mathbf{d}\mathbf{F}, \tag{2.12}$$

where $\mathbf{d}=\frac{1}{2}\left(\mathbf{l}+\mathbf{l}^{T}\right)$ is the symmetric part of the spatial velocity gradient $\mathbf{l}$ (i.e. the rate of the deformation tensor), and the antisymmetric part of the spatial velocity gradient $\mathbf{l}$ is $\mathbf{w}=\frac{1}{2}\left(\mathbf{l}-\mathbf{l}^{T}\right)$ (i.e. the spin tensor, also called the rate of the rotation tensor or the vorticity tensor).

2.2.3 Stress tensors

Here, important forms of stress measures are provided and summarized. The Cauchy stress tensor $\boldsymbol{\sigma}$ is the internal stress measurement in the spatial description, also known as the true stress tensor. The first Piola-Kirchhoff stress tensor $\mathbf{P}$ (or the Piola stress tensor) is the internal stress measurement in the material description, also called the nominal stress tensor. Note that like $\mathbf{F}$, the first Piola-Kirchhoff stress tensor is an asymmetric two-point tensor in general and relates an area vector in the initial

configuration to the corresponding force vector in the current configuration. The relationship between the Cauchy stress tensor and the first Piola-Kirchhoff stress tensor is

$$\mathbf{P} = J\boldsymbol{\sigma}\mathbf{F}^{-T}. \tag{2.13}$$

For convenience, the so-called Kirchhoff stress tensor is introduced by multiplying the Cauchy stress tensor by the volume ratio J as

$$\boldsymbol{\tau} = J\boldsymbol{\sigma}. \tag{2.14}$$

Further, the second Piola-Kirchhoff stress tensor $\mathbf{S}$ is introduced as a symmetric stress tensor and results from a complete transformation of the Cauchy stress to the reference configuration as,

$$\mathbf{S} = \mathbf{F}^{-1}\mathbf{P} = J\mathbf{F}^{-1}\boldsymbol{\sigma}\mathbf{F}^{-T}. \tag{2.15}$$

Even though it cannot be interpreted physically, this pure mathematical quantity is an important stress measure in continuum theory and computational formulations, which will be discussed further in Chapter 3.

2.2.4 Push-forward, pull-back operations

The transformations of vector and tensor-valued quantities between the reference and current configuration are called push-forward and pull-back operations and are denoted by $\chi_*(\bullet)$ and $\chi_*^{-1}(\bullet)$, respectively. Specifically, a push-forward operation transforms first and second order tensor-valued quantities based on the reference configurations to the current configurations. The push-forward and pull-back operations on covariant second-order tensors (such as $\mathbf{E}$, $\mathbf{C}$, $\mathbf{e}$, $\mathbf{b}^{-1}$ in continuum mechanics) are defined as

$$\chi_*(\bullet) = \mathbf{F}^{-T}(\bullet)\mathbf{F}^{-1}, \chi_*^{-1}(\bullet) = \mathbf{F}^{T}(\bullet)\mathbf{F}. \tag{2.16}$$

For example, we can transform the material based Green-Lagrange strain tensor, $\mathbf{E}$, to the spatial based Euler-Almansi strain tensor, $\mathbf{e}$, through a push-forward operation as,

$$\mathbf{e} = \frac{1}{2}\left(\mathbf{I} - \mathbf{b}^{-1}\right) = \mathbf{F}^{-T}\left[\frac{1}{2}\left(\mathbf{C} - \mathbf{I}\right)\right]\mathbf{F}^{-1} = \mathbf{F}^{-T}\mathbf{E}\mathbf{F}^{-1} = \chi_*(\mathbf{E}). \tag{2.17}$$

A push-back is the inverse operation and transforms first and second order tensor-valued quantities based on the current configurations to the reference configurations. Similar to Eq. (2.17), the pull-back of Euler-Almansi strain tensor, **e**, is the Green-Lagrange strain tensor,

$$\mathbf{E} = \frac{1}{2}\left(\mathbf{C} - \mathbf{I}\right) = \mathbf{F}^{T}\left[\frac{1}{2}\left(\mathbf{C} - \mathbf{I}\right)\right]\mathbf{F} = \mathbf{F}^{T}\mathbf{e}\mathbf{F} = \chi_*^{-1}(\mathbf{e}). \tag{2.18}$$

Therefore, the push-forward and pull-back operations are based on multiplying by one of the following forms of the deformation gradient, i.e. $\mathbf{F}^{-T}, \mathbf{F}^{-1}, \mathbf{F}^{T}, \mathbf{F}$. In contrast, the push-forward and pull-back operations on contravariant second-order tensors (such as most of the common stress tensors, $\mathbf{C}^{-1}$, and $\mathbf{b}$) are defined as

$$\chi_*(\bullet)^{\#} = \mathbf{F}(\bullet)^{\#}\mathbf{F}^{T}, \chi_*^{-1}(\bullet)^{\#} = \mathbf{F}^{-1}(\bullet)^{\#}\mathbf{F}^{-T}. \tag{2.19}$$

The conversion of the Kirchhoff stress tensor to the second Piola-Kirchhoff stress tensor is through the pull-back operation

$$\mathbf{S} = \chi_*^{-1}(\boldsymbol{\tau}^{\#}) = \mathbf{F}^{-1}\boldsymbol{\tau}\mathbf{F}^{-T}, \tag{2.20}$$

and the conversion of the second Piola-Kirchhoff stress tensor to the Kirchhoff stress tensor is through the push-forward operation, i.e.

$$\boldsymbol{\tau} = \chi_*(\mathbf{S}^{\#}) = \mathbf{F}\mathbf{S}\mathbf{F}^{T}. \tag{2.21}$$

2.2.5 Lie derivatives

Many possible objective stress rates may be defined through the Lie derivative, which is critical when deriving the tangent modulus (as shown in the computational

implementations of Chapter 3). The Lie derivative of a spatial tensor with a contravariant basis (such as $\mathbf{C}^{-1}$ and $\mathbf{b}$) is defined by (Marsden and Hughes, 1994)

$$\mathcal{L}_v(\mathbf{g}) = \mathbf{F}\left\{\frac{\partial}{\partial t}\left[\mathbf{F}^{-1}\mathbf{g}\mathbf{F}^{-T}\right]\right\}\mathbf{F}^T. \tag{2.22}$$

That is, the tensor $\mathbf{g}$ is transformed first to the reference configuration by a pull-back operation, and then the material time derivative is applied before a push forward operation to transform it to the current configuration. The Lie derivative of a spatial tensor with a covariant basis (such as $\mathbf{E}$, $\mathbf{C}$, $\mathbf{e}$, $\mathbf{b}^{-1}$) is defined by (Marsden and Hughes, 1994)

$$\mathcal{L}_v(\mathbf{g}) = \mathbf{F}^{-T}\left\{\frac{\partial}{\partial t}\left[\mathbf{F}^T\mathbf{g}\mathbf{F}\right]\right\}\mathbf{F}^{-1}. \tag{2.23}$$

The Lie time derivative of the Piola-Kirchhoff stress is derived as

$$\begin{aligned}
\mathcal{L}_v(\boldsymbol{\tau}) &= \mathbf{F}\left\{\frac{\partial}{\partial t}\left[\mathbf{F}^{-1}\boldsymbol{\tau}\mathbf{F}^{-T}\right]\right\}\mathbf{F}^T = \mathbf{F}\left\{\frac{\partial \mathbf{F}^{-1}}{\partial t}\boldsymbol{\tau}\mathbf{F}^{-T} + \mathbf{F}^{-1}\frac{\partial \boldsymbol{\tau}}{\partial t}\mathbf{F}^{-T} + \mathbf{F}^{-1}\boldsymbol{\tau}\frac{\partial \mathbf{F}^{-T}}{\partial t}\right\}\mathbf{F}^T \\
&= \mathbf{F}\left\{\dot{\mathbf{F}}^{-1}\boldsymbol{\tau}\mathbf{F}^{-T} + \mathbf{F}^{-1}\dot{\boldsymbol{\tau}}\mathbf{F}^{-T} + \mathbf{F}^{-1}\boldsymbol{\tau}\dot{\mathbf{F}}^{-T}\right\}\mathbf{F}^T \\
&= -\mathbf{l}\boldsymbol{\tau} + \dot{\boldsymbol{\tau}} - \boldsymbol{\tau}\mathbf{l}^T,
\end{aligned} \tag{2.24}$$

which will be used in the derivatives of the tangent modulus in Chapter 3. For another example, the Lie derivative of the Euler-Almansi strain tensor is

$$\mathcal{L}_v(\mathbf{e}) = \mathbf{F}^{-T}\left\{\frac{\partial}{\partial t}\left[\mathbf{F}^T\mathbf{e}\mathbf{F}\right]\right\}\mathbf{F}^{-1} = \mathbf{F}^{-T}\dot{\mathbf{E}}\mathbf{F}^{-1}, \tag{2.25}$$

which can be rewritten as

$$\dot{\mathbf{E}} = \mathbf{F}^T\mathcal{L}_v(\mathbf{e})\mathbf{F}. \tag{2.26}$$

Comparing Eq.(2.26) with Eq.(2.12), it demonstrates that the Lie derivative of the Euler-Almansi strain tensor is equivalent to the symmetric part of the spatial velocity gradient $\mathbf{d}$.

2.3 Multiplicative decomposition of the deformation gradient

In the current work, we choose a broadly adopted internal variable approach using the multiplicative decomposition of the deformation gradient to model the finite inelastic behavior of viscoelasticity in soft materials. The multiplicative decomposition of the deformation gradient into thermoelastic and plastic parts was originally proposed by (Lee, 1969; Lee and Liu, 1967) in elastoplasticity and later borrowed for nonlinear viscoelastic materials by (Sidoroff, 1974). Later on, the multiplicative decomposition and evolution equations were formalized in a general nonlinear viscoelastic theory. (Haupt, 1993; Holzapfel, 1996; Kaliske and Rothert, 1997; Koh and Eringen, 1962; Lion, 1996; Simo, 1987; Simo and Miehe, 1992) The split of the free energy functions into equilibrium and a nonequilibrium parts was proposed by (Reese and Govindjee, 1998), which was an extension of a previous theory by (Lubliner, 1985), who divided the free energy function into rate-independent and time dependent parts. Subsequently, the stress expressions in the constitutive equations are naturally separated into equilibrium and nonequilibrium parts as well. One important point in developing constitutive models in this form is the formulation of the evolution equations for the internal variable.

The deformation gradient is decomposed into elastic and inelastic parts (viscous part for a viscoelastic material) as

$$\mathbf{F} = \mathbf{F}_e\mathbf{F}_{in} = \mathbf{F}_e\mathbf{F}_p = \mathbf{F}_e\mathbf{F}_v , \tag{2.27}$$

where $\mathbf{F}_e$ is the elastic part of deformation gradient, and $\mathbf{F}_{in}$ (or $\mathbf{F}_p$, $\mathbf{F}_v$) is the inelastic (or plastic, viscous) part of the deformation gradient. An intermediate configuration is introduced and the inelastic part of the deformation gradient maps the reference configuration to the intermediate configuration and elastic part of the deformation

gradient maps the intermediate configuration to the current configuration (see Figure 8). It is noted that the intermediate configuration is a theoretical concept to describe the unloaded state in a small neighborhood of a particle and to assist in understanding the mathematical decomposition of the deformation gradient.

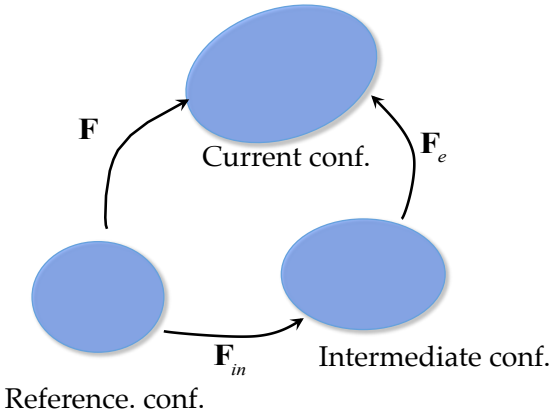

Figure 8. Schematics of multiplicative decomposition in the small neighborhood of a particle.

Strain measurements which are independent of rigid body rotations, such as the elastic and viscous right and left Cauchy-Green strain tensors, can be defined as

$$\mathbf{C}_e = \mathbf{F}_e^T \mathbf{F}_e,\ \mathbf{C}_{in} = \mathbf{F}_{in}^T \mathbf{F}_{in},\ \mathbf{b}_e = \mathbf{F}_e \mathbf{F}_e^T,\ \mathbf{b}_{in} = \mathbf{F}_{in} \mathbf{F}_{in}^T, \tag{2.28}$$

which are often used in the development of constitutive laws. For a fiber-reinforced solid, the parallel multiplicative decompositions of the deformation gradient into elastic and viscous parts for the matrix and fibers is

$$\mathbf{F} = \mathbf{F}_M^e \mathbf{F}_M^v = \mathbf{F}_F^e \mathbf{F}_F^v \ . \tag{2.29}$$

The viscous deformation gradients $\mathbf{F}_M^v$ and $\mathbf{F}_F^v$ describe the mappings from the reference configurations to the intermediate configurations. The elastic deformation gradients $\mathbf{F}_M^e$ and $\mathbf{F}_F^e$ describe the mappings from the intermediate configurations to the current configurations. Correspondingly, strain measurements which are independent of rigid

body rotations, such as the elastic and viscous right Cauchy-Green strain tensors, can be defined for the matrix and fiber as

$$\mathbf{C}_M^e = \mathbf{F}_M^{e\,T}\mathbf{F}_M^e,\ \mathbf{C}_M^v = \mathbf{F}_M^{v\,T}\mathbf{F}_M^v,\ \mathbf{C}_F^e = \mathbf{F}_F^{eT}\mathbf{F}_F^e,\ \mathbf{C}_F^v = \mathbf{F}_F^{vT}\mathbf{F}_F^v. \tag{2.30}$$

2.4 Invariants for hyperelastic and viscoelastic materials

The material couplings between mechanical and chemical or electrical effects are incorporated directly into the proposed constitutive models in Chapters 4 and 6. It is essentially assumed that the microscale structural analysis and microscopic properties (chemical and electrical quantities) are extracted to the homogenized macroscale based on the assumption that the active fibers are homogeneously and continuously distributed throughout the continuum.

Isotropic materials

For isotropic materials, the strain energy function takes the general form

$$\Psi(\mathbf{F}) = \Psi(I_1, I_2, I_3), \tag{2.31}$$

where I_1, I_2, I_3 are the principal invariants. These are defined as

$$I_1 = \mathbf{C} : \mathbf{I} = tr(\mathbf{C}), \tag{2.32}$$

$$I_2 = \frac{1}{2}\left(I_1^2 - \mathbf{C}^2 : \mathbf{I}\right) = tr\left(cof\left(\mathbf{C}\right)\right), \tag{2.33}$$

$$I_3 = \det(\mathbf{C}), \tag{2.34}$$

and represent the length, area, and volume change of the solid; $tr(\mathbf{C})$ and $cof(\mathbf{C})$ are the trace and cofactor of the right Cauchy Green tensor $\mathbf{C}$, respectively. For an isotropic viscoelastic material, the strain energy function takes the following general form

$$\Psi(\mathbf{F}, \mathbf{F}_v) = \Psi(I_1, I_2, I_3, I_1^v, I_2^v, I_3^v), \tag{2.35}$$

where $I_1^v \sim I_3^v$ are the nonequilibrium principal invariants. Since the right elastic Cauchy-Green tensor can be expressed by $\mathbf{C}_M^e = \mathbf{F}_M^{v,-T}\mathbf{C}\mathbf{F}_M^{v,-1}$, the principal invariants of the right elastic Cauchy-Green tensor have the two alternative expressions

$$I_1^e = \mathbf{C}_M^e : \mathbf{I} = \mathbf{C} : \mathbf{C}_M^{v,-1} \ , \tag{2.36}$$

$$I_2^e = \frac{1}{2}\left(I_{M_1}^{e\ 2} - \mathbf{C}_M^{e\ 2} : \mathbf{I}\right) = \frac{1}{2}\left(I_{M_1}^{e\ 2} - \mathbf{C}\mathbf{C}_M^{v,-1} : \mathbf{C}_M^{v,-1}\mathbf{C}\right) \ , \tag{2.37}$$

$$I_3^e = \det\left(\mathbf{C}_M^e\right) = \det\left(\mathbf{C}\mathbf{C}_M^{v,-1}\right) \ . \tag{2.38}$$

Additionally, the principal invariants of the right viscous Cauchy-Green tensor are

$$I_1^v = \mathbf{C}_M^v : \mathbf{I}, \tag{2.39}$$

$$I_2^v = \frac{1}{2}\left(I_{M_1}^{v\ 2} - \mathbf{C}_M^{v\ 2} : \mathbf{I}\right), \tag{2.40}$$

$$I_3^v = \det\left(\mathbf{C}_M^v\right). \tag{2.41}$$

Anisotropic materials

Here, we consider two families of fibers embedded in a three dimensional matrix. These two families of fibers are oriented in two distinct directions. In addition, each family of fibers is assumed to line in its direction perfectly, i.e. fiber distributions are not considered in the current work. For further information about the fiber distributions, refer to (Gasser et al., 2006; Gizzi et al., 2016; Holzapfel et al., 2015; Wang et al., 2012). The isotropic material invariants for the matrix are identical to those previously derived. Fiber orientation vectors are $\mathbf{V}_1$ and $\mathbf{V}_2$ in the reference configuration, corresponding to $\mathbf{v}_1$ and $\mathbf{v}_2$ in the current configuration. Thus we have for anisotropic media

$$\Psi\left(\mathbf{F}, \mathbf{V}_1, \mathbf{V}_2\right) = \Psi\left(I_1 \sim I_9\right). \tag{2.42}$$

where $I_1 \sim I_9$ are the principal invariants characterized by $\mathbf{C}$, $\mathbf{V}_1$ and $\mathbf{V}_2$. The fiber invariants are

$$\begin{aligned} I_4 &= \mathbf{V}_1 \cdot \mathbf{C}\mathbf{V}_1, \quad I_5 = \mathbf{V}_1 \cdot \mathbf{C}^2\mathbf{V}_1, \\ I_6 &= \mathbf{V}_2 \cdot \mathbf{C}\mathbf{V}_2, \quad I_7 = \mathbf{V}_2 \cdot \mathbf{C}^2\mathbf{V}_2, \\ I_8 &= \mathbf{V}_1 \cdot \mathbf{C}\mathbf{V}_2, \quad I_9 = \mathbf{V}_1 \cdot \mathbf{C}^2\mathbf{V}_2, \end{aligned} \tag{2.43}$$

where I_4 and I_6 are the square of the fiber stretches (see Eq (2.51)), I_5 and I_7 are a higher order term of I_4 and I_6 respectively, I_8 and I_9 are the cross terms of these two fiber families.

For anisotropic viscoelastic materials, the strain energy function takes the following form

$$\Psi\left(\mathbf{F}, \mathbf{F}_v, \mathbf{V}_1, \mathbf{V}_2\right) = \Psi\left(I_1 \sim I_9, I_1^v \sim I_9^v\right). \tag{2.44}$$

where $I_1^v \sim I_9^v$ are the viscous principal invariants. The elastic and viscous parts are defined as

$$\begin{aligned} I_4^v &= \mathbf{V}_1 \cdot \mathbf{C}_F^v \mathbf{V}_1, \quad I_5^v = \mathbf{V}_1 \cdot \mathbf{C}_F^{v,2} \mathbf{V}_1, \\ I_6^v &= \mathbf{V}_2 \cdot \mathbf{C}_F^v \mathbf{V}_2, \quad I_7^v = \mathbf{V}_2 \cdot \mathbf{C}_F^{v,2} \mathbf{V}_2, \\ I_8^v &= \mathbf{V}_1 \cdot \mathbf{C}_F^v \mathbf{V}_2, \quad I_9^v = \mathbf{V}_1 \cdot \mathbf{C}_F^{v,2} \mathbf{V}_2. \end{aligned} \tag{2.45}$$

$$\begin{aligned} I_4^e &= \mathbf{V}_1 \cdot \mathbf{C}_F^e \mathbf{V}_1, \quad I_5^e = \mathbf{V}_1 \cdot \mathbf{C}_F^{e,2} \mathbf{V}_1, \\ I_6^e &= \mathbf{V}_2 \cdot \mathbf{C}_F^e \mathbf{V}_2, \quad I_7^e = \mathbf{V}_2 \cdot \mathbf{C}_F^{e,2} \mathbf{V}_2, \\ I_8^e &= \mathbf{V}_1 \cdot \mathbf{C}_F^e \mathbf{V}_2, \quad I_9^e = \mathbf{V}_1 \cdot \mathbf{C}_F^{e,2} \mathbf{V}_2. \end{aligned} \tag{2.46}$$

It is noted that the total invariants I_4 and I_6 have relationships with their elastic and viscous parts as

$$I_4^e = \frac{\mathbf{V}_1 \cdot \mathbf{C}\mathbf{V}_1}{\mathbf{V}_1 \cdot \mathbf{C}_F^v \mathbf{V}_1} = \frac{I_4}{I_4^v}, \quad I_6^e = \frac{\mathbf{V}_2 \cdot \mathbf{C}\mathbf{V}_2}{\mathbf{V}_2 \cdot \mathbf{C}_F^v \mathbf{V}_2} = \frac{I_6}{I_6^v}. \tag{2.47}$$

Next, we introduce the fiber stretch and show its relationship with the invariants I_4 and I_6. Any fiber with fiber orientation vector $\mathbf{V}$ in the reference configuration is mapped to the current configuration according to

$$\begin{aligned} \mathbf{FV} &= \lambda_F \mathbf{v}, \\ \mathbf{FV} &= \left(\mathbf{F}_F^e \mathbf{F}_F^v\right)\mathbf{V} = \mathbf{F}_F^e\left(\mathbf{F}_F^v \mathbf{V}\right), \end{aligned} \tag{2.48}$$

where λ_F is the fiber stretch; a fiber mapping from the reference configuration to the intermediate configuration is denoted by $\mathbf{F}_F^v\mathbf{V}$; and $\mathbf{F}_F^e\left(\mathbf{F}_F^v\mathbf{V}\right)$ is the subsequent fiber mapping from the intermediate configuration to the current configuration. The unit fiber orientation vector in the intermediate configuration is thus defined as $\mathbf{V}^* = \mathbf{F}_F^v\mathbf{V} / \left\|\mathbf{F}_F^v\mathbf{V}\right\|$. Specifically, the fiber deformation mapped from the reference to the intermediate configuration and from the intermediate to the current configuration are defined as the viscous fiber stretch (λ_F^v) and the elastic fiber stretch (λ_F^e) respectively, that is,

$$\lambda_F^v \mathbf{V}^* = \mathbf{F}_F^v \mathbf{V}, \quad \lambda_F^e \mathbf{v} = \mathbf{F}_F^e \mathbf{V}^* \tag{2.49}$$

Thus, from Eq (2.48) and Eq (2.49), λ_F, λ_F^v, and λ_F^e have the following relationship:

$$\lambda_F = \lambda_F^v \lambda_F^e. \tag{2.50}$$

Furthermore, the fiber stretches can be expressed using the right Cauchy-Green tensor as

$$\left(\lambda_F\right)^2 = \left(\lambda_F \mathbf{v}\right)\cdot\left(\lambda_F \mathbf{v}\right) = \left(\mathbf{FV}\right)\cdot\left(\mathbf{FV}\right) = \mathbf{V}\cdot\mathbf{CV} = I_4, \tag{2.51}$$

$$\left(\lambda_F^v\right)^2 = \mathbf{V}\cdot\mathbf{C}_F^v\mathbf{V} = I_4^v, \quad \left(\lambda_F^e\right)^2 = \mathbf{V}\cdot\mathbf{C}_F^e\mathbf{V} = I_4^e. \tag{2.52}$$

where $I_4\left(\text{or } I_6\right)$ is the square of the fiber stretch.

For an electro-active material, the constitutive formulation depends on the electric field **E**. The invariants for an anisotropic electroactive material are

$$\Psi\left(\mathbf{F},\mathbf{F}_v,\mathbf{V}_1,\mathbf{V}_2,\mathbf{E}\right)=\Psi\left(I_1\sim I_9,I_1^v\sim I_9^v,I_{10}\sim I_{12}\right) \tag{2.53}$$

where $I_{10}\sim I_{12}$ are the principal invariants associated with the electric field. They are defined as

$$I_{10}=\mathbf{E}\cdot\mathbf{E},\ I_{11}=\mathbf{E}\cdot\mathbf{C}^{-1}\cdot\mathbf{E},\ I_{12}=\mathbf{E}\cdot\mathbf{C}^{-2}\cdot\mathbf{E}, \tag{2.54}$$

where I_{10} and I_{11} represent the quadratics of the nominal and true electric field **E** and **e**, since the true electric field **e** is expressed in term of the nominal electric field **E** as

$$\mathbf{e}=\mathbf{F}^{-T}\mathbf{E}, \tag{2.55}$$

the invariant I_{11} is essentially the quadratic of the magnitude of the true electric field

$$I_{11}=\mathbf{E}\cdot\mathbf{C}^{-1}\cdot\mathbf{E}=\mathbf{E}\cdot\left(\mathbf{F}^T\mathbf{F}\right)^{-1}\cdot\mathbf{E}=\mathbf{E}\cdot\left(\mathbf{F}^{-1}\mathbf{F}^{-T}\right)\cdot\mathbf{E}=\mathbf{F}^{-T}\mathbf{E}\cdot\mathbf{F}^{-T}\mathbf{E}=\mathbf{e}\cdot\mathbf{e}. \tag{2.56}$$

2.5 Balance equations

Initial boundary value problems of nonlinear elastic and viscoelastic materials satisfy the balance equations, and their mechanical responses are calculated by solving the balance equations for given boundary and loading conditions together with their specific constitutive laws. In this section, we discuss the consequence of fundamental balance principles, i.e. the momentum balance and the second law of thermodynamics (in inequality form). The balance equations introduced here are in local form (also called strong form since they must be satisfied for each particle of the body at each time). The constitutive laws for the materials are discussed in the subsequent section.

From the balance of linear momentum, a spatial tensor field (Cauchy stress) $\boldsymbol{\sigma}$ satisfies Cauchy's first equation of motion in the local form (spatial description) as

$$div\boldsymbol{\sigma}+\mathbf{b}-\rho\dot{\mathbf{v}}=0. \tag{2.57}$$

where $\mathbf{b}$ is the body force, ρ is the density, $\dot{\mathbf{v}}$ is the acceleration, and *div* denotes the divergence operation with respect to the current configuration. In the absence of body forces, it reduces to Cauchy's equation of equilibrium for zero inertial effects,

$$div\boldsymbol{\sigma} = 0. \tag{2.58}$$

In the reference configuration, Cauchy's equation of equilibrium takes the form

$$DIV\mathbf{P} = 0, \tag{2.59}$$

where $\mathbf{P}$ is the first Piola-Kirchhoff stress. The balance of angular momentum yields one crucial result that the Cauchy stress tensor $\boldsymbol{\sigma}$ is symmetric, i.e.

$$\boldsymbol{\sigma} = \boldsymbol{\sigma}^T, \tag{2.60}$$

which is often referred to as Cauchy's second equation of motion. Thus the Kirchhoff stress tensor $\boldsymbol{\tau}$ and the second Piola-Kirchhoff stress tensor $\mathbf{S}$ is also symmetric. However, the first Piola-Kirchhoff stress tensor $\mathbf{P}$ is not symmetric in general.

The Clausius-Planck inequality is one strong form of the second law of thermodynamics and takes the following form in the material description,

$$D_{\text{int}} = \mathbf{P} : \dot{\mathbf{F}} - \dot{\Psi} - \eta\dot{\Theta} \geq 0 \tag{2.61}$$

where η is the entropy, Θ is the absolute temperature, and Ψ refers to the Helmholtz free-energy function when incorporating the thermal variables η or Θ. The internal dissipation is zero for reversible processes and larger than zero for irreversible processes. In a pure mechanical regime where thermal effects are negligible, the inequality (2.61) reduces to

$$D_{\text{int}} = \underbrace{\mathbf{P} : \dot{\mathbf{F}}}_{w_{\text{int}}} - \dot{\Psi} = w_{\text{int}} - \dot{\Psi} \geq 0, \tag{2.62}$$

where $w_{\text{int}} = \mathbf{P} : \dot{\mathbf{F}}$ is the rate of internal mechanical work (or stress-power) per unit reference volume. The alternative expressions for the rate of internal mechanical work can be derived in alternative forms as

$$w_{\text{int}} = \mathbf{P} : \dot{\mathbf{F}} = \mathbf{S} : \dot{\mathbf{E}} = \mathbf{S} : \frac{1}{2}\dot{\mathbf{C}} = J\boldsymbol{\sigma} : \mathbf{d} = \boldsymbol{\tau} : \mathbf{d} \,. \tag{2.63}$$

The internal virtual work done by the stresses with respect to the undeformed volume is expressed as

$$\delta w_{\text{int}} = \int_{\Omega_0} \mathbf{P} : \dot{\mathbf{F}} \, dV = \int_{\Omega_0} \mathbf{S} : \dot{\mathbf{E}} dV = \int_{\Omega_0} \mathbf{S} : \frac{1}{2}\dot{\mathbf{C}} dV = \int_{\Omega_0} J\boldsymbol{\sigma} : \mathbf{d} dV = \int_{\Omega_0} \boldsymbol{\tau} : \mathbf{d} dV \,. \tag{2.64}$$

The above equation indicates that the first Piola-Kirchhoff stress tensor is work conjugate to the rate of the deformation gradient $\dot{\mathbf{F}}$. The second Piola-Kirchhoff stress tensor is work conjugate to $1/2\dot{\mathbf{C}}$, and the Kirchhoff stress tensor is work conjugate to $\mathbf{d}$ with respect to the initial volume. Alternatively, the internal virtual work can be expressed in the material coordinate system by applying $dv = JdV$ and rewriting Eq (2.64) as

$$\delta w_{\text{int}} == \int_{\Omega_0} J\boldsymbol{\sigma} : \mathbf{d} dV = \int_{\Omega} \boldsymbol{\sigma} : \mathbf{d} dv \,, \tag{2.65}$$

which calculates the internal virtual work with respect to the current deformed volume and gives the work per unit current volume. The Cauchy stress tensor is work conjugate to $\mathbf{d}$ with respect to the current volume.

2.6 Strain energy function and constitutive equations

The strain energy functions are further particularized in this section. The rate of the strain energy function is obtained by chain rule as

$$\dot{\Psi} = \frac{\partial \Psi\left(\mathbf{F}(\mathbf{X}), \mathbf{X}\right)}{\partial \mathbf{F}} : \dot{\mathbf{F}} \,. \tag{2.66}$$

Here, we derive the constitutive equation for hyperelastic materials from the Clausius-Planck inequality. Inserting Eq (2.66) into Eq (2.62) gives

$$D_{\text{int}} = \mathbf{P} : \dot{\mathbf{F}} - \dot{\Psi} = \left(\mathbf{P}\left(\mathbf{F}(\mathbf{X}),\mathbf{X}\right) - \frac{\partial \Psi\left(\mathbf{F}(\mathbf{X}),\mathbf{X}\right)}{\partial \mathbf{F}} \right) : \dot{\mathbf{F}}(\mathbf{X}) = 0 \tag{2.67}$$

which reveals the general constitutive equation in terms of first Piola-Kirchhoff stress as

$$\mathbf{P}\left(\mathbf{F}(\mathbf{X}),\mathbf{X}\right) = \frac{\partial \Psi\left(\mathbf{F}(\mathbf{X}),\mathbf{X}\right)}{\partial \mathbf{F}} \ , \tag{2.68}$$

since $\mathbf{F}$ and hence $\dot{\mathbf{F}}$ can be chosen arbitrarily. From the concept of objectivity, Ψ must remain invariant for rigid body rotations because it is a scalar

$$\Psi\left(\mathbf{F},\mathbf{X}\right) = \Psi\left(\mathbf{Q}\mathbf{F},\mathbf{X}\right), \tag{2.69}$$

which indicates that Ψ depends on the stretch components of $\mathbf{F}$. Recalling that $\mathbf{C} = \mathbf{F}^T\mathbf{F} = \mathbf{U}^2$, therefore, for convenience, Ψ is often expressed as a function of $\mathbf{C}$ as

$$\Psi\left(\mathbf{F}(\mathbf{X}),\mathbf{X}\right) = \Psi\left(\mathbf{C}(\mathbf{X}),\mathbf{X}\right), \tag{2.70}$$

which automatically satisfies the requirement of objectivity. The time derivative of the strain energy function can also be written as

$$\dot{\Psi} = \frac{\partial \Psi\left(\mathbf{C}(\mathbf{X}),\mathbf{X}\right)}{\partial \mathbf{C}} : \dot{\mathbf{C}} = \frac{\partial \Psi\left(\mathbf{C}(\mathbf{X}),\mathbf{X}\right)}{\partial \mathbf{C}} : \frac{1}{2}\dot{\mathbf{E}} = \frac{1}{2}\frac{\partial \Psi\left(\mathbf{C}(\mathbf{X}),\mathbf{X}\right)}{\partial \mathbf{C}} : \dot{\mathbf{E}} = \frac{\partial \Psi\left(\mathbf{C}(\mathbf{X}),\mathbf{X}\right)}{\partial \mathbf{E}} : \dot{\mathbf{E}} \, . \tag{2.71}$$

Similarly, we have the general constitutive equation in terms of the second Piola-Kirchhoff stress $\mathbf{S}$ as

$$\mathbf{S} = 2\frac{\partial \Psi\left(\mathbf{C}(\mathbf{X}),\mathbf{X}\right)}{\partial \mathbf{C}} = \frac{\partial \Psi\left(\mathbf{C}(\mathbf{X}),\mathbf{X}\right)}{\partial \mathbf{E}} \, . \tag{2.72}$$

The strain energy function describes the stored elastic energy in the material. For a viscoelastic material, the strain energy is a function of the elastic right Cauchy-Green tensor, $\mathbf{C}_e$, as

$$\Psi = \Psi\left(\mathbf{C}_e, \mathbf{X}\right). \tag{2.73}$$

For isotropic materials, it is often convenient to formulate the constitutive equations in the current configuration by using the elastic left Cauchy-Green tensor, $\mathbf{b}_e$, as

$$\Psi = \Psi\left(\mathbf{b}_e, \mathbf{X}\right). \tag{2.74}$$

Furthermore, the strain energy function Ψ can be rewritten as

$$\Psi = \hat{\Psi}\left(\mathbf{C}, \mathbf{C}_v^{-1}, \mathbf{X}\right) = \tilde{\Psi}\left(\mathbf{b}, \mathbf{b}_e, \mathbf{X}\right). \tag{2.75}$$

Applying Eqs (2.75) and Eq (2.63) to the Clausius-Duhem inequality in (2.62) gives the isothermal dissipation inequality for viscoelastic materials,

$$\left(\mathbf{S} - 2\frac{\partial \Psi}{\partial \mathbf{C}}\right) : \frac{1}{2}\dot{\mathbf{C}} - 2\frac{\partial \Psi}{\partial \mathbf{C}_v} : \frac{1}{2}\dot{\mathbf{C}}_v \geq 0, \tag{2.76}$$

which has to be satisfied at every point of the body at every time during the process. Since $\mathbf{C}$ can be chosen arbitrarily, when $\dot{\mathbf{C}}$ is chosen arbitrarily as well, it gives the same second Piola-Kirchhoff stress expression as for hyperelastic materials

$$\mathbf{S} = 2\frac{\partial \Psi}{\partial \mathbf{C}}. \tag{2.77}$$

Therefore, Eq (2.76) reduces to

$$-2\frac{\partial \Psi}{\partial \mathbf{C}_v} : \frac{1}{2}\dot{\mathbf{C}}_v \geq 0, \tag{2.78}$$

where $-2\frac{\partial \Psi}{\partial \mathbf{C}_v}$ is the stress driving the viscous relaxation of the material and sometimes called the fictitious non-equilibrium stress. Evolution equations governing the internal variable $\mathbf{C}_v$ can be developed based on the reduced dissipation inequality (Eq (2.78)).

2.7 Constitutive formulations for active anisotropic media

For completeness, we present an outline of the two constitutive models developed in this research. The physical basis for the active components of the models (i.e. chemo-mechanical and electro-mechanical coupling) are individually derived in detail in Chapters 4 (for smooth muscle tissue) and 6 (for dielectric elastomer composites).

2.7.1 Smooth muscle rich arterial tissue

In the constitutive formulation, the strain energy is composed of active parts representing the active contractile units and passive parts for the remainder of the tissue. The passive matrix includes extracellular ground substance and the passive part of the smooth muscle cells. The active force and active viscous stretch due to the relative sliding of thin and thick filaments are defined as P_d and λ_F^v, respectively. The thermodynamics requirement for the constitutive law is that the internal energy dissipation should always be non-negative. For a viscoelastic material, the free energy is assumed to be a function of the Cauchy Green tensor and corresponding internal variables. Here, considering the smooth muscle rich arterial media contains one family of active and passive fibers, decomposing the free energy into equilibrium and non-equilibrium parts, there are two sets of internal variables $\left(\mathbf{C}_M^v, \mathbf{C}_F^v\right)$ or $\left(I_1^v \sim I_3^v, I_4^v\right)$. The strain energy function is written as

$$\Psi(\mathbf{C}, \mathbf{C}_M^v, \mathbf{C}_F^v) = \Psi(I_1, I_2, I_3, I_1^v, I_2^v, I_3^v, I_4, I_4^v). \tag{2.79}$$

Evolution equations for the internal variables can be appropriately chosen to satisfy the second law of thermodynamics. The collagen fibers and smooth muscle 'fibers' cause material anisotropy, so the strain energy function is decomposed into isotropic and anisotropic components as

$$\Psi(I_1, I_2, I_3, I_1^v, I_2^v, I_3^v, I_4, I_4^v)$$
$$= \underbrace{\Psi_{Meq}(I_1, I_2, I_3) + \Psi_{Mneq}(I_1, I_2, I_3, I_1^v, I_2^v, I_3^v)}_{\text{isotropic passive matrix}} + \underbrace{\Psi_{pF}(I_4)}_{\text{passive fibers}} + \underbrace{\Psi_{aF}(I_4, I_4^v)}_{\text{active fibers}}. \quad (2.80)$$

The matrix is assumed hyperelastic for simplicity of the presentation and modeled as Neo-Hookean as

$$\Psi_{\text{Meq}} = \frac{\mu_p}{2}(I_1 - 3), \quad (2.81)$$

where μ_p is a material constant for the matrix. For the passive anisotropic part, we adopt a general exponential form

$$\Psi_{\text{pF}} = \frac{k_1}{2k_2}\left(\exp\left(k_2(I_4 - 1)^2\right) - 1\right) \quad (2.82)$$

where k_1 and k_2 are material constants. Experiments on smooth muscle show a parabolic or bell-shaped tension - stretch relationship. From the sliding filament theory this suggests that the total force is proportional to the extent of overlap of thin and thick filaments. Therefore, for the active part of the smooth muscle contribution, the strain energy function depends on the instantaneous fraction of crossbridges, and is assigned the quadratic form

$$\Psi_{aF} = O_{lap}(AMp + AM)\frac{\mu_f}{4}\left(\frac{I_4}{I_4^v} - 1\right)^2, \quad (2.83)$$

where, μ_f is a shear modulus for the fibers, O_{lap} is the overlap coefficient function (Yang et al., 2003) and $O_{lap}(AMp + AM)$ is the fraction of cross-bridges in the overlap zone (producing active stress). In order to describe the viscoelastic process, the constitutive laws given above should be complemented by suitable evolution equations satisfying the fundamental Clausius-Planck inequality. Since the initial stretch rates in isotonic tests are nonlinear, the non-equilibrium stress is defined as third order. Our proposed

nonlinear viscoelastic equation is motivated by the observation that the cycle rate of latch bridges is much slower than the fast cycling of phosphorylated cross-bridges. The lower cycling rate of the latch bridges has the effect of a pulling (resistive) load on fast myosin cycling, which decreases the velocity of thin filament sliding. Therefore, assuming this molecular level resistance of the latch bridges, we introduce a total viscous coefficient in the evolution equation via the term $\left(1+n_d O_{lap} AM\right)\eta$, where $O_{lap}AM$ is the effective fraction of latch bridges and n_d is a constant modifying the viscous coefficient. The evolution equation for the non-equilibrium stress is

$$\left(P_d - 2\lambda_F^v \frac{\partial \Psi}{\partial I_4^v}\right) + \alpha\left(P_d - 2\lambda_F^v \frac{\partial \Psi}{\partial I_4^v}\right)^3 = (1+n_d O_{lap} AM)\eta \dot{\lambda}_F^v, \tag{2.84}$$

where, α is a positive constant parameter. The term $-2\lambda_F^v \partial\Psi / \partial I_4^v$ is the fictitious nonequilibrium stress. The model formulations of the smooth muscle rich artery are summarized in Table 1. In addition, the variables in the model formulation are $I_1, I_4,$ and I_4^v.

Table 1. Proposed model formulation for the smooth muscle rich artery.

Chemical part	$\begin{Bmatrix} \dot{M} \\ \dot{M}p \\ A\dot{M}p \\ A\dot{M} \end{Bmatrix} = \begin{bmatrix} -K_1 & K_2 & 0 & K_7 \\ K_1 & -K_2-K_3 & K_4 & 0 \\ 0 & K_3 & -K_4-K_5 & K_6 \\ 0 & 0 & K_5 & -K_6-K_7 \end{bmatrix} \begin{Bmatrix} M \\ Mp \\ AMp \\ AM \end{Bmatrix}$

Mechanical part (media)	Strain energy function: $\Psi = \frac{\mu_p}{2}(I_1 - 3) + \frac{k_1}{2k_2}\left(\exp\left(k_2(I_4 - 1)^2\right) - 1\right) + O_{lap}(AMp + AM)\frac{\mu_f}{4}\left(\frac{I_4}{I_4^v} - 1\right)^2$ Second Piola-Kirchhoff stress: $\mathbf{S} = \mu_p \mathbf{I} + 2k_1 \exp\left(k_2(I_4 - 1)^2\right)(I_4 - 1)\mathbf{V} \otimes \mathbf{V} + O_{lap}(AMp + AM)\mu_f \left(I_4 - I_4^v\right)/\left(I_4^v\right)^2 \mathbf{V} \otimes \mathbf{V}$ Evolution equation: $\left(P_d - 2\lambda_F^v \frac{\partial \Psi}{\partial I_4^v}\right) + \alpha\left(P_d - 2\lambda_F^v \frac{\partial \Psi}{\partial I_4^v}\right)^3 = (1 + n_d O_{lap} AM)\eta \dot{\lambda}_F^v,$ with driving force $P_d = -\kappa O_{lap} AMp$

2.7.2 Dielectric elastomer composites

In the case of the newly proposed dielectric elastomer composites, we consider a family of embedded contractile units having a preferred orientation within an isotropic dielectric elastomer matrix. One way that the contractile units could be realized is by arranging micron sized DEs in a stacked configuration to form a planar distribution of 1D fibers. The active fibers would then contract along the fiber stack direction due to the Maxwell stress effect when an electric field is applied in the fiber direction. If the top and bottom surfaces of the homogenized composite membrane are then electroded, then a matrix dominated Maxwell stress effect would also occur. In this way, multiaxial activation is realized.

To model dielectric elastomers, we first introduce additional invariants into the constitutive formulation (2.53). The Maxwell stress is related to the I_{11} invariant (quadratics of the true electric field). Assuming a linear relationship between the electric displacement vector and the electric field, the Maxwell stress tensor is defined as

$$\sigma_{\max\_m} = \varepsilon_0 \varepsilon_r \mathbf{e}_m \otimes \mathbf{e}_m - \frac{\varepsilon_0 \varepsilon_r}{2} \mathbf{e}_m \cdot \mathbf{e}_m \mathbf{I}, \tag{2.85}$$

where, $\mathbf{e}_m$ is the true electric field vector in the matrix, ε_0 and ε_{rm} are the dielectric constants.

To model the proposed DEC, we consider a strain energy function of the following form

$$\begin{aligned} \Psi(\mathbf{F}, \mathbf{F}_v, \mathbf{V}, \mathbf{E}) &= \Psi\left(I_1 \sim I_5, I_1^v \sim I_5^v, I_{10} \sim I_{12}\right) \\ &= \Psi_{mech}\left(I_1 \sim I_5, I_1^v \sim I_5^v\right) + \Psi_{\max}\left(I_{10} \sim I_{12}\right). \end{aligned} \tag{2.86}$$

Based on this, we can decompose the total Cauchy stress as:

$$\boldsymbol{\sigma} = \boldsymbol{\sigma}_{mech}\left(I_1 \sim I_5, I_1^v \sim I_5^v\right) + \boldsymbol{\sigma}_{\max}\left(I_{10} \sim I_{12}\right), \tag{2.87}$$

where $\boldsymbol{\sigma}_{mech}$ is the mechanical stress component, which has isotropic and anisotropic parts, and $\boldsymbol{\sigma}_{\max}$ is the electrostatic or Maxwell stress component, which has matrix and fiber parts. For ease of notation, we also split the electric field vector into two vectors, reflecting the electric field component in the thickness direction for 'matrix' activation, and a component for activating the in-plane fibers (fiber activation):

$$\begin{aligned} \mathbf{E} &= \begin{bmatrix} E_1 & E_2 & E_3 \end{bmatrix}^T \\ &= \mathbf{E}_f + \mathbf{E}_m = \begin{bmatrix} E_1 & E_2 & 0 \end{bmatrix}^T + \begin{bmatrix} 0 & 0 & E_3 \end{bmatrix}^T. \end{aligned} \tag{2.88}$$

Now, consider activating the fibers along their length direction, $\mathbf{V} = \begin{bmatrix} \cos\alpha & \sin\alpha & 0 \end{bmatrix}^T$ (α is the fiber angle), the component of the field in that direction is $E_f = \mathbf{E} \cdot \mathbf{V} = \mathbf{E}_f \cdot \mathbf{V} = E_1 \cos\alpha + E_2 \sin\alpha$ which is the magnitude of the nominal electric field in the fiber direction. Therefore, the resultant coupling can be treated as a fiber coupling

E_f and a matrix coupling $\mathbf{E}_m$ (the remainder of the total electric field). The principal invariants I_{11} for matrix and fibers are $I_{11}^m = \mathbf{E}_m \cdot \mathbf{C}^{-1} \cdot \mathbf{E}_m, I_{11}^f = \left(E_f / \lambda\right)^2 = E_f^2 / I_4$.

Since the 1D contractile units are based on the same Maxwell stress mechanism, we employ a similar form for the fiber electromechanical coupling as

$$\begin{aligned} \Psi_{\max\_f} &= \frac{\varepsilon_0 \varepsilon_{rf}}{2} I_{11}^f, \\ \sigma_{\max\_f} &= \varepsilon_0 \varepsilon_{rf} \frac{{E_f}^2}{I_4} \frac{\mathbf{v}}{\sqrt{I_4}} \otimes \frac{\mathbf{v}}{\sqrt{I_4}} = \varepsilon_0 \varepsilon_{rf} \left(\frac{E_f}{\sqrt{I_4}} \frac{\mathbf{v}}{\sqrt{I_4}} \right) \otimes \left(\frac{E_f}{\sqrt{I_4}} \frac{\mathbf{v}}{\sqrt{I_4}} \right), \end{aligned} \tag{2.89}$$

where $E_f / \sqrt{I_4}$ is the magnitude of the true electric field in the fibers ($\sqrt{I_4} = \lambda$ is the fiber stretch) and $\mathbf{v} / \sqrt{I_4}$ is the unit fiber orientation vector in the current configuration representing the direction of the true electric field in the fibers.

The isotropic elastomeric matrix is modeled as Neo-Hookean

$$\begin{aligned} \Psi_{mech\_iso} &= \frac{\mu}{2}\left(I_1 - 3\right), \\ \sigma_{mech\_iso} &= \mu \mathbf{b}, \end{aligned} \tag{2.90}$$

where μ is the shear modulus of the matrix. It is noted that other widely-used formulations can be applied to describe the isotropic behaviors as well, such as Mooney-Rivlin, Ogden, Yeoh, and Gent models. Viscous effects of the matrix are considered negligible. The strain energy function of the passive fiber component takes on a quadratic form of I_4 and depends on the first order only, and the stress expression is derived as

$$\begin{aligned} \Psi_{mech\_aniso} &= \frac{\mu_{feq}}{2}\left(I_4 - 1\right)^2 + \frac{\mu_{fneq}}{2}\left(\frac{I_4}{I_4^{\,v}} - 1 \right)^2, \\ \sigma_{mech\_aniso} &= 2\mu_{feq}\left(I_4 - 1\right)\mathbf{v} \otimes \mathbf{v} + 2\mu_{fneq}\left(\frac{I_4}{I_4^{\,v}} - 1 \right) \frac{1}{I_4^{\,v}} \mathbf{v} \otimes \mathbf{v}, \end{aligned} \tag{2.91}$$

where μ_{feq} and μ_{fneq} are the moduli for the equilibrium and nonequilibrium parts of fibers.

Finally, the proposed constitutive formulation is

$$\begin{aligned}\boldsymbol{\sigma} = &\underbrace{\mu\mathbf{b} + 2\mu_{feq}\left(I_4 - 1\right)\mathbf{v}\otimes\mathbf{v} + 2\mu_{fneq}\left(\frac{I_4}{I_4^{v}} - 1\right)\frac{1}{I_4^{v}}\mathbf{v}\otimes\mathbf{v}}_{mechanical} \\ &+ \underbrace{\varepsilon_0\varepsilon_{rf}\frac{E_f^{\,2}}{I_4}\frac{\mathbf{v}}{\sqrt{I_4}}\otimes\frac{\mathbf{v}}{\sqrt{I_4}}}_{electrical-fiber} + \underbrace{\varepsilon_0\varepsilon_{rm}\mathbf{e}_m\otimes\mathbf{e}_m - \frac{\varepsilon_0\varepsilon_{rm}}{2}\mathbf{e}_m\cdot\mathbf{e}_m\mathbf{I}}_{electrical-matrix} + p\mathbf{I}.\end{aligned} \tag{2.92}$$

We adopt the following linear evolution equation for $\dot{I}_4^v$ from (Reese and Govindjee, 1998) as

$$-\tau_{neq} = \eta\dot{I}_4^v, \tag{2.93}$$

where τ_{neq} is the nonequilibrium stress in the fibers and $\tau_{neq} = 4\mu_{fneq}\left(\frac{I_4}{I_4^v} - 1\right)\frac{I_4}{I_4^v}$. Table 2 summarizes the model formulations of dielectric elastomer composites. In addition, the variables in the model formulations are $I_1, I_4, I_4^v, I_{11}^f,$ and I_{11}^m.

Table 2. Proposed model formulation for novel dielectric elastomer composites.

Strain energy function:

$$\Psi = \underbrace{\frac{\mu}{2}\left(I_1 - 3\right) + \frac{\mu_{feq}}{2}\left(I_4 - 1\right)^2 + \frac{\mu_{fneq}}{2}\left(\frac{I_4}{I_4^{v}} - 1\right)^2}_{mechanical} \underbrace{- \frac{\varepsilon_0 \varepsilon_{rf}}{2} I_{11}^{f}}_{electrical-fiber} \underbrace{- \frac{\varepsilon_0 \varepsilon_{rm}}{2} I_{11}^{m}}_{electrical-matrix},$$

Cauchy stress:

$$\boldsymbol{\sigma} = \underbrace{\mu \mathbf{b} + 2\mu_{feq}\left(I_4 - 1\right)\mathbf{v} \otimes \mathbf{v} + 2\mu_{fneq}\left(\frac{I_4}{I_4^{v}} - 1\right)\frac{1}{I_4^{v}}\mathbf{v} \otimes \mathbf{v}}_{mechanical}$$

$$+ \underbrace{\varepsilon_0 \varepsilon_{rf} \frac{E_f^{\,2}}{I_4} \frac{\mathbf{v}}{\sqrt{I_4}} \otimes \frac{\mathbf{v}}{\sqrt{I_4}}}_{electrical-fiber} + \underbrace{\varepsilon_0 \varepsilon_{rm} \mathbf{e}_m \otimes \mathbf{e}_m - \frac{\varepsilon_0 \varepsilon_{rm}}{2} \mathbf{e}_m \cdot \mathbf{e}_m \mathbf{I}}_{electrical-matrix} + p\mathbf{I}.$$

Evolution equation:

$$-\tau_{neq} = \eta \dot{I}_4^{v} \text{ with } \tau_{neq} = 4\mu_{fneq}\left(\frac{I_4}{I_4^{v}} - 1\right)\frac{I_4}{I_4^{v}}$$

2.8 Summary

In this dissertation, active anisotropic materials are homogeneous fiber-filled composites and the coupling effects (chemical or electrical) are treated phenomenologically through the proposed constitutive equations. In this chapter, we introduced the continuum mechanics framework for modeling nonlinear materials undergoing large deformations. Specifically, concepts in kinematics, balance equations, free energy functions, and constitutive formulations are summarized adopting the invariant-based approach of Spencer and Rivlin and others. (Pipkin and Rogers, 1968; Spencer, 1971; Spencer, 2004) For modeling the inelastic behavior of the materials (viscoelastic effects), the internal variable approach is employed. From the multiplicative decomposition of the deformation gradient, free energy functions and Cauchy stresses are divided into equilibrium and nonequilibrium parts for describing

the time independent and rate dependent responses. In the following chapters, the specific constitutive formulations for smooth muscle tissue and dielectric elastomer composites are explicitly derived using this framework.

References

Böl, M., Schmitz, A., Nowak, G., Siebert, T., 2012. A three-dimensional chemo-mechanical continuum model for smooth muscle contraction. Journal of the Mechanical Behavior of Biomedical Materials 13, 215-229, doi:10.1016/j.jmbbm.2012.05.015.

Gasser, T. C., Ogden, R. W., Holzapfel, G. A., 2006. Hyperelastic modelling of arterial layers with distributed collagen fibre orientations. Journal of The Royal Society Interface 3, 15-35, doi:10.1098/rsif.2005.0073.

Gizzi, A., Pandolfi, A., Vasta, M., 2016. Statistical characterization of the anisotropic strain energy in soft materials with distributed fibers. Mechanics of Materials 92, 119-138, doi:10.1016/j.mechmat.2015.09.008.

Haupt, P., 1993. Thermodynamics of Solids. In: Muschik, W., (Ed.), Non-Equilibrium Thermodynamics with Application to Solids. Springer Vienna, pp. 65-138.

Holzapfel, G. A., 1996. On Large Strain Viscoelasticity: Continuum Formulation and Finite Element Applications to Elastomeric Structures. International Journal for Numerical Methods in Engineering 39, 3903-3926, doi:10.1002/(SICI)1097-0207(19961130)39:22<3903::AID-NME34>3.0.CO;2-C.

Holzapfel, G. A., Niestrawska, J. A., Ogden, R. W., Reinisch, A. J., Schriefl, A. J., 2015. Modelling non-symmetric collagen fibre dispersion in arterial walls. Journal of The Royal Society Interface 12, 20150188, doi:10.1098/rsif.2015.0188.

Kaliske, M., Rothert, H., 1997. Formulation and implementation of three-dimensional viscoelasticity at small and finite strains. Computational Mechanics 19, 228-239, doi:10.1007/s004660050171.

Koh, S. L., Eringen, A. C., 1962. ON THE FOUNDATIONS OF NON-LINEAR THERMO-VISCO-ELASTICITY.

Kroon, M., 2010. A constitutive model for smooth muscle including active tone and passive viscoelastic behaviour. Mathematical Medicine and Biology 27, 129-155, doi:10.1093/imammb/dqp017.

Lee, E. H., 1969. Elastic-Plastic Deformation at Finite Strains. Journal of Applied Mechanics 36, 1-6, doi:10.1115/1.3564580.

Lee, E. H., Liu, D. T., 1967. Finite-Strain Elastic—Plastic Theory with Application to Plane-Wave Analysis. Journal of Applied Physics 38, 19-27, doi:10.1063/1.1708953.

Lion, A., 1996. A constitutive model for carbon black filled rubber: Experimental investigations and mathematical representation. Continuum Mechanics and Thermodynamics 8, 153-169, doi:10.1007/BF01181853.

Liu, T., 2014. A constitutive model for cytoskeletal contractility of smooth muscle cells. Proceedings of the Royal Society A: Mathematical, Physical and Engineering Science 470, 1-19, doi:10.1098/rspa.2013.0771.

Lubliner, J., 1985. A model of rubber viscoelasticity. Mechanics Research Communications 12, 93-99, doi:10.1016/0093-6413(85)90075-8.
Marsden, J. E., Hughes, T. J. R., 1994. Mathematical Foundations of Elasticity. Dover Publications, New York.
Murtada, S.-I., Holzapfel, G. A., 2014. Investigating the role of smooth muscle cells in large elastic arteries: a finite element analysis. Journal of Theoretical Biology 358, 1-10, doi:10.1016/j.jtbi.2014.04.028.
Murtada, S. C., Kroon, M., Holzapfel, G. A., 2010. A calcium-driven mechanochemical model for prediction of force generation in smooth muscle. Biomechanics and Modeling in Mechanobiology 9, 749-762, doi:10.1007/s10237-010-0211-0.
Murtada, S. C., Arner, A., Holzapfel, G. A., 2012. Experiments and mechanochemical modeling of smooth muscle contraction: Significance of filament overlap. Journal of Theoretical Biology 297, 176-186, doi:10.1016/j.jtbi.2011.11.012.
Pipkin, A. C., Rogers, T. G., 1968. A non-linear integral representation for viscoelastic behaviour. Journal of the Mechanics and Physics of Solids 16, 59-72, doi:10.1016/0022-5096(68)90016-1.
Reese, S., Govindjee, S., 1998. A theory of finite viscoelasticity and numerical aspects. International Journal of Solids and Structures 35, 3455-3482, doi:10.1016/S0020-7683(97)00217-5.
Sidoroff, F., 1974. Nonlinear Viscoelastic Model with an Intermediate Configuration.[UN MODELE VISCOELASTIQUE NON LINEAIRE AVEC CONFIGURATION INTERMEDIAIRE.]. Journal de Mecanique.
Simo, J. C., 1987. On a fully three-dimensional finite-strain viscoelastic damage model: Formulation and computational aspects. Computer Methods in Applied Mechanics and Engineering 60, 153-173, doi:10.1016/0045-7825(87)90107-1.
Simo, J. C., Miehe, C., 1992. Associative coupled thermoplasticity at finite strains: Formulation, numerical analysis and implementation. Computer Methods in Applied Mechanics and Engineering 98, 41-104, doi:10.1016/0045-7825(92)90170-O.
Spencer, A. J. M., 1971. Part III - Theory of Invariants. In: Eringen, A. C., (Ed.), Mathematics. Academic Press, pp. 239-353.
Spencer, A. J. M., 2004. Continuum Mechanics. Dover Publications, Mineola, N.Y.
Stålhand, J., Klarbring, A., Holzapfel, G. A., 2008. Smooth muscle contraction: Mechanochemical formulation for homogeneous finite strains. Progress in Biophysics and Molecular Biology 96, 465-481, doi:10.1016/j.pbiomolbio.2007.07.025.
Stålhand, J., Klarbring, A., Holzapfel, G. A., 2011. A mechanochemical 3D continuum model for smooth muscle contraction under finite strains. Journal of Theoretical Biology 268, 120-130, doi:10.1016/j.jtbi.2010.10.008.
Wang, Y., Son, S., Swartz, S. M., Goulbourne, N. C., 2012. A mixed von Mises distribution for modeling soft biological tissues with two distributed fiber properties. International Journal of Solids and Structures 49, 2914-2923, doi:10.1016/j.ijsolstr.2012.04.004.
Yang, J., Clark Jr, J. W., Bryan, R. M., Robertson, C., 2003. The myogenic response in isolated rat cerebrovascular arteries: smooth muscle cell model. Medical Engineering & Physics 25, 691-709, doi:10.1016/S1350-4533(03)00100-0.

Chapter 3. Computational formulations

3.1 Introduction

Constitutive models can be directly implemented into a finite element environment to solve problems that involve complex geometry, loading, and boundary conditions. The theoretical foundation for implementing inelastic constitutive models in FEM is described in this chapter. Since the material multiphysics coupling is described using constitutive models, the traditional weak form for solving problems in continuum mechanics is used for the initial boundary value problem. That is to say, we are not solving the fully coupled multiphysics field equations, but rather treat the electrical and chemical quantities and variables as direct inputs in the constitutive models. The proposed constitutive equations are explicitly derived in Chapter 4 (for smooth muscle tissue) and Chapter 6 (for dielectric elastomer composites). See Table 3 and Table 10 in Chapter 4 and 6 for model summary. Explicit formulations of the user material subroutines that were developed in this work for the commercial finite element software ABAQUS are outlined in Appendices C and D. In subsequent chapters, the effect of active contractility on the deformation behavior of active anisotropic membranes is explored in a computational setting using ABAQUS for various loading conditions and for different architectures and or geometries.

Solving computational mechanics problems in a finite element environment with Newton type iteration techniques requires the use of linearized constitutive equations. Inelastic formulations can be implemented using either the user material subroutines

(UMAT) or (UANISOHYPER) in ABAQUS. The user material subroutine requires that the components of the Cauchy stress, the fourth order elasticity tensor in the spatial description, and any solution dependent state variables are specified.

When user subroutines (UMAT) are provided, ABAQUS will call the UMAT to calculate the stress and stiffness matrix $\mathbb{C}^{ABAQUS}$ for the linearized equilibrium equations. A summary of the workflow is provided in the flowchart below (Figure 9). The procedure is:

i) For a given displacement field $\mathbf{u}$, the UMAT is called and in this first call, kinematic measures and Cauchy stresses are calculated. Their values are passed to ABAQUS from the UMAT to calculate the residual form of equilibrium (Eq (3.33)) to see if it is within the tolerance. If it is, go to step iv). If not, go to ii).

ii) For a displacement increment $\Delta\mathbf{u}$, the UMAT is called for a second time to calculate the kinematic measures, Cauchy stresses, and tangent modulus. The values are passed into ABAQUS from the UMAT to solve the linearization of the residual form of the equilibrium equations (Eq(3.33)).

iii) The displacement $\mathbf{u}$ is updated by $\mathbf{u}+\Delta\mathbf{u}$ and goes back to i)

iv) Solutions of the displacement field, stresses, strains, and state value fields are output.

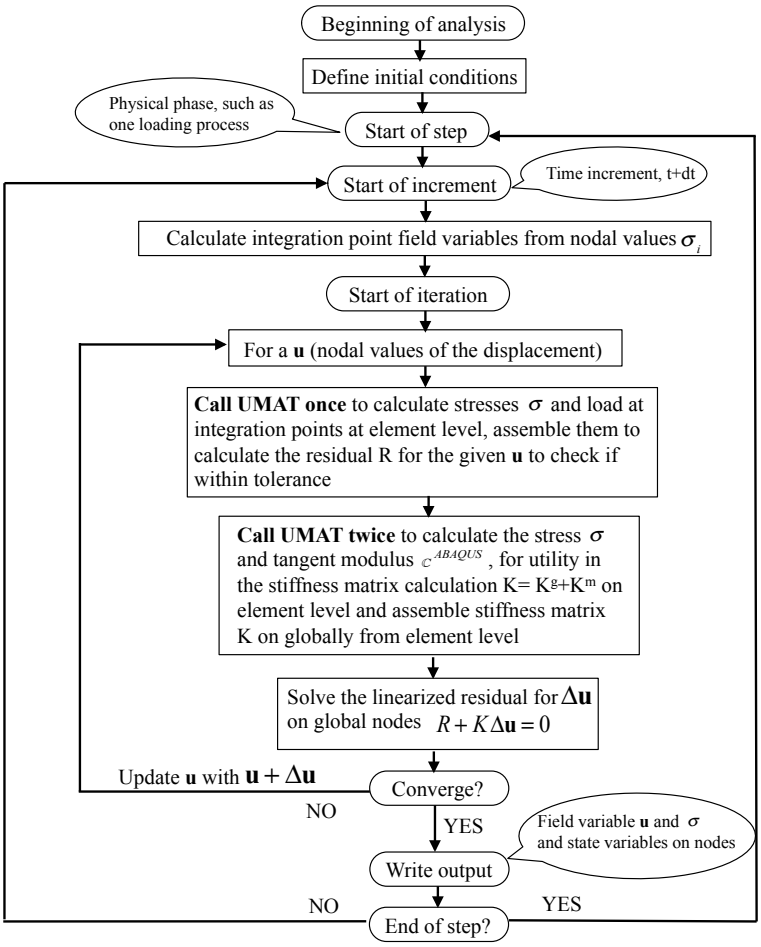

Figure 9. Flow chart of ABAQUS and UMAT procedures.

This chapter is organized as follows: a general weak form of the equilibrium equations and its linearization are presented first in section 3.2. There we emphasize some aspects relevant to the formulation and implementation of nonlinear constitutive models. For detailed treatments, refer to (Gurtin, 1981; Truesdell and Toupin, 1960) and more recent ones such as (Bonet and Wood, 2008; Holzapfel, 2000; Hughes, 2000; Lemaitre and Chaboche, 1994; Marsden and Hughes, 1994; Ogden and Engineering, 1997; Simo and Hughes, 2000). Next, various objective stress rates are introduced and specifically the Jaumann rate is discussed since it is the one used in ABAQUS. In section 3.3, the general form of the tangent moduli in material and spatial descriptions are derived. A summary of the chapter is provided in section 3.4.

3.2 Weak form of the equilibrium equations

In Chapter 2, we introduced the strong form of the equilibrium equations together with the general constitutive equations. In a typical initial boundary value problem, the equilibrium equations are solved in the weak form for the unknown displacement field, and the stress and strain fields are obtained by the constitutive equations. We introduce the weak form from the principle of virtual work, which is fundamental in establishing finite element formulations. In a finite deformation framework, we take the product of the strong form of the balance of linear momentum (Eq (2.58)) and multiply by an arbitrary vector-valued function ($\delta\mathbf{u}$) and integrate over the body to yield the internal and external virtual work

$$\begin{aligned}\delta w &= \int_\Omega -div\boldsymbol{\sigma}\cdot\delta\mathbf{u}dv = \int_\Omega \boldsymbol{\sigma}:\nabla(\delta\mathbf{u})dv - \int_\Omega div(\boldsymbol{\sigma}\delta\mathbf{u})dv \\ &= \underbrace{\int_\Omega \boldsymbol{\sigma}:\nabla(\delta\mathbf{u})dv}_{\delta w_{int}} - \underbrace{\int_{\partial\Omega^t}\bar{\mathbf{t}}\cdot\delta\mathbf{u}dV}_{\delta w_{ext}} \\ &= \underbrace{\int_\Omega \boldsymbol{\sigma}:\delta\mathbf{e}dv}_{\delta w_{int}} - \underbrace{\int_{\partial\Omega^t}\delta\mathbf{u}^T\bar{\mathbf{t}}dV}_{\delta w_{ext}} = 0,\end{aligned} \tag{3.1}$$

where $div\boldsymbol{\sigma}\cdot\delta\mathbf{u} = div(\boldsymbol{\sigma}\delta\mathbf{u}) - \boldsymbol{\sigma}:\nabla(\delta\mathbf{u})$ and $\delta\mathbf{e} = \frac{1}{2}\left(grad^T\delta\mathbf{u} + grad\delta\mathbf{u}\right) = sym(\nabla(\delta\mathbf{u}))$ are used, $\mathbf{u}$ is the displacement vector, $\delta\mathbf{u}$ is an arbitrary variation of the displacement, $\bar{\mathbf{t}}$ denotes the given traction on the boundary $\partial\Omega^t$ in the current configuration, δw_{int} is the internal virtual work, and δw_{ext} is the external virtual work. Eq (3.1) also is called the *residual form*, and the first term is the stress divergence term. For displacement boundary conditions, on each point of the boundary $\partial\Omega_u$, boundary conditions are given $\mathbf{u} = \bar{\mathbf{u}}$ and therefore are not in Eq (3.1). In this dissertation, the problems are static or quasi-static so that the virtual kinetic energy is omitted here. Recall from chapter 2 that

$$J\boldsymbol{\sigma} : \delta\mathbf{e} = \mathbf{P} : \delta\mathbf{F} = \mathbf{S} : \delta\mathbf{E} = \mathbf{S} : \frac{1}{2}\delta\mathbf{C} = \boldsymbol{\tau} : \delta\mathbf{e}, \tag{3.2}$$

and inserting Eq (3.2) to Eq (3.1), the residual form of the equilibrium equations in the material description is obtained as

$$\delta w = \int_{\Omega_0} \mathbf{P} : \delta\mathbf{F}^T dV - \int_{\partial\Omega_0^t} \delta\mathbf{u}^T \bar{\mathbf{T}} dV = 0, \tag{3.3}$$

where $\bar{\mathbf{T}}$ denotes the given traction on the boundary $\partial\Omega_0^t$ in the reference configuration. The residual form can also be written in terms of the second Piola-Kirchhoff stress or Kirchhoff stress according to Eq (3.2) as

$$\delta w = \int_{\Omega_0} \mathbf{S} : \delta\mathbf{E} dV - \int_{\partial\Omega_0^t} \delta\mathbf{u}^T \bar{\mathbf{T}} dV = 0, \tag{3.4}$$

$$\delta w = \int_{\Omega_0} \boldsymbol{\tau} : \delta\mathbf{e} dV - \int_{\partial\Omega_0^t} \delta\mathbf{u}^T \bar{\mathbf{T}} dV = 0. \tag{3.5}$$

Linearization

To solve an initial boundary value problem, we first linearize the above nonlinear equation and determine the rate of change of the stress divergence term. (This will be used later when solving the equations using Newton's method.) Using the second Piola-Kirchhoff stress, we rewrite the first Piola-Kirchhoff stress in Eq (3.3) as

$$\int_{\Omega_0} \mathbf{P} : \delta\mathbf{F}^T dV = \int_{\Omega_0} \mathbf{FS} : \delta\mathbf{F}^T dV = \int_{\Omega_0} tr\left(\delta\mathbf{F}^T\mathbf{FS}\right) dV = \int_{\Omega_0} tr\left(\delta\mathbf{FSF}^T\right) dV. \tag{3.6}$$

Now the linearization is computed as

$$\Delta\left(\int_{\Omega_0} tr\left(\delta\mathbf{FSF}^T\right) dV\right) = \int_{\Omega_0} tr\left(\delta\mathbf{FS}\Delta\mathbf{F}^T\right) dV + \int_{\Omega_0} tr\left(\delta\mathbf{F}\Delta\mathbf{SF}^T\right) dV. \tag{3.7}$$

Alternatively, it can be written in the current configuration by using

$$\delta\mathbf{F} = Grad\,\delta\mathbf{u} = grad\,\delta\mathbf{u}\mathbf{F} = \nabla\left(\delta\mathbf{u}\right)\mathbf{F}, \quad \Delta\mathbf{F} = Grad\,\Delta\mathbf{u} = grad\,\Delta\mathbf{u}\mathbf{F} = \nabla\left(\Delta\mathbf{u}\right)\mathbf{F}, \tag{3.8}$$

as

$$\Delta\left(\int_{\Omega_0} tr\left(\delta\mathbf{F}\mathbf{S}\mathbf{F}^T\right)dV\right)=\int_{\Omega_0} tr\left(\nabla\left(\delta\mathbf{u}\right)\underbrace{\mathbf{F}\mathbf{S}\mathbf{F}^T}_{J\boldsymbol{\sigma}}\nabla\left(\Delta\mathbf{u}\right)^T\right)dV+\int_{\Omega_0} tr\left(\nabla\left(\delta\mathbf{u}\right)\underbrace{\mathbf{F}\Delta\mathbf{S}\mathbf{F}^T}_{J\Delta\boldsymbol{\sigma}}\right)dV$$
$$=\int_{\Omega} tr\left(\nabla\left(\delta\mathbf{u}\right)\boldsymbol{\sigma}\nabla\left(\Delta\mathbf{u}\right)^T\right)dv+\int_{\Omega} tr\left(\nabla\left(\delta\mathbf{u}\right)\Delta\boldsymbol{\sigma}\right)dv, \tag{3.9}$$

where the first term leads to the geometric stiffness term in finite element formulations and the second term leads to the material part of the stiffness since it depends on the constitutive equations. In addition, based on the above equation another form of the linearized stress divergence term in the reference configuration may be rewritten in terms of the Piola-Kirchhoff stress by applying the relationship $\Delta\boldsymbol{\tau}=\mathbf{F}\Delta\mathbf{S}\mathbf{F}^T$ as

$$\Delta\left(\int_{\Omega_0} tr\left(\delta\mathbf{F}\mathbf{S}\mathbf{F}^T\right)dV\right)=\int_{\Omega_0} tr\left(\nabla\left(\delta\mathbf{u}\right)\boldsymbol{\tau}\nabla\left(\Delta\mathbf{u}\right)^T\right)dV+\int_{\Omega_0} tr\left(\nabla\left(\delta\mathbf{u}\right)\Delta\boldsymbol{\tau}\right)dV, \tag{3.10}$$

where because of the equivalence of the material time derivatives and the directional derivatives, $\Delta\boldsymbol{\tau}$ can be written as Lie time derivatives

$$\Delta\boldsymbol{\tau}=\mathbf{F}\Delta\mathbf{S}\mathbf{F}^T=\chi_*\left(\Delta\mathbf{S}\right)=\chi_*\left(\Delta\left(\mathbf{F}^{-1}\boldsymbol{\tau}\mathbf{F}^{-T}\right)\right)=\chi_*\left(\Delta\chi_*^{-1}\left(\boldsymbol{\tau}\right)\right)=\mathcal{L}\left(\boldsymbol{\tau}\right). \tag{3.11}$$

We will come back to Eqs (3.10) and (3.11) later in this section when we discuss the objective stress rate in ABAQUS. The calculation of the first term on the right hand side (geometric stiffness) among all the above given linearized formulations is relatively straightforward and can be obtained directly if the stresses are known, while the second term in the right hand side (material part of stiffness) involves calculating $\Delta\mathbf{S}$ $(\Delta\boldsymbol{\sigma},\Delta\boldsymbol{\tau})$ through the constitutive equations. The general form of the expression is

$$\Delta\mathbf{S}=\mathbb{C}:\Delta\mathbf{E}=\frac{1}{2}\mathbb{C}:\Delta\mathbf{C}\ , \tag{3.12}$$

where $\mathbb{C}$ is the elasticity tensor (calculated for an explicit constitutive equation). The material moduli in the spatial description, denoted by $\mathbb{c}$, can be defined as a push-forward operation of $\mathbb{C}$ times J^{-1}, which is the Piola transformation of $\mathbb{C}$ as

$$\mathbb{c} = \frac{1}{J}\mathbf{F}\mathbf{F}\mathbb{C}\mathbf{F}^T\mathbf{F}^T\,, \tag{3.13}$$

which is used to express $\Delta\boldsymbol{\sigma}$ and $\Delta\boldsymbol{\tau}$ as

$$\Delta\boldsymbol{\sigma} = \mathbb{c} : \Delta\mathbf{e}\,, \tag{3.14}$$

$$\Delta\boldsymbol{\tau} = J\mathbb{c} : \Delta\mathbf{e}\,, \tag{3.15}$$

where

$$\Delta\mathbf{e} = \frac{1}{2}\left(grad^T\Delta\mathbf{u} + grad\Delta\mathbf{u}\right) = sym\left(grad\Delta\mathbf{u}\right) = sym\left(\nabla\left(\Delta\mathbf{u}\right)\right). \tag{3.16}$$

Inserting Eq (3.14) and Eq (3.15) back into the stiffness term of the linearized stress divergence terms in Eq (3.9) and Eq (3.10) respectively, yields the material and spatial descriptions

$$\int_\Omega tr\left(\nabla\left(\delta\mathbf{u}\right)\Delta\boldsymbol{\sigma}\right)dv = \int_\Omega tr\left(\delta\mathbf{e}\mathbb{c}\Delta\mathbf{e}\right)dv\,, \tag{3.17}$$

$$\int_{\Omega_0} tr\left(\nabla\left(\delta\mathbf{u}\right)\Delta\boldsymbol{\tau}\right)dV = \int_{\Omega_0} tr\left(\delta\mathbf{e}J\mathbb{c}\Delta\mathbf{e}\right)dV\,. \tag{3.18}$$

The linearized stress divergence terms in Eq (3.9) and Eq (3.10) can be expressed in the material and spatial descriptions, respectively, as

$$\Delta\left(\int_{\Omega_0} tr\left(\delta\mathbf{F}\mathbf{S}\mathbf{F}^T\right)dV\right) = \int_\Omega tr\left(\nabla\left(\delta\mathbf{u}\right)\boldsymbol{\sigma}\nabla\left(\Delta\mathbf{u}\right)^T\right)dv + \int_\Omega tr\left(\delta\mathbf{e}\mathbb{c}\Delta\mathbf{e}\right)dv\,, \tag{3.19}$$

$$\Delta\left(\int_{\Omega_0} tr\left(\delta\mathbf{F}\mathbf{S}\mathbf{F}^T\right)dV\right) = \int_{\Omega_0} tr\left(\nabla\left(\delta\mathbf{u}\right)\boldsymbol{\tau}\nabla\left(\Delta\mathbf{u}\right)^T\right)dV + \int_{\Omega_0} tr\left(\delta\mathbf{e}J\mathbb{c}\Delta\mathbf{e}\right)dV\,. \tag{3.20}$$

Spatial discretization and finite element formulations

Spatial discretization is performed to divide the body into finite elements. The displacement, incremental displacement, and the virtual displacements can be written by adopting an isoparametric formulation as

$$\mathbf{u} = N_I\left(\boldsymbol{\xi}\right)\mathbf{u}^I\left(t\right),\ \ \Delta\mathbf{u} = N_I\left(\boldsymbol{\xi}\right)\Delta\mathbf{u}^I\left(t\right),\ \ \delta\mathbf{u} = N_I\left(\boldsymbol{\xi}\right)\delta\mathbf{u}^I, I = 1,2,\cdots,nen\,, \tag{3.21}$$

where nen is the number of nodes on an individual element Ω_e with $\Omega = \sum_e \Omega_e$ being the domain of interest, I are node labels for the elements, $N_I(\boldsymbol{\xi})$ are shape functions for node I. The gradients are

$$\nabla(\Delta\mathbf{u}) = grad(N_I)\Delta\mathbf{u}^I = N_{I,J}\Delta\mathbf{u}^I,\ \ \nabla(\delta\mathbf{u}) = grad(N_I)\delta\mathbf{u}^I = N_{I,J}\delta\mathbf{u}^I, I = 1,2,\cdots,nen\ . \quad (3.22)$$

In the following, the residual form is expressed using the above spatial discretization. First, the stress divergence term in Eq (3.1) on a typical individual element is written as

$$\int_{\Omega_e} \boldsymbol{\sigma} : \delta\mathbf{e} dv = \int_{\Omega_e} \boldsymbol{\sigma}_{ij}\delta\mathbf{e}_{ji} dv\ . \quad (3.23)$$

By rewriting $\boldsymbol{\sigma}$ and $\delta\mathbf{e}$ in Voigt notation, we have

$$\boldsymbol{\sigma} = \begin{bmatrix} \boldsymbol{\sigma}_{11} & \boldsymbol{\sigma}_{22} & \boldsymbol{\sigma}_{33} & \boldsymbol{\sigma}_{12} & \boldsymbol{\sigma}_{13} & \boldsymbol{\sigma}_{23} \end{bmatrix}^T, \quad (3.24)$$

$$\delta\mathbf{e} = \begin{bmatrix} \delta\mathbf{e}_{11} & \delta\mathbf{e}_{22} & \delta\mathbf{e}_{33} & 2\delta\mathbf{e}_{12} & 2\delta\mathbf{e}_{13} & 2\delta\mathbf{e}_{23} \end{bmatrix}^T, \quad (3.25)$$

Eq (3.23) can be rewritten as

$$\int_{\Omega_e} \delta\mathbf{e}^T \boldsymbol{\sigma} dv\ . \quad (3.26)$$

Next, $\delta\mathbf{e}$ can be written out in terms of the discretized virtual displacement as (recall the expression $\delta\mathbf{e} = \frac{1}{2}\left(grad^T\delta\mathbf{u} + grad\delta\mathbf{u}\right)$)

$$\begin{aligned} \delta\mathbf{e} &= \begin{bmatrix} \frac{\partial\delta u_1}{\partial x_1} & \frac{\partial\delta u_2}{\partial x_2} & \frac{\partial\delta u_3}{\partial x_3} & \frac{\partial\delta u_1}{\partial x_2} + \frac{\partial\delta u_2}{\partial x_1} & \frac{\partial\delta u_1}{\partial x_3} + \frac{\partial\delta u_3}{\partial x_1} & \frac{\partial\delta u_2}{\partial x_3} + \frac{\partial\delta u_3}{\partial x_1} \end{bmatrix}^T \\ &= \begin{bmatrix} N_{I,1} & 0 & 0 & N_{I,2} & N_{I,3} & 0 \\ 0 & N_{I,2} & 0 & N_{I,1} & 0 & N_{I,3} \\ 0 & 0 & N_{I,3} & 0 & N_{I,1} & N_{I,1} \end{bmatrix}^T \begin{bmatrix} \delta u_1{}^I \\ \delta u_2{}^I \\ \delta u_3{}^I \end{bmatrix} = \mathbf{B}^I\delta\mathbf{u}^I, \end{aligned} \quad (3.27)$$

where the $\mathbf{B}$ matrix maps the virtual displacement $\delta\mathbf{u}$ to $\delta\mathbf{e}$. The stress divergence term in Eq (3.26) can be further rewritten as

$$\int_{\Omega_e} \delta\mathbf{e}^T \boldsymbol{\sigma} dv = \left(\delta\mathbf{u}^I\right)^T \int_{\Omega_e} \mathbf{B}^I \boldsymbol{\sigma} dv \,. \tag{3.28}$$

The loading terms in Eq (3.1) on a typical individual element are written as

$$\int_{\partial\Omega_e^t} \delta\mathbf{u}^T \bar{\mathbf{t}} dv = \left(\delta\mathbf{u}^I\right)^T \left(\int_{\Omega_e} N_I \rho \mathbf{b} dv + \int_{\partial\Omega_e^t} N_I \bar{\mathbf{t}} dv \right) \,. \tag{3.29}$$

Finally, the residual form of the equilibrium equations in Eq (3.1) can be rewritten using Eq (3.28) and (3.29) into a finite element formulation as

$$\mathbf{R} = \sum_e \left(\delta\mathbf{u}^I\right)^T \left(\int_{\Omega_e} \mathbf{B}^I \boldsymbol{\sigma} dv - \int_{\partial\Omega_e^t} N_I \bar{\mathbf{t}} dv \right) = 0 \,. \tag{3.30}$$

Since the virtual displacement $\delta\mathbf{u}^I$ is arbitrary, the residual form of the equilibrium equations reduce to

$$\mathbf{R} = \sum_e \left(\int_{\Omega_e} \mathbf{B}^I \boldsymbol{\sigma} dv - \int_{\partial\Omega_e^t} N_I \bar{\mathbf{t}} dv \right) = 0 \,. \tag{3.31}$$

For a specific constitutive equation, solving the residual form of the equilibrium equations and satisfying the displacement boundary conditions yields the solution to the initial boundary value problem. Newton's method is widely used to linearize the equations. The finite element formulation of Eq (3.19) is obtained as

$$\begin{aligned}
&\int_{\Omega_e} tr\left(\nabla(\delta\mathbf{u})\boldsymbol{\sigma}\nabla(\Delta\mathbf{u})^T\right) dv + \int_{\Omega_e} tr\left(\delta\mathbf{e}\, \mathbb{C}\, \Delta\mathbf{e}\right) dv \\
&= \left(\delta\mathbf{u}^I\right)^T \int_{\Omega_e} tr\left(\nabla N_I^T \boldsymbol{\sigma} \nabla N_J^T\right) dv \Delta\mathbf{u}^J + \int_{\Omega_e} \delta\mathbf{e}^T \mathbb{C}\, \Delta\mathbf{e} dv \\
&= \left(\delta\mathbf{u}^I\right)^T \Big(\underbrace{\int_{\Omega_e} tr\left(\nabla N_I^T \boldsymbol{\sigma} \nabla N_J^T\right) dv \mathbf{I}}_{\mathbf{K}^g{}_{IJ}} + \underbrace{\int_{\Omega_e} \mathbf{B}_I^T \mathbb{C} \mathbf{B}_J dv}_{\mathbf{K}^m{}_{IJ}} \Big) \Delta\mathbf{u}^J \\
&= \left(\delta\mathbf{u}^I\right)^T \left(\mathbf{K}^g{}_{IJ} + \mathbf{K}^m{}_{IJ}\right) \Delta\mathbf{u}^J \,.
\end{aligned} \tag{3.32}$$

Therefore, the linearization of the residual form of the equilibrium equation in Eq (3.31) gives

$$\mathbf{R} + \mathbf{K}\Delta\mathbf{u} \doteq 0, \quad \mathbf{K} = \mathbf{K}^g + \mathbf{K}^m \,. \tag{3.33}$$

It is noted that the total stiffness has two parts: the geometric stiffness and the material stiffness. The solution of the above equations (for $\Delta\mathbf{u}$) renders the iterative updates for the displacement as $\Delta\mathbf{u}+\mathbf{u}\rightarrow\mathbf{u}$ until the tolerance is satisfied.

Jaumann stress rate in ABAQUS

Here, we discuss some of the equivalent objective stress rates used in ABAQUS. Objective rates are essentially modified time derivatives of the Cauchy stress tensor. Many objective rates have been constructed in the literature and they just provide different options. Truesdell and Noll (1965) states that 'Despite claims and whole papers to the contrary, any advantage claimed for one such rate over another is pure illusion'. Here we start from the Lie time derivative $\mathcal{L}_v(\boldsymbol{\tau})$ in Eq (3.11) in the linearized stress divergence term, the Lie time derivative which is the same as Oldroyd rate, may be written as

$$\mathcal{L}_v(\boldsymbol{\tau})=\dot{\boldsymbol{\tau}}-\mathbf{l}\cdot\boldsymbol{\tau}-\boldsymbol{\tau}\cdot\mathbf{l}^T. \tag{3.34}$$

Various types of objective rates can be written in a unified form as (Ji et al., 2013)

$$\overset{\nabla}{\boldsymbol{\tau}}{}^{(n)}=\mathcal{L}_v(\boldsymbol{\tau})+\frac{1}{2}(2-n)(\mathbf{d}\cdot\boldsymbol{\tau}+\boldsymbol{\tau}\cdot\mathbf{d}), \tag{3.35}$$

where $n=2$ is the Oldroyd stress rate and $n=0$ is the Jaumann stress rate. Since the Jaumann stress rate is the objective stress rate used in ABAQUS and many other commercial software, we use it to derive the linearization of the residual form of Eq (3.33). This later used to calculate the unknown displacement field by the Newton's method in the finite element formulation. Based on the equivalence of the material time derivatives and the directional derivatives, Eq (3.15) with Eq (3.17) for the linearized stress divergence term can be rewritten by replacing the linear increment $\Delta\mathbf{u}$ by the spatial velocity field $\mathbf{v}$ as

$$\mathcal{L}_v(\boldsymbol{\tau}) = J\mathbb{C} : \mathbf{d}, \tag{3.36}$$

and similarly the Jaumann stress rate in Eq (3.35) is rewritten as

$$\overset{\nabla}{\boldsymbol{\tau}} = \mathcal{L}_v(\boldsymbol{\tau}) + \mathbf{d}\cdot\boldsymbol{\tau} + \boldsymbol{\tau}\cdot\mathbf{d}^T = J\mathbb{C} : \mathbf{d} + \mathbf{d}\cdot\boldsymbol{\tau} + \boldsymbol{\tau}\cdot\mathbf{d}^T = \mathbb{C}^{\nabla} : \mathbf{d}, \tag{3.37}$$

where $\mathbb{C}^{\nabla}$ is defined as the Jaumann tangent modulus. Assume $\mathbf{d}\cdot\boldsymbol{\tau} + \boldsymbol{\tau}\cdot\mathbf{d}^T$ can be written in the same form as the other terms in Eq (3.37) as the double contraction of a fourth order tensor with $\mathbf{d}$,

$$\mathbf{d}\cdot\boldsymbol{\tau} + \boldsymbol{\tau}\cdot\mathbf{d}^T = J\mathbb{C}' : \mathbf{d}. \tag{3.38}$$

That way, Eq (3.37) can be rewritten as

$$\overset{\nabla}{\boldsymbol{\tau}} = \mathbb{C}^{\nabla} : \mathbf{d} = J\mathbb{C} : \mathbf{d} + J\mathbb{C}' : \mathbf{d} = \left(J\mathbb{C} + J\mathbb{C}'\right) : \mathbf{d}. \tag{3.39}$$

It is noted that even though $\mathbf{A} : \mathbf{B} = \mathbf{C} : \mathbf{B}$, it cannot be concluded that $\mathbf{A} = \mathbf{C}$. However, when $\mathbf{A} = \mathbf{C}$, it is guaranteed that $\mathbf{A} : \mathbf{B} = \mathbf{C} : \mathbf{B}$. Therefore, the Jaumann tangent modulus can be written as

$$\mathbb{C}^{\nabla} = J\mathbb{C} + J\mathbb{C}'. \tag{3.40}$$

Consider the formulation of $\mathbb{C}'$ in Eq (3.38), we know there are an infinite number of fourth order tensors satisfying that equation based on the above double contraction rule. One such formulation can be formed by requiring major and minor symmetries as

$$\mathbb{C}'_{ijkl} = \frac{1}{2}\left(\delta_{ik}\sigma_{jl} + \delta_{il}\sigma_{jk} + \delta_{jk}\sigma_{il} + \delta_{jl}\sigma_{ik}\right). \tag{3.41}$$

The tangent modulus for ABAQUS is thus obtained through the Jaumann tangent modulus as

$$\mathbb{C}^{ABAQUS} = \frac{1}{J}\mathbb{C}^{\nabla}, \tag{3.42}$$

which is symmetric, which may be a main reason many commercial software use the Jaumann rate in their finite element formulations.

3.3 Tangent modulus

In this section, the general form of the tangent modulus for ABAQUS user subroutines is derived so that it can be directly employed for the material constitutive equations provided in the following chapters. In Chapter 2, the decoupled second Piola-Kirchhoff stress is

$$\mathbf{S} = 2\frac{\partial \Psi}{\partial \mathbf{C}} = \mathbf{S}_{iso} + \mathbf{S}_{vol}\,. \tag{3.43}$$

Accordingly, the tangent modulus in the material description can be written in the decoupled form as

$$\mathbb{C} = 2\frac{\partial \mathbf{S}}{\partial \mathbf{C}} = 2\frac{\partial \mathbf{S}_{iso}}{\partial \mathbf{C}} + 2\frac{\partial \mathbf{S}_{vol}}{\partial \mathbf{C}} = \mathbb{C}_{iso} + \mathbb{C}_{vol}\,, \tag{3.44}$$

where $\mathbb{C}_{iso}$ is the purely isochoric contribution and $\mathbb{C}_{vol}$ is the purely volumetric contribution. Before the discussion of the expressions for the isochoric and volumetric tangent modulus, some useful definitions are introduced as follows,

$$\frac{\partial J}{\partial \mathbf{C}} = \frac{J}{2}\mathbf{C}^{-1}, \tag{3.45}$$

$$\frac{\partial \bar{\mathbf{C}}}{\partial \mathbf{C}} = \frac{\partial \left(J^{-2/3}\mathbf{C}\right)}{\partial \mathbf{C}} = J^{-2/3}\left(\mathbb{I}^{sym} + J^{2/3}\mathbf{C}\otimes\frac{\partial J^{-2/3}}{\partial \mathbf{C}}\right) = J^{-2/3}\underbrace{\left(\mathbb{I}^{sym} - \frac{1}{3}\mathbf{C}\otimes\mathbf{C}^{-1}\right)}_{\mathbb{P}^T} = J^{-2/3}\mathbb{P}^T, \tag{3.46}$$

$$\mathbb{P} = \mathbb{I}^{sym} - \frac{1}{3}\mathbf{C}^{-1}\otimes\mathbf{C},\quad \mathbb{I}^{sym} = \frac{1}{2}\left(\mathbb{I} + \bar{\mathbb{I}}\right), \tag{3.47}$$

$$\frac{\partial \mathbf{C}^{-1}}{\partial \mathbf{C}} = -\mathbf{C}^{-1}\odot\mathbf{C}^{-1},\quad \left(-\mathbf{C}^{-1}\odot\mathbf{C}^{-1}\right)_{ABCD} = -\frac{1}{2}\left(C^{-1}_{AC}C^{-1}_{BD} + C^{-1}_{AD}C^{-1}_{BC}\right) = \frac{\partial C^{-1}_{AB}}{\partial C_{CD}}, \tag{3.48}$$

$$\left(\mathbf{A}\otimes\mathbf{B}\right):\mathbf{C} = \mathbf{A}\left(\mathbf{B}:\mathbf{C}\right) = \left(\mathbf{B}:\mathbf{C}\right)\mathbf{A}\,. \tag{3.49}$$

where $\bar{\mathbf{C}} = J^{-2/3}\mathbf{C}$ is the isochoric part of $\mathbf{C}$, and the tensor notation $-\mathbf{C}^{-1}\odot\mathbf{C}^{-1}$ is used to represent a fourth order tensor.

We start with the volumetric tangent modulus. Its explicit form for a given constitutive equation is derived using the chain rule as (details refer to (Holzapfel, 2000))

$$\begin{aligned}\mathbb{C}_{vol} &= 2\frac{\partial \mathbf{S}_{vol}}{\partial \mathbf{C}} = 2\frac{\partial\left(Jp\mathbf{C}^{-1}\right)}{\partial \mathbf{C}} = 2\mathbf{C}^{-1}\otimes\left(p\frac{\partial J}{\partial \mathbf{C}} + J\frac{\partial p}{\partial \mathbf{C}}\right) + 2Jp\frac{\partial \mathbf{C}^{-1}}{\partial \mathbf{C}} \\ &= 2\mathbf{C}^{-1}\otimes\left(p\frac{J}{2}\mathbf{C}^{-1} + J\frac{\partial p}{\partial J}\underbrace{\frac{J}{2}\mathbf{C}^{-1}}_{\partial J/\partial \mathbf{C}}\right) - 2Jp\mathbf{C}^{-1}\odot\mathbf{C}^{-1} \\ &= J\left(p + J\frac{\partial p}{\partial J}\right)\mathbf{C}^{-1}\otimes\mathbf{C}^{-1} - 2Jp\mathbf{C}^{-1}\odot\mathbf{C}^{-1},\end{aligned} \tag{3.50}$$

where only p needs to be specified for a given material. Similarly, the explicit expression for the isochoric tangent modulus is (details refer to (Holzapfel, 2000))

$$\begin{aligned}\mathbb{C}_{iso} &= 2\frac{\partial \mathbf{S}_{iso}}{\partial \mathbf{C}} = 2\frac{\partial\left(J^{-2/3}\mathbb{P}:\bar{\mathbf{S}}\right)}{\partial \mathbf{C}} = 2\left(\mathbb{P}:\mathbf{S}\right)\otimes\frac{\partial J^{-2/3}}{\partial \mathbf{C}} + 2J^{-2/3}\frac{\partial\left(\mathbb{P}:\bar{\mathbf{S}}\right)}{\partial \mathbf{C}} \\ &= \mathbb{P}:\bar{\mathbb{C}}:\mathbb{P}^{T} - \frac{2}{3}\left(\mathbf{S}_{iso}\otimes\mathbf{C}^{-1} + \mathbf{C}^{-1}\otimes\mathbf{S}_{iso}\right) - \frac{2}{3}J^{-2/3}tr\left(\bar{\mathbf{S}}\right)\tilde{\mathbb{P}},\end{aligned} \tag{3.51}$$

where $\bar{\mathbb{C}} = 2J^{-4/3}\partial\bar{\mathbf{S}}/\partial\bar{\mathbf{C}}$ is the fourth-order fictitious elasticity tensor in the material description and is symmetric with $\bar{\mathbb{C}} = \bar{\mathbb{C}}^{T}$, and $\tilde{\mathbb{P}} = \mathbf{C}^{-1}\odot\mathbf{C}^{-1} - \frac{1}{3}\mathbf{C}^{-1}\otimes\mathbf{C}$ is the modified projection tensor. We can also write it as

$$\mathbb{C}_{iso} = \mathbb{C}_{iso,Dev} - \frac{2}{3}\left(\mathbf{S}_{iso}\otimes\mathbf{C}^{-1} + \mathbf{C}^{-1}\otimes\mathbf{S}_{iso}\right) - \frac{2}{3}J^{-2/3}tr\left(\bar{\mathbf{S}}\right)\tilde{\mathbb{P}}, \tag{3.52}$$

where $\mathbb{C}_{iso,Dev} = \mathbb{P}:\bar{\mathbb{C}}:\mathbb{P}^{T}$ is the fourth-order tensor of the deviatoric tangent modulus. Therefore, the explicit form of the tangent modulus in the material description is

$$\begin{aligned}\mathbb{C} = \mathbb{C}_{iso} + \mathbb{C}_{vol} &= \mathbb{C}_{iso,Dev} - \frac{2}{3}\left(\mathbf{S}_{iso}\otimes\mathbf{C}^{-1} + \mathbf{C}^{-1}\otimes\mathbf{S}_{iso}\right) - \frac{2}{3}J^{-2/3}tr\left(\bar{\mathbf{S}}\right)\tilde{\mathbb{P}} \\ &\quad + J\left(p + J\frac{\partial p}{\partial J}\right)\mathbf{C}^{-1}\otimes\mathbf{C}^{-1} - 2Jp\mathbf{C}^{-1}\odot\mathbf{C}^{-1}.\end{aligned} \tag{3.53}$$

Lastly, the tangent modulus in the spatial description is obtained by taking the Piola transformation of $\mathbb{C}$, i.e. by applying push-forward operation of $\mathbb{C}$ times a factor J^{-1} as

$$\mathbb{c} = J^{-1}\chi_*(\mathbb{C}), \quad \mathbb{c}_{abcd} = J^{-1}F_{aA}F_{bB}F_{cC}F_{dD}\mathbb{C}_{ABCD}. \tag{3.54}$$

The explicit form for the tangent modulus in the spatial description is

$$\begin{aligned}\mathbb{c} = \mathbb{c}_{iso} + \mathbb{c}_{vol} = \mathbb{c}_{iso,Dev} &- \frac{2}{3}\left(\boldsymbol{\tau}_{iso}\otimes\mathbf{I} + \mathbf{I}\otimes\boldsymbol{\tau}_{iso}\right) - \frac{2}{3}tr\left(\bar{\boldsymbol{\tau}}\right)\mathbb{P} \\ &+ J\left(p + J\frac{\partial p}{\partial J}\right)\mathbf{I}\otimes\mathbf{I} - 2Jp\mathbb{I}^{sym},\end{aligned} \tag{3.55}$$

where the deviatoric part of the tangent modulus is $\mathbb{c}_{iso,Dev} = J^{-1}\chi_*\left(\mathbb{C}_{iso,Dev}\right)$, $\left(\mathbb{c}_{iso,Dev}\right)_{ijkl} = J^{-1}F_{iI}F_{jJ}F_{kK}F_{lL}\left(\mathbb{C}_{iso,Dev}\right)_{IJKL}$. The Eqs (3.53) and (3.55) are the general forms of the tangent modulus in material and spatial descriptions which can be used for constitutive equations with the strain energy formulated as functions of the right or left Cauchy-Green tensors and / or internal variables.

For viscoelastic materials, the internal variables are treated as solution-dependent state variables in computational user subroutines (ABAQUS). The evolution equations are solved with the user-defined subroutines by applying the finite-difference method, such as the Euler forward and the Euler backward methods etc., to the time derivative equation. The internal variables at the next time step can be solved directly from the explicit nonlinear evolution equations if the Euler forward method is applied. Otherwise if other methods, such as the Euler backward method, are applied, the evolution equations are implicit nonlinear equations and numerical methods are needed to solve them. Newton iteration is a general method used to solve nonlinear equations. If the internal variables are vector- or tensor-valued variables, the solutions

need to be rotated (multiply by the rotation increment matrix DROT (3,3) in the UMAT) before being passed to ABAQUS (blackbox) to account for the rigid body motion.

3.4 Summary

In this chapter, we summarized the formulations needed for computational implementation of constitutive models in a FEM environment. A general weak form of the equilibrium equations for initial boundary value problems and its linearization are presented. This is the framework used for the constitutive models developed in Chapters 4 and 6. Specifically, the Jaumann rate used in the commercial software ABAQUS is derived and discussed. Lastly, general formulations of the tangent modulus are introduced and the tangent modulus based on the Jaumann rate is derived. In the following chapter, specific constitutive models are proposed for smooth muscle tissue and dielectric elastomer composites on the basis of the theoretical background and foundations outlined in Chapters 2 and 3.

References

Bonet, D. J., Wood, D. R. D., 2008. Nonlinear Continuum Mechanics for Finite Element Analysis. Cambridge University Press, Cambridge, UK ; New York.

Gurtin, M. E., 1981. An Introduction to Continuum Mechanics, Volume 158. Academic Press, New York.

Holzapfel, G. A., 2000. Nonlinear Solid Mechanics: A Continuum Approach for Engineering. Wiley, Chichester ; New York.

Hughes, T. J. R., 2000. The Finite Element Method: Linear Static and Dynamic Finite Element Analysis. Dover Publications, Mineola, NY.

Ji, W., Waas, A. M., Bazant, Z. P., 2013. On the Importance of Work-Conjugacy and Objective Stress Rates in Finite Deformation Incremental Finite Element Analysis. Journal of Applied Mechanics 80, 041024-041024-9, doi:10.1115/1.4007828.

Lemaitre, J., Chaboche, J.-L., 1994. Mechanics of Solid Materials. Cambridge University Press.

Marsden, J. E., Hughes, T. J. R., 1994. Mathematical Foundations of Elasticity. Dover Publications, New York.

Ogden, R. W., Engineering, 1997. Non-Linear Elastic Deformations. Dover Publications, Mineola, N.Y.

Simo, J. C., Hughes, T. J. R., 2000. Computational Inelasticity. Springer, New York.

Truesdell, C., Toupin, R., 1960. The Classical Field Theories. In: Flügge, S., (Ed.), Principles of Classical Mechanics and Field Theory / Prinzipien der Klassischen Mechanik und Feldtheorie. Springer Berlin Heidelberg, pp. 226-858.

Chapter 4. A nonlinear constitutive model for smooth muscle tissue

4.1 Introduction

Smooth muscle plays an integral role in supporting contractile function in the artery. Medical interventions involve drug treatments to modulate artery physiology and invasive stent deployment to hold diseased arteries open and preserve hollow lumen geometry for blood flow. The potential for employing sensors implanted in deployed stents or the artery itself to monitor the state of disease after treatment is of critical interest. (Barkam et al., 2013; Green et al., 2013; Lawson and Wallace, 2012; Li et al., 2012; Nuxoll, 2013; Son and Goulbourne, 2012) Theoretical physiological modeling of the artery, particularly those involving the role of structure, is a potentially critical enabling tool to increase understanding of disease and design suitable intervention strategies. Here, we present recent developments of such a modeling tool. In this chapter, a coupled chemo-mechanical model is proposed to describe the active viscoelastic response of smooth muscle rich tissue in the arterial walls (media layer).

Generally, there are two theoretical approaches to modeling smooth muscle contractile behavior: cell-based models and continuum models. Cell models are structural crossbridge models, which are generally based on the sliding-filament theory of Huxley. (Huxley, 1957; Huxley, 1974; Huxley, 2000; Huxley and Niedergerke, 1954; Huxley and Hanson, 1954; Huxley, 1969; Huxley, 2004) These models focus on the

specifics of a detailed crossbridge structure and the mechanics of myosin head cycling in the contractile apparatus. (Donovan, 2013; Gestrelius and Borgstrom, 1986; Hai and Murphy, 1988; Laforet and Guiraud, 2008; Wang et al., 2008; Yu et al., 1997) A continuum model approach at the tissue scale is attractive since it can be easily implemented in a finite element environment to solve numerical problems involving complex structural geometries, loading conditions, and boundary conditions. This approach employs a phenomenological constitutive formulation to describe smooth muscle contraction and whole artery deformation where the material parameters are calibrated to muscle strip and whole artery experimental data. Hill's three-element model and related work is the earliest smooth muscle model developed using a continuum approach. (Fung, 1970; Fung, 1993; Hill, 1938; Humphrey and Wilson, 2003; Rachev and Hayashi, 1999; Zulliger et al., 2004) Essential features of muscle contractility are captured but one of the drawbacks in these models is that the discrete mechanism of smooth muscle contraction is not explicitly considered.

More structure-based continuum tissue models were developed which coupled the sliding-filament theory (contractile apparatus scale) within a continuum mechanics framework so that the models can capture the characteristics of smooth muscle based on the physical mechanism of smooth muscle contraction. (Böl et al., 2012; Kroon, 2010; Liu, 2014; Murtada et al., 2010; Murtada et al., 2012; Stålhand et al., 2008; Stålhand et al., 2011; Yang et al., 2003) For example, based on Yang's cell-scale electro-chemo-mechanical model, Stalhand et al. formulated a mechano-chemical finite strain model by considering the interaction between mechanical and biochemical components. (Stålhand et al., 2008; Stålhand et al., 2011; Yang et al., 2003) Murtada et al. developed a model that combined microscopic filament displacement within a continuum mechanics framework and developed a model with relative sliding filament displacement as an

internal variable. (Murtada et al., 2010) The model is able to capture isometric behavior and a part of the isotonic response. The evolution equation in their model was extended to a hyperbolic function inspired by Hill's equation to capture the force-velocity relationship. (Murtada et al., 2012) Using a finite strain nonlinear viscoelastic approach, Kroon proposed a chemo-mechanical model where the viscous fiber stretch was employed as an internal variable in the continuum constitutive model. (Kroon, 2010) The model can capture the isometric and isotonic experiments partly through adjusting the passive material parameters. Overall, these studies are promising and provide a solid foundation for our current work.

Here, we present a nonlinear viscoelastic model within a large deformation framework for the media layer of the artery wall considering active smooth muscle tone following (Kroon, 2010). We use an approach consistent with that employed by Stalhand et al., Murtada et al. for coupling chemo-mechanical equations. (Murtada et al., 2010; Murtada et al., 2012; Stålhand et al., 2008; Stålhand et al., 2011) The current work can be distinguished in several ways. Most notably, the model separates the function of slow cycling and fast cycling crossbridges, by suggesting a structural origin for active viscoelastic behavior (slow cycling crossbridges) in the contractile unit and deriving the driving force of the contractile unit from fast cycling crossbridges only. The proposed constitutive equations are derived from fundamental mechanical principles and are shown to be thermodynamically consistent. The paper outline is as follows. In section 4.2, we review cycling kinetics of smooth muscle cell contraction. Next, we adopt Hai and Murphy's four-state chemical model to describe myosin head cycling and propose a viscous model based on experimental observations that the much slower cycling of attached latchbridges acts as a resistive force decreasing the velocity of thin filaments moved by the fast cycling myosin heads. In section 4.3, the chemical and

mechanical parts are coupled in a continuum description. The microscopic structure of individual contractile units is not modeled explicitly. Instead, the properties of the microscopic structure are simply extrapolated to the macroscale as in Kroon, Stalhand et al., and Wong et al. etc. (Kroon, 2010; Stålhand et al., 2008; Stålhand et al., 2011; Wong et al., 2013) A nonlinear evolution equation is proposed to capture the hyperbolic force-velocity relationship. In the evolution equation, we introduce for the first time a microscopic mechanism for the active viscoelastic behavior of smooth muscle originating from the instantaneous fraction of latch bridges and the driving force from fast cycling crossbridges only. In section 4.4, the model parameters are calibrated by experimental data from isometric and isotonic tests on swine carotid artery media strips. In section 4.5, a wide range of numerical values for model parameters are studied. The proposed model is able to capture the characteristics of smooth muscle contraction under isometric and isotonic test conditions as well as passive behavior. A summary from the current work is presented in section 4.6.

4.2 Mechanism of smooth muscle contraction

The artery wall consists of three layers: the intima, media, and adventitia. The innermost layer of the artery is the intima – a single cell layer with negligible stiffness, which is often not included in mechanical models as it is considered structurally negligible. The physiological function of the endothelial layer, however, is of significant importance in regards to local cell signaling for the myogenic response and calcification, for example. (Furchgott and Zawadzki, 1980; Yanagisawa et al., 1988) The media layer is the thickest layer in the artery wall. It is often referred to as the muscular layer because the tissue is mostly composed of smooth muscle cells, which are circumferentially oriented with a very small pitch, less than 10°. (An et al., 2007; Clark and Glagov, 1985;

Flamini et al., 2010; O'Connell et al., 2008; Shiraishi et al., 1986; Takahashi et al., 1994; Walmsley et al., 1983) Activity in the media layer plays an important role in regulating circulatory dynamics such as maintaining blood pressure and continuous blood circulation. The media also contains circumferentially oriented collagen fibers, which closely envelop smooth muscle cells; a low concentration of elastin fibers are also present. (Flamini et al., 2010; Gasser et al., 2006; Ghazanfari et al., 2012; O'Connell et al., 2008) For the sake of simplicity, the small fiber dispersion is not considered in the present work (see (Gasser et al., 2006; Kroon, 2011; Wang et al., 2012)). The adventitia is largely composed of loosely woven collagen fibers that protect the blood vessels and anchor them to surrounding structures. The orientation of collagen fibers in the adventitia is helical with some angular dispersion. (Gasser et al., 2006)

Here we briefly review the smooth muscle contraction cycle as it forms the basis for the proposed active damper model. Within the smooth muscle cell, the thin and thick filaments, consisting of actin and myosin, are organized in bundles to form the contractile apparatus. (Rüegg, 1992) The contractile apparatus generates active force and contraction through relative sliding of the thick and thin filaments caused by cycling movement of myosin heads called cross-bridge cycling (see Chapter 1Figure 2). The cross-bridge cycle consists of four states (see Chapter 1 Figure 3). Initially, the myosin bound ATP, which makes the myosin heads return to their resting conformation from the last cycle position, is hydrolyzed to ADP plus inorganic phosphate (Pi) retained on the myosin under the activation of CaCAM with MLCK (myosin light-chain kinase). Next, the myosin heads move from the resting conformation to a new position on the actin filament forming the crossbridge. Thirdly, the dissociation of Pi from the myosin heads causes myosin heads to change

conformation resulting in the power stroke. This conformational change results in the filaments sliding past each other and active force generation. Finally, ADP is released from myosin and a new ATP attaches returning to the beginning point of the crossbridge cycle. The sliding filament theory describing the overall contractile mechanism has been used as a basis for many different models of cross-bridge cycling. (Huxley, 1957; Huxley, 1974; Huxley, 2000; Huxley and Niedergerke, 1954; Huxley and Hanson, 1954; Huxley, 1969; Huxley, 2004) Unlike striated muscle, smooth muscle is able to maintain high force for a long period at a low rate of ATP hydrolysis. This unique low-energy consumption/ high-tension state is referred to as the latch state. (Boron and Boulpaep, 2009) The latchbridges refer to a population of dephosphorylated crossbridge heads that stay attached to the thin filaments after the power stroke. This population of crossbridges have a much slower cycling rate compared to the rest of the fast cycling myosin heads. (Boron and Boulpaep, 2009; Hai and Murphy, 1988; Murphy and Rembold, 2005) Hai and Murphy proposed a four-state kinetic model to capture both slow and fast cycling kinetics of the myosin heads, which is introduced in the following subsection. (Hai and Murphy, 1988)

4.3 Coupled chemo-mechanical model framework

In this section, a structure-based continuum model is proposed to capture the active viscoelastic behavior of the smooth muscle tissue. The constitutive model is based on an existing model framework in the literature (Kroon, 2010; Murtada et al., 2010; Murtada et al., 2012; Stålhand et al., 2008; Stålhand et al., 2011) and we propose a third order nonlinear evolution equation to describe the nonlinear behavior of smooth muscle contraction. The model formulation is attractive because it incorporates a structure-based description of smooth muscle contraction and a detailed description of

the chemical stimulus for muscle activation. The model has two parts: a chemical part and a mechanical part.

4.3.1 Chemical model for the smooth muscle contractile unit

Following Kroon and others, the widely-used Hai and Murphy four-state model is used to describe cross-bridge kinetics as a function of intracellular calcium concentrations. (Hai and Murphy, 1988; Kroon, 2010; Murtada et al., 2010; Stålhand et al., 2008; Stålhand et al., 2011) The contractile unit is operative via myosin cycling, whereby four fractional states of the myosin-actin interaction are described: unphosphorylated (free) myosin (M), phosphorylated myosin (Mp), attached phosphorylated cycling cross-bridges (AMp), and attached dephosphorylated non-cycling cross-bridges i.e. latch-bridges (AM). A schematic of the chemical state model proposed by Hai and Murphy is in Figure 10. The state equations are given by Eq. (4.1) where all species (states) are constrained to satisfy the conservation equality (M) + (Mp) + (AMp) + (AM) = 1 where $K_1 \sim K_7$ are the seven rate parameters calibrated by experiments on smooth muscle tissue strips (for more details refer to Hai and Murphy (Hai and Murphy, 1988)). K_3 and K_4 describe fast cycling kinetics. The parameters K_1 and K_6 are functions of intracellular calcium concentration. (Hai and Murphy, 1988; Huxley, 1957)

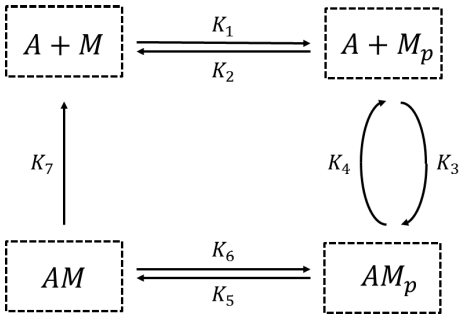

Figure 10. Kinetics of the four-state chemical model. Note that rate constants K_3 and K_4 describe fast cycling kinetics and AM describes the latchbridge state.

$$\begin{Bmatrix} \dot{M} \\ \dot{M}p \\ A\dot{M}p \\ A\dot{M} \end{Bmatrix} = \begin{bmatrix} -K_1 & K_2 & 0 & K_7 \\ K_1 & -K_2 - K_3 & K_4 & 0 \\ 0 & K_3 & -K_4 - K_5 & K_6 \\ 0 & 0 & K_5 & -K_6 - K_7 \end{bmatrix} \begin{Bmatrix} M \\ Mp \\ AMp \\ AM \end{Bmatrix}. \quad (4.1)$$

The rate constants K_3 and K_4 describe fast cycling kinetics, which involves the attachment and detachment of thin and thick filaments. The constants K_1 and K_6 are phosphorylation rates for the conversion of M and AM to Mp and AMp by the active MLCK and CaCAM. The constant K_2 and K_5 are the dephosphorylation rates of Mp and AMp to M and AM by the MLCP (myosin light-chain phosphatase). The rate constant K_7 is the detachment rate of the latchbridges, which is generally much smaller than the other rate parameters so that it can describe latchbridges. (Boron and Boulpaep, 2009; Hai and Murphy, 1988; Murphy and Rembold, 2005)

Several experiments show that the latchbridges act as a resistive load on the whole contractile unit while the remaining fraction of phosphorylated myosin heads cycle, and this decreases the velocity at which the fast cycling myosin heads move the thin filaments. (Aksoy et al., 1982; Aksoy et al., 1983; Dillon et al., 1981; Gerthoffer and Murphy, 1983; Harris et al., 1994; Seow and Stephens, 1986; Warshaw and Trybus, 1991; Warshaw et al., 1990) Specifically, Warshaw et al. performed experiments in vitro on a single actin filament interacting with various ratios of phyosphorylated and dephosphorylated myosin heads and showed that dephosphorylated myosin heads act as a load to slow down the rate at which an actin filament is moved by fast cycling phosphorylated crossbridges. (Warshaw and Trybus, 1991; Warshaw et al., 1990) Harris et al. showed that different combinations of crossbridge cycling rates affect the actin filament velocity. (Harris et al., 1994) A striking observation from (Aksoy et al., 1982;

Dillon et al., 1981; Gerthoffer and Murphy, 1983; Seow and Stephens, 1986) is that the transition from phosphorylated crossbridges to dephosphorylated crossbridges was related to a decline in velocity of shortening and Aksoy et al. suggested that the observed dependence of velocity on the ratio of phosphorylated and dephosphoralyted crossbridges is a physiological consequence of latchbridges acting as an internal load to slow the cycling rate of phosphorylated crossbridges (Aksoy et al., 1983). Based on this kinematic observation, we propose that the latchbridges have a drag-like effect on the relative movement of thin and thick filaments and thus the viscous coefficient of the active contractile units depends on the fraction of engaged latchbridges (AM). Figure 11 shows a schematic of the structure-based active contractile unit which is modeled as an active damper in the present work. As can be seen in Figure 11 the thin filament slides to the right under the action of slow cycling (blue) and fast cycling (red) myosin heads during the power stroke. Because the slow cycling crossbridge (latchbridge) remains attached to the thin filament, it acts as a resistive load on the relative movement of the thin filament driven by the fast cycling crossbridges. Therefore, in the present work, the viscous coefficient of the active damper depends on the fraction of attached latchbridges and the driving force of the active damper is produced by the fast cycling crossbridges only. This structurally based active damper is described by an evolution equation in the mechanics model given in detail in section 4.3.2.

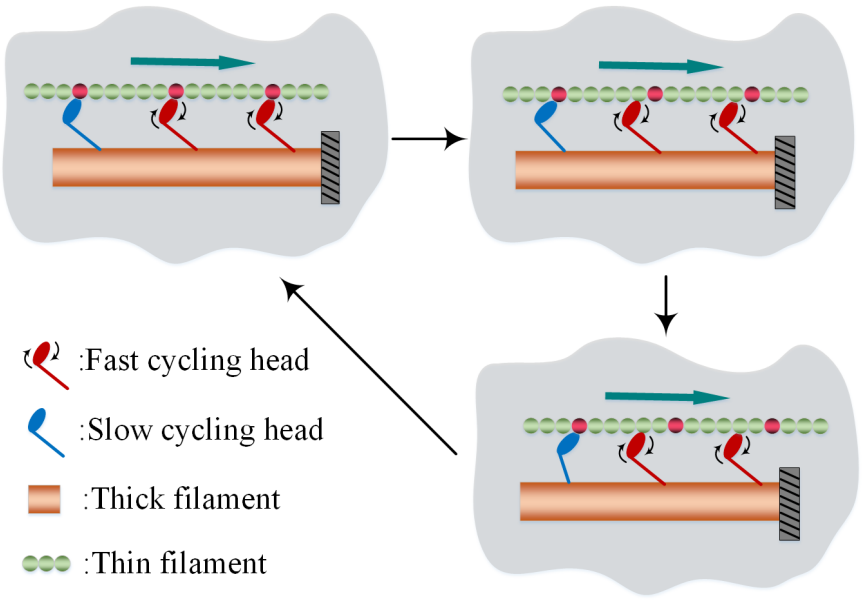

Figure 11. Schematic of the active damper: drag-like effect of latchbridges (slow cycling heads) and the driving force of the contractile unit produced by the fast cycling crossbridges (fast cycling heads).

Other assumptions for the kinetic model are adopted from Hai and Murphy such as setting identical affinities of MLCK and MLCP for the detached and attached cross bridges and 4:1 attachment-to-detachment ratio for the phosphorylated cycling crossbridges, that is, $K_1 = K_6$, $K_2 = K_5$, and $K_3 = 4K_4$. (Hai and Murphy, 1988) The extent of overlap between thin and thick filaments depends on smooth muscle deformation. Experimental results show that the active stress-stretch relationship is parabolic or bell-shaped. (An et al., 2007; Hai and Murphy, 1988; Herlihy and Murphy, 1973; Kamm et al., 1989; Ramsey and Street, 1940) A Gaussian function describing this overlap effect was first introduced by Yang et al. and is referred to as the overlap coefficient function, labeled as O_{lap} in the present work, where $O_{lap} \in [0,1]$. (Yang et al., 2003) Thus, the effective fraction of myosin heads which is assumed to be able to produce active force is

$(AMp + AM)O_{lap}$. (Hai and Murphy, 1988; Murphy and Rembold, 2005) The explicit form for the overlap coefficient function used is given in section 4.3.2.

At the cell scale, we assume that each smooth muscle cell consists of contractile units oriented with the cell long axis. At the tissue scale, we consider that all the smooth muscle cells are homogeneously and continuously distributed throughout the media layer with an overall dominant orientation and thus series of contractile units are treated as a homogeneously distributed fiber family in a passive matrix. Hence, at the macroscale we work with the continuum assumption of infinitely repeating contractile units of a particular orientation. Intracellular microscopic properties (chemical quantities) are extracted to the homogenized macroscopic scale, that is, $AMp + AM$ (fraction of cycling myosin) is directly passed into the strain energy formulation of the mechanical model. (Kroon, 2010; Stålhand et al., 2008; Stålhand et al., 2011; Wong et al., 2013)

4.3.2 Mechanical model of the artery media layer

Working in a continuum framework, we present a constitutive model for the media layer that is additively composed of three parts based on the composite media layer of the artery: the isotropic passive matrix, passive fibers, and the contractile units (active fibers). The ground substance is modeled as an isotropic passive matrix containing embedded collagen fibers. Smooth muscle has both passive and active parts. The passive part refers to smooth muscle in an inactive state where the actin filaments and myosin heads are detached, and the contractile units produce no active force. The passive part of the smooth muscle fibers gives rise to a passive anisotropic effect together with the collagen fibers, which are modeled as passive fibers. The active part

refers to the contractile units when smooth muscle is in an active state, and the series contractile units are modeled as an active fiber family.

Soft tissue in nearly incompressible; therefore I_3 dependence of the strain energy function is omitted. Furthermore, I_2 dependence of strain energy function is omitted as is typical of soft tissue models for simplicity and reduction of parameters. Thus, the simplified strain energy function takes the following form,

$$\Psi\left(\mathbf{C}, \mathbf{C}_F^v, \mathbf{V}\right) = \Psi\left(I_1, I_f, I_f^v\right), \tag{4.2}$$

where $I_f = \mathbf{V} \cdot \mathbf{CV}$ and $\mathbf{V}$ is unit vector representing the orientation of the smooth muscle and collagen fibers in the media layer. The strain energy density function for the media layer is split into three parts according to the composition of media layer: an isotropic passive matrix with equilibrium and nonequilibrium parts, hyperelastic passive fibers, and the nonequilibrium part of the active fibers. The most general form is

$$\Psi(I_1, I_f, I_f^v) = \underbrace{\Psi_{\mathrm{M}}(I_1)}_{\text{isotropic passive matrix}} + \underbrace{\Psi_{\mathrm{pF}}(I_f)}_{\text{passive fibers}} + \underbrace{\Psi_{\mathrm{aF}}(I_f, I_f^v)}_{\text{active fibers}} . \tag{4.3}$$

The model can be represented schematically by a linear rheological model is shown in Figure 12. (Hill, 1938) The schematic contains four branches arranged in parallel. The active mechanism of the contractile apparatus is characterized by the driving force produced by the fast cycling crossbridges in the active damper, which we define as P_d. The active damper is described by a nonlinear evolution equation in a large deformation framework. The energy stored in the springs of the rheological model is described by the strain energy function.

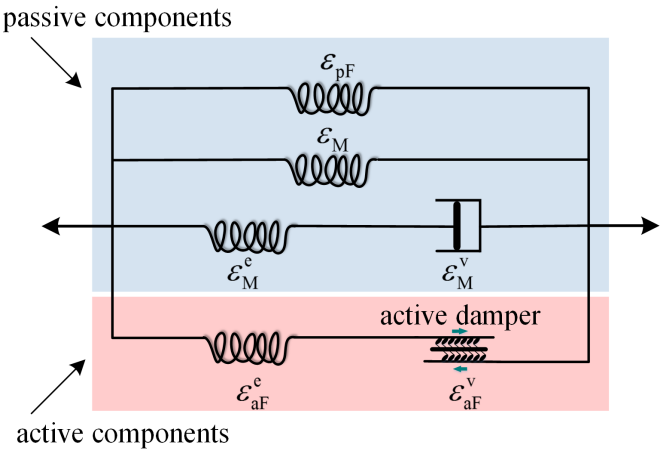

Figure 12. A linear rheological model of the media layer.

The strain energy function for the media layer with smooth muscle include an isotropic passive part (NeoHookean form), an anisotropic passive part (exponential form), and an active part (square form), (Fung, 1970; Kroon, 2010)

$$\Psi = \frac{\mu_p}{2}(I_1 - 1) + \frac{k_1}{2k_2}\left(\exp\left(k_2(I_f - 1)^2\right) - 1\right) + (AMp + AM)O_{lap}\frac{\mu_f}{4}\left(\frac{I_f}{I_f^v} - 1\right)^2, \tag{4.4}$$

where μ_p, μ_f, k_1 are modulus like material constants for the matrix, passive and active fiber respectively, k_2 is material constants for passive fiber, O_{lap} is the overlap coefficient function describing the degree of overlap of thin and thick filaments with $O_{lap} \in [0,1]$, and the produce of $AMp + AM$ and O_{lap}, i.e. $(AMp + AM)O_{lap}$ is the fraction of cross-bridges in the overlap zone (producing active stress). The overlap coefficient is phenomenologically described by a Gaussian function of viscous stretch (the stretch of the active damper) introduced by Yang et al. (and by Stalhand et al.), which defines the relationship of the degree of overlap to the maximum active stress generated by the contractile unit, (Stålhand et al., 2008; Stålhand et al., 2011; Yang et al., 2003)

$$O_{lap} = \exp\left(-\left(\left(I_f^v\right)^{1/2} - \left(I_f^v\right)_{opt}^{1/2}\right)^2 / \left(2\xi^2\right)\right), \tag{4.5}$$

where the constant ξ is the bandwidth controlling the shape of the function, the stretch at which smooth muscle tissue develops the maximum stress is the so-called 'optimal stretch' and the corresponding viscous stretch of the active fiber is defined as the optimal viscous stretch, $\left(I_f^v\right)_{opt}^{1/2} = \lambda_{Fopt}^v$. The parameters in the overlap function are determined by experiments on smooth muscle tissue strips.

In Kroon's and Murtada et al.'s models (Kroon, 2010; Murtada et al., 2010), the evolution equation governing the internal variable I_f^v is given by a proportional relationship between the active viscous fiber stretch rate ($\dot{\lambda}_F^v = \sqrt{\dot{I}_f^v}$) and the resultant stress with a constant viscous coefficient η. The resultant stress τ_{res} on the active damper is defined as $\tau_{res} = P_d - P_r$, i.e. the difference between the driving stress P_d exerted by the attached crossbridges and the resistance stress P_r coming from the surrounding tissue of the contractile units which is physically related to the energy stored in the contractile units. The resistance stress takes the following form (first Piola-Kirchhoff stress in the active fiber), (see (Kroon, 2010; Murtada et al., 2010) for details)

$$P_r = \frac{\partial \Psi}{\partial \lambda_F^v} \tag{4.6}$$

Muscle behaviors are typically characterized using isotonic and isometric tests. (Dillon et al., 1981) We notice that experimentally the initial velocity (stretch rate) and the afterload (the external force) in isotonic tests have a nonlinear relationship for shortening and an S-shaped relationship for shortening and lengthening, the same as in skeletal muscle (see Figure 13 and Figure 16 (b) and Figure 16 (d)). (Hanks and Stephens, 1981; Koeppen and Stanton, 2009; Lieber and Ward, 2011; Ruiter and Haan, 2001) Two distinct regimes occur based on the value of the afterload under isotonic

conditions. If the afterload is larger than the maximum isometric force, the smooth muscle will lengthen, which is also referred to as eccentric contraction when studying skeletal muscle. If the afterload is smaller than the maximum isometric force, the smooth muscle will shorten, which is referred to as concentric contraction. Accounting for the complete range of contraction behaviors is important in modeling smooth muscle tissue such as airway smooth muscle (ASM) and vascular smooth muscle (VSM) that may encounter this kinetic range of motion for example during surgical treatments such as stent implantation.

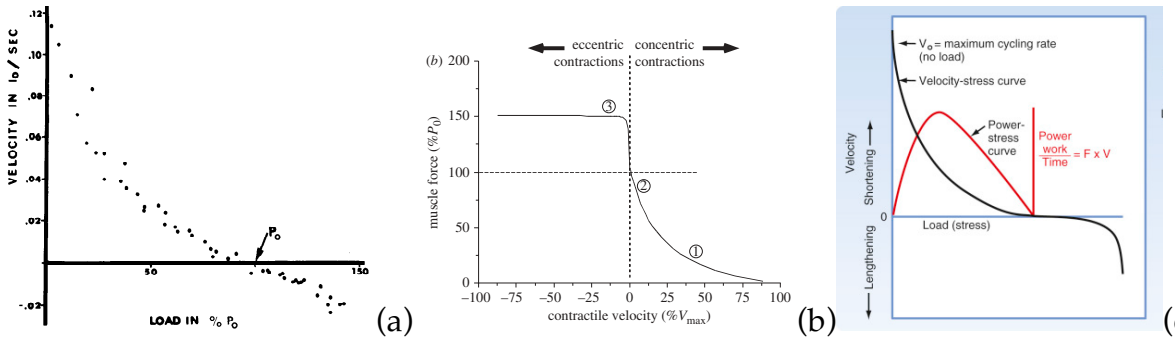

Figure 13. S-shaped force-velocity relationships for (a) airway smooth muscles and (b-c) skeletal muscles. (figures are taken from (Hanks and Stephens, 1981; Lieber and Ward, 2011; Ruiter and Haan, 2001))

Mathematically, we study the following general simplified nonlinear formulations besides the linear formulation

$$\begin{aligned} (1-x)+a(1-x)^2 &= y, \\ (1-x)+a(1-x)^3 &= y, \\ (1-x)+a(1-x)^4 &= y, \end{aligned} \tag{4.7}$$

as potential options for capturing such nonlinear initial velocity and afterloads in Figure 13, where y corresponding to the initial velocity and x corresponding to the afterloads. We plot x-y relationships in Figure 14 for a=0 (linear case used in the literatures), a=1,

2,3,4 (nonlinear cases) for the above three formulations. As can be seen, the third order formulation yields the most promising results as a potential formulation to capture the nonlinear relationships between the initial velocity and the afterloads.

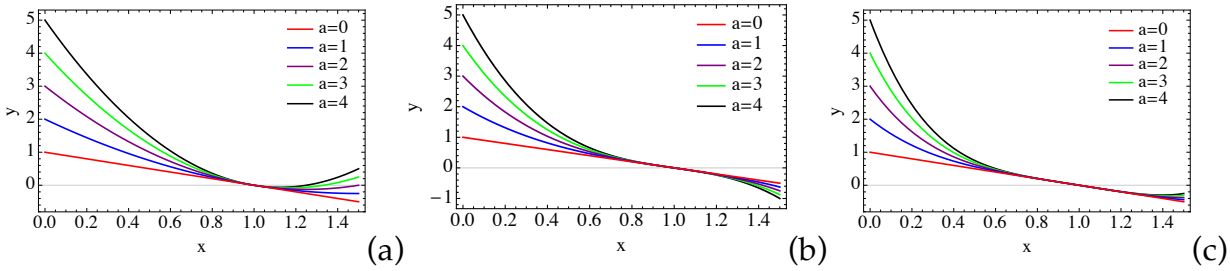

Figure 14. Plots for the (a) second, (b) third, and (c) fourth order formulations between x and y in Eq (4.7) for a ranging from 0 (linear case) to 4.

In addition, from the thermodynamics perspective, only the third order formulation among the above nonlinear formulations satisfies the Clausius-Planck inequality derived from the second thermodynamic law, which is shown in the following. It is noted that any other odd function, for example $\tau_{res}^{2i+1}, i=1,2,...$ would satisfy the Clausius-Plank inequality as well. However, the third order form is the simplest besides the linear form. The Clausius-Planck inequality under isothermal conditions can be expressed as (Murtada et al., 2010; Reese and Govindjee, 1997)

$$D = \mathbf{S} : \frac{1}{2}\dot{\mathbf{C}} - \dot{\Psi} + P_d \dot{\lambda}_F^v \geq 0 \tag{4.8}$$

where, $\mathbf{S}$ is the second Piola-Kirchhoff stress tensor, λ_F^v is the viscous part of fiber stretch, $P_d \dot{\lambda}_F^v$ represents the energy dissipation due to relative sliding of thin and thick filaments driven by P_d, which origins from the biochemical potential of the system. The time derivative of Ψ in Eq. (4.8) is

$$\dot{\Psi} = \frac{\partial \Psi}{\partial \mathbf{C}} : \dot{\mathbf{C}} + \frac{\partial \Psi}{\partial \mathbf{C}_F^v} : \dot{\mathbf{C}}_F^v = 2\frac{\partial \Psi}{\partial \mathbf{C}} : \frac{1}{2}\dot{\mathbf{C}} + \underbrace{2\lambda_F^v \frac{\partial \Psi}{\partial I_4^v}}_{P_r} \dot{\lambda}_F^v \tag{4.9}$$

Inserting Eq. (4.9) into Eq. (4.8) leads to the expression

$$\begin{aligned} D &= \mathbf{S} : \frac{1}{2}\dot{\mathbf{C}} - \left(2\frac{\partial \Psi}{\partial \mathbf{C}} : \frac{1}{2}\dot{\mathbf{C}} + 2\lambda_F^v \frac{\partial \Psi}{\partial I_4^v}\dot{\lambda}_F^v \right) + P_d \dot{\lambda}_F^v \\ &= \left(\mathbf{S} - 2\frac{\partial \Psi}{\partial \mathbf{C}} \right) : \frac{1}{2}\dot{\mathbf{C}} + \underbrace{\left(P_d - P_r \right)}_{\tau_{res}} \dot{\lambda}_F^v \\ &= \tau_{res}\dot{\lambda}_F^v \geq 0. \end{aligned} \tag{4.10}$$

That is to say, any proposed relationship between τ_{res} and $\dot{\lambda}_F^v$ has to satisfy Eq (4.10). The second and fourth order relations are not guaranteed to satisfy the reduced inequality.

We propose a modified evolution equation for the active damper with the following nonlinear third order formulation:

$$\tau_{res} + \alpha \bullet \tau_{res}^3 = \eta_{tot}\dot{\lambda}_F^v \ , \tag{4.11}$$

with the assumption that the driving force is produced by the fast crossbridges only, i.e. $P_d = -\kappa O_{lap} AMp$, where κ is a material parameter, and the coefficient α is a nonlinear fit parameter, λ_F^v is the viscous part of active fiber stretch, and η_{tot} is the total viscous coefficient. Hence, the damping force is mathematically defined by a third order polynomial consisting of a first order resultant force term and a third order resultant force term so that i) it captures the nonlinear relationship between initial velocity and afterloads in isotonic tests and ii) satisfies the Clausius-Planck inequality. Based on the active damper mechanism (see Figure 7), the total viscous coefficient in the evolution equation is composed of two parts: a nonvarying part from the viscous effect of the cycling/contraction process represented by the constant term η and a varying part that depends on the effective fraction of engaged latchbridges ($O_{lap} AM$) to capture the passive resisting effect of the slow-cycling myosin, the so-called clutch mechanism.

(Physically speaking, the viscosity could also vary with the fraction of fast cycling crossbridges but that is not considered here). Therefore, the total viscous coefficient is

$$\eta_{tot} = \left(1 + n_d O_{lap} AM\right)\eta \,, \tag{4.12}$$

where n_d is a fit parameter. The above evolution law (Eq.(4.11)) is an alternate expression to that of Kroon and Murtada et al. (Kroon, 2010; Murtada et al., 2010). There, the relationship between the viscous stretch rate and the resultant force is linear with a constant viscous coefficient associated with the cycling/contraction process and a constant overlap between actin and myosin filaments is used instead. These four viscous parameters ($\kappa, \alpha, \eta, n_d$) in the proposed evolution equation are obtained by fitting the constitutive equations to the isotonic and isometric experiments.

4.3.3 Constitutive model summary

The second Piola-Kirchhoff stresses for the media layer is obtained by taking appropriate derivatives of the strain energy density function in Eq. (4.4), where $\mathbf{S} = 2\partial\Psi/\partial\mathbf{C}$ resulting in the following equations:

$$\mathbf{S} = \mu_p \mathbf{I} + \left[2k_1 \left(\exp\left(k_2 (I_f - 1)^2\right)\right)(I_f - 1) + (AMp + AM) O_{lap} \mu_f \left(I_f - I_f^v\right) / \left(I_f^v\right)^2 \right] \mathbf{V} \otimes \mathbf{V} \,, \tag{4.13}$$

The chemical and mechanical parts of the model formulation are summarized in Table 3. The chemical model representing crossbridge cycling has 7 parameters ($K_1 \sim K_7$). The mechanical part of the model has 10 parameters ($\mu_p, k_1, k_2, \mu_f, \kappa, \eta, \alpha, \lambda^{v}_{\text{Fopt}}, \xi, n_d$). The calibration of the model is outlined in the next subsection.

Table 3. Model formulations of the smooth muscle rich artery

Chemical part	$\begin{Bmatrix} \dot{M} \\ \dot{M}p \\ A\dot{M}p \\ A\dot{M} \end{Bmatrix} = \begin{bmatrix} -K_1 & K_2 & 0 & K_7 \\ K_1 & -K_2-K_3 & K_4 & 0 \\ 0 & K_3 & -K_4-K_5 & K_6 \\ 0 & 0 & K_5 & -K_6-K_7 \end{bmatrix} \begin{Bmatrix} M \\ Mp \\ AMp \\ AM \end{Bmatrix}$
Mechanical part	Strain energy function: $\Psi = \frac{\mu_p}{2}(I_1-3) + \frac{k_1}{2k_2}\left(\exp\left(k_2(I_4-1)^2\right)-1\right) + (AMp+AM)O_{lap}\frac{\mu_f}{4}\left(\frac{I_4}{I_4^{\mathrm{v}}}-1\right)^2$ Second Piola-Kirchhoff stress: $\mathbf{S} = \mu_p\mathbf{I} + 2k_1\exp\left(k_2(I_4-1)^2\right)(I_4-1)\mathbf{M_1} + (AMp+AM)O_{lap}\mu_f\left(I_4-I_4^{\mathrm{v}}\right)/\left(I_4^{\mathrm{v}}\right)^2\mathbf{V}\otimes\mathbf{V}$ Evolution equation: $\left(P_d - 2\lambda_{\mathrm{F}}^{\mathrm{v}}\frac{\partial\Psi}{\partial I_4^{\mathrm{v}}}\right) + \alpha\left(P_d - 2\lambda_{\mathrm{F}}^{\mathrm{v}}\frac{\partial\Psi}{\partial I_4^{\mathrm{v}}}\right)^3 = (1+n_dO_{lap}AM)\eta\dot{\lambda}_{\mathrm{F}}^{\mathrm{v}}$, with driving force $P_d = -\kappa O_{lap}AMp$

4.4 Calibration of model parameters

In this section, calibration of the constitutive model is performed. Two classical experiments used to study the active properties of smooth muscle tissue are isometric and isotonic tests (details refer to Dillion et al., Kamm et al., and Herlihy et al., where carotid artery strips from swine were used). (Dillon et al., 1981; Herlihy and Murphy, 1973; Kamm et al., 1989) The former is also referred to as the length clamp tests since the total length of the specimen is held fixed during the experiment. The active stress evolution (transient characteristic) is recorded in isometric tests for certain stimuli. Generally, the isometric test is performed at the optimal external stretch of the specimen, and for the smooth muscle in the present work, the optimal external stretch is around 1.6. (Kamm et al., 1989) The steady-state properties of the active stress are also

studied during isometric tests for specimen stimulated at various fixed external stretches. Experiments show that smooth muscle has a parabolic or bell-shaped steady-state isometric stress-stretch relationship. (Herlihy and Murphy, 1973; Kamm et al., 1989; Murtada et al., 2012) During isometric tests, the so-called load-bearing capacity (LBC) measurement can be performed, that is, the active stress is recorded when the activated muscle strip is subjected to a quick-stretch of sufficient rate (>0.05 L_0 / sec) and magnitude (>0.018 L_0). (Dillon et al., 1981)

In isotonic tests, also referred to as load clamp tests, the load acting on the specimen is held fixed. Isometric tests are performed before isotonic tests generally so that the specimen is in a steady activated state for a certain fixed length or stretch. Isotonic tests can then be performed in which the external force is suddenly changed to another fixed value, and the amount and rate of length change are recorded. The force applied in isotonic tests is called the afterload. The increase or decrease in the specimen length immediately following application of the afterload is called the elastic recoil. The rate at which elastic recoil occurs is called the initial velocity (that is, steady-state shortening rate after afterload is applied, which is at 75 millisec according to (Dillon et al., 1981)). The elastic recoil and the initial velocity are two main characteristics of isotonic tests.

The active mechanical parameters of the media layer are determined by isometric and isotonic tests. Since the experiments were conducted under high potassium stimulation, K_1 and K_6 are set to be 0.14 s^{-1} following Kroon (Kroon, 2010), and the time-dependent of chemical variables (M, Mp, AMp, and AM) are calculated by the governing Eq.(4.1) in the chemical model for the initial conditions M=1 as stimulation input to the mechanical model shown in Figure 15.

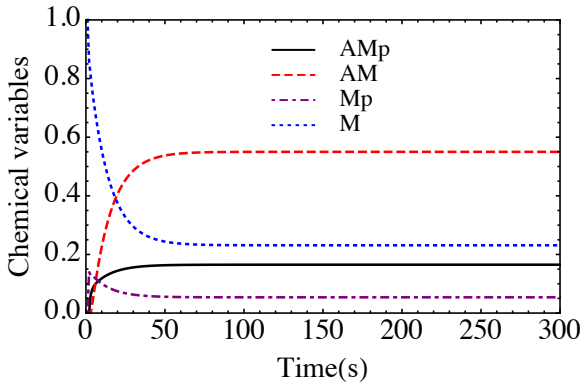

Figure 15. Chemical variables for model parameter calibration.

In the following, first, we determine the optimal stretch λ^{v}_{Fopt} from the steady state value in the load bearing capacity (LBC) measurement during isometric tests. Isometric tests are performed at the optimal stretch of the specimen ($\lambda_{opt}=1.6$). (Dillon et al., 1981; Kamm et al., 1989) In the load bearing capacity (LBC) measurement during isometric tests, we assume that the number of crossbridge heads and the viscous stretch do not change (due to the very quick rate), that is, $\lambda^{v}_{F}=\lambda^{v}_{Fopt}$ for a prescribed $\Delta\lambda$. The resulting active stress is the sum of the (pre-existing) isometric active stress and the stress increase due to elongation of the crossbridge heads when the quick-stretch is applied. We use the single point value (at 250s) in the LBC curve at the quick stretch $\Delta\lambda=0.025\lambda_{opt}$ to obtain the optimal viscous stretch λ^{v}_{Fopt} . The load-bearing capacity (LBC) is reported by Dillon et al. as approximately 1.6 times the developed force under steady-state conditions (Dillon et al., 1981), from the active part of Eq. (4.13) we have

$$\frac{O_{lap}(AMp+AM)\mu_f / {\lambda^{v}_{Fopt}}^2({\lambda_{opt}}^2 / {\lambda^{v}_{Fopt}}^2-1)\lambda_{opt}}{O_{lap}(AMp+AM)\mu_f / {\lambda^{v}_{Fopt}}^2((\lambda_{opt}+\Delta\lambda)^2 / {\lambda^{v}_{Fopt}}^2-1)(\lambda_{opt}+\Delta\lambda)}=\frac{1}{1.6}. \tag{4.14}$$

Solving Eq. (4.14) for λ^{v}_{Fopt} , we have optimal viscous stretch as

$$\lambda^{v}_{Fopt}=1.517 \tag{4.15}$$

Next, the calibration procedure for parameters in the active part of the model (μ_f , κ , η , α , λ_{Fopt}^{v} , ξ) is as follows. First, the latch bridge viscous parameter n_d is assigned a value of 1 since to date there are no experiments to isolate the effect. Next, the other four parameters μ_f , κ , η and α are obtained by fitting Equations in Appendix A and Eq. (4.11) with $AMp + AM$ from the chemical model (see Figure 15) to the active stress evolution curve from isometric tests and the initial velocity data in isotonic tests at the optimal stretch (see Figure 16 (a) and Figure 16 (c)). The parameter ξ (of the overlap function) in Eq (4.5) is adjusted to fit the normalized maximum active stresses in isometric tests at different stretches from Kamm et al., Herlihy et al., and Murtada et al. and the fitting results are shown in Figure 16 (b). Figure 16 (b) also shows model fitting results of passive behavior with $AMp + AM = 0$ (passive state) to uniaxial length-tension experimental data from (Herlihy and Murphy, 1973). (Herlihy and Murphy, 1973; Kamm et al., 1989; Murtada et al., 2012) The Gaussian function describes the bell-shaped tension-length relationship very well. Figure 16 (d) shows the model prediction of the elastic recoil and S-shaped initial velocity and afterloads relationships in isotonic tests. Table 4 summarizes the chemical parameters taken from Kroon and Hai and Murphy. Table 5 summarizes the determined numerical values of mechanical parameters for the media layer from swine carotid artery.

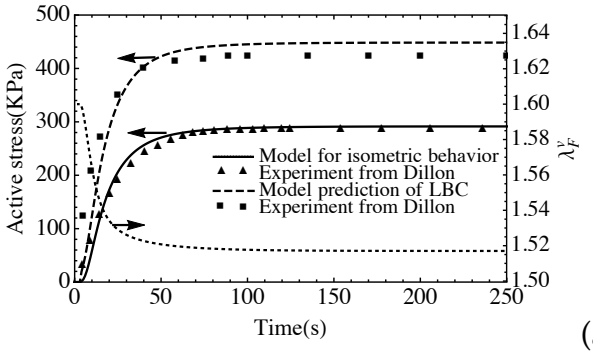

(a)

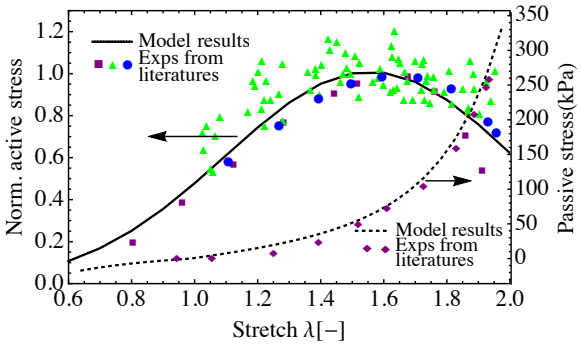

(b)

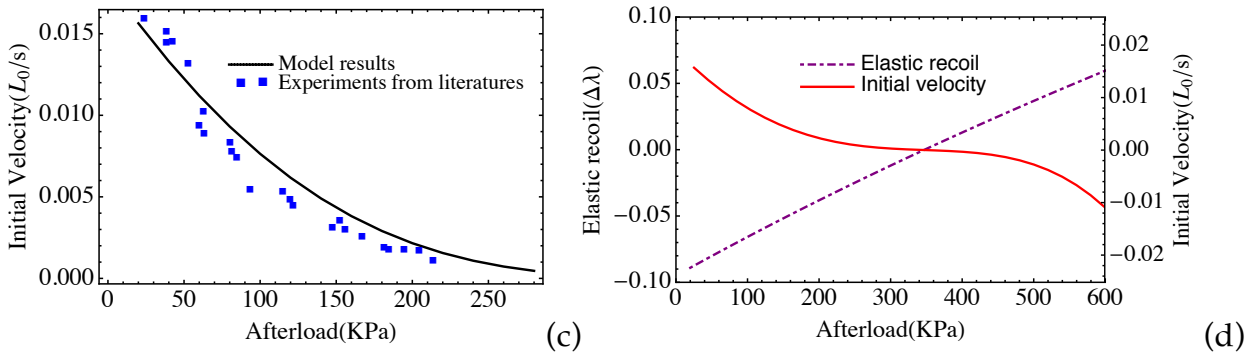

Figure 16. (a) Evolution of active stress in an isometric test at optimal external stretch (experimental data from (Dillon et al., 1981)) and the internal variable, and prediction of LBC comparing with experimental data from (Dillon et al., 1981); (b) Normalized steady-state active stress for different stretches under isometric conditions with experimental data from (Kamm et al., 1989) (▪), (Herlihy and Murphy, 1973) (•) and (Murtada et al., 2012) (▲), and passive stresses with experimental data (◆) from (Herlihy and Murphy, 1973); (c) Isotonic test: initial velocity for different afterloads, the fitting results of the model with experimental data from (Dillon et al., 1981); (d) simulation results of elastic recoil and initial velocity curves for afterloads in isotonic tests.

Table 4. Chemical parameters.

Parameters	K_1	K_2	K_3	K_4	K_5	K_6	K_7
Values	0.14 /s	0.5 /s	0.44 /s	0.11 /s	0.5 /s	0.14 /s	0.01 /s

Table 5. Mechanical parameters.

Parameters	μ_p	κ_1	κ_2	μ_f	κ	η	α	n_d	λ^{v}_{Fopt}	ξ
Values	1kPa	8kPa	0.13	5.22MPa	1.86MPa	186MPa·s	220MPa^{-2}	1	1.517	1/2.3

4.5 Parameter variations

In this section, parameter variations of the theoretical model is studied to compare how the numerical values affect the mechanical responses. These kind of variations would occur because of two main reasons: i) the variation in smooth muscle

tissue among patients, and ii) the nonlinear fit parameters are not unique and it is instructive to study the influence of perturbations of the obtained numerical values. Figure 17 shows the isometric active stress, elastic recoil, and initial velocity in isotonic conditions (from left column to right column) with increments of μ_f, κ, η, and α for variation among 0.2, 0.5, 0.8,1, 2, 5, 8, 10 times its original values.

The first column shows the analytical solutions of the active stress in isometric responses for varying μ_f, κ, η, and α. Parameter μ_f affects the transient rate and steady state values. The parameter κ has influence on both the transient rate and the steady state values, its influence on the steady state values is more dominant. Increasing the parameter η has the opposite influence to increasing μ_f. In contrast, parameter α only affects the transient rate not the steady state values. The second and third columns show the analytical solutions of the elastic recoil and initial velocities in isotonic responses for varying μ_f, κ, η, and α. Parameter μ_f affects the slope of the elastic recoil in relation to the applied afterload. Increasing μ_f increases the initial velocity at smaller afterloads. Increasing κ increases the elastic recoil, and the initial velocity increases dramatically for larger κ values especially for values greater than 2 times its original value. Elastic recoil is much less sensitive to parameter η with constant slopes and no influence at all from parameter α. However, both parameters η and α influence the initial velocities largely but with opposite effect, i.e. increasing η reduces the initial velocity at smaller afterloads while increasing α increases the initial velocity at smaller afterloads.

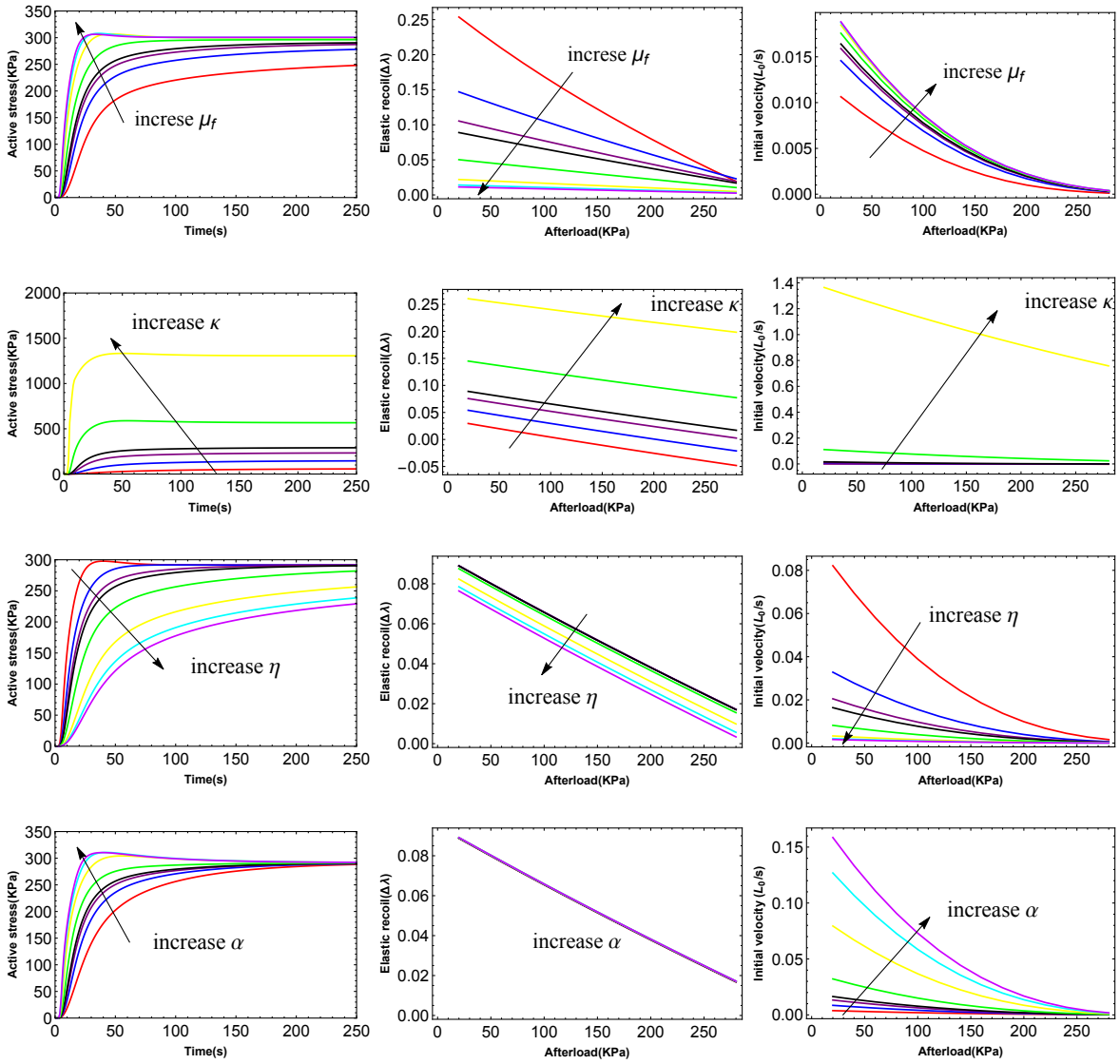

Figure 17. The isometric active stress, the elastic recoil, and initial velocity in isotonic conditions (from left to right) with increment of μ_f, κ, η, and α (from top to bottom) for variations among 0.2, 0.5, 0.8,1, 2, 5, 8, 10 times its original values.

4.6 Summary

In summary, a coupled chemo-mechanical constitutive model for smooth muscle tissue has been presented based on the existing model framework (Kroon, 2010; Murtada et al., 2010; Murtada et al., 2012; Stålhand et al., 2008; Stålhand et al., 2011). The contractile apparatus is modeled as an active damper considering the characteristics and functions

of the slow cycling crossbridges (latchbridges) and fast cycling crossbridges, which have different cycling rates. Specifically, the viscous effect of the latch bridges relative to the motion of the thin filaments driven by fast cycling crossbridges is considered in the present work for the first time. It is assumed that the driving force of the contractile unit is produced only by the fast cycling crossbridges. A third order nonlinear evolution equation is proposed to describe the active damper mathematically based on the second law of thermodynamics. The model parameters are calibrated using isometric and isotonic tests. It demonstrates the proposed nonlinear evolution equation can capture the S-shaped relationships between the afterloads and initial velocities in isotonic tests. In addition, a numerical parameter analysis is conducted to explore the mechanical response of the material.

There are a number of assumptions that went into the formulation of the model. In the present work, we do not consider the viscous effects of the matrix. Like many other models, we treat the passive behavior as hyperelastic. It is assumed the smooth muscle fibers are uniformly and continuously distributed throughout the matrix. That is to say, variations in fiber density, orientation distributions, and size are neglected. This type of assumption is common when target output is on the bulk or macroscopic scale as in the applications in Chapter 5.

The model can be implemented in a finite element environment to analyze realistic structures with complicated geometries and boundary value problems (in Chapter 5). In this way, adaptations can be made to investigate muscle functionality in a wide range of physical systems containing smooth muscle tissue besides arteries, such as airway, intestine, and stomach tissues.

References

Aksoy, M. O., Murphy, R. A., Kamm, K. E., 1982. Role of Ca2+ and myosin light chain phosphorylation in regulation of smooth muscle. The American Journal of Physiology 242, C109-116.

Aksoy, M. O., Mras, S., Kamm, K. E., Murphy, R. A., 1983. Ca2+, cAMP, and changes in myosin phosphorylation during contraction of smooth muscle. American Journal of Physiology - Cell Physiology 245, C255-C270.

An, S. S., Bai, T. R., Bates, J. H. T., etc., 2007. Airway smooth muscle dynamics: a common pathway of airway obstruction in asthma. The European respiratory journal 29, 834-860, doi:10.1183/09031936.00112606.

Barkam, S., Saraf, S., Seal, S., 2013. Fabricated Micro-Nano Devices for In vivo and In vitro Biomedical Applications. Wiley Interdisciplinary Reviews: Nanomedicine and Nanobiotechnology 5, 544-568, doi:10.1002/wnan.1236.

Böl, M., Schmitz, A., Nowak, G., Siebert, T., 2012. A three-dimensional chemo-mechanical continuum model for smooth muscle contraction. Journal of the Mechanical Behavior of Biomedical Materials 13, 215-229, doi:10.1016/j.jmbbm.2012.05.015.

Boron, W. F., Boulpaep, E. L., 2009. Medical physiology: a cellular and molecular approach. Saunders/Elsevier, Philadelphia, PA.

Clark, J. M., Glagov, S., 1985. Transmural organization of the arterial media. The lamellar unit revisited. Arteriosclerosis, Thrombosis, and Vascular Biology 5, 19-34, doi:10.1161/01.ATV.5.1.19.

Dillon, P. F., Aksoy, M. O., Driska, S. P., Murphy, R. A., 1981. Myosin phosphorylation and the cross-bridge cycle in arterial smooth muscle. Science 211, 495-497, doi:10.1126/science.6893872.

Donovan, G. M., 2013. Modelling airway smooth muscle passive length adaptation via thick filament length distributions. Journal of Theoretical Biology 333, 102-108, doi:10.1016/j.jtbi.2013.05.013.

Flamini, V., Kerskens, C., Moerman, K., Simms, C., Lally, C., 2010. Imaging Arterial Fibres Using Diffusion Tensor Imaging—Feasibility Study and Preliminary Results. EURASIP Journal on Advances in Signal Processing 2010, 1-13, doi:10.1155/2010/904091.

Fung, Y. C., 1970. Mathematical representation of the mechanical properties of the heart muscle. Journal of Biomechanics 3, 381-404, doi:10.1016/0021-9290(70)90012-6.

Fung, Y. C., 1993. Biomechanics: mechanical properties of living tissues. Springer-Verlag, New York.

Furchgott, R. F., Zawadzki, J. V., 1980. The obligatory role of endothelial cells in the relaxation of arterial smooth muscle by acetylcholine. Nature 288, 373-376, doi:10.1038/288373a0.

Gasser, T. C., Ogden, R. W., Holzapfel, G. A., 2006. Hyperelastic modelling of arterial layers with distributed collagen fibre orientations. Journal of The Royal Society Interface 3, 15-35, doi:10.1098/rsif.2005.0073.

Gerthoffer, W. T., Murphy, R. A., 1983. Myosin phosphorylation and regulation of cross-bridge cycle in tracheal smooth muscle. The American Journal of Physiology 244, C182-187.

Gestrelius, S., Borgstrom, P., 1986. A dynamic model of smooth muscle contraction. Biophysical Journal 50, 157-169.

Ghazanfari, S., Driessen-Mol, A., Strijkers, G. J., Kanters, F. M. W., Baaijens, F. P. T., Bouten, C. V. C., 2012. A comparative analysis of the collagen architecture in the carotid artery: Second harmonic generation versus diffusion tensor imaging. Biochemical and Biophysical Research Communications 426, 54-58, doi:10.1016/j.bbrc.2012.08.031.

Green, S. R., Kwon, R. S., Elta, G. H., Gianchandani, Y. B., 2013. In vivo and in situ evaluation of a wireless magnetoelastic sensor array for plastic biliary stent monitoring. Biomedical Microdevices 15, 509-517, doi:10.1007/s10544-013-9750-3.

Hai, C. M., Murphy, R. A., 1988. Cross-bridge phosphorylation and regulation of latch state in smooth muscle. The American journal of physiology 254, C99-106.

Hanks, B. S., Stephens, N. L., 1981. Mechanics and energetics of lengthening of active airway smooth muscle. The American Journal of Physiology 241, C42-46.

Harris, D. E., Work, S. S., Wright, R. K., Alpert, N. R., Warshaw, D. M., 1994. Smooth, cardiac and skeletal muscle myosin force and motion generation assessed by cross-bridge mechanical interactions in vitro. Journal of Muscle Research & Cell Motility 15, 11-19, doi:10.1007/BF00123828.

Herlihy, J. T., Murphy, R. A., 1973. Length-Tension Relationship of Smooth Muscle of the Hog Carotid Artery. Circulation Research 33, 275-283, doi:10.1161/01.RES.33.3.275.

Hill, A. V., 1938. The Heat of Shortening and the Dynamic Constants of Muscle. Proceedings of the Royal Society of London. Series B, Biological Sciences 126, 136-195, doi:10.2307/82135.

Humphrey, J. D., Wilson, E., 2003. A potential role of smooth muscle tone in early hypertension: a theoretical study. Journal of Biomechanics 36, 1595-1601, doi:10.1016/S0021-9290(03)00178-7.

Huxley, A. F., 1957. Muscle structure and theories of contraction. Progress in biophysics and biophysical chemistry 7, 255-318.

Huxley, A. F., 1974. Muscular contraction. The Journal of Physiology 243, 1-43.

Huxley, A. F., 2000. Mechanics and models of the myosin motor. Philosophical Transactions of the Royal Society B: Biological Sciences 355, 433-440.

Huxley, A. F., Niedergerke, R., 1954. Structural Changes in Muscle During Contraction: Interference Microscopy of Living Muscle Fibres. Nature 173, 971-973, doi:10.1038/173971a0.

Huxley, H., Hanson, J., 1954. Changes in the Cross-Striations of Muscle during Contraction and Stretch and their Structural Interpretation. Nature 173, 973-976, doi:10.1038/173973a0.

Huxley, H. E., 1969. The Mechanism of Muscular Contraction. Science 164, 1356-1366, doi:10.1126/science.164.3886.1356.

Huxley, H. E., 2004. Fifty years of muscle and the sliding filament hypothesis. European Journal of Biochemistry 271, 1403-1415, doi:10.1111/j.1432-1033.2004.04044.x.

Kamm, K. E., Gerthoffer, W. T., Murphy, R. A., Bohr, D. F., 1989. Mechanical properties of carotid arteries from DOCA hypertensive swine. Hypertension 13, 102-109, doi:10.1161/01.HYP.13.2.102.

Koeppen, B. M., Stanton, B. A., 2009. Berne & Levy Physiology, 6th Updated Edition, with Student Consult Online Access. Mosby, Philadelphia, PA.

Kroon, M., 2010. A constitutive model for smooth muscle including active tone and passive viscoelastic behaviour. Mathematical Medicine and Biology 27, 129-155, doi:10.1093/imammb/dqp017.

Kroon, M., 2011. Influence of dispersion in myosin filament orientation and anisotropic filament contractions in smooth muscle. Journal of Theoretical Biology 272, 72-82, doi:10.1016/j.jtbi.2010.11.037.
Laforet, J., Guiraud, D., 2008. Smooth muscle model for functional electrical stimulation applications : Simulation of realistic bladder behavior under FES. 30th Annual International Conference of the IEEE Engineering in Medicine and Biology Society, pp. 3702-3705.
Lawson, E. F., Wallace, M. S., 2012. Advances in intrathecal drug delivery. [Miscellaneous Article]. Current Opinion in Anaesthesiology October 2012 25, 572-576, doi:10.1097/ACO.0b013e3283572319.
Li, T., Evans, A. T., Chiravuri, S., Gianchandani, R. Y., Gianchandani, Y. B., 2012. Compact, power-efficient architectures using microvalves and microsensors, for intrathecal, insulin, and other drug delivery systems. Advanced Drug Delivery Reviews 64, 1639-1649, doi:10.1016/j.addr.2012.05.002.
Lieber, R. L., Ward, S. R., 2011. Skeletal muscle design to meet functional demands. Philosophical Transactions of the Royal Society B: Biological Sciences 366, 1466-1476, doi:10.1098/rstb.2010.0316.
Liu, T., 2014. A constitutive model for cytoskeletal contractility of smooth muscle cells. Proceedings of the Royal Society A: Mathematical, Physical and Engineering Science 470, 1-19, doi:10.1098/rspa.2013.0771.
Murphy, R. A., Rembold, C. M., 2005. The Latch-bridge Hypothesis of Smooth Muscle Contraction. Canadian journal of physiology and pharmacology 83, 857-864, doi:10.1139/y05-090.
Murtada, S. C., Kroon, M., Holzapfel, G. A., 2010. A calcium-driven mechanochemical model for prediction of force generation in smooth muscle. Biomechanics and Modeling in Mechanobiology 9, 749-762, doi:10.1007/s10237-010-0211-0.
Murtada, S. C., Arner, A., Holzapfel, G. A., 2012. Experiments and mechanochemical modeling of smooth muscle contraction: Significance of filament overlap. Journal of Theoretical Biology 297, 176-186, doi:10.1016/j.jtbi.2011.11.012.
Nuxoll, E., 2013. BioMEMS in drug delivery. Advanced Drug Delivery Reviews 65, 1611-1625, doi:10.1016/j.addr.2013.07.003.
O'Connell, M. K., Murthy, S., Phan, S., Xu, C., Buchanan, J., Spilker, R., Dalman, R. L., Zarins, C. K., Denk, W., Taylor, C. A., 2008. The three-dimensional micro- and nanostructure of the aortic medial lamellar unit measured using 3D confocal and electron microscopy imaging. Matrix Biology 27, 171-181, doi:10.1016/j.matbio.2007.10.008.
Rachev, A., Hayashi, K., 1999. Theoretical Study of the Effects of Vascular Smooth Muscle Contraction on Strain and Stress Distributions in Arteries. Annals of Biomedical Engineering 27, 459-468, doi:10.1114/1.191.
Ramsey, R. W., Street, S. F., 1940. The isometric length-tension diagram of isolated skeletal muscle fibers of the frog. Journal of Cellular and Comparative Physiology 15, 11-34, doi:10.1002/jcp.1030150103.
Reese, S., Govindjee, S., 1997. Theoretical and Numerical Aspects in the Thermo-Viscoelastic Material Behaviour of Rubber-Like Polymers. Mechanics of Time-Dependent Materials 1, 357-396, doi:10.1023/A:1009795431265.
Rüegg, J. C., 1992. Calcium in Muscle Contraction - Cellular and Molecular Physiology.
Ruiter, C. J. D., Haan, A. D., 2001. Similar effects of cooling and fatigue on eccentric and concentric force-velocity relationships in human muscle. Journal of Applied Physiology 90, 2109-2116.

Seow, C. Y., Stephens, N. L., 1986. Force-velocity curves for smooth muscle: analysis of internal factors reducing velocity. American Journal of Physiology - Cell Physiology 251, C362-C368.
Shiraishi, D. T., Sakaki, S., Uehara, Y., 1986. Architecture of the media of the arterial vessels in the dog brain: A scanning electron-microscopic study. Cell and Tissue Research 243, 329-335, doi:10.1007/BF00251048.
Son, S., Goulbourne, N. C., 2012. Large strain analysis of a soft polymer electromechanical sensor coupled to an arterial segment. Journal of Intelligent Material Systems and Structures 23, 575-586, doi:10.1177/1045389X12436733.
Stålhand, J., Klarbring, A., Holzapfel, G. A., 2008. Smooth muscle contraction: Mechanochemical formulation for homogeneous finite strains. Progress in Biophysics and Molecular Biology 96, 465-481, doi:10.1016/j.pbiomolbio.2007.07.025.
Stålhand, J., Klarbring, A., Holzapfel, G. A., 2011. A mechanochemical 3D continuum model for smooth muscle contraction under finite strains. Journal of Theoretical Biology 268, 120-130, doi:10.1016/j.jtbi.2010.10.008.
Takahashi, A., Ushiki, T., Abe, K., Houkin, K., Abe, H., 1994. Scanning electron microscopic studies of the medial smooth muscles in human major intracranial arteries. Archives of Histology and Cytology 57, 341-350.
Walmsley, J. G., Campling, M. R., Chertkow, H. M., 1983. Interrelationships among wall structure, smooth muscle orientation, and contraction in human major cerebral arteries. Stroke 14, 781-790, doi:10.1161/01.STR.14.5.781.
Wang, I., Politi, A. Z., Tania, N., Bai, Y., Sanderson, M. J., Sneyd, J., 2008. A Mathematical Model of Airway and Pulmonary Arteriole Smooth Muscle. Biophysical Journal 94, 2053-2064, doi:10.1529/biophysj.107.113977.
Wang, Y., Son, S., Swartz, S. M., Goulbourne, N. C., 2012. A mixed von Mises distribution for modeling soft biological tissues with two distributed fiber properties. International Journal of Solids and Structures 49, 2914-2923, doi:10.1016/j.ijsolstr.2012.04.004.
Warshaw, D., Trybus, K., 1991. In vitro evidence for smooth muscle crossbridge mechanical interactions. Advances in Experimental Medicine and Biology 304, 53-59.
Warshaw, D. M., Desrosiers, J. M., Work, S. S., Trybus, K. M., 1990. Smooth muscle myosin cross-bridge interactions modulate actin filament sliding velocity in vitro. The Journal of Cell Biology 111, 453-463, doi:10.1083/jcb.111.2.453.
Wong, J., Göktepe, S., Kuhl, E., 2013. Computational modeling of chemo-electro-mechanical coupling: A novel implicit monolithic finite element approach. International Journal for Numerical Methods in Biomedical Engineering 29, 1104-1133, doi:10.1002/cnm.2565.
Yanagisawa, M., Kurihara, H., Kimura, S., Tomobe, Y., Kobayashi, M., Mitsui, Y., Yazaki, Y., Goto, K., Masaki, T., 1988. A novel potent vasoconstrictor peptide produced by vascular endothelial cells. Nature 332, 411-415, doi:10.1038/332411a0.
Yang, J., Clark Jr, J. W., Bryan, R. M., Robertson, C., 2003. The myogenic response in isolated rat cerebrovascular arteries: smooth muscle cell model. Medical Engineering & Physics 25, 691-709, doi:10.1016/S1350-4533(03)00100-0.
Yu, S. N., Crago, P. E., Chiel, H. J., 1997. A nonisometric kinetic model for smooth muscle. The American Journal of Physiology 272, C1025-1039.

Zulliger, M. A., Rachev, A., Stergiopulos, N., 2004. A constitutive formulation of arterial mechanics including vascular smooth muscle tone. American journal of physiology. Heart and circulatory physiology 287, H1335-1343, doi:10.1152/ajpheart.00094.2004.

Chapter 5. Numerical and computational analysis of artery stresses considering active contractility

5.1 Introduction

In this chapter, the constitutive model presented in Chapter 4 is employed in a thick-walled model to investigate effects of smooth muscle contraction on artery stresses and quantify the role of active viscoelasticity in the artery mechanical responses. Though previous simulations have shown that viscoelastic effects are minimally important in the normal pulsatile response of healthy arteries for timescales (over 1 minute) on the order of seconds. Our results show that the active viscoelastic behavior has a non-negligible effect on artery wall stress when longer timescales are considered. The current work focuses on the artery being overstretched on longer timescales for example during surgical events. A new user subroutine is implemented in ABAQUS via UANISOHYPER, so that complex geometries and loading scenarios can be simulated in the future.

Balloon angioplasty with stent deployment is an effective invasive therapy to treat atherosclerotic arteries. (Iqbal et al., 2013) Vascular injury during balloon angioplasty with stent deployment is hypothesized to be the trigger of neointimal hyperplasia and phenotype change and migration of smooth muscle cells, which can lead to the subsequent restenosis of stented arteries. (Farb et al., 1999; Gunn et al., 2002; Kornowski et al., 1998; Rogers et al., 1999) There are numerous research efforts focused on the optimization of balloon and stent design in an effort to reduce artery wall

trauma, where the artery is treated as a passive material. (Gastaldi et al., 2010; Grogan et al., 2013; Li and Wang, 2013; Mortier et al., 2010; Pant et al., 2012; Tammareddi et al., 2016) Computational simulations have evolved as an attractive tool to study the mechanical performance of the artery, balloon, stent, and atherosclerotic lesion rupture over the last decade. (Auricchio et al., 2011; Delfino et al., 1997; Gasser and Holzapfel, 2006; Holzapfel et al., 2002; Lally et al., 2005; Schiavone et al., 2014; Schmidt et al., 2015) Holzapfel et al. developed nonlinear strain-energy functions for characterizing the biomechanical response of arterial tissues and plaque during normal physiological loading and for simulating balloon and stent procedures. (Gasser and Holzapfel, 2006; Holzapfel et al., 2002; Holzapfel et al., 2014; Kiousis et al., 2009; Mortier et al., 2010) Buffinton et al., Gastaldi et al., and Conway et al. studied the effects of plaque material, geometry, and stenting approach for artery bifurcation during stent angioplasty. (Conway et al., 2014; Ebenstein, 2014; Gastaldi et al., 2010; Morlacchi et al., 2013) Other researchers have focused on the influence of the balloon configuration on the deployment of the stent and resulting wall response. (Martin and Boyle, 2013; Schiavone and Zhao, 2015) There have also been numerical model results reported for fissuring, rupture, and dissection of the plaque and artery during the balloon angioplasty procedure. (Badel et al., 2014; Ferrara and Pandolfi, 2008; Gasser and Holzapfel, 2007a; Morlacchi et al., 2014) In all of these studies, the artery is modeled as a passive hyperelastic material and smooth muscle contractility is neglected. In the current work, we investigate the impact of this assumption on calculating artery and plaque wall stresses due to overstretch loadings.

Here, the mechanical performance of the artery wall being overstretched during events with time scales on the order of minutes is modeled. We employ a two-layer thick wall model for the artery (the intima layer is assumed structurally negligible) and

a three-layer thick wall model for the artery-plaque complex. A comparison of the artery wall and plaque for both active and passive materials is carried out and analyzed. Supra-physiological internal pressures and imposed diameter changes are prescribed as mathematical inputs to the model following Badel et al., Gasser et al, Schmidt et al, and Ferrara and Pandolfi. (Badel et al., 2014; Ferrara and Pandolfi, 2008; Gasser and Holzapfel, 2007a; Schmidt et al., 2015) Interventional tools such as catheter, balloon, and stent deformation are not modeled explicitly. The media layer consists of densely packed smooth muscle cells and the adventitia is collagen rich. Both layers of the artery are treated as incompressible and anisotropic; the plaque is considered isotropic.

Accurate simulations of artery wall stresses are a valuable tool in designing medical devices and providing guidelines for surgical interventions. Murtada et al. found that normal calcium oscillation of smooth muscle cells hardly affect artery mechanical behavior (3D cylinder simulations on an axisymmetric ring) for normal blood pressure cycles (period of one second). (Murtada and Holzapfel, 2014) Medical and surgical interventions, however, are on longer timescales where the material viscoelastic response may be non-negligible and worth detailed consideration. The time of balloon inflation in balloon angioplasty procedures is from around half a minute to over one minute, which is on the same timescale as smooth muscle viscoelasticity. (Azarnoush et al., 2012; Blankenship et al., 1999; Dorros et al., 1998; Leibowitz et al., 2009a; Leibowitz et al., 2009b; Miketic et al., 1998; Ohman et al., 1994; Sarembock et al., 1989; Sowton et al., 1986; Tenaglia et al., 1992)

The material model for the media layer was presented in detail in Chapter 4. The media layer considered the active viscoelastic properties of the smooth muscle tissue. The adventitia is modeled as an anisotropic layer using an existing exponential form

and an isotropic symmetric plaque layer is incorporated using Yeoh's model. Three types of plaques for various degrees of artery stenosis are considered in this work. The surrounding tissue is modeled as an outer pressure for a constant calcium concentration in the smooth muscle cells. The model material parameters are calibrated for swine common carotid artery. The wall and plaque stress distributions and corresponding deformations are calculated for healthy and diseased arteries for imposed displacements and tractions. The current findings are based on a ring model, so it is expected that further refinement of the results will occur for full 3D cylinder simulations – an aspect of future work. The outline of the current work is described as follows: In section 5.2, we introduce the problem formulation for calculating the stress distributions in the artery and plaque considering active properties of smooth muscle tissue. In section 5.3, results are generated for a healthy two-layer artery ring and a diseased three-layer plaque-artery ring. Numerical results comparing the simulation results and analysis of the wall and plaque stress distributions are also presented. In section 5.4, the constitutive model is implemented into a finite element framework and simulations are conducted on an asymmetric artery to examine the stress distributions for the artery-plaque complex. A summary is presented in section 5.5.

5.2 Methodology

In this section, we introduce the method used to calculate the stress distributions in the artery wall considering the active properties of smooth muscle tissue. The boundary value problems for two-layer and three-layer thick wall models are described. The artery deformation response and stress distributions for a prescribed diameter are calculated.

5.2.1 Constitutive formulations summary

The strain energy function for the media layer is (recalling from Chapter 4)

$$\Psi_m = \frac{\mu_p}{2}(I_1 - 1) + \frac{k_1}{2k_2}\left(\exp\left(k_2(I_f - 1)^2\right) - 1\right) + (AMp + AM)O_{lap}\frac{\mu_f}{4}\left(\frac{I_f}{I_f^v} - 1\right)^2. \quad (5.1)$$

The strain energy function for the adventitia layer takes the following exponential form to describe the fiber reinforced anisotropic material (Ferrara and Pandolfi, 2008; Gasser and Holzapfel, 2006; Holzapfel et al., 2000; Holzapfel et al., 2002; Holzapfel et al., 2014)

$$\Psi_a = \frac{\mu_{pa}}{2}(I_1 - 1) + \sum_{i=4,6}\frac{k_{a1}}{2k_{a2}}\left(\exp\left(k_{a2}(I_i - 1)^2\right) - 1\right), \quad (5.2)$$

where μ_{pa}, k_{a1} are modulus like material constants for the matrix and fiber, respectively, k_{a2} is a material constant for the fiber, and $I_4 = \mathbf{V}_1 \cdot \mathbf{C}\mathbf{V}_1$ and $I_6 = \mathbf{V}_2 \cdot \mathbf{C}\mathbf{V}_2$ ($\mathbf{V}_1$ and $\mathbf{V}_2$ are unit vectors representing the orientation of two families of collagen fibers in the adventitia layer). Plaque is treated as an isotropic material and takes the form of the Yeoh model (n=3 in the current work) (Lawlor et al., 2011; Yeoh, 1993)

$$\Psi_p = \sum_{i=1}^{n} C_{i0}\left(I_1 - 1\right)^i, \quad (5.3)$$

where $C_{i0}, i = 1,2,3$ are material coefficients. The second Piola-Kirchhoff stresses for the media, adventitia, and plaque layers are obtained by taking appropriate derivatives of the strain energy density function in Eqs (5.1), (5.2), and (5.3) where $\mathbf{S} = 2\partial\Psi/\partial\mathbf{C}$ resulting in the following equations:

$$\mathbf{S}_m = \mu_p\mathbf{I} + \left[2k_1\left(\exp\left(k_2(I_f - 1)^2\right)\right)(I_f - 1) + (AMp + AM)O_{lap}\mu_f\left(I_f - I_f^v\right)/\left(I_f^v\right)^2\right]\mathbf{V}\otimes\mathbf{V}, \quad (5.4)$$

$$\mathbf{S}_a = \mu_{pa}\mathbf{I} + 2k_{a1}\left(\exp\left(k_{a2}\left(I_4 - 1\right)^2\right)\left(I_4 - 1\right)\right)\mathbf{V}_1\otimes\mathbf{V}_1 + 2k_{a1}\left(\exp\left(k_{a2}\left(I_6 - 1\right)^2\right)\left(I_6 - 1\right)\right)\mathbf{V}_2\otimes\mathbf{V}_2, \quad (5.5)$$

$$\mathbf{S}_p = \left[2C_{10} + 4C_{20}(I_1 - 3) + 6C_{30}(I_1 - 3)^2\right]\mathbf{I}. \quad (5.6)$$

The parameters for the media layer are calibrated from isometric and isotonic tests in Chapter 4, and parameters for the adventitia layer for swine carotid artery are from (Murtada and Holzapfel, 2014) and for the plaque are taken from (Lawlor et al., 2011) for human carotid artery (i.e. in the absence of experimental data for swine carotid artery plaque). Numerical values for the material parameters are summarized in Table 6 and Table 7 (in section 5.3.2).

Table 6. Model parameters for artery media and adventitia layers.

Chemical	K_2	K_3	K_4	K_5	K_7		
	$0.5s^{-1}$	$0.44s^{-1}$	$0.11s^{-1}$	$0.5s^{-1}$	$0.01s^{-1}$		
Active	μ_f	κ	η	α	n_d	$\lambda^{v}_{\text{Fopt}}$	ξ
	5.22 MPa	1.86 MPa	93 MPas	100MPa	1	1.517	1/2.3
Passive	μ_p	k_1	k_2	μ_{pa}	k_{a1}	k_{a2}	β
	1 kPa	8 kPa	0.13	409.3 Pa	23.07 kPa	0.2329	49.8°

5.2.2 Boundary value problem formulation

In this subsection, we summarize the main equations for the two-layered (media and adventitia) and three-layered (plaque, media and adventitia) thick wall models and related boundary conditions. (Holzapfel et al., 2000; Humphrey and Na, 2002; Rachev and Hayashi, 1999) Considering the reference configuration (R,Θ,Z) and current configuration (r,θ,z) in a cylindrical coordinate system, we have $r=r(R,t)$, $\theta=\Theta$, and $z=\lambda_z Z$. The deformation gradient and the unit vectors for fiber orientation in the media and adventitia layers are

$$\left[\mathrm{F}_{jk}\right]=\begin{bmatrix} \dfrac{\partial r}{\partial R} & \dfrac{\partial r}{R\partial\Theta} & \dfrac{\partial r}{\partial Z} \\ \dfrac{r\partial\theta}{\partial R} & \dfrac{r\partial\theta}{R\partial\Theta} & \dfrac{r\partial\theta}{\partial Z} \\ \dfrac{\partial z}{\partial R} & \dfrac{\partial z}{R\partial\Theta} & \dfrac{\partial z}{\partial Z} \end{bmatrix}=\begin{bmatrix} \lambda_r & 0 & 0 \\ 0 & \lambda_\theta & 0 \\ 0 & 0 & \lambda_z \end{bmatrix},\ \mathbf{V}=\begin{bmatrix} 0 \\ 1 \\ 0 \end{bmatrix},\ \mathbf{V}_1=\begin{bmatrix} 0 \\ \mathrm{Sin}\,\beta \\ \mathrm{Cos}\,\beta \end{bmatrix},\ \mathbf{V}_2=\begin{bmatrix} 0 \\ -\mathrm{Sin}\,\beta \\ \mathrm{Cos}\,\beta \end{bmatrix}, \quad (5.7)$$

where $\lambda_r=\dfrac{dr}{dR}$, $\lambda_\theta=\dfrac{r}{R}$, and $\lambda_z=\dfrac{dz}{dZ}$. We assume the material is incompressible, that is, $\det\mathbf{F}=\lambda_r\lambda_\theta\lambda_z=1$. Solving $\lambda_r\lambda_\theta\lambda_z=\dfrac{dr}{dR}\dfrac{r}{R}\lambda_z=1$ and using $R=R_i$, $r=r_i$ ($\lambda_{\theta i}=\dfrac{r_i}{R_i}$), we get

$$r=\sqrt{r_i^2+\frac{R^2-R_i^{\,2}}{\lambda_z}}\ . \quad (5.8)$$

where R_i is the stress free inner radius and r_i is the deformed inner radius. Therefore, λ_θ and λ_r can be expressed as functions of r for a given λ_z. Cauchy stresses can be obtained by $\sigma_{jk}=\mathrm{F}_{ji}\mathrm{S}_{lm}\mathrm{F}_{mk}{}^{\mathrm{T}}+p\delta_{jk}$ where p is an unknown hydrostatic pressure (which is a function of the radius) enforcing the incompressibility constraint. The nontrivial artery and plaque stresses are

$$\begin{aligned} \sigma_{rr}&=\lambda_r{}^2\mathrm{S}_{rr}+p, \\ \sigma_{\theta\theta}&=\lambda_\theta{}^2\mathrm{S}_{\theta\theta}+p, \\ \sigma_{zz}&=\lambda_z{}^2\mathrm{S}_{zz}+p, \end{aligned} \quad (5.9)$$

where S_{rr}, $\mathrm{S}_{\theta\theta}$, and S_{zz} are the second Piola-Kirchhoff stress components in radial, circumferential, and axial directions. The equilibrium equations for the adventitia layer, media layer, and plaque layer is

$$\frac{d\sigma_{rr}}{dr}+\frac{\sigma_{rr}-\sigma_{\theta\theta}}{r}=0\ . \quad (5.10)$$

Considering the boundary condition of a prescribed pressure $\sigma_{rr}(r_o)=-P_o$ at the outer surface of the thick wall tube, Eq (5.10) is then integrated from the outer radius to

any radius position r to obtain the Cauchy stress in the radial direction and with Eq (5.9), the Cauchy stresses at any radius r are (Holzapfel et al., 2000; Humphrey and Na, 2002) and

$$\begin{aligned}
\sigma_{rr}(r) &= -P_o + \int_r^{r_o} \frac{\sigma_{rr}(r) - \sigma_{\theta\theta}(r)}{r} dr = -P_o + \int_r^{r_o} \frac{\lambda_r{}^2 \mathrm{S}_{rr} - \lambda_\theta{}^2 \mathrm{S}_{\theta\theta}}{r} dr, \\
\sigma_{\theta\theta}(r) &= \lambda_\theta{}^2 \mathrm{S}_{\theta\theta} + \left(\sigma_{rr}(r) - \lambda_r{}^2 \mathrm{S}_{rr}\right), \\
\sigma_{zz}(r) &= \lambda_z{}^2 \mathrm{S}_{zz} + \left(\sigma_{rr}(r) - \lambda_r{}^2 \mathrm{S}_{rr}\right),
\end{aligned} \tag{5.11}$$

which are solved by Gaussian integration. Appendix B outlines the numerical procedure for computing the Cauchy stresses in the two-layer and three-layer thick wall tube with the finite difference method. Perfect interfaces of the media and adventitia (or plaque) are assumed, i.e. the deformation in the radial direction is continuous according to Eq (5.8).

5.3 Numerical results

In this section, the results are presented for the two-layer and three-layer thick wall models of the artery being overstretched. During balloon angioplasty, say, the balloon pressure is controlled according to a profile supplied by the manufacturer, where balloon deformation generally includes unfolding, contact with the artery, stretching, and stiffening upon further expansion. (Gasser and Holzapfel, 2006; Kiousis et al., 2009) Since the main focus is the stress and deformation response of the artery being overstretched, the simulations can be thought of as capturing the point from full contact of the balloon or stent with the artery. Therefore, the portion of events that involves balloon expansion is extracted and a mathematical approximation of the relevant physical piece is used to formulate the mathematical input to our model. In the 2D

model employed here, we do not consider the stress distribution along the axial direction but focus on the mechanical behavior in the artery cross section.

Unlike previous work where the artery was modeled as a passive material, here we consider the active viscoelastic properties of smooth muscle. All properties are listed in Table 6 and Table 7. The radial and circumferential stress and stretch distributions in the adventitia, media, and plaque layers are calculated (see Eq. (5.11)), and analyzed for both passive ($K_1 = K_6 = 0$) and active tissue material models.

5.3.1 Two-layer healthy artery model

In the current work, we use the properties of swine common carotid artery represented as a two-layer symmetric ring. The in vivo configuration is taken from (Duivenvoorden et al., 2009) for piglet carotid artery with an inner radius of 2.2 mm and media thickness of 0.32 mm under a mean blood pressure of 100 mmHg (see Figure 18). The thickness ratio of the media to adventitia layers is assumed to be 65%/35% (Gasser and Holzapfel, 2006; Holzapfel et al., 2005). The in vivo axial pre-stretch for porcine media (swine or pig) has a range of approximately 1.3 to 1.6 (García et al., 2011; Kochová et al., 2012; Liu et al., 2007; Perrée et al., 2003; Roy et al., 2005) and in vivo circumferential pre-stretch of approximately 1.4 to 1.5 (Liu et al., 2007; Roy et al., 2005). A constant strain in the axial direction is assumed and the axial pre-stretch is set to 1.5. The initial circumferential pre-stretch is set to 1.4. Also, assuming that the stress free and load free configurations are the same, the residual stress is not explicitly considered in the current work. The stress free configuration is calculated assuming incompressibility from the in vivo deformation and in vivo dimensions of the piglet carotid artery to be: inner radius 1.57 mm, media thickness 0.61mm, and adventitia 0.33mm by Eq (5.8). The ratio of wall thickness to mean artery radius is 46% and much larger than the 10% value

limit for the Laplace thin wall model. The thick wall model is an improvement over the Laplace model since it accounts for stress variations in the artery wall. For uniform inflation of a symmetric structure where there are no significant bending effects (zero resistance to bending) and distortion is negligible, the thick wall ring model may be sufficient. It should be noted that the model does not account for stress variations in the axial direction, for which a full simulation would be required, such an extension will be considered in future work.

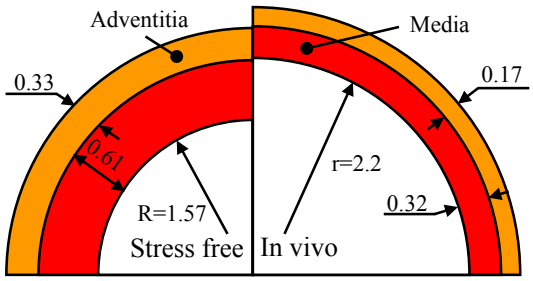

Figure 18. The stress free geometry and in vivo geometry under an inflation pressure of 100 mmHg (geometry units in mm).

In the chemical model of smooth muscle tissue in media, the parameter K_1 is assumed to be a function of Ca^{2+} as $\left(Ca^{2+}\right)^2 / \left(Ca^{2+}\right)^2 + K_h^{\,2}$ where K_h (the half-activation constant) is 1500 nM following (Yang et al., 2003). Murtada et al. demonstrated that the calcium wave barely affects the responses of the pressurized artery under normal pulsatile physiological loading conditions (Murtada and Holzapfel, 2014). For simplicity, we don't consider the calcium oscillation due to temporal and spatial effects of the nerve and agonist stimulation in vivo, but employ constant calcium concentrations to the parameter K_1 in the chemical model. In the resting smooth muscle the concentration of intracellular calcium is less than 10^{-7} M, and elevated calcium concentrations develop smooth muscle tones. (Bohr and Webb, 1984; Hill-Eubanks et

al., 2011; Knot and Nelson, 1998) In the current work, we consider a low activation level with a calcium concentration of 120 nM (yielding $K_1 = 0.006$) and two high activation levels with calcium concentrations 200 nM and 250 nM. First we calculate the pressure-like contribution from the surrounding tissue with in vivo stretch for a physiological blood pressure P_i =100 mmHg and assign it a constant value P_o. The external pressure due to the surrounding tissue is obtained via the following expression through integrating Eq. (5.10) from inner radius to outer radius

$$P_o = -\sigma_{rr}(r_o) = -\sigma_{rr}(r_i) + \int_{r_i}^{r_o} \frac{\sigma_{rr}(r) - \sigma_{\theta\theta}(r)}{r} dr = P_i + \int_{r_i}^{r_o} \frac{\sigma_{rr}(r) - \sigma_{\theta\theta}(r)}{r} dr \tag{5.12}$$

to be 48 mmHg for the chosen artery parameters (Table 6). This outer pressure is then used in simulations for the two-layered and three-layered models. The outer pressure is typically neglected in many models to simplify the problem formulation (Buffinton and Ebenstein, 2014; Gasser and Holzapfel, 2006; Lally et al., 2005; Murtada and Holzapfel, 2014). Physically, the surrounding tissue could be represented as a bed of springs or viscoelastic–type foundation. (Badel et al., 2014; Ferrara and Pandolfi, 2008; Figueroa et al., 2006; Moireau et al., 2011; Morlacchi et al., 2014) This effect could be included in future work in a generalized 3D simulation.

Responses for step displacement functions and sinusoidal pressure loads

Since the timescale of smooth muscle contraction is over 1 minute, we examine the response for a range of timescales. Here the viscoelastic properties of the two-layer arteries are studied for two different loading conditions: i) step increase of the internal diameter expanding the artery from $\lambda_\theta = 1.4$ (diameter 4.4 mm) to $\lambda_\theta = 1.68$ (diameter 5.28 mm) for different step sizes to study the relaxation of the material (see Figure 19 (a)); and ii) sinusoidal internal pressures with an amplitude of 40 mmHg oscillating

between 80 and 120 mmHg with various periods (50s, 100s, 200s, and 400s) to study the creep of the material (see Figure 20 (a)). For the first loading scenario, the four displacement loadings in Figure 19 (a) have different step sizes: 2s, 10s, 50s, and 100s. The circumferential and radial stretches at the inner surface are calculated using $\lambda_r = \frac{dr}{dR}, \lambda_\theta = \frac{r}{R}$ and shown in Figure 19 (b~c). Figure 19 (d~e) demonstrate that the step size of a 100-second loading provides the smallest circumferential stresses and internal pressures due to the stress relaxation. The smallest step size (2 sec) has the greatest circumferential stresses and internal pressures since it has a shorter relaxation time.

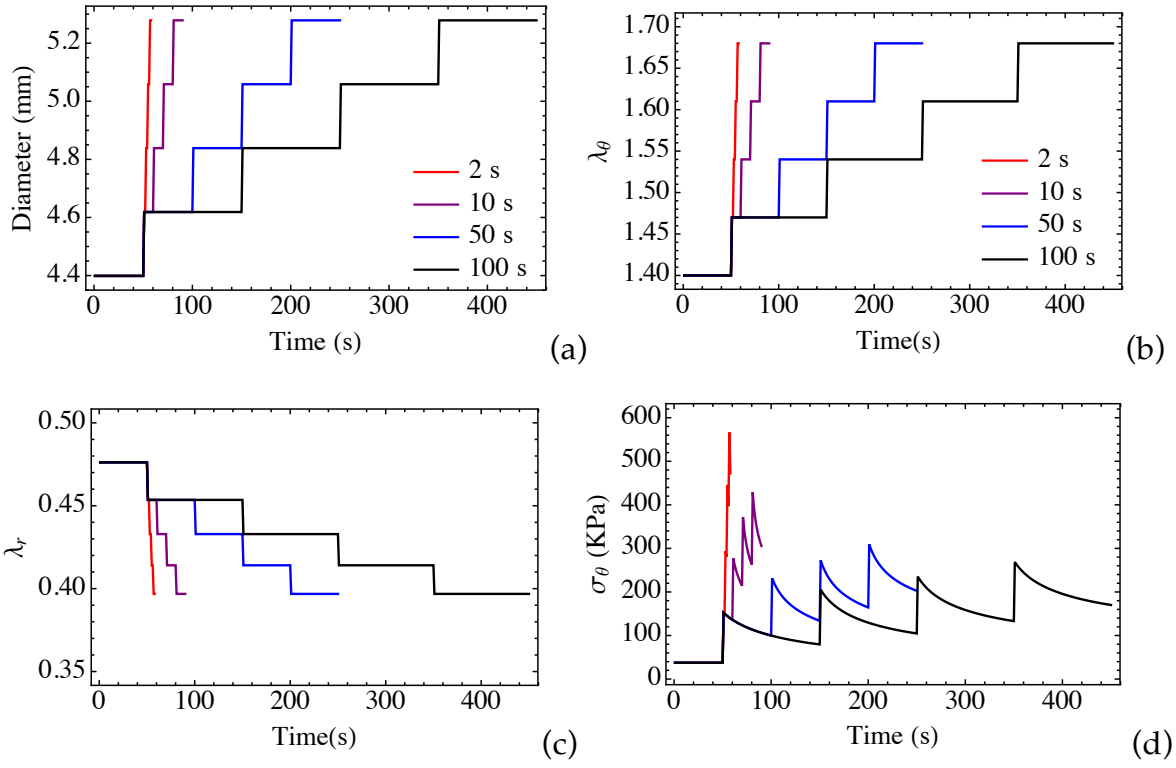

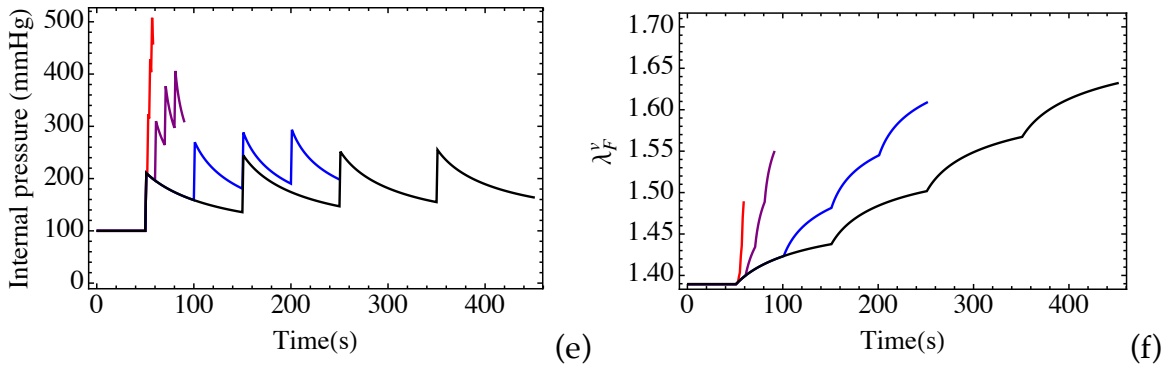

Figure 19. (a) The internal diameter displacement loadings; (b-c) calculated circumferential and radial stretches at the internal surface; (d-e) calculated circumferential stresses and internal pressures at the internal surface; (f) calculated internal variable.

Figure 20 (a) shows the sinusoidal internal pressures with amplitude 40 mmHg oscillating between 80 ~ 120 mmHg with various periods (50s, 100s, 200s, and 400s) to study the creep of the material. Figure 20 (b~d) show the calculated internal variable of the active damper and deformations (circumferential and radial stretches) at the inner surface.

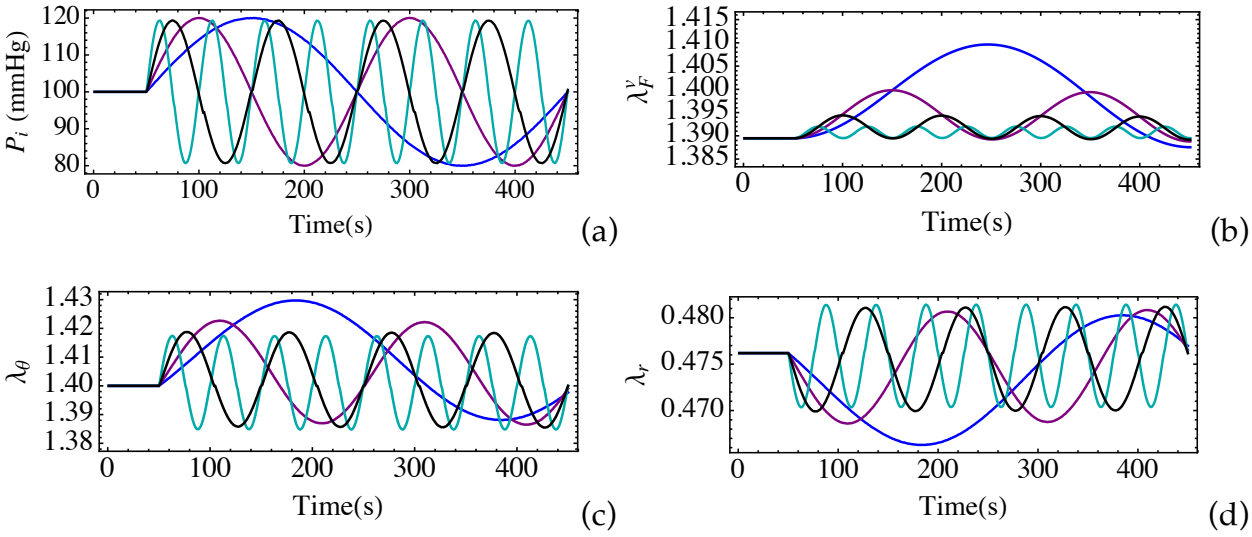

Figure 20. (a) Internal pressure loadings with amplitude 40 mmHg and periods 50s (Cyan), 100s (black), 200s (purple), and 400s (Blue); (b) calculated internal variables as a

function of time; (c) calculated circumferential stretches as a function of time; and (d) calculated radial stretches as a function of time for the internal pressure loadings.

Displacement loading

Consider a linearly increasing internal diameter prescribed from d_1=4.4 mm (the in vivo lumen diameter) to d_2 =5.3 mm (20% of the in vivo lumen diameter) over 30 seconds (from t_1 = 0 seconds to t_2 = 30 seconds in Figure 21). The time of typical balloon inflation in balloon angioplasty procedures is from 30 seconds to over a minute. (Azarnoush et al., 2012; Blankenship et al., 1999; Dorros et al., 1998; Leibowitz et al., 2009a; Leibowitz et al., 2009b; Miketic et al., 1998; Ohman et al., 1994; Sarembock et al., 1989; Sowton et al., 1986; Tenaglia et al., 1992) The displacement loading protocol is subdivided into two main parts. The first part is an increasing internal diameter from the in vivo state (4.4 mm i.e. under 100 mmHg of mean physiological blood pressure) to the overstretched state (5.3 mm i.e. 20% increase of in vivo internal diameter) from t_1 to t_2. The second part is a constant internal diameter from t_2 to t_3 to further study the active viscoelastic response. Consider the low activation level of calcium 120 nM in this subsection, that is, $K_1 = 0.006$, the chemical variables AMp and AM are calculated from the chemical model and shown in Figure 21.

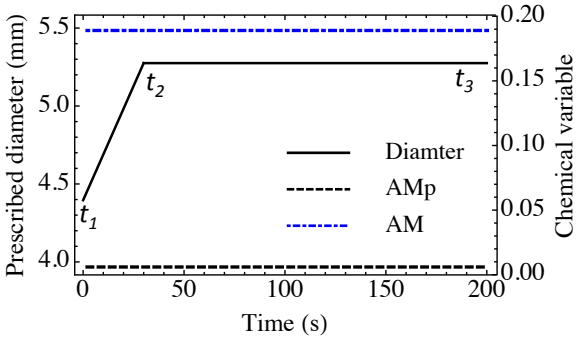

Figure 21. Displacement protocol for artery being overstretched: a linearly increasing internal diameter from d_1=4.4 mm to d_2=5.3 mm over a 30 seconds timespan. Chemical activation is prescribed constant over the duration of the event.

Stress and stretch distributions are shown in Figure 22 as functions of the normalized thickness ($(r-r_i)/(r_o-r_i)$) and time (red part for media layer and orange part for adventitia layer). The stretch results in Figure 22 (a~b) show that the circumferential and radial stretches vary nonlinearly with distance from the inner surface. From Figure 22 (c~d), the stresses in the adventitia layer increase with increasing displacement (along the thickness). As the displacement is prescribed and this is a 2D model, there are no cross-over viscous effects in the adventitia layer. The circumferential stresses in the media layer increase dramatically to very large peak values at t_2 before eventually reaching the new steady state at t_3. The stress relaxation in the media layer (when displacement is held constant) takes several seconds (45 ~ 90 s) to occur. Since smooth muscle is predominantly aligned in the near circumferential direction, the quick displacement of the internal artery surface causes a steep rise in the stress because of the active viscoelastic properties. The nonlinear viscous part means that there will be increasing resistance to deformation proportional to the rate of imposed displacement (expected of a typical damper element). Also, the contractile force generated is proportional to the rate of quick stretch and the degree of stretch (i.e. amount of cross-bridge overlap), which will be highlighted in the following subsections.

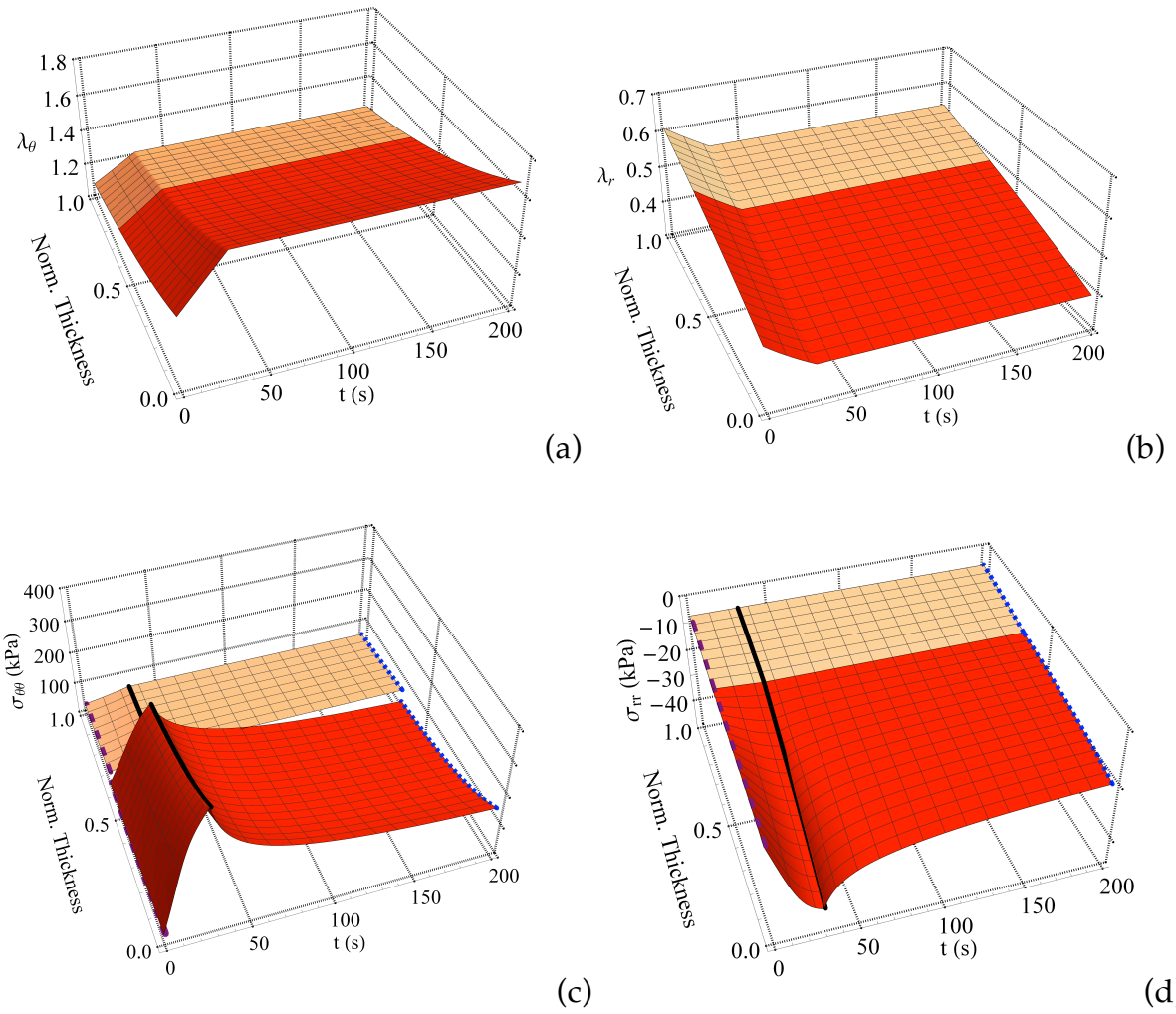

Figure 22. (a~b) Stretch distributions, and (c~d) stress distributions through the wall thickness over a 200 s timespan considering the active viscoelastic properties of smooth muscle tissue.

From the 3D stress plots in Figure 22 (c) and Figure 22 (d), the stress values at t_1, t_2, and t_3 are extracted to 2D plots in Figure 6 for better visualization and analysis. We highlight the stresses at t_1 as the steady state stress under a physiological blood pressure before the artery wall is overstretched, the peak stresses during overexpansion at t_2, and new steady state stresses after overexpansion at t_3 (corresponding to the dashed purple, solid black, and dotted blue curves marked in Figure 22). Circumferential and

radial Cauchy stresses at these time points are plotted and compared with the passive case in Figure 23. In the passive case, K_1 and K_6 in the chemical part are set to zero, that is, there is no calcium to stimulate smooth muscle to generate active force (AMp=AM=0), and the media layer becomes hyperelastic modeled by NeoHookean and exponential forms in Eq (5.1). As can be seen, for the active state, the stresses increase significantly to a peak value at t_2 and then go to steady state around t_3. It is noticeable that for the passive case, the stresses increase from t_1 to t_2 and are unchanged afterwards (t_2 and t_3 have the same values) showing no viscous effect. The results show that considering active viscoelasticity, large compression stresses in the radial direction are attained, and very large tensile stresses develop in the circumferential direction. Quantitatively an over fourfold increase in circumferential stresses and twofold increase in radial stresses occur. Overall, the largest stresses are in the circumferential direction. The media layer supports much of the circumferential and radial stresses during overexpansion (from t_1 to t_2). The adventitia plays a more dominant role in offsetting the load in the circumferential direction at the new steady state (t_3).

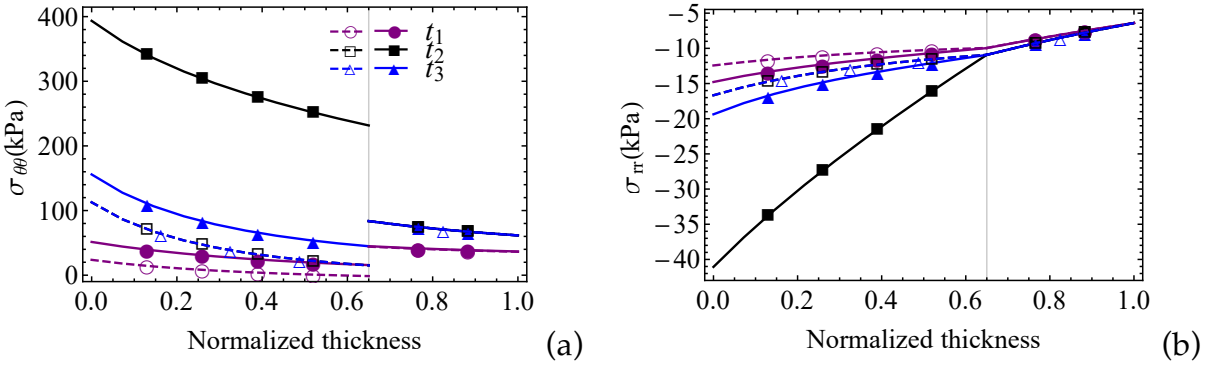

Figure 23. Stress distributions as a function of the normalized thickness at t_1 (previous steady state, in circle), t_2 (the peak, in square), and t_3 (new steady state, in triangle), for

active (solid curves with closed markers) and passive (dash curves with open markers) artery cases.

Next, we calculate and compare stress distributions in the artery wall for various displacement rates shown in Figure 24 (a). In Figure 24 (a) and Figure 24 (b), the stress evolutions at the mid-wall radius of the media layer are presented as a function of time. The results show that the stress magnitudes for the active case are much larger than those for the passive case when arteries are overstretched by 20% of the in vivo deformation (radial stresses can be twice as large, and circumferential stresses can reach six times larger) even though they do not differ very much at the steady state. Figure 24 (a) and Figure 24 (b) show higher circumferential and radial stress magnitudes for quicker stretches. Slower deformation rates reduce the stress magnitudes and it is expected that this would be consistent with lower restenosis rates since lower stresses cause less trauma in the artery. (Leibowitz et al., 2009a; Leibowitz et al., 2009b) Overstretch rate and total overexpansion time are competing mechanisms in minimizing the overall stress. Therefore, because the surgical protocol is on the same time scale as artery viscous effects, the simulations performed here clearly show that active viscoelastic behavior is an important consideration. We also calculate the pressure on the inner surface of the artery for passive and active cases for the displacement input of Figure 24 (a) and show the results in Figure 24 (d). The pressure increases significantly for the active case in comparison with the passive case. Specifically, maximum pressures are around 240 ~ 350 mmHg for the active case while for the passive case the maximum is approximately 127 mmHg. Thus, the maximum pressure on the inner surface of the active case can reach more than twice that of the passive case due to the active viscous properties of smooth muscle. Since pressure is

typically controlled during inflation, the results can be interpreted as the target pressure profiles to achieve the desired artery wall displacement.

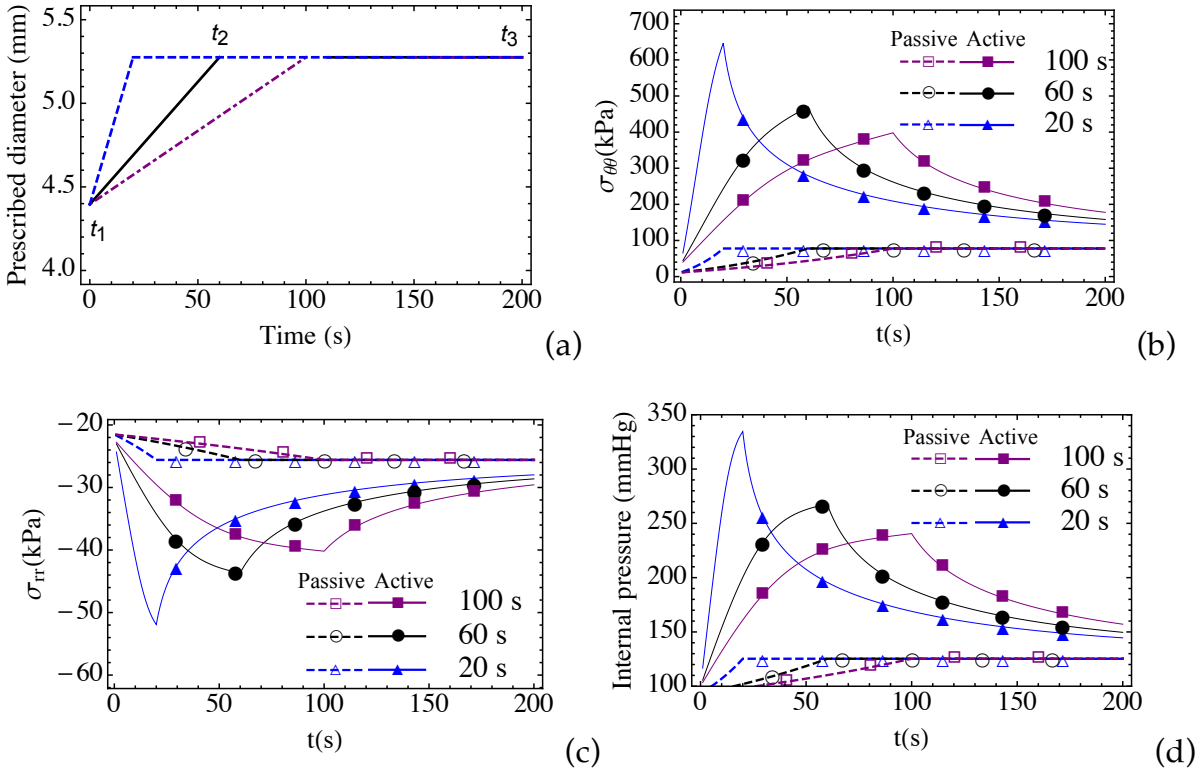

Figure 24. (a) Model input for prescribed overstretch rates: linearly increasing from d_1=4.4 mm to d_2=5.3 mm within 20 seconds, 60 seconds, and 100 seconds; (b-c) Stress distributions at the mid-wall radius in the media layer for different input deformation rates; (d) calculated pressures on the inner artery surface.

Effect of activation levels

Here we study the response for three different activation levels (calcium 120nM, 200 nM and 250 nM in the chemical model). For ease of comparison, we assume they have the same in vivo configurations for the three activation levels (for the mean physiological blood pressure 100 mmHg). The external pressures are calculated first for these three activation levels as 48.1 mmHg for 120 nM calcium, 26.4 mmHg for 200 nM calcium, and 3.3 mmHg for 250 nM calcium. Next, the obtained external pressures are used as the boundary conditions on the external surface of the artery for the prescribed supra-

physiological pressure input on the internal surfaces (Figure 25 (a)). The deformation and stress distributions in the arterial walls are calculated and shown in Figure 25 (b~c) and Figure 26. As seen in Figure 25 (b~c), for the pressure protocol in Figure 25 (a), higher activation levels induce more contraction and reduce the lumen diameter. Figure 26 shows the stress distributions at t_1, t_2 and t_3 for the induced deformation in Figure 25. For higher activation levels, the media layer becomes stiffer and subsequently carries more load. Recall the numerical results in the previous subsection where the adventitia was shown to dominate the load–carrying in the circumferential direction at t_1 and t_3, similar as the case of calcium 120 nM in this subsection. Considering Figure 26 (a) and Figure 26 (c), the results show that the activation level changes this trend, that is, higher activation levels increase the load carried by the media layer at t_1 and t_3 in comparison to the low activation level. In fact, the media layer can eventually become more dominant than the adventitia layer at steady-states.

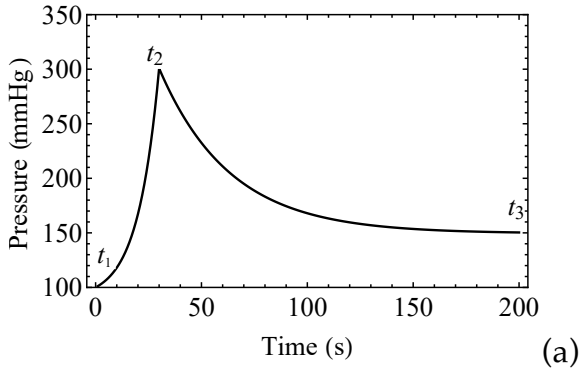

(a)

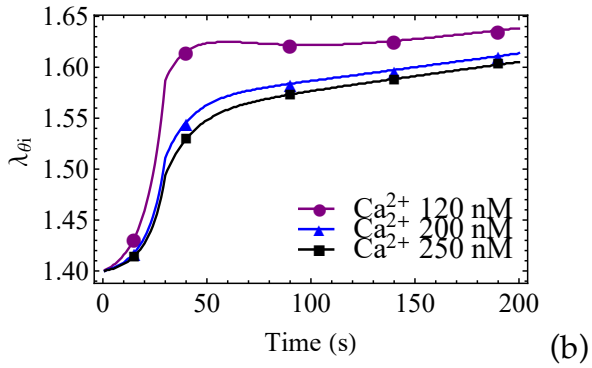

(b)

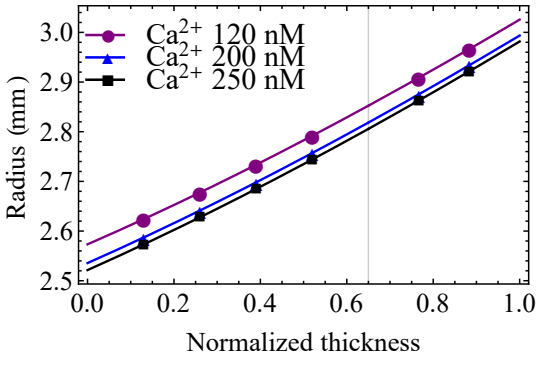

Figure 25. (a) the pressure input, (b) the calculated internal radial stretch, and (c) steady state radial coordinate over the thickness for three different activation levels.

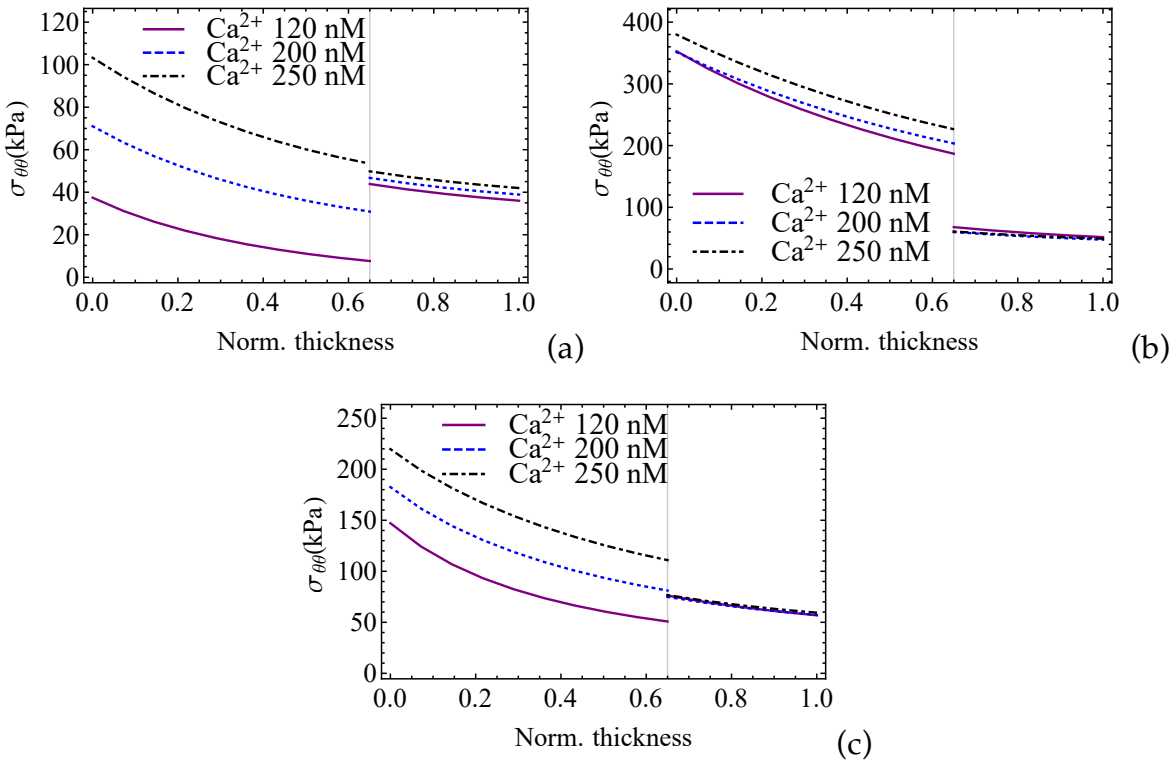

Figure 26. Circumferential Cauchy stresses for the pressure protocol under various activation levels at t_1=0s (a), t_2=30s (b), and t_3=200 (c).

5.3.2 Three-layer plaque-artery with various stenosis ratios

In the following, we study the active viscoelastic properties of smooth muscle tissue on plaque stress when the occluded artery is overstretched. Stress distributions in the plaque and artery for three levels of stenoses of 20%, 40%, 60% (the plaque area over the

original lumen area) as shown in Figure 27 are analyzed. For any stenosis, we prescribe a linearly varying change in diameter from the occluded state to the original in vivo lumen radius (see Figure 27 and Figure 28). For diseased or aged artery walls, the media layer tends to become thicker through hypertrophy (increasing smooth muscle cell volume) and hyperplasia (increasing smooth muscle cell number) and the adventitia tends to become stiffer. In the current study, we assume the diseased artery wall properties do not change and use the undiseased media and adventitia material properties to focus on the effect of active viscoelasticity of smooth muscle. We adopted Yeoh's material formulation to model the mechanical behavior of the plaque (see Table 7). We use the parameters for three types of plaque for human carotid artery (experimental data for swine carotid artery plaque is lacking) (Lawlor et al., 2011). The uniaxial stress-stretch behavior and corresponding model fits are shown in Figure 73 (b) in Appendix A.

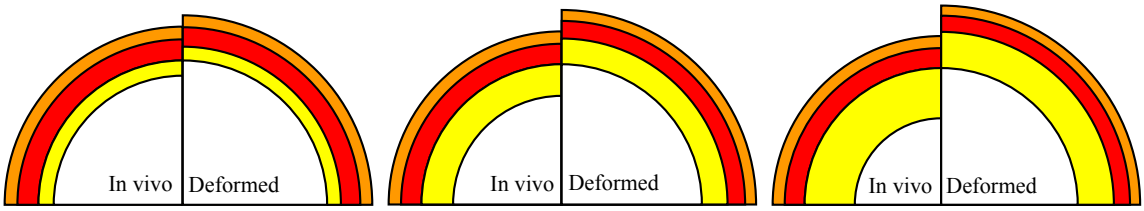

Figure 27. Schematic of the in vivo and overstretched configurations (quarter ring) for stenosis ratios 20%, 40%, and 60% from left to right (the inner most layer is plaque (yellow), the middle is media (red), and the outer most layer is adventitia (orange)).

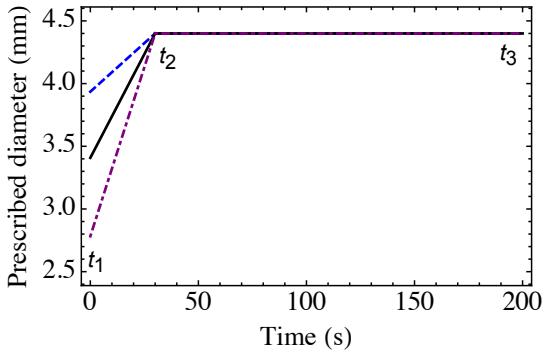

Figure 28. Displacement protocols for artery-plaque being overstretched: a linearly increasing internal diameter from d_1= 2.8 mm, 3.4 mm, and 3.9 mm to d_2=4.4 mm over 30 seconds for stenoses of 20%, 40%, and 60%, respectively.

Table 7. Model parameters for soft, mixed, and hard plaque(Lawlor et al., 2011).

	C_{10} (MPa)	C_{20} (MPa)	C_{30} (MPa)
Calcified	3.021E-1	–2.28E-1	2.61E-1
Hypocellular	2.35E-2	1.26E-1	1.12E-1
Cellular (soft)	2.96E-2	–3.32E-2	1.285E-1

We calculate the stress distributions of the plaque-artery as functions of the normalized thickness ($(r-r_i)/(r_o-r_i)$) and time for cellular (soft), hypocellular (mixed), and calcified (hard) types of plaque for the low activation level with calcium concentration of 120 nM same as section 5.3.1. We show in Figure 29 the stress distributions for the stenosis ratio 40% with and without considering active viscoelastic properties of smooth muscles. As can be seen from the comparison of the first three columns, for the active case, the radial stresses increase to the peak values from t_1 to t_2, and then eventually go to the new steady state at t_3 while the circumferential stress increases from t_1 to t_2 and continually increase from t_2 to the maximum at t_3; for the passive case, stresses increase from t_1 to t_2 and are unchanged afterwards. The active contractility of the media influences the mechanical responses of the plaque during

artery overstretch. As expected, the magnitude of the stresses increases with plaque stiffness and for softer plaques there is greater cross-over viscous effects due to the interface coupling with the active viscoelastic media. Thus when considering active viscoelasticity of smooth muscle tissue during artery overstretch, larger compression values in the plaque are predicted.

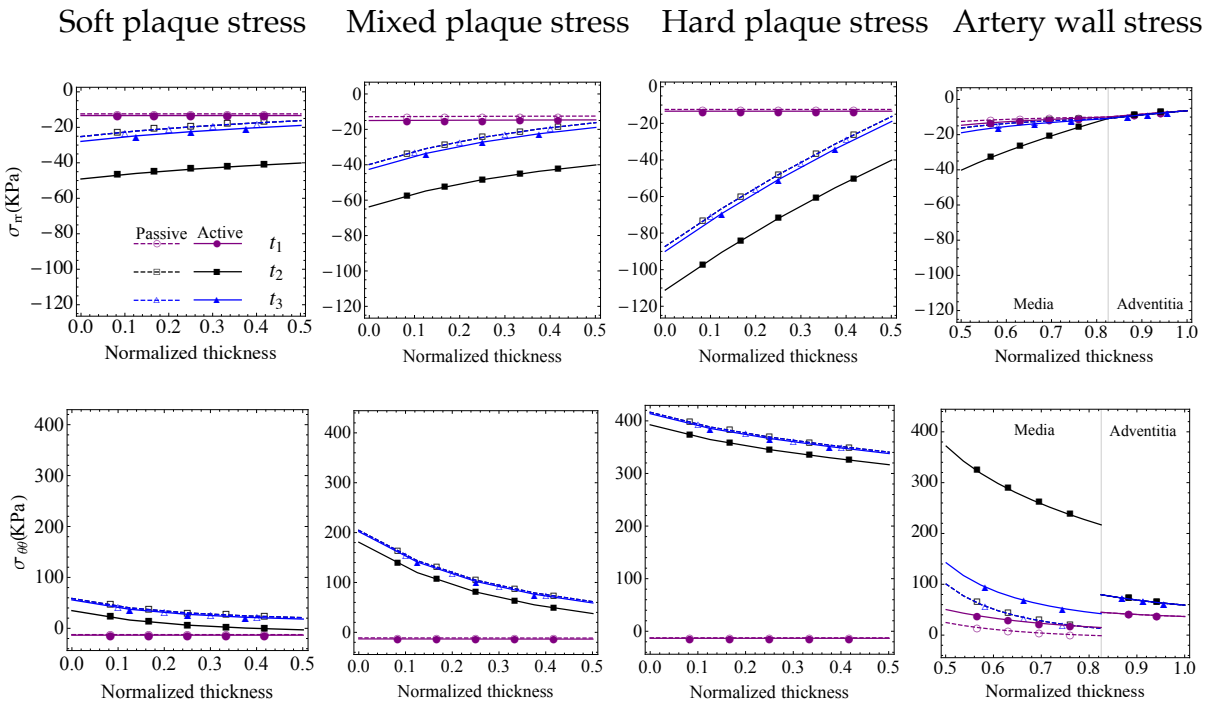

Figure 29. Stress distributions in the artery-plaque composite as a function of the normalized thickness. Active properties are denoted by the solid curves and passive properties given by the dashed curves (the legend applies for all the plots).

We also compare the stress distributions for stenosis ratios of 20%, 40% and 60% in Table 8. The stress distributions have a similar trend as shown in Figure 29. The results show that a higher degree of stenosis leads to larger stresses resulting from larger overstretch comparing with lower stenosis cases (see Figure 27) and that much larger stresses are generated overall in all the layers when active viscoelastic effects of

the smooth muscle cells is considered (the maximum stress of the active cases can reach twice that of the passive cases).

Table 8. The maximum stress magnitude for various stenosis ratios in the artery-plaque complex.

	20% (kPa)		40% (kPa)		60% (kPa)	
	Active	Passive	Active	Passive	Active	Passive
Cellular (σ_{rr})	32.5	16.2	49.1	25.2	120.0	93.6
Hypocelluar(σ_{rr})	33.0	16.7	63.8	39.9	215.5	189.0
Calcified (σ_{rr})	51.5	35.2	111.1	87.2	249.0	222.5
Artery (σ_{rr})	30.5	14.1	40.1	16.2	45.3	18.8
Artery ($\sigma_{\theta\theta}$)	227.9	52.7	371.9	100.3	503.1	178.6

5.4 Asymmetric artery with calcified plaque

Asymmetric intima-media thickening occurs in atherosclerotic arteries. In this section, we study the mechanical responses of asymmetric artery-plaque complex. The constitutive model for the arterial media layer is implemented in the ABAQUS user subroutine (UANISOHYPER_INV) in the Appendix. The computational simulations verify the main points concluded from the above mathematical results on symmetric artery and artery-plaque configurations. It demonstrates the important role active viscoelasticity played in the artery being overstretched in a longer timescale together with the asymmetry of the configuration. Furthermore, the provided user subroutine can be applied to calculate complex systems involving the external tools operating on the artery-plaque segment to examine the influence of the operating procedure and tools when considering the active viscoelasticity of the smooth muscle tissue.

The stress-free geometry of the asymmetric artery in the current work is assumed to have an outer diameter of d_{outer} =6 mm and inner diameter of d_{inner} =3.14 mm, and the thickness of the arterial wall is non-uniform, due to the media thickening, with the maximum and minimum thicknesses of the arterial wall being 1.9 mm and 0.94 mm (see Figure 30). Here, we assume the thickness ratio of the media to the adventitia is 65%/35% at the thinner wall side and the thickness of the adventitia is uniform (Gasser and Holzapfel, 2007b; Holzapfel et al., 2005) and plaque is an ellipse-shaped calcified plaque. The model is meshed into 14988 eight nodes brick elements (C3D8) with 3 elements in the thickness.

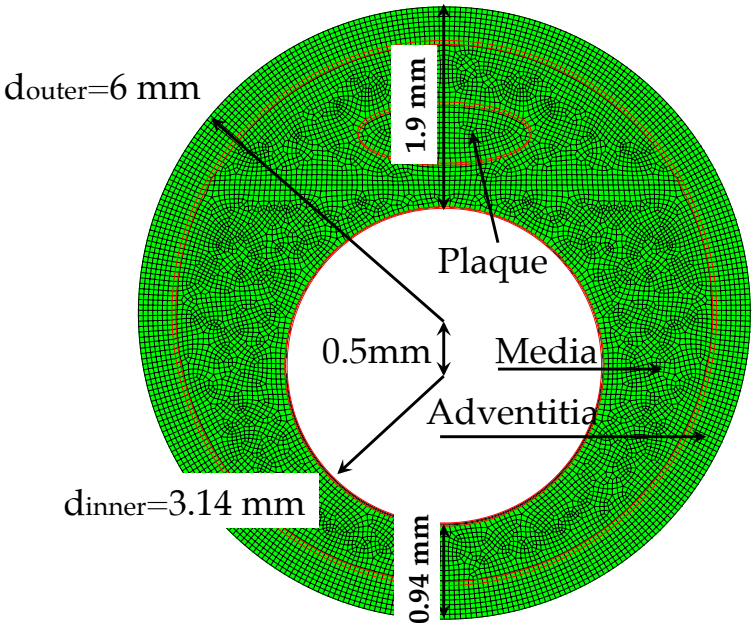

Figure 30. Geometry of the asymmetric artery with ellipse-shaped with an outer diameter of d_{outer} =6 mm and inner diameter of d_{inner} =3.14 mm, and the maximum and minimum thicknesses of the arterial wall being 1.9 mm and 0.94 mm.

The calcified plaque parameters are in Table 7. The artery and plaque components are assumed to bond perfectly, i.e. the stretch is continuous along the boundary of the artery-plaque complex. The axial length is fixed and kept at 1 (Gasser

and Holzapfel, 2007a). The pressure on the outer surface is assumed to be zero, which is a common simplifying assumption in artery simulations for supra-pressure and physiological pressure loading. First, we expand the artery internal surface radially from diameter 3.14 mm to 4.4 mm where the internal pressure on the inner surface is 170 mmHg as prestretch. Then this configuration is treated as the in vivo configuration and marked as t=0. The in vivo internal pressure of the arterial wall is targeted at stage 2 hypertension (over 160 mmHg), where patients' situations are considered severe and critical. (Varon and Marik, 2003) Next, the arterial wall is overstretched from t=0 (the in vivo state) by linearly expanding the diameters within 40 seconds to a state we refer to as the overstretch state (see Figure 31). Afterwards, the artery is allowed to relax for another 100 seconds until it reaches a new steady state. The displacement applied at the inner surface with loading history is summarized in Table 9 and plotted in Figure 31.

Table 9. Numerical values for diameters during overstretch.

	Diameters	Comments
t=0s (in vivo state)	4.4 mm	Internal pressure 170 mmHg
t=40s (overstretched state)	5.0 mm	113% of in vivo diameter
t=136s (steady state)	5.0 mm	---

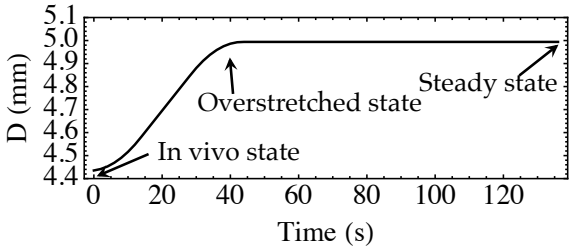

Figure 31. Displacement protocol of time-dependent diameter for artery being overstretched.

The radial and circumferential strains and stresses of artery with an ellipse calcified plaque at t=0 s (in vivo state), t=40 s (overstretched state), and t=136 s (steady state) are shown at the first, second, and third columns respectively of Figure 32. Because the asymmetric configuration resulted from media thickening, the radial and circumferential stresses and strains are asymmetric. The maximum compressive radial strain and the maximum tensile circumferential strain happen at the interface of the media and adventitia near the thin wall regions. In this example, the peak compressive radial stresses occur around the calcified plaque in the artery. The simulations illustrate the potential of the computational tool developed here to generate full field results of the stresses and strains in the artery, which can be used to design interventional tools and protocols whilst avoiding damage to the artery.

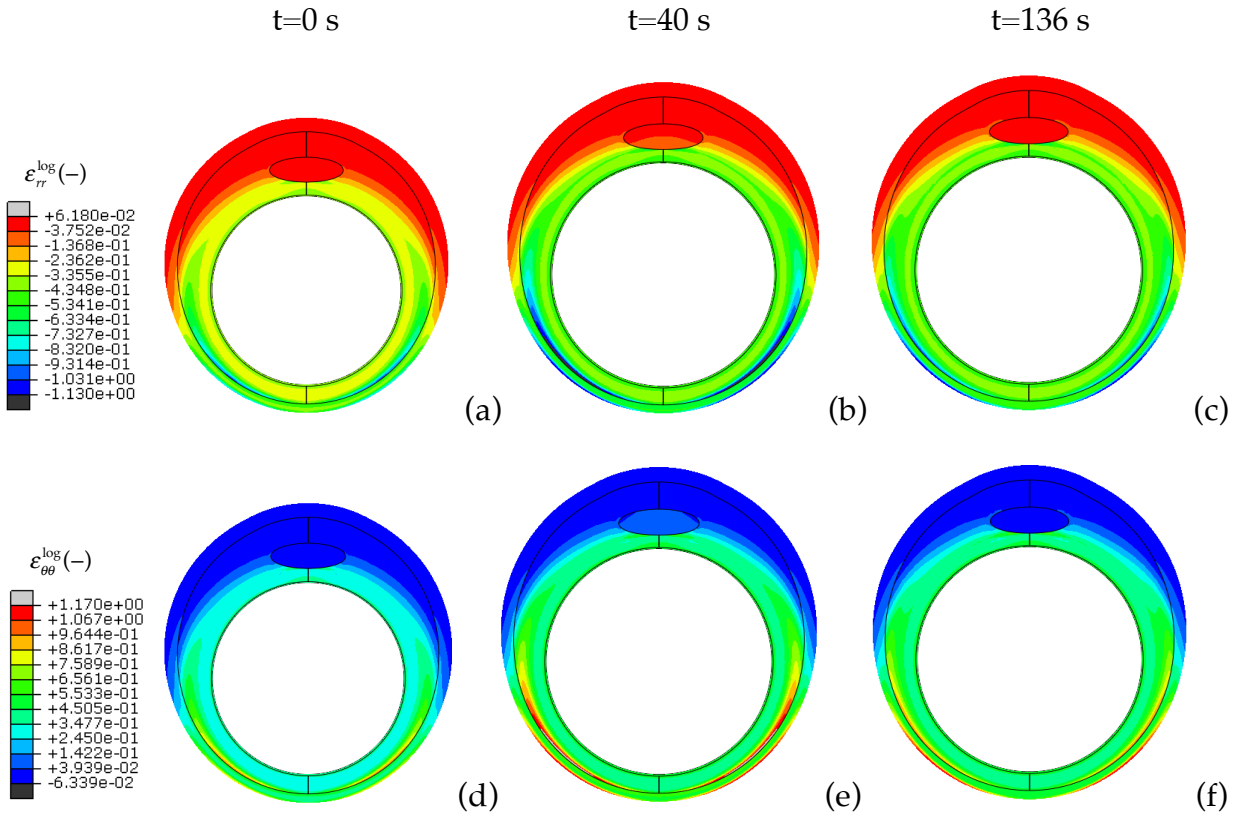

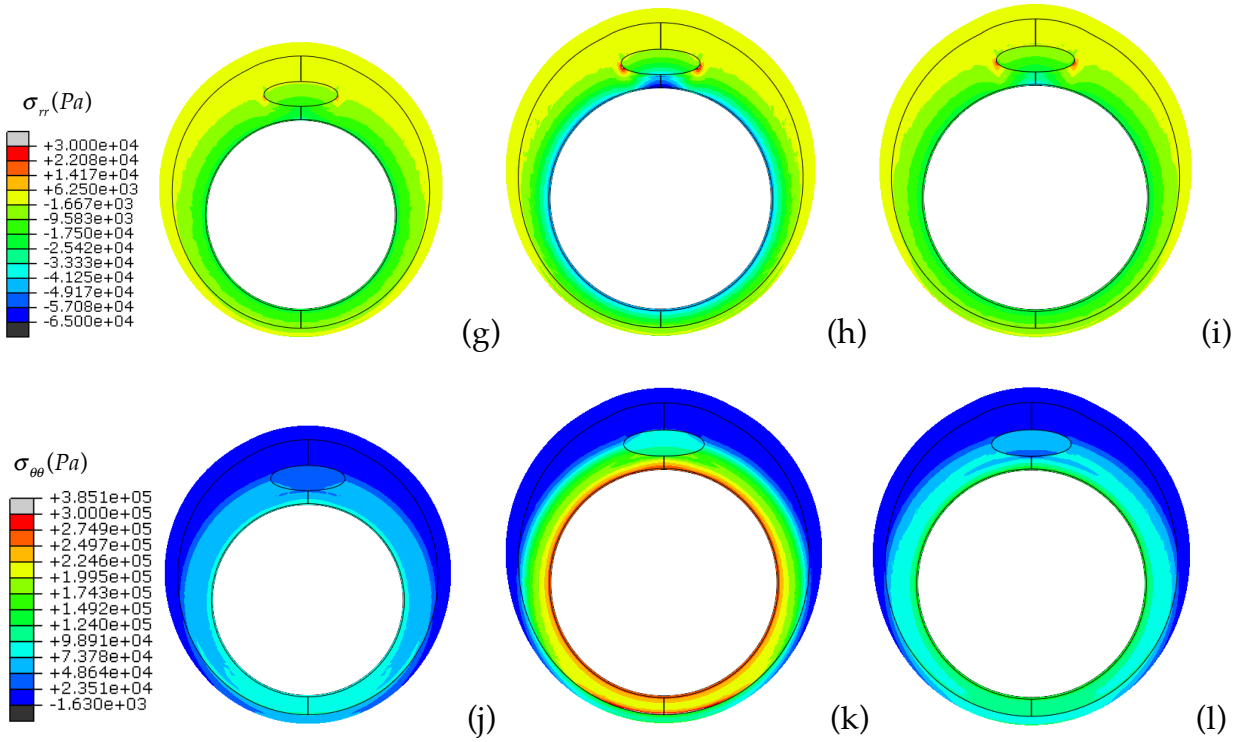

Figure 32. Strains and tresses for the artery with an ellipse-shaped calcified plaque at in vivo state (the first column), overstretched state (the second column), and steady state (the third column).

5.5 Conclusion

In summary, we employed a thick-walled model to calculate the stress distributions in healthy two-layer arteries and diseased three-layered artery-plaque assemblies to study the time dependent response due to an imposed overstretch. Significant differences between the simulations using passive hyperelastic materials and active viscoelastic materials are observed: an over fourfold increase in circumferential stresses and twofold increase in radial stresses for the cases considered here. These results quantify and qualify the role of active viscoelastic smooth muscle in the artery mechanical response on a longer time scale. Results clearly show that the active viscoelastic behavior has a non-negligible impact on the stresses developed in the artery wall. It reveals that only

considering the passive properties of arteries during overexpansion may grossly underestimate tissue stresses.

Since the contractile force generated is proportional to the rate of overstretch, higher circumferential and radial stress magnitudes are observed for quicker stretches. It suggests that slower deformation rates reduce the stress magnitudes and it is expected this would be consistent with lower restenosis rates since lower stresses cause less trauma in the artery. It is established that during balloon angioplasty and stent implementation, plaque fracture and damage is one of the negative outcomes. (Badel et al., 2014; Ferrara and Pandolfi, 2008; Gasser and Holzapfel, 2007a; Morlacchi et al., 2014) Results on a three-layer diseased artery-plaque complex have shown that the contractile behavior of smooth muscle in the media layer affects the stresses in the plaque, i.e. larger compression in the plaque is observed. It indicates that the stresses in the plaque without considering the active viscoelastic properties of smooth muscle tissue may be underestimated in the literature (Conway et al., 2014; Ebenstein, 2014; Gastaldi et al., 2010; Morlacchi et al., 2013).

The constitutive model is implemented into a finite element framework and the mechanical performance of an asymmetric artery-plaque was studied. The simulations provide the stress and strain distributions accounting for active viscoelastic behavior of smooth muscle in the artery. This numerical tool can be used to study artery and plaque behavior during interventional events. In the next chapter, we develop a new constitutive model and user subroutine for a second class of active anisotropic materials: dielectric elastomer composites. We adopt the same general framework outlined in Chapters 2 and 3 as was employed here.

References

Auricchio, F., Conti, M., De Beule, M., De Santis, G., Verhegghe, B., 2011. Carotid artery stenting simulation: From patient-specific images to finite element analysis. Medical Engineering & Physics 33, 281-289, doi:10.1016/j.medengphy.2010.10.011.

Azarnoush, H., Vergnole, S., Boulet, B., Sowa, M., Lamouche, G., 2012. Real-time control of angioplasty balloon inflation based on feedback from intravascular optical coherence tomography: experimental validation on an excised heart and a beating heart model. IEEE transactions on bio-medical engineering 59, 1488-1495, doi:10.1109/TBME.2012.2189884.

Badel, P., Avril, S., Sutton, M. A., Lessner, S. M., 2014. Numerical simulation of arterial dissection during balloon angioplasty of atherosclerotic coronary arteries. Journal of Biomechanics 47, 878-889, doi:10.1016/j.jbiomech.2014.01.009.

Blankenship, J. C., Krucoff, M. W., Werns, S. W., Anderson, H. V., Landau, C., White, H. J., Green, C. L., Spokojny, A. M., Bach, R. G., Raymond, R. E., Pinkston, J., Rawert, M., Talley, J. D., 1999. Comparison of slow oscillating versus fast balloon inflation strategies for coronary angioplasty. The American Journal of Cardiology 83, 675-680.

Bohr, D. F., Webb, R. C., 1984. Vascular Smooth Muscle Function and Its Changes in Hypertension. The American Journal of Medicine 77, 3-16, doi:10.1016/S0002-9343(84)80032-7.

Buffinton, C. M., Ebenstein, D. M., 2014. Effect of Calcification Modulus and Geometry on Stress in Models of Calcified Atherosclerotic Plaque. Cardiovascular Engineering and Technology 5, 244-260, doi:10.1007/s13239-014-0186-6.

Conway, C., McGarry, J. P., McHugh, P. E., 2014. Modelling of atherosclerotic plaque for use in a computational test-bed for stent angioplasty. Annals of Biomedical Engineering 42, 2425-2439, doi:10.1007/s10439-014-1107-4.

Delfino, A., Stergiopulos, N., Moore, J. E., Meister, J. J., 1997. Residual strain effects on the stress field in a thick wall finite element model of the human carotid bifurcation. Journal of Biomechanics 30, 777-786.

Dorros, G., Cohn, J. M., Palmer, L. E., 1998. Stent deployment resolves a petrous carotid artery angioplasty dissection. AJNR. American journal of neuroradiology 19, 392-394.

Duivenvoorden, R., de Groot, E., Afzali, H., Vanbavel, E. T., de Boer, O. J., Laméris, J. S., Fayad, Z. A., Stroes, E. S. G., Kastelein, J. J. P., Nederveen, A. J., 2009. Comparison of in vivo carotid 3.0-T magnetic resonance to B-mode ultrasound imaging and histology in a porcine model. JACC. Cardiovascular imaging 2, 744-750, doi:10.1016/j.jcmg.2008.12.030.

Ebenstein, D., 2014. Effects of Calcification Modulus and Geometry on Stress in Models of Calcified Atherosclerotic Plaque. Cardiovascular Engineering and Technology, 244-260.

Farb, A., Sangiorgi, G., Carter, A. J., Walley, V. M., Edwards, W. D., Schwartz, R. S., Virmani, R., 1999. Pathology of Acute and Chronic Coronary Stenting in Humans. Circulation 99, 44-52, doi:10.1161/01.CIR.99.1.44.

Ferrara, A., Pandolfi, A., 2008. Numerical modelling of fracture in human arteries. Computer Methods in Biomechanics and Biomedical Engineering 11, 553-567, doi:10.1080/10255840701771743.

Figueroa, C. A., Vignon-Clementel, I. E., Jansen, K. E., Hughes, T. J. R., Taylor, C. A., 2006. A coupled momentum method for modeling blood flow in three-dimensional deformable arteries. Computer Methods in Applied Mechanics and Engineering 195, 5685-5706, doi:10.1016/j.cma.2005.11.011.

García, A., Peña, E., Laborda, A., Lostalé, F., De Gregorio, M. A., Doblaré, M., Martínez, M. A., 2011. Experimental study and constitutive modelling of the passive mechanical properties of the porcine carotid artery and its relation to histological analysis: Implications in animal cardiovascular device trials. Medical Engineering & Physics 33, 665-676, doi:10.1016/j.medengphy.2011.01.016.

Gasser, T. C., Holzapfel, G. A., 2006. Finite Element Modeling of Balloon Angioplasty by Considering Overstretch of Remnant Non-diseased Tissues in Lesions. Computational Mechanics 40, 47-60, doi:10.1007/s00466-006-0081-6.

Gasser, T. C., Holzapfel, G. A., 2007a. Modeling plaque fissuring and dissection during balloon angioplasty intervention. Annals of Biomedical Engineering 35, 711-723, doi:10.1007/s10439-007-9258-1.

Gasser, T. C., Holzapfel, G. A., 2007b. Finite Element Modeling of Balloon Angioplasty by Considering Overstretch of Remnant Non-diseased Tissues in Lesions. Computational Mechanics 40, 47-60, doi:10.1007/s00466-006-0081-6.

Gastaldi, D., Morlacchi, S., Nichetti, R., Capelli, C., Dubini, G., Petrini, L., Migliavacca, F., 2010. Modelling of the provisional side-branch stenting approach for the treatment of atherosclerotic coronary bifurcations: effects of stent positioning. Biomechanics and Modeling in Mechanobiology 9, 551-561, doi:10.1007/s10237-010-0196-8.

Grogan, J. A., Leen, S. B., McHugh, P. E., 2013. Optimizing the design of a bioabsorbable metal stent using computer simulation methods. Biomaterials 34, 8049-8060, doi:10.1016/j.biomaterials.2013.07.010.

Gunn, J., Arnold, N., Chan, K. H., Shepherd, L., Cumberland, D. C., Crossman, D. C., 2002. Coronary artery stretch versus deep injury in the development of in-stent neointima. Heart 88, 401-405, doi:10.1136/heart.88.4.401.

Hill-Eubanks, D. C., Werner, M. E., Heppner, T. J., Nelson, M. T., 2011. Calcium Signaling in Smooth Muscle. Cold Spring Harbor Perspectives in Biology 3, a004549, doi:10.1101/cshperspect.a004549.

Holzapfel, G. A., Gasser, T. C., Ogden, R. W., 2000. A New Constitutive Framework for Arterial Wall Mechanics and a Comparative Study of Material Models. Journal of elasticity and the physical science of solids 61, 1-48, doi:10.1023/A:1010835316564.

Holzapfel, G. A., Stadler, M., Schulze-Bauer, C. A. J., 2002. A Layer-Specific Three-Dimensional Model for the Simulation of Balloon Angioplasty using Magnetic Resonance Imaging and Mechanical Testing. Annals of Biomedical Engineering 30, 753-767, doi:10.1114/1.1492812.

Holzapfel, G. A., Sommer, G., Gasser, C. T., Regitnig, P., 2005. Determination of layer-specific mechanical properties of human coronary arteries with nonatherosclerotic intimal thickening and related constitutive modeling. American Journal of Physiology. Heart and Circulatory Physiology 289, H2048-2058, doi:10.1152/ajpheart.00934.2004.

Holzapfel, G. A., Mulvihill, J. J., Cunnane, E. M., Walsh, M. T., 2014. Computational approaches for analyzing the mechanics of atherosclerotic plaques: a review. Journal of Biomechanics 47, 859-869, doi:10.1016/j.jbiomech.2014.01.011.

Humphrey, J. D., Na, S., 2002. Elastodynamics and Arterial Wall Stress. Annals of Biomedical Engineering 30, 509-523, doi:10.1114/1.1467676.

Iqbal, J., Gunn, J., Serruys, P. W., 2013. Coronary stents: historical development, current status and future directions. British Medical Bulletin 106, 193-211, doi:10.1093/bmb/ldt009.

Kiousis, D. E., Wulff, A. R., Holzapfel, G. A., 2009. Experimental studies and numerical analysis of the inflation and interaction of vascular balloon catheter-stent systems. Annals of Biomedical Engineering 37, 315-330, doi:10.1007/s10439-008-9606-9.

Knot, H. J., Nelson, M. T., 1998. Regulation of arterial diameter and wall [Ca2+] in cerebral arteries of rat by membrane potential and intravascular pressure. The Journal of Physiology 508 (Pt 1), 199-209.

Kochová, P., Kuncová, J., Svíglerová, J., Cimrman, R., Miklíková, M., Liška, V., Tonar, Z., 2012. The contribution of vascular smooth muscle, elastin and collagen on the passive mechanics of porcine carotid arteries. Physiological Measurement 33, 1335-1351, doi:10.1088/0967-3334/33/8/1335.

Kornowski, R., Hong, M. K., Tio, F. O., Bramwell, O., Wu, H., Leon, M. B., 1998. In-stent restenosis: contributions of inflammatory responses and arterial injury to neointimal hyperplasia. Journal of the American College of Cardiology 31, 224-230.

Lally, C., Dolan, F., Prendergast, P. J., 2005. Cardiovascular stent design and vessel stresses: a finite element analysis. Journal of Biomechanics 38, 1574-1581, doi:10.1016/j.jbiomech.2004.07.022.

Lawlor, M. G., O'Donnell, M. R., O'Connell, B. M., Walsh, M. T., 2011. Experimental determination of circumferential properties of fresh carotid artery plaques. Journal of Biomechanics 44, 1709-1715, doi:10.1016/j.jbiomech.2011.03.033.

Leibowitz, D., Abu-Gazala, M., Katz, I., Danenberg, H., Nassar, H., Boguslavsky, L., Mosseri, M., Varshitzsky, B., Lotan, C., Weiss, A. T., 2009a. Computerized gradual balloon inflation: a novel strategy of coronary angioplasty superior to a standard manual approach. Cardiovascular Revascularization Medicine: Including Molecular Interventions 10, 45-48, doi:10.1016/j.carrev.2008.06.002.

Leibowitz, D., Lotan, C., Katz, I., Nassar, H., Boguslavsky, L., Mosseri, M., Jabara, R., Varshitzsky, B., Danenberg, H., Weiss, A. T., 2009b. Effect of gradual computerized angioplasty on outcomes of patients undergoing coronary stenting. The American Journal of Cardiology 104, 223-226, doi:10.1016/j.amjcard.2009.03.035.

Li, H., Wang, X., 2013. Design optimization of balloon-expandable coronary stent. Structural and Multidisciplinary Optimization 48, 837-847, doi:10.1007/s00158-013-0926-5.

Liu, Y., Dang, C., Garcia, M., Gregersen, H., Kassab, G. S., 2007. Surrounding tissues affect the passive mechanics of the vessel wall: theory and experiment. American Journal of Physiology. Heart and Circulatory Physiology 293, H3290-3300, doi:10.1152/ajpheart.00666.2007.

Martin, D., Boyle, F., 2013. Finite element analysis of balloon-expandable coronary stent deployment: influence of angioplasty balloon configuration. International Journal for Numerical Methods in Biomedical Engineering 29, 1161-1175, doi:10.1002/cnm.2557.

Miketic, S., Carlsson, J., Tebbe, U., 1998. Influence of gradually increased slow balloon inflation on restenosis after coronary angioplasty. American Heart Journal 135, 709-713.

Moireau, P., Xiao, N., Astorino, M., Figueroa, C. A., Chapelle, D., Taylor, C. A., Gerbeau, J. F., 2011. External tissue support and fluid–structure simulation in blood flows. Biomechanics and Modeling in Mechanobiology 11, 1-18, doi:10.1007/s10237-011-0289-z.

Morlacchi, S., Pennati, G., Petrini, L., Dubini, G., Migliavacca, F., 2014. Influence of plaque calcifications on coronary stent fracture: a numerical fatigue life analysis including cardiac wall movement. Journal of Biomechanics 47, 899-907, doi:10.1016/j.jbiomech.2014.01.007.

Morlacchi, S., Colleoni, S. G., Cárdenes, R., Chiastra, C., Diez, J. L., Larrabide, I., Migliavacca, F., 2013. Patient-specific simulations of stenting procedures in coronary bifurcations: two clinical cases. Medical Engineering & Physics 35, 1272-1281, doi:10.1016/j.medengphy.2013.01.007.

Mortier, P., Holzapfel, G. A., De Beule, M., Van Loo, D., Taeymans, Y., Segers, P., Verdonck, P., Verhegghe, B., 2010. A novel simulation strategy for stent insertion and deployment in curved coronary bifurcations: comparison of three drug-eluting stents. Annals of Biomedical Engineering 38, 88-99, doi:10.1007/s10439-009-9836-5.

Murtada, S.-I., Holzapfel, G. A., 2014. Investigating the role of smooth muscle cells in large elastic arteries: a finite element analysis. Journal of Theoretical Biology 358, 1-10, doi:10.1016/j.jtbi.2014.04.028.

Ohman, E. M., Marquis, J. F., Ricci, D. R., Brown, R. I., Knudtson, M. L., Kereiakes, D. J., Samaha, J. K., Margolis, J. R., Niederman, A. L., Dean, L. S., 1994. A randomized comparison of the effects of gradual prolonged versus standard primary balloon inflation on early and late outcome. Results of a multicenter clinical trial. Perfusion Balloon Catheter Study Group. Circulation 89, 1118-1125.

Pant, S., Bressloff, N. W., Limbert, G., 2012. Geometry parameterization and multidisciplinary constrained optimization of coronary stents. Biomechanics and Modeling in Mechanobiology 11, 61-82, doi:10.1007/s10237-011-0293-3.

Perrée, J., van Leeuwen, T. G., Kerindongo, R., Spaan, J. A. E., VanBavel, E., 2003. Function and structure of pressurized and perfused porcine carotid arteries: effects of in vitro balloon angioplasty. The American Journal of Pathology 163, 1743-1750, doi:10.1016/S0002-9440(10)63533-X.

Rachev, A., Hayashi, K., 1999. Theoretical Study of the Effects of Vascular Smooth Muscle Contraction on Strain and Stress Distributions in Arteries. Annals of Biomedical Engineering 27, 459-468, doi:10.1114/1.191.

Rogers, C., Tseng, D. Y., Squire, J. C., Edelman, E. R., 1999. Balloon-Artery Interactions During Stent Placement. Circulation Research 84, 378-383, doi:10.1161/01.RES.84.4.378.

Roy, S., Silacci, P., Stergiopulos, N., 2005. Biomechanical proprieties of decellularized porcine common carotid arteries. American Journal of Physiology - Heart and Circulatory Physiology 289, H1567-H1576, doi:10.1152/ajpheart.00564.2004.

Sarembock, I. J., LaVeau, P. J., Sigal, S. L., Timms, I., Sussman, J., Haudenschild, C., Ezekowitz, M. D., 1989. Influence of inflation pressure and balloon size on the development of intimal hyperplasia after balloon angioplasty. A study in the atherosclerotic rabbit. Circulation 80, 1029-1040.

Schiavone, A., Zhao, L. G., 2015. A study of balloon type, system constraint and artery constitutive model used in finite element simulation of stent deployment. Mechanics of Advanced Materials and Modern Processes 1, 1-15, doi:10.1186/s40759-014-0002-x.

Schiavone, A., Zhao, L. G., Abdel-Wahab, A. A., 2014. Effects of material, coating, design and plaque composition on stent deployment inside a stenotic artery—Finite element simulation. Materials Science and Engineering: C 42, 479-488, doi:10.1016/j.msec.2014.05.057.

Schmidt, T., Pandya, D., Balzani, D., 2015. Influence of isotropic and anisotropic material models on the mechanical response in arterial walls as a result of supra-physiological loadings. Mechanics Research Communications 64, 29-37, doi:10.1016/j.mechrescom.2014.12.008.

Sowton, E., Timmis, A. D., Crick, J. C., Griffin, B., Yates, A. K., Deverall, P., 1986. Early results after percutaneous transluminal coronary angioplasty in 400 patients. British Heart Journal 56, 115-120.

Tammareddi, S., Sun, G., Li, Q., 2016. Multiobjective robust optimization of coronary stents. Materials & Design 90, 682-692, doi:10.1016/j.matdes.2015.10.153.

Tenaglia, A. N., Quigley, P. J., Kereiakes, D. J., Abbottsmith, C. W., Phillips, H. R., Tcheng, J. E., Rendall, D., Ohman, E. M., 1992. Coronary angioplasty performed with gradual and prolonged inflation using a perfusion balloon catheter: procedural success and restenosis rate. American Heart Journal 124, 585-589.

Varon, J., Marik, P. E., 2003. Clinical review: The management of hypertensive crises. Critical Care 7, 374-384, doi:10.1186/cc2351.

Yang, J., Clark Jr, J. W., Bryan, R. M., Robertson, C., 2003. The myogenic response in isolated rat cerebrovascular arteries: smooth muscle cell model. Medical Engineering & Physics 25, 691-709, doi:10.1016/S1350-4533(03)00100-0.

Yeoh, O. H., 1993. Some Forms of the Strain Energy Function for Rubber. Rubber Chemistry and Technology 66, 754-771, doi:10.5254/1.3538343.

Chapter 6. A constitutive model for contractile dielectric elastomer composites

6.1 Introduction

In previous work, we proposed a constitutive formulation for isotropic dielectric elastomers under hyperelastic conditions. (Goulbourne et al., 2005) The model has been shown to be robust under generalized 3D loading, finite deformations, and large electric fields. It is well known that an isotropic thin membrane expands laterally in both main directions for an applied electric field through the thickness direction. Schemes for fabricating anisotropic dielectric elastomers via passive embedded fibers have been developed. (He et al., 2017a; He et al., 2017b; Huang et al., 2012; Lee and Tawfick, 2016; Lu et al., 2016; Lu et al., 2012; Shian et al., 2015a; Shian et al., 2015b; Subramani et al., 2014; Suo, 2010) Here an active fiber composite is proposed. The main distinction of our anisotropic composite from the existing anisotropic composites is that the embedded fibers are soft and actively contractile. Depending on the application time scale, the viscoelastic properties of dielectric elastomers may become important. Efforts to model this behavior have been pursued in recent years. (Ask et al., 2012; Ask et al., 2015; Bortot et al., 2016; Henann et al., 2013; Hong, 2011; S. Park and D. Nguyen, 2013; Thylander et al., 2017; Wang et al., 2013; Wang et al., 2016; Zhang et al., 2015) In a general formulation, we assume the contractile fibers in the proposed dielectric elastomer composite (DEC) are also viscoelastic. This is similar to the structural formulation for

active contractile muscle tissue. The new anisotropic constitutive model is based on current models of physiological muscle.

The DEC model couples invariant-based anisotropic nonlinear continuum mechanics with Maxwell stress. The composite material is treated as homogenous. The evolution equation for the contractile fibers is based on the existing evolution laws in Reese and Govindjee but in one dimensional form for the fibers. (Reese and Govindjee, 1998) In addition, theoretical modeling and computational simulations are convenient, efficient, and low-cost tools to assess the feasibility and properties of novel dielectric elastomer composites and to facilitate the development and optimization of their related applications. A numerical tool is needed to conduct simulations involving complex geometries and boundary conditions. Consequently, the proposed anisotropic model is implemented into a commercial finite element code by employing a user-defined subroutine. The outline of this chapter is as follows. In section 6.2, the electromechanical coupling and material properties are summarized. The constitutive model is derived in section 6.3. In section 6.4, computational formulations for implementing the constitutive model are derived. In section 6.5, the FEM formulation is verified by comparing analytical solutions for uniaxial, biaxial, and simple shear tests. Additionally, parameter studies are carried out to assess the composite's behaviors. A summary is given in section 6.6.

6.2 Soft dielectric elastomer composites structure

The dielectric elastomer composite consists of a soft polymer membrane matrix and uniformly distributed contractile fibers (see Figure 7 in Chapter 1). Theoretically, the composite is treated as a homogenous material, i.e. each material point consists of the same matrix with embedded fiber structure. It is assumed that the electric fields are

applied along the 1D fibers. The electromechanical coupling is presumed due to the Maxwell stress effect. If the top and bottom surfaces of the homogenized composite membrane are electroded, then a matrix dominated Maxwell stress effect also occurs (see Figure 7 (b) in Chapter 1). In this way, multiaxial activation is realized via i) fiber activation and ii) through thickness matrix activation.

6.3 Constitutive model for dielectric elastomer composites

Recall from Chapter 4 that smooth muscle tissue was treated as a fibrous composite consisting of directional smooth muscle cells and modeled as a homogenous material. A similar approach is taken here for modeling the electro-active composite. At the macroscale, we consider that all the fibers are homogeneously and continuously distributed throughout the matrix with an overall dominant orientation. We employ an invariant based formulation to describe an active anisotropic solid undergoing finite deformations within a nonlinear viscoelastic framework. We consider a strain energy function of the following form (the invariant numbering is consistent with the general formulations in Chapter 2) as

$$\begin{aligned}\Psi\left(\mathbf{F},\mathbf{F}_F^v,\mathbf{V},\mathbf{E}\right)&=\Psi\left(I_1\sim I_5,I_1^v\sim I_5^v,I_{10}\sim I_{12}\right)\\&=\Psi_{mech}\left(I_1\sim I_5,I_1^v\sim I_5^v\right)+\Psi_{\max}\left(I_{10}\sim I_{12}\right),\end{aligned}\tag{6.1}$$

where, $\mathbf{F}$ and $\mathbf{F}_F^v$ are the deformation gradients, $\mathbf{V}$ is the fiber orientation, I_i is the principal invariants of Cauchy-Green tensors, and $\mathbf{E}$ is the nominal electric field (kinematics are introduced in detail in the following). Based on this, the total Cauchy stress can be written using principal invariants and decomposed into a purely mechanical stress tensor and the Maxwell stress tensor (Goulbourne et al., 2005) as:

$$\boldsymbol{\sigma}=\boldsymbol{\sigma}_{mech}\left(I_1\sim I_5,I_1^v\sim I_5^v\right)+\boldsymbol{\sigma}_{\max}\left(I_{10}\sim I_{12}\right).\tag{6.2}$$

A one dimensional rheological model in the fiber direction for infinitesimal deformation is presented in Figure 1 for our electro-active composites and the constitutive model is an extension of the rheological model for infinitesimal deformation to finite deformation. The rheological model consists of three elements arranged in parallel: a mechanical matrix element, a mechanical fiber element, and an electrical active element representing matrix and fiber activation. The mechanical part of the constitutive model is based on the nonlinear viscoelastic theory of solids in Reese and Govindjee. (Reese and Govindjee, 1998) Generally, the mechanical properties of the matrix can be considered isotropic and viscoelastic; here it is purely elastic as part of a simplifying assumption. The fibers in the composite matrix are treated as viscoelastic and is described by a spring representing the equilibrium response in parallel with a nonequilibruim response represented by a spring-damper for the time-dependent relaxation (see Figure 33).

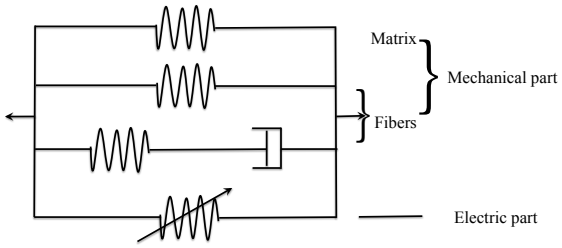

Figure 33. Rheological model for the anisotropic viscoelastic soft polymer composites.

Kinematic

The unit vector for the contractile fiber orientation is defined as **V** (see Figure 34). The fiber orientation vector in the current configuration are $\mathbf{v} = \mathbf{FV}$. The electric field vector is $\mathbf{E} = \begin{bmatrix} E_1 & E_2 & E_3 \end{bmatrix}^T$.

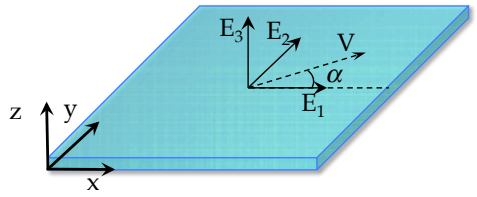

Figure 34. Schematic of anisotropic dielectric elastomer with one directional vector $\mathbf{V}=\begin{bmatrix} \cos\alpha & \sin\alpha & 0 \end{bmatrix}^T$ and the nominal electric field $\mathbf{E}=\begin{bmatrix} E_1 & E_2 & E_3 \end{bmatrix}^T$.

Following previous efforts on the principal invariants depending on the electric fields (Dorfmann and Ogden, 2006; Son, 2011), a set of first order principal invariants associated with the electric field are defined as

$$I_{10}=\mathbf{E}\cdot\mathbf{E}, I_{11}=\mathbf{E}\cdot\mathbf{C}^{-1}\cdot\mathbf{E}. \tag{6.3}$$

where I_{10} and I_{11} represent the quadratics of the nominal and true electric field $\mathbf{E}$ and $\mathbf{e}$ (see Chapter 2). The solid is configured such that the electric field is applied to the matrix only in the thickness direction, therefore E_3 in the electric field vector $\mathbf{E}=\begin{bmatrix} E_1 & E_2 & E_3 \end{bmatrix}^T$ couples with the matrix. For ease of notation, we also split the electric field vector into two vectors, reflecting the electric field component in the thickness direction for 'matrix' activation, and a component for activating the in-plane fibers (fiber activation):

$$\begin{aligned}\mathbf{E}&=\begin{bmatrix} E_1 & E_2 & E_3 \end{bmatrix}^T \\ &=\mathbf{E}_f+\mathbf{E}_m=\begin{bmatrix} E_1 & E_2 & 0 \end{bmatrix}^T+\begin{bmatrix} 0 & 0 & E_3 \end{bmatrix}^T.\end{aligned} \tag{6.4}$$

Now, consider activating the fibers along the length direction, $\mathbf{V}=\begin{bmatrix} \cos\alpha & \sin\alpha & 0 \end{bmatrix}^T$ (α is the fiber angle), the component of the field in that direction is $E_f=\mathbf{E}\cdot\mathbf{V}=\mathbf{E}_f\cdot\mathbf{V}=E_1\cos\alpha+E_2\sin\alpha$ which is the magnitude of the nominal electric field in

the fiber direction. Therefore, the resultant coupling can be treated as a fiber coupling E_f and a matrix coupling $\mathbf{E}_m$ (the remainder of the total electric field). The principal invariants for matrix and fibers are

$$I_{11}^m = \mathbf{E}_m \cdot \mathbf{C}^{-1} \cdot \mathbf{E}_m, I_{11}^f = \left(\frac{E_f}{\lambda} \right)^2 = \frac{E_f^2}{I_4}, \tag{6.5}$$

where λ is the fiber stretch and therefore E_f / λ is the true electric field in the fiber.

Constitutive formulations for dielectric elastomer composites

At the macroscale, the composite material is treated as having a homogeneously distributed fiber family in an active matrix. The mechanical part of the strain energy function includes a component for the isotropic matrix using a NeoHookean form, and equilibrium and nonequilibrium components for the active contractile fiber. For simplicity, a quadratic form is used to model the equilibrium and nonequilibrium fiber components. The electromechanical coupling is modeled using a quadratic dependence on the true electric field. The explicit form of the strain energy and the Cauchy stress for the dielectric elastomer composite are

$$\Psi = \underbrace{\frac{\mu}{2}\left(I_1 - 3\right) + \frac{\mu_{feq}}{2}\left(I_4 - 1\right)^2 + \frac{\mu_{fneq}}{2}\left(\frac{I_4}{I_4^{\,v}} - 1 \right)^2}_{mechanical} \underbrace{- \frac{\varepsilon_0 \varepsilon_{rf}}{2} I_{11}^f}_{electrical-fiber} \underbrace{- \frac{\varepsilon_0 \varepsilon_{rm}}{2} I_{11}^m}_{electrical-matrix}, \tag{6.6}$$

$$\begin{aligned} \boldsymbol{\sigma} = & \underbrace{\mu \mathbf{b} + 2\mu_{feq}\left(I_4 - 1\right)\mathbf{v} \otimes \mathbf{v} + 2\mu_{fneq}\left(\frac{I_4}{I_4^{\,v}} - 1 \right)\frac{1}{I_4^{\,v}} \mathbf{v} \otimes \mathbf{v}}_{mechanical} \\ & + \underbrace{\varepsilon_0 \varepsilon_{rf} \frac{E_f^{\,2}}{I_4} \frac{\mathbf{v}}{\sqrt{I_4}} \otimes \frac{\mathbf{v}}{\sqrt{I_4}}}_{electrical-fiber} + \underbrace{\varepsilon_0 \varepsilon_{rm} \mathbf{e}_m \otimes \mathbf{e}_m - \frac{\varepsilon_0 \varepsilon_{rm}}{2} \mathbf{e}_m \cdot \mathbf{e}_m \mathbf{I}}_{electrical-matrix} + p\mathbf{I}, \end{aligned} \tag{6.7}$$

where E_f is the magnitude of the nominal electric field in the fiber direction and $\mathbf{E}_m = \begin{bmatrix} 0 & 0 & E_3 \end{bmatrix}^T$ is the nominal electric field in the thickness direction, ε_{rf} and ε_{rm} are

the dielectric constants for fibers and matrix, μ is the shear modulus of the matrix, and μ_{feq} and μ_{fneq} are the moduli for the equilibrium and nonequilibrium parts of fibers, the true electric field for fibers is $E_f/\left(I_4\right)^{1/2}=E_f/\lambda$, the true electric field for the isotropic matrix is $\mathbf{e}_m=\mathbf{F}^{-T}\mathbf{E}_m$, $\mathbf{v}$ is the fiber vector in the current configuration, and $\mathbf{v}/\sqrt{I_4}$ is the unit fiber vector in the current configuration.

For zero electric field in the fibers, i.e. $E_1=0$, $E_2=0$, and $E_f=0$, the usual Maxwell stress term due to a through thickness electric field is recovered, and the stress expression in Eq (6.7) is reduced to an anisotropic mechanical formulation (passive fibers)

$$\boldsymbol{\sigma}=\underbrace{\mu\mathbf{b}+2\mu_{feq}\left(I_4-1\right)\mathbf{v}\otimes\mathbf{v}+2\mu_{fneq}\left(\frac{I_4}{I_4^{\,v}}-1\right)\frac{1}{I_4^{\,v}}\mathbf{v}\otimes\mathbf{v}}_{mechanical}+\underbrace{\varepsilon_0\varepsilon_{rm}\mathbf{e}_m\otimes\mathbf{e}_m-\frac{\varepsilon_0\varepsilon_{rm}}{2}\mathbf{e}_m\cdot\mathbf{e}_m\mathbf{I}}_{\text{Maxwell stress tensor}}+p\mathbf{I},. \quad (6.8)$$

Furthermore, when there are no fibers, i.e. $\mu_{feq}=\mu_{fneq}=0$ and $E_f=0$, the stress expression in Eq (6.7) is reduced to an isotropic formulation as

$$\boldsymbol{\sigma}=\underbrace{\mu\mathbf{b}}_{mechanical}+\underbrace{\varepsilon_0\varepsilon_{rm}\mathbf{e}_m\otimes\mathbf{e}_m-\frac{\varepsilon_0\varepsilon_{rm}}{2}\mathbf{e}_m\cdot\mathbf{e}_m\mathbf{I}}_{Maxwell\ \text{stress tensor}}+p\mathbf{I}. \quad (6.9)$$

The mechanical stress formulation in Eq (6.7) can take other widely used models for soft polymers such as Mooney-Rivlin model, Yeoh's model, and Gent model etc. as follows,

$$\begin{aligned}\boldsymbol{\sigma}=&\underbrace{\underbrace{\mu\left(\mathbf{b}+\gamma\mathbf{b}^{-1}\right)}_{Moony-Rivlin}+2\mu_{feq}\left(I_4-1\right)\mathbf{v}\otimes\mathbf{v}+2\mu_{fneq}\left(\frac{I_4}{I_4^{\,v}}-1\right)\frac{1}{I_4^{\,v}}\mathbf{v}\otimes\mathbf{v}}_{mechanical}\\&+\underbrace{\varepsilon_0\varepsilon_{rf}\frac{E_f^{\,2}}{I_4}\frac{\mathbf{v}}{\sqrt{I_4}}\otimes\frac{\mathbf{v}}{\sqrt{I_4}}}_{electrical-fiber}+\underbrace{\varepsilon_0\varepsilon_{rm}\mathbf{e}_m\otimes\mathbf{e}_m-\frac{\varepsilon_0\varepsilon_{rm}}{2}\mathbf{e}_m\cdot\mathbf{e}_m\mathbf{I}}_{electrical-matrix}+p\mathbf{I},\end{aligned} \quad (6.10)$$

$$\boldsymbol{\sigma} = \underbrace{\underbrace{\sum_{i=1}^{n} i\mu_i \left(I_1 - 3\right)^{i-1}}_{\text{Yeoh's model}} \mathbf{b} + 2\mu_{feq}\left(I_4 - 1\right)\mathbf{v}\otimes\mathbf{v} + 2\mu_{fneq}\left(\frac{I_4}{I_4^{v}} - 1\right)\frac{1}{I_4^{v}}\mathbf{v}\otimes\mathbf{v}}_{mechanical}$$
$$+ \underbrace{\varepsilon_0\varepsilon_{rf}\frac{E_f^{\,2}}{I_4}\frac{\mathbf{v}}{\sqrt{I_4}}\otimes\frac{\mathbf{v}}{\sqrt{I_4}}}_{electrical-fiber} + \underbrace{\varepsilon_0\varepsilon_{rm}\mathbf{e}_m\otimes\mathbf{e}_m - \frac{\varepsilon_0\varepsilon_{rm}}{2}\mathbf{e}_m\cdot\mathbf{e}_m\mathbf{I}}_{electrical-matrix} + p\mathbf{I}, \tag{6.11}$$

$$\boldsymbol{\sigma} = \underbrace{\underbrace{\frac{\mu J_m}{J_m - I_1 + 3}}_{\text{Gent model}}\mathbf{b} + 2\mu_{feq}\left(I_4 - 1\right)\mathbf{v}\otimes\mathbf{v} + 2\mu_{fneq}\left(\frac{I_4}{I_4^{v}} - 1\right)\frac{1}{I_4^{v}}\mathbf{v}\otimes\mathbf{v}}_{mechanical}$$
$$+ \underbrace{\varepsilon_0\varepsilon_{rf}\frac{E_f^{\,2}}{I_4}\frac{\mathbf{v}}{\sqrt{I_4}}\otimes\frac{\mathbf{v}}{\sqrt{I_4}}}_{electrical-fiber} + \underbrace{\varepsilon_0\varepsilon_{rm}\mathbf{e}_m\otimes\mathbf{e}_m - \frac{\varepsilon_0\varepsilon_{rm}}{2}\mathbf{e}_m\cdot\mathbf{e}_m\mathbf{I}}_{electrical-matrix} + p\mathbf{I}, \tag{6.12}$$

where γ, n, J_m are models parameters.

The Cauchy stress equation is complemented with an evolution equation for viscoelastic materials. The evolution equation governs the internal variable I_4^v and needs to satisfy the Clausius-Duhem inequality derived from the second law of thermodynamics. Here, we employ the following linear form (Reese and Govindjee, 1998)

$$-\tau_{neq} = \eta \dot{I}_4^v, \tag{6.13}$$

with $\tau_{neq} = 4I_4^v\frac{\partial\Psi}{\partial I_4^v} = 4\mu_{fneq}\left(\frac{I_4}{I_4^v} - 1\right)\frac{I_4}{I_4^v}$. The model formulation is summarized in Table 10.

Table 10. Model formulations of dielectric elastomer composites.

Strain energy function:

$$\Psi = \underbrace{\frac{\mu}{2}\left(I_1-3\right)+\frac{\mu_{feq}}{2}\left(I_4-1\right)^2+\frac{\mu_{fneq}}{2}\left(\frac{I_4}{I_4^{v}}-1\right)^2}_{mechanical}\underbrace{-\frac{\varepsilon_0\varepsilon_{rf}}{2}I_{11}^{f}}_{electrical-fiber}\underbrace{-\frac{\varepsilon_0\varepsilon_{rm}}{2}I_{11}^{m}}_{electrical-matrix},$$

Cauchy stress:

$$\boldsymbol{\sigma} = \underbrace{\mu\mathbf{b}+2\mu_{feq}\left(I_4-1\right)\mathbf{v}\otimes\mathbf{v}+2\mu_{fneq}\left(\frac{I_4}{I_4^{v}}-1\right)\frac{1}{I_4^{v}}\mathbf{v}\otimes\mathbf{v}}_{mechanical}$$
$$+\underbrace{\varepsilon_0\varepsilon_{rf}\frac{E_f^{\,2}}{I_4}\frac{\mathbf{v}}{\sqrt{I_4}}\otimes\frac{\mathbf{v}}{\sqrt{I_4}}}_{electrical-fiber}+\underbrace{\varepsilon_0\varepsilon_{rm}\mathbf{e}_m\otimes\mathbf{e}_m-\frac{\varepsilon_0\varepsilon_{rm}}{2}\mathbf{e}_m\cdot\mathbf{e}_m\mathbf{I}}_{electrical-matrix}+p\mathbf{I}.$$

Evolution equation:

$$-\tau_{neq}=\eta\dot{I}_4^{v} \text{ with } \tau_{neq}=4\mu_{fneq}\left(\frac{I_4}{I_4^{v}}-1\right)\frac{I_4}{I_4^{v}}$$

6.4 Computational formulations for dielectric elastomer composites

The proposed constitutive model is implemented in a finite element framework through the user subroutine UMAT in ABAQUS. The Cauchy stress tensor (mechanical tensor and Maxwell stress tensor) is explicitly defined in the user subroutine. The internal variable in the evolution equation is defined through state variables in the UMAT and the evolution equation is solved by Euler forward difference in explicit form. It is noted that the evolution equation can also be solved by Euler backward difference in the implicit form and solved using Newton's method. The tangent modulus is provided in the user subroutine as well. Since the tangent modulus does not affect the accuracy of the solution but the rate of convergence when solving the residual equations, only the mechanical part of the strain energy function is used (or second Piola-Kirchhoff stress).

In the following, the formulation of the tangent modulus for the UMAT is derived. In ABAQUS, it is better to decompose the kinematic quantities, stress, and tangent modulus into isochoric and volumetric parts even for incompressible materials. The bulk modulus in the volumetric part is set to be a large value (normally $10^4 \sim 10^6$ times of the shear modulus) to simulate the almost incompressible condition. Therefore, we decompose the total tangent modulus into isochoric and volumetric parts as

$$\mathbb{C} = 2\frac{\partial \mathbf{S}}{\partial \mathbf{C}} = 2\frac{\partial^2 \Psi_{iso}}{\partial \mathbf{C}\partial \mathbf{C}} + 2\frac{\partial^2 \Psi_{vol}}{\partial \mathbf{C}\partial \mathbf{C}} = \mathbb{C}_{iso} + \mathbb{C}_{vol}, \tag{6.14}$$

where Ψ_{iso} and Ψ_{vol} are the isochoric and volumetric parts of the mechanical component of the total strain energy function, and $\mathbb{C}_{iso}$ and $\mathbb{C}_{vol}$ are the isochoric and volumetric parts of the tangent modulus in the material description. Since the strain energy function is in terms of the principal invariants, the fictitious tangent modulus in the material description is defined as (Holzapfel, 2000)

$$\begin{aligned}\bar{\mathbb{C}} &= 2J^{-4/3}\frac{\partial \bar{\mathbf{S}}}{\partial \bar{\mathbf{C}}} = 4J^{-4/3}\frac{\partial^2 \Psi_{iso}}{\partial \bar{\mathbf{C}}\partial \bar{\mathbf{C}}} \\ &= J^{-4/3}\left(\bar{\delta}_1 \mathbf{I}\otimes\mathbf{I} + \bar{\delta}_5\left(\mathbf{I}\otimes\mathbf{V}\otimes\mathbf{V} + \mathbf{V}\otimes\mathbf{V}\otimes\mathbf{I}\right) + \bar{\delta}_7 \mathbf{V}\otimes\mathbf{V}\otimes\mathbf{V}\otimes\mathbf{V}\right), \\ &= J^{-4/3}\left(\bar{\delta}_1 \mathbf{I}\otimes\mathbf{I} + \bar{\delta}_5\left(\mathbf{I}\otimes\mathbf{M} + \mathbf{M}\otimes\mathbf{I}\right) + \bar{\delta}_7 \mathbf{M}\otimes\mathbf{M}\right)\end{aligned} \tag{6.15}$$

where $\delta_1 = 4\left(\frac{\partial^2 \Psi_{iso}}{\partial \bar{I}_1 \partial \bar{I}_1}\right)$, $\delta_5 = 4\left(\frac{\partial^2 \Psi_{iso}}{\partial \bar{I}_1 \partial \bar{I}_4}\right)$, $\delta_7 = 4\frac{\partial^2 \Psi_{iso}}{\partial \bar{I}_4 \partial \bar{I}_4}$, $\mathbf{M} = \mathbf{V}\otimes\mathbf{V}$, and the isochoric part of the mechanical component of the strain energy function is

$$\Psi_{iso} = \frac{\mu}{2}\left(\bar{I}_1 - 3\right) + \frac{\mu_{feq}}{2}\left(\bar{I}_4 - 1\right)^2 + \frac{\mu_{fneq}}{2}\left(\frac{\bar{I}_4}{I_4^{\,v}} - 1\right). \tag{6.16}$$

The isochoric part of the tangent modulus in the material description is

$$
\begin{aligned}
\mathbb{C}_{iso} &= \mathbb{P} : \bar{\mathbb{C}} : \mathbb{P}^T - \frac{2}{3}\left(\mathbf{S}_{iso} \otimes \mathbf{C}^{-1} + \mathbf{C}^{-1} \otimes \mathbf{S}_{iso}\right) - \frac{2}{3} J^{-2/3} tr\left(\bar{\mathbf{S}}\right) \tilde{\mathbb{P}} \\
&= \bar{\mathbb{C}} - \frac{1}{3}\mathbf{C}^{-1} \otimes \mathbf{C} : \bar{\mathbb{C}} - \frac{1}{3}\bar{\mathbb{C}} : \mathbf{C} \otimes \mathbf{C}^{-1} + \frac{1}{9}\mathbf{C}^{-1} \otimes \mathbf{C} : \bar{\mathbb{C}} : \mathbf{C} \otimes \mathbf{C}^{-1} \\
&\quad - \frac{2}{3}\left(\mathbf{S}_{iso} \otimes \mathbf{C}^{-1} + \mathbf{C}^{-1} \otimes \mathbf{S}_{iso}\right) - \frac{2}{3} J^{-2/3} tr\left(\bar{\mathbf{S}}\right) \tilde{\mathbb{P}}.
\end{aligned}
\tag{6.17}
$$

Plugging Eq (6.15) in the double contractions in Eq (6.17) and applying the general relation

$$
\left(\mathbf{A} \otimes \mathbf{B}\right) : \left(\mathbf{C} \otimes \mathbf{D}\right) = \left(\mathbf{B} : \mathbf{C}\right)\left(\mathbf{A} \otimes \mathbf{D}\right) = tr\left(\mathbf{BC}\right)\left(\mathbf{A} \otimes \mathbf{D}\right), \tag{6.18}
$$

we have

$$
\begin{aligned}
\mathbb{C}_{iso} &= \bar{\mathbb{C}} - \frac{J^{-4/3}}{3}\left(\bar{\delta}_1 tr\left(\mathbf{C}\right)\left(\mathbf{C}^{-1} \otimes \mathbf{I}\right) + \bar{\delta}_5\left(tr\left(\mathbf{C}\right)\left(\mathbf{C}^{-1} \otimes \mathbf{M}\right) + \left(\mathbf{C} : \mathbf{M}\right)\left(\mathbf{C}^{-1} \otimes \mathbf{I}\right)\right) + \bar{\delta}_7\left(\mathbf{C} : \mathbf{M}\right)\left(\mathbf{C}^{-1} \otimes \mathbf{M}\right)\right) \\
&\quad - \frac{J^{-4/3}}{3}\left(\bar{\delta}_1 tr\left(\mathbf{C}\right)\left(\mathbf{I} \otimes \mathbf{C}^{-1}\right) + \bar{\delta}_5\left(tr\left(\mathbf{C}\right)\left(\mathbf{M} \otimes \mathbf{C}^{-1}\right) + \left(\mathbf{C} : \mathbf{M}\right)\left(\mathbf{I} \otimes \mathbf{C}^{-1}\right)\right) + \bar{\delta}_7\left(\mathbf{C} : \mathbf{M}\right)\left(\mathbf{M} \otimes \mathbf{C}^{-1}\right)\right) \\
&\quad + \frac{J^{-4/3}}{9}\left(\bar{\delta}_1 tr\left(\mathbf{C}\right) tr\left(\mathbf{C}\right)\left(\mathbf{C}^{-1} \otimes \mathbf{C}^{-1}\right) + 2\bar{\delta}_5 tr\left(\mathbf{C}\right)\left(\mathbf{C} : \mathbf{M}\right)\left(\mathbf{C}^{-1} \otimes \mathbf{C}^{-1}\right) + \bar{\delta}_7\left(\mathbf{C} : \mathbf{M}\right)^2\left(\mathbf{C}^{-1} \otimes \mathbf{C}^{-1}\right)\right) \\
&\quad - \frac{2}{3}\left(\mathbf{S}_{iso} \otimes \mathbf{C}^{-1} + \mathbf{C}^{-1} \otimes \mathbf{S}_{iso}\right) - \frac{2}{3} J^{-2/3} tr\left(\bar{\mathbf{S}}\right) \tilde{\mathbb{P}}.
\end{aligned}
\tag{6.19}
$$

Further reduction is taken by using $tr\left(\mathbf{C}\right) = I_1$ and $\mathbf{C} : \mathbf{M} = I_4$ to get the isochoric part of the tangent modulus as

$$
\begin{aligned}
\mathbb{C}_{iso} &= \bar{\mathbb{C}} - \frac{J^{-4/3}}{3}\left(\left(\bar{\delta}_1 I_1 + \bar{\delta}_5 I_4\right)\left(\mathbf{C}^{-1} \otimes \mathbf{I}\right) + \left(\bar{\delta}_5 I_1 + \bar{\delta}_7 I_4\right)\left(\mathbf{C}^{-1} \otimes \mathbf{M}\right)\right) \\
&\quad - \frac{J^{-4/3}}{3}\left(\left(\bar{\delta}_1 I_1 + \bar{\delta}_5 I_4\right)\left(\mathbf{I} \otimes \mathbf{C}^{-1}\right) + \left(\bar{\delta}_5 I_1 + \bar{\delta}_7 I_4\right)\left(\mathbf{M} \otimes \mathbf{C}^{-1}\right)\right) \\
&\quad + \frac{J^{-4/3}}{9}\left(\bar{\delta}_1 {I_1}^2 + 2\bar{\delta}_5 I_1 I_4 + \bar{\delta}_7 {I_4}^2\right)\left(\mathbf{C}^{-1} \otimes \mathbf{C}^{-1}\right) \\
&\quad - \frac{2}{3}\left(\mathbf{S}_{iso} \otimes \mathbf{C}^{-1} + \mathbf{C}^{-1} \otimes \mathbf{S}_{iso}\right) - \frac{2}{3} J^{-2/3} tr\left(\bar{\mathbf{S}}\right) \tilde{\mathbb{P}}.
\end{aligned}
\tag{6.20}
$$

The isochoric part of the tangent modulus in the spatial description is then obtained by operating the push-forward on the isochoric part of the tangent modulus in the material description in Eq (6.20) as

$$
\begin{aligned}
\mathbb{C}_{iso} &= \frac{1}{J}\left(\bar{\delta}_1 \bar{\mathbf{b}} \otimes \bar{\mathbf{b}} + \bar{\delta}_5 \left(\bar{\mathbf{b}} \otimes \mathbf{m} + \mathbf{m} \otimes \bar{\mathbf{b}}\right) + \bar{\delta}_7 \mathbf{m} \otimes \mathbf{m}\right) \\
&- \frac{1}{3J}\left(\left(\bar{\delta}_1 I_1 + \bar{\delta}_5 I_4\right)\left(\mathbf{I} \otimes \bar{\mathbf{b}}\right) + \left(\bar{\delta}_5 I_1 + \bar{\delta}_7 I_4\right)\left(\mathbf{I} \otimes \mathbf{m}\right)\right) \\
&- \frac{1}{3J}\left(\left(\bar{\delta}_1 I_1 + \bar{\delta}_5 I_4\right)\left(\bar{\mathbf{b}} \otimes \mathbf{I}\right) + \left(\bar{\delta}_5 I_1 + \bar{\delta}_7 I_4\right)\left(\mathbf{m} \otimes \mathbf{I}\right)\right) \\
&+ \frac{1}{9J}\left(\bar{\delta}_1 I_1^{\,2} + 2\bar{\delta}_5 I_1 I_4 + \bar{\delta}_7 I_4^{\,2}\right)\left(\mathbf{I} \otimes \mathbf{I}\right) \\
&- \frac{2}{3J}\left(\boldsymbol{\tau}_{iso} \otimes \mathbf{I} + \mathbf{I} \otimes \boldsymbol{\tau}_{iso}\right) - \frac{2}{3J} J^{-2/3} tr\left(\bar{\boldsymbol{\tau}}\right)\left(\mathbb{I}^{sym} - \frac{1}{3}\mathbf{I} \otimes \mathbf{I}\right).
\end{aligned}
\tag{6.21}
$$

The volumetric part of the mechanical component of the strain energy function takes the general form as

$$
\Psi_{vol} = K\gamma^{-2}\left(\gamma LnJ + J^{-\gamma} - 1\right), \tag{6.22}
$$

and in the current work, we use $\gamma = -1$ in Eq (6.22). Recall from Chapter 3, the volumetric part of the tangent modulus in the spatial description is

$$
\mathbb{C}_{vol} = J\left(p + J\frac{\partial p}{\partial J}\right)\mathbf{I} \otimes \mathbf{I} - 2Jp\mathbb{I}^{sym}, \tag{6.23}
$$

where $p = \dfrac{d\Psi_{vol}}{dJ} = \dfrac{1}{J}K\left(J - 1\right)$. Finally, the total tangent modulus in the spatial description is the sum of the isochoric and volumetric tangent modulus in Eq (6.21) and (6.23)

$$
\mathbb{C} = \mathbb{C}_{iso} + \mathbb{C}_{vol}\,. \tag{6.24}
$$

Together with Eq (6.21) and (6.23), the tangent modulus (in ABAQUS) in the spatial description is thus

$$
\mathbb{C}^{ABAQUS}{}_{ijkl} = \mathbb{C}_{ijkl} + \frac{1}{2}\left(\delta_{ik}\sigma_{jl} + \delta_{il}\sigma_{jk} + \delta_{jk}\sigma_{il} + \delta_{jl}\sigma_{ik}\right). \tag{6.25}
$$

6.5 Model parameters exploration and verification of FEM formulation

The model formulation is in a general form and suitable for soft rubber-like materials. It is instructive to study the responses (stress strain relationships) under simple conditions before the model and computational formulation are applied to solve complex boundary value problems. The FEM formulation is verified by comparing with analytical solutions. In this section, a range of parameters is studied for uniaxial, biaxial, and simple shear tests in a rectangular coordinate system.

6.5.1 Model parameters exploration

For uniaxial loading, the deformation gradient is $\mathbf{F} = diag\left[\begin{array}{ccc} \lambda & \lambda^{-1/2} & \lambda^{-1/2} \end{array}\right]$, and the fiber is assumed to be in the x-direction denoted by the unit vector $\mathbf{V} = \left[\begin{array}{ccc} 1 & 0 & 0 \end{array}\right]^T$. The electric field in the fibers is thus $\mathbf{E} = \left[\begin{array}{ccc} E_1 & 0 & 0 \end{array}\right]^T$. The left Cauchy Green tensor is $\mathbf{b} = diag\left[\begin{array}{ccc} \lambda^2 & \lambda^{-1} & \lambda^{-1} \end{array}\right]$ and the fiber vector in the current configuration is $\mathbf{v} = \mathbf{FV} = \left[\begin{array}{ccc} \lambda & 0 & 0 \end{array}\right]^T$. The stress expression in the x-direction is obtained by applying Eq (6.7) and using $\sigma_{22} = \sigma_{33} = 0$ as

$$\sigma_{11} = \mu\left(\lambda^2 - \frac{1}{\lambda}\right) + 2\mu_{feq}\left(\lambda^2 - 1\right)\lambda^2 + 2\mu_{fneq}\left(\frac{\lambda^2}{I_4^{\,v}} - 1\right)\frac{\lambda^2}{I_4^{\,v}} + \varepsilon_0\varepsilon_{rf}\frac{E^2}{\lambda^2} \ . \tag{6.26}$$

The nondimensional (denoted by an overbar) stress is obtained by dividing by the matrix shear modulus as

$$\bar{\sigma} = \left(\lambda^2 - \frac{1}{\lambda}\right) + 2\bar{\mu}_{feq}\left(\lambda^2 - 1\right)\lambda^2 + 2\bar{\mu}_{fneq}\left(\frac{\lambda^2}{I_4^{\,v}} - 1\right)\frac{\lambda^2}{I_4^{\,v}} + \frac{\bar{E}^2}{\lambda^2}, \tag{6.27}$$

where the relationship between the dimensional and nondimensional variables are $\bar{\sigma}_{11} = \frac{\sigma_{11}}{\mu}$, $\bar{\mu}_{feq} = \frac{\mu_{feq}}{\mu}$, $\bar{\mu}_{fneq} = \frac{\mu_{fneq}}{\mu}$, and $\bar{E} = \left(\frac{\varepsilon_0 \varepsilon_{rf}}{\mu} \right)^{1/2} E$ (Goulbourne et al., 2005). It is noted that when $\bar{\mu}_{fneq} = 0$, i.e. $\mu_{fneq} = 0$, the material is isotropic and the stress is recovered to the Neohooken mechanical term and the typical DE Maxwell stress term (also refers to Eq (6.9)). The nondimensional evolution equation is obtained by dividing by the nonequliubrium fiber shear modulus μ_{fneq} (which yields the characteristic relaxation time) as

$$\left(\frac{\lambda^2}{I_4^v} - 1 \right) \frac{\lambda^2}{I_4^v} = \bar{\eta} \dot{I}_4^v \ , \tag{6.28}$$

where $\bar{\eta} = \frac{\eta}{4\mu_{fneq}}$ is the characteristic relaxation time.

First, we set $\bar{E} = 0$ and focus on the mechanical stress stretch relationships for a range of fiber moduli values $\bar{\mu}_{feq}$. Figure 35 shows the stress stretch curves for quasi-static loading ($\dot{\lambda} = 0.001/s$) and shows a significant increase in overall stress as fiber stiffness is increased.

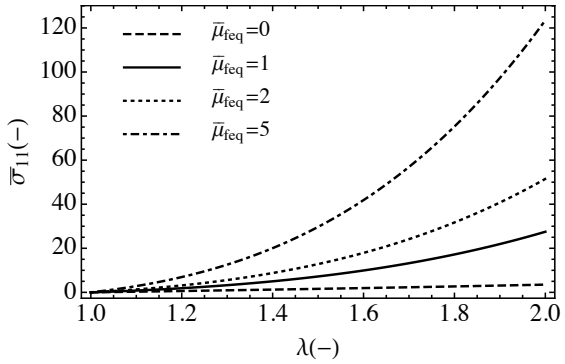

Figure 35. Stress stretch relationships for various $\bar{\mu}_{feq}$ values (fiber and matrix modulus ratios).

Next, we consider various loading/unloading rates ($\bar{E}=0$, $\lambda=2$ in the x-direction). Figure 36 shows the stress stretch behavior for a range of viscous parameters $\bar{\eta}$ at various stretch rates. It shows that for the same $\bar{\eta}\cdot\dot{\lambda}$ the stress stretch curves are the same. Overall, comparing with the different $\bar{\eta}\cdot\dot{\lambda}$ in four groups in Figure 36 (a~d), it larger stresses result from faster loadings, which is to be expected for the linear viscous model employed here.

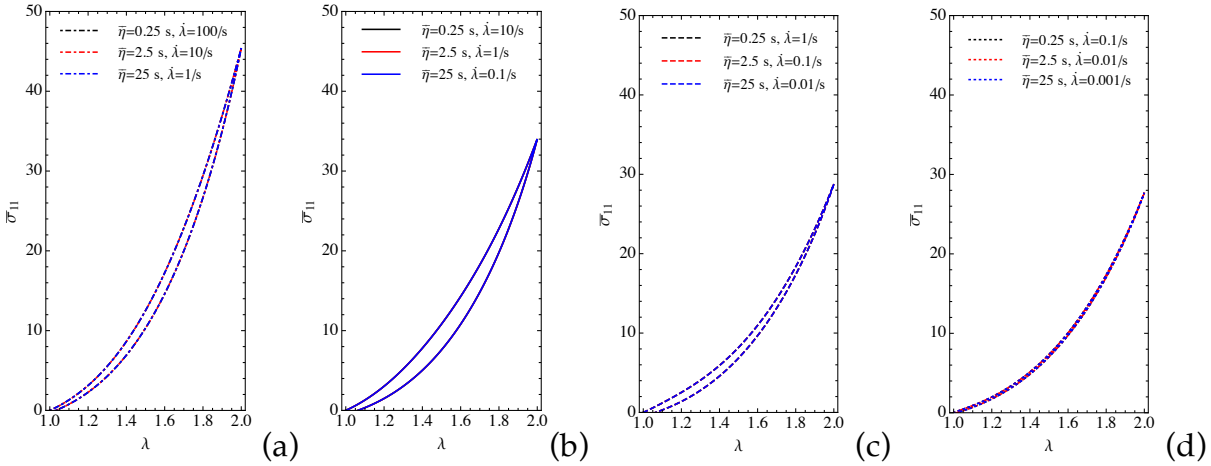

Figure 36. Stress stretch curves for various loading and unloading rates.

For a nonzero electric field ($E=$ 12 MV/m), we calculate the active and passive stress under uniaxial isometric conditions for a composite with fibers oriented in x-direction, 30° with x-direction, 45° with x-direction, 60° with x-direction, and 90° with x-direction (y-direction) (see Figure 37). Overall for various fiber orientations, i) smaller than stretch 1.05, the active stresses dominate; ii) around stretch 1.1, the active stresses and the passive stresses are on the same order; and iii) larger than stretch 1.1, the passive stresses increased significantly. With the increment of fiber angles with respect to x-direction, the stresses (active and passive stresses) in the x-direction decrease and for the fiber oriented in the y-direction (Figure 37 (e)) the active stress in the x-direction is zero.

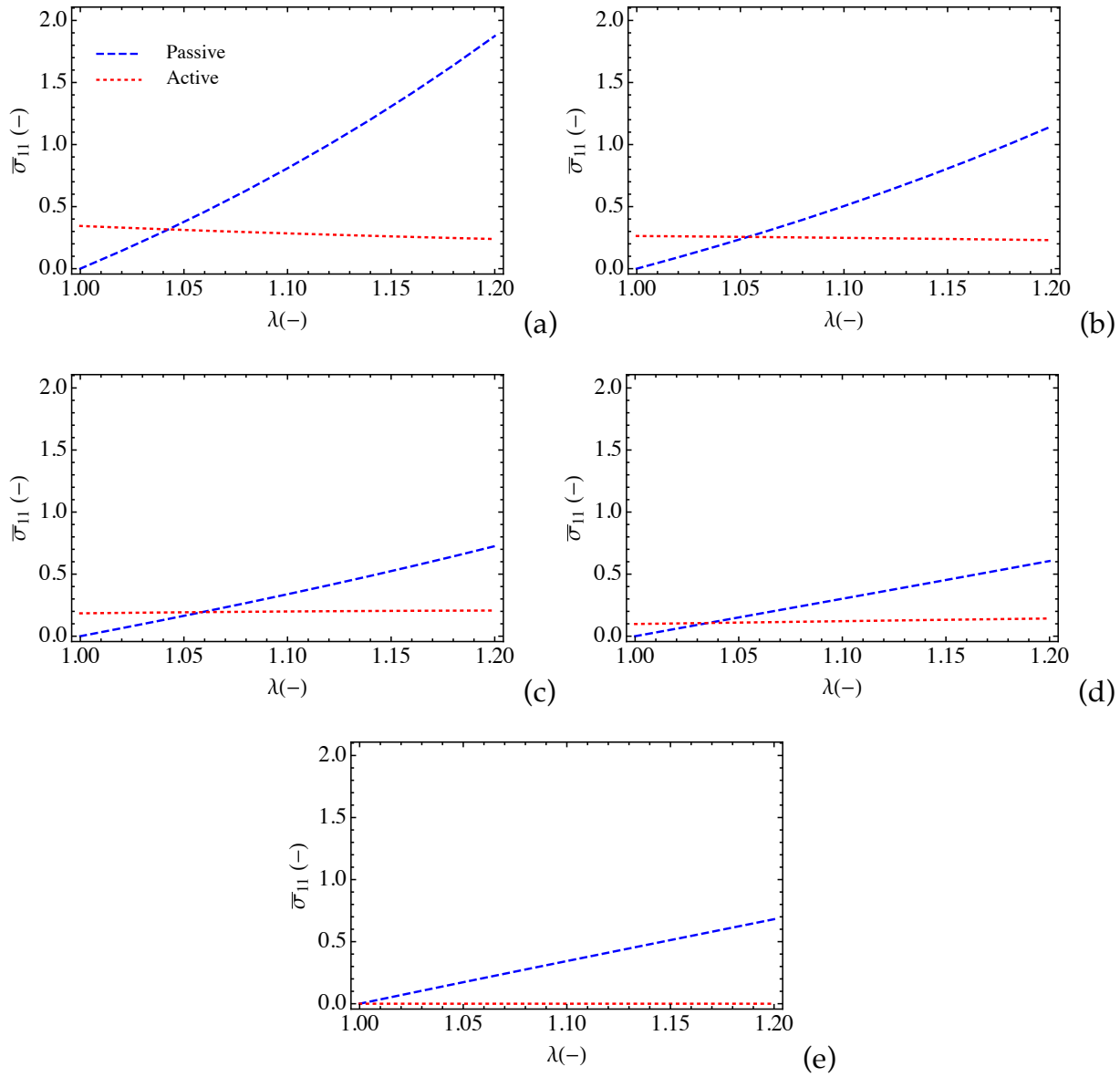

Figure 37. Active and passive stresses in x-direction for (a) fiber in x-direction, (b) fiber oriented in 30° with respect to x-direction, (c) fiber oriented in 45° with respect to x-direction, (d) fiber oriented in 60° with respect to x-direction, (e) fiber in y-direction.

For equibiaxial conditions, the fiber is also assumed to be in the x-direction with and the electric field is applied in the fiber direction. The deformation gradient is $\mathbf{F} = diag\left[\begin{array}{ccc} \lambda & \lambda & \lambda^{-2} \end{array}\right]$. The left Cauchy Green tensor is $\mathbf{b} = diag\left[\begin{array}{ccc} \lambda^2 & \lambda^2 & \lambda^{-4} \end{array}\right]$ and the

fiber vector in the current configuration is $\mathbf{v} = \mathbf{FV} = \begin{bmatrix} \lambda & 0 & 0 \end{bmatrix}^T$. The stress in the x- and y-directions are obtained using Eq (6.7) and the condition $\sigma_{33} = 0$

$$\bar{\sigma}_{11} = \left(\lambda^2 - \frac{1}{\lambda^4}\right) + 2\bar{\mu}_{feq}\left(\lambda^2 - 1\right)\lambda^2 + 2\bar{\mu}_{fneq}\left(\frac{\lambda^2}{I_4^v} - 1\right)\frac{\lambda^2}{I_4^v} + \frac{\bar{E}^2}{\lambda^2}\ , \tag{6.29}$$

$$\bar{\sigma}_{22} = \left(\lambda^2 - \frac{1}{\lambda^4}\right)\ . \tag{6.30}$$

Figure 38 shows the stress stretch relationships for various modulus ratios $\bar{\mu}_{feq}$ ($\bar{E} = 0$). The stress ratio indicates the degree of material anisotropy.

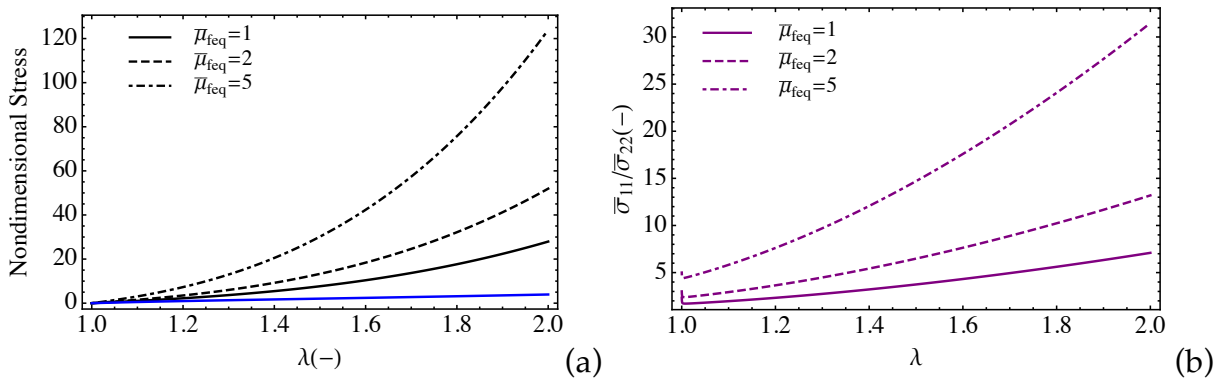

Figure 38. Nondimensional stress stretch relationships for various nondimensional $\bar{\mu}_{feq}$ (Black curves are for $\bar{\sigma}_{11}$ and blue ones are for $\bar{\sigma}_{22}$).

For a nonzero electric field in the fiber direction ($E = 12$ MV/m), we calculate the active and passive stress under equibiaxial isometric conditions for fibers oriented in the x-direction, at 30°, and at 45° (Figure 39).

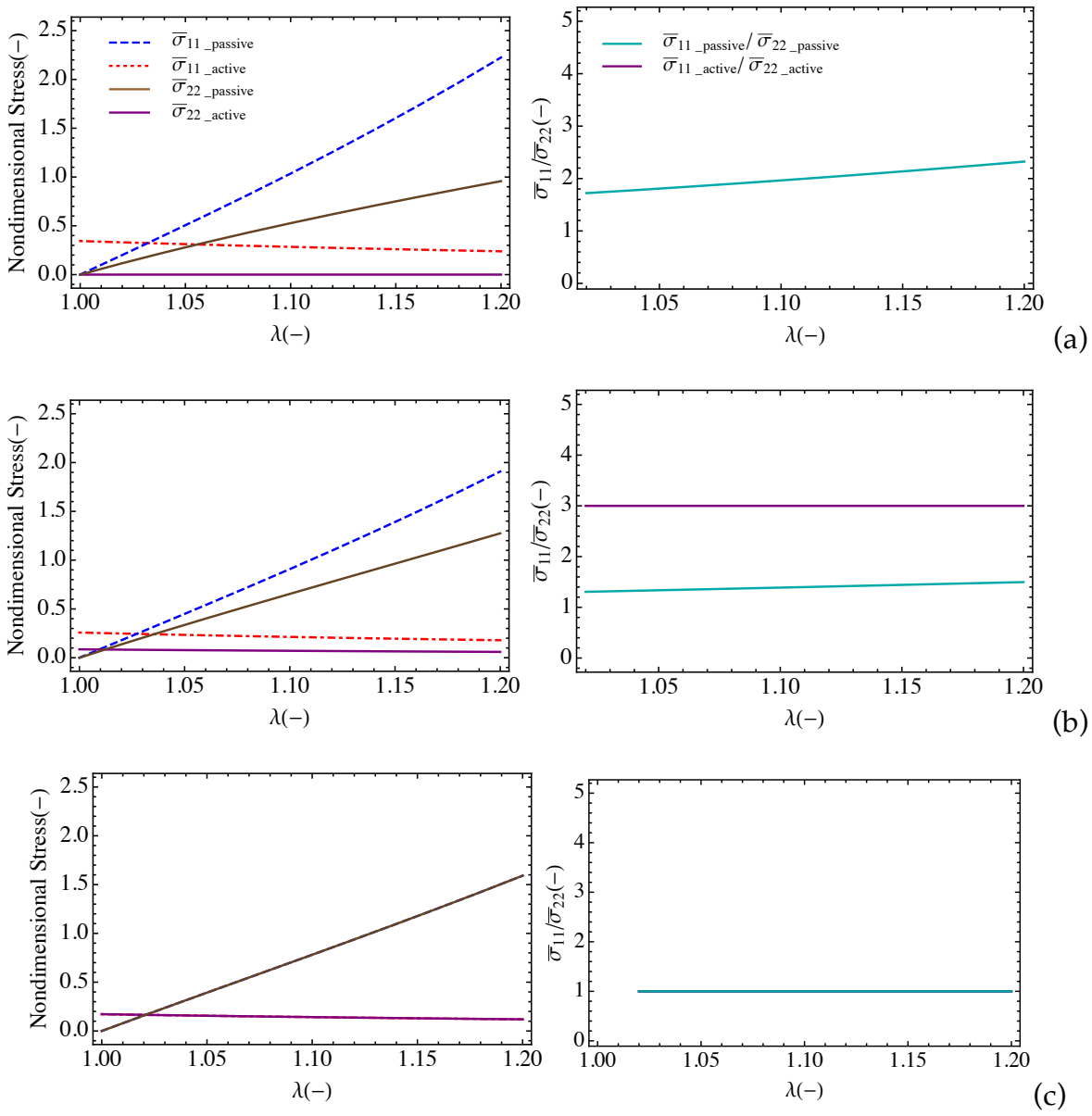

Figure 39. Nondimensional active and passive stresses in x- and y-directions for (a) fiber in x-direction, (b) fiber oriented in 30° with respect to x-direction, (c) fiber oriented in 45° with respect to x-direction.

6.5.2 Verification of FEM formulation

In the following, the finite element formulation is verified by comparing with analytical solutions for uniaxial, biaxial, and simple shear tests. A set of starting numerical values for model parameters in Table 11 is chosen to generate simulation

results. Fibers are oriented in the x direction for the uniaxial, biaxial, and the first simple shear tests, i.e. $\mathbf{V} = \begin{bmatrix} 1 & 0 & 0 \end{bmatrix}^T$; and oriented in the y direction for the second simple shear test, i.e. $\mathbf{V} = \begin{bmatrix} 0 & 1 & 0 \end{bmatrix}^T$. Analytical solutions are derived from Eq (6.7) with a zero electric field and a constant electric field magnitude of 12 MV/m in fibers and deformation gradients $\mathbf{F} = diag\begin{bmatrix} \lambda & \lambda^{-1/2} & \lambda^{-1/2} \end{bmatrix}$, $\mathbf{F} = diag\begin{bmatrix} \lambda & \lambda & \lambda^{-2} \end{bmatrix}$, and $\mathbf{F} = \mathbf{I} + \gamma \mathbf{e}_1 \otimes \mathbf{e}_2$ for uniaxial, equibiaxial, and simple shear tests, respectively. For quasi-static loading, the stretch rate is very slow ($\dot{\lambda} = 0.001/s$).

Table 11. Numerical values of material parameters.

Parameters	μ (kPa)	$\bar{\mu}_{feq}$ (-)	$\bar{\mu}_{fneq}$ (-)	$\bar{\eta}$ (s)	ε_0 (F/m)	ε_{mr} (-)	$\varepsilon_{fr}/\varepsilon_{mr}$ (-)
Values	10	1	1	0.25	8.85E-12	4.7	2.7/4.7

In the finite element framework, we consider a DE composite unit cube ($1m \times 1m \times 1m$) subjected to uniaxial, equibixial, and simple shear tests (Figure 40 (left column)). The model is meshed using one element to eliminate error from element interaction. The analytical stress-stretch curves for the three typical tests for zero electric field and 12 MV/m electric field in fibers are presented in Figure 40 (middle and right column) overlaying with ABAQUS results. It shows that the computational results and the analytical results agree perfectly and verifies the computational formulations.

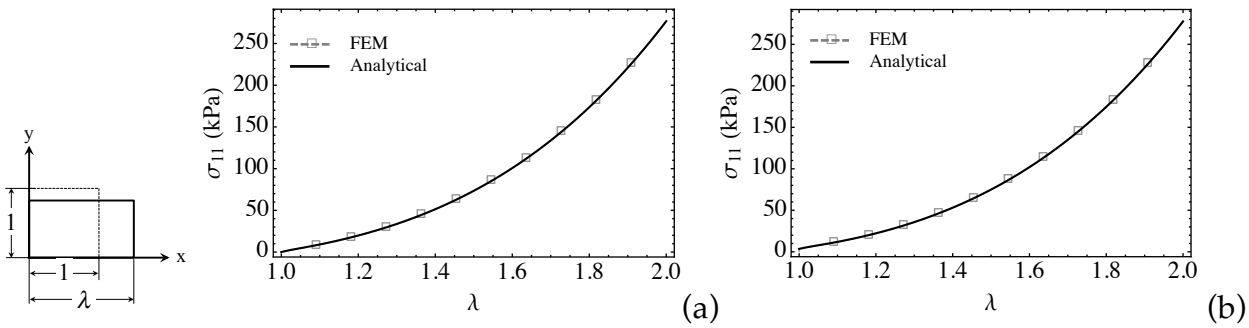

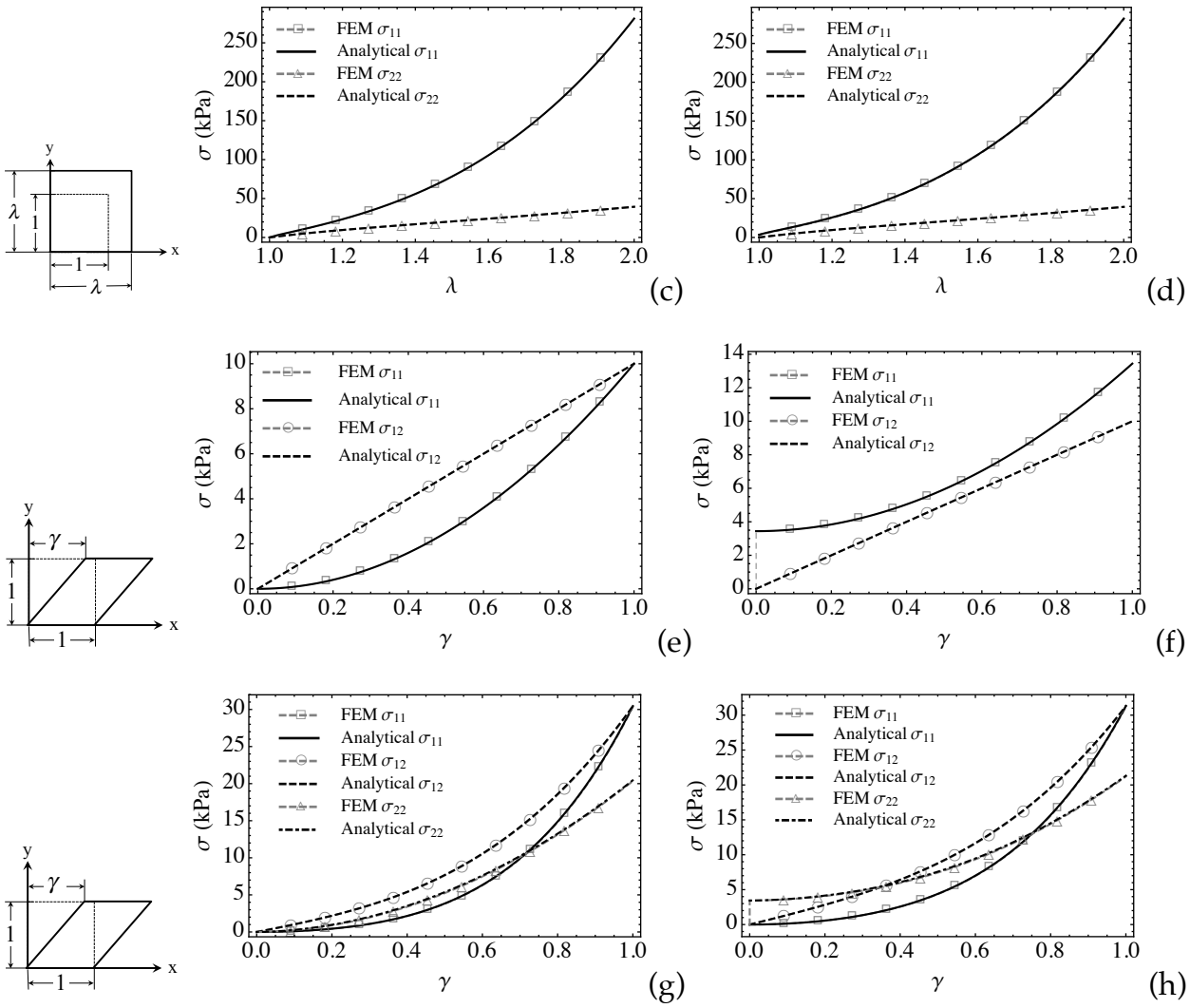

Figure 40. The analytical solutions for the relationship of stress and stretch for uniaxial test (a-b) with fibers in x-direction, equibiaxial test (c-d) with fibers in x-direction, and simple shear tests (e-h) with (e-f) having fibers in x-direction and (g-h) having fibers in y-direction (middle column for zero electric field and the right column for electric field 12 MV/m).

6.6 Summary

A new soft electroactive polymer composite consisting of contractile dielectric elastomer fibers is proposed in the current work. Numerical based design tools are investigated, which includes a new constitutive model for the DE composite and a computational tool by implementing the proposed model into a FEM framework. The stress-stretch

relationships are examined for a wide range of parameter numerical values. The computational formulations are verified by comparing with analytical uniaxial, biaxial, and simple shear stress stretch curves. One of the advantages of computational simulations is that they handle more complex boundary and loading conditions easily. One potential application is surface morphing, i.e. changing height, slope, and curvature through multiaxial activation and spatial activations. Furthermore, dual-mode activation through the activation of matrix and fibers render a larger range of tailorable configurations and hence performance. In the next chapter, we explore a series of preliminary 3D simulations to illustrate the broad design space generated by these novel composites.

References

Ask, A., Menzel, A., Ristinmaa, M., 2012. Phenomenological modeling of viscous electrostrictive polymers. International Journal of Non-Linear Mechanics 47, 156-165, doi:10.1016/j.ijnonlinmec.2011.03.020.

Ask, A., Menzel, A., Ristinmaa, M., 2015. Modelling of Viscoelastic Dielectric Elastomers with Deformation Dependent Electric Properties. Procedia IUTAM 12, 134-144, doi:10.1016/j.piutam.2014.12.015.

Bortot, E., Denzer, R., Menzel, A., Gei, M., 2016. Analysis of viscoelastic soft dielectric elastomer generators operating in an electrical circuit. International Journal of Solids and Structures 78–79, 205-215, doi:10.1016/j.ijsolstr.2015.06.004.

Dorfmann, A., Ogden, R. W., 2006. Nonlinear Electroelastic Deformations. Journal of Elasticity 82, 99-127, doi:10.1007/s10659-005-9028-y.

Goulbourne, N., Mockensturm, E., Frecker, M., 2005. A Nonlinear Model for Dielectric Elastomer Membranes. Journal of Applied Mechanics 72, 899-906, doi:10.1115/1.2047597.

He, L., Lou, J., Du, J., 2017a. Analytical Solutions for Inextensible Fiber-Reinforced Dielectric Elastomer Torsional Actuators. Journal of Applied Mechanics 84, 051003-051003-11, doi:10.1115/1.4036193.

He, L., Lou, J., Du, J., Wu, H., 2017b. Voltage-induced torsion of a fiber-reinforced tubular dielectric elastomer actuator. Composites Science and Technology 140, 106-115, doi:10.1016/j.compscitech.2016.12.032.

Henann, D. L., Chester, S. A., Bertoldi, K., 2013. Modeling of dielectric elastomers: Design of actuators and energy harvesting devices. Journal of the Mechanics and Physics of Solids 61, 2047-2066, doi:10.1016/j.jmps.2013.05.003.

Holzapfel, G. A., 2000. Nonlinear Solid Mechanics: A Continuum Approach for Engineering. Wiley, Chichester ; New York.

Hong, W., 2011. Modeling viscoelastic dielectrics. Journal of the Mechanics and Physics of Solids 59, 637-650, doi:10.1016/j.jmps.2010.12.003.
Huang, J., Lu, T., Zhu, J., Clarke, D. R., Suo, Z., 2012. Large, uni-directional actuation in dielectric elastomers achieved by fiber stiffening. Applied Physics Letters 100, 211901, doi:10.1063/1.4720181.
Lee, K., Tawfick, S., 2016. Fiber micro-architected Electro–Elasto-Kinematic muscles. Extreme Mechanics Letters 8, 64-69, doi:10.1016/j.eml.2016.03.003.
Lu, T., Shi, Z., Shi, Q., Wang, T. J., 2016. Bioinspired bicipital muscle with fiber-constrained dielectric elastomer actuator. Extreme Mechanics Letters 6, 75-81, doi:10.1016/j.eml.2015.12.008.
Lu, T., Huang, J., Jordi, C., Kovacs, G., Huang, R., Clarke, D. R., Suo, Z., 2012. Dielectric elastomer actuators under equal-biaxial forces, uniaxial forces, and uniaxial constraint of stiff fibers. Soft Matter 8, 6167-6173, doi:10.1039/C2SM25692D.
Reese, S., Govindjee, S., 1998. A theory of finite viscoelasticity and numerical aspects. International Journal of Solids and Structures 35, 3455-3482, doi:10.1016/S0020-7683(97)00217-5.
S. Park, H., D. Nguyen, T., 2013. Viscoelastic effects on electromechanical instabilities in dielectric elastomers. Soft Matter 9, 1031-1042, doi:10.1039/C2SM27375F.
Shian, S., Bertoldi, K., Clarke, D. R., 2015a. Dielectric Elastomer Based "Grippers" for Soft Robotics. Advanced Materials 27, 6814-6819, doi:10.1002/adma.201503078.
Shian, S., Bertoldi, K., Clarke, D. R., 2015b. Use of aligned fibers to enhance the performance of dielectric elastomer inchworm robots. Vol. 9430, pp. 94301P-94301P-9.
Son, S., 2011. Nonlinear Electromechanical Deformation of Isotropic and Anisotropic Electro-Elastic Materials.
Subramani, K. B., Cakmak, E., Spontak, R. J., Ghosh, T. K., 2014. Enhanced Electroactive Response of Unidirectional Elastomeric Composites with High-Dielectric-Constant Fibers. Advanced Materials 26, 2949-2953, doi:10.1002/adma.201305821.
Suo, Z., 2010. Theory of dielectric elastomers. Acta Mechanica Solida Sinica 23, 549-578, doi:10.1016/S0894-9166(11)60004-9.
Thylander, S., Menzel, A., Ristinmaa, M., 2017. A non-affine electro-viscoelastic microsphere model for dielectric elastomers: Application to VHB 4910 based actuators. Journal of Intelligent Material Systems and Structures 28, 627-639, doi:10.1177/1045389X16651157.
Wang, H., Lei, M., Cai, S., 2013. Viscoelastic deformation of a dielectric elastomer membrane subject to electromechanical loads. Journal of Applied Physics 113, 213508, doi:10.1063/1.4807911.
Wang, S., Decker, M., Henann, D. L., Chester, S. A., 2016. Modeling of dielectric viscoelastomers with application to electromechanical instabilities. Journal of the Mechanics and Physics of Solids 95, 213-229, doi:10.1016/j.jmps.2016.05.033.
Zhang, J., Chen, H., Tang, L., Li, B., Sheng, J., Liu, L., 2015. Modelling of spring roll actuators based on viscoelastic dielectric elastomers. Applied Physics A 119, 825-835, doi:10.1007/s00339-015-9034-2.

Chapter 7. Computational simulations of contractile dielectric elastomer composites

7.1 Introduction

In this chapter, we present a range of computational simulations to illustrate novel actuation modes of the proposed dielectric elastomer composite. Activation through the matrix and fibers render a larger range of tailorable configurations and hence performance than previously achievable by their isotropic counterparts. The concepts of multiaxial activation and spatially distributed actuation are presented. These activation mechanisms yield a composite membrane with tailorable compliance that can realize multiple and distinct 3D shapes. We also carried out a series of simulations involving electro-hydrostatic actuation of 3D geometries to illustrate the broad design space for potential applications that is generated by these novel composites. The outline of the chapter is as follows: in section 7.2, we explore dual activation through matrix activation, fiber activation, and combined matrix-fiber activation. In section 7.3, distributed activation via spatially activating fibers in a pressure-loaded circular membrane configuration is demonstrated. The role of fiber orientation in influencing membrane shape is highlighted. Finally, we utilize our computational tool to design DEC structures configured for electro-hydrostatic coupling. Electro-hydrostatic actuation combines hydrostatic pressure loading with electric field activation of the

membrane. A fluid-filled spherical ball, inflatable ring, and flat membrane are analyzed in section 7.4. A summary is provided in section 7.5.

7.2 Multiaxial activation of DECs

Consider a circular DEC membrane that is pinned around its circumference and subjected to a bias inflation pressure (100 Pa is applied to the bottom surface). The diameter is 20 mm and the thickness is 0.5 mm. The material parameters are taken from Chapter 6 and shown in Table 12. Consider a rectangular coordinate system whereby the contractile dielectric elastomer fibers are oriented in the y-direction, i.e. $\mathbf{V}=\begin{bmatrix} 0 & 1 & 0 \end{bmatrix}^T$ (see Figure 41). The circular membrane is meshed into 40460 hybrid 8-node brick elements with three elements through the thickness (sufficient per mesh convergence studies). We calculate the response for two types of activation: i) fiber activation, with electric field in fibers assumed to be $\mathbf{E}=\begin{bmatrix} 0 & 12 & 0 \end{bmatrix}^T \mathrm{MV/m}$ and ii) matrix activation, with electric field in matrix assumed to be $\mathbf{E}=\begin{bmatrix} 0 & 0 & 9 \end{bmatrix}^T \mathrm{MV/m}$, i.e. applied voltage 4500 V, as compared to the passive case (see Figure 42).

Figure 43 shows the deformation fields for the passive, active matrix, and active fiber cases. Overall, comparing with the passive case, the matrix activation increases the out of plane deflection of the thin membrane while fiber activation reduces the out of plane deflection of the thin membrane – this is dual mode activation. Isotropic DEs will only inflate when activated and cannot deflate when activated.

Table 12. Initial numerical values of model material parameters.

Parameters	μ (kPa)	$\bar{\mu}_{feq}$ (-)	$\bar{\mu}_{fneq}$ (-)	$\bar{\eta}$ (s)	ε_0 (F/m)	ε_{mr} (-)	$\varepsilon_{fr}/\varepsilon_{mr}$ (-)
Values	10	1	1	0.25	8.85E-12	4.7	2.7/4.7

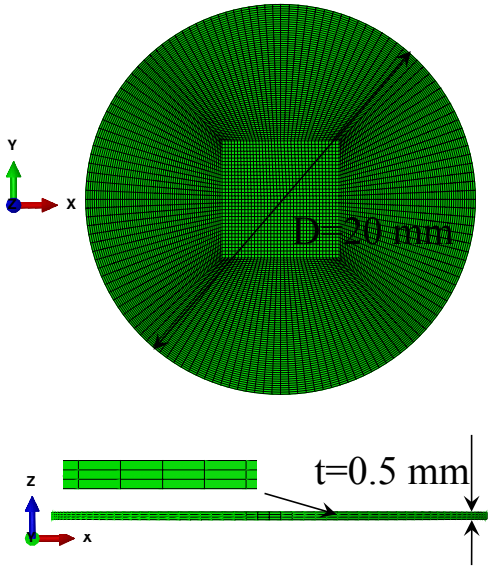

Figure 41. Thin circular membrane with diameter 20 mm and thickness 0.5 mm meshed into 40460 elements with three elements in thickness direction.

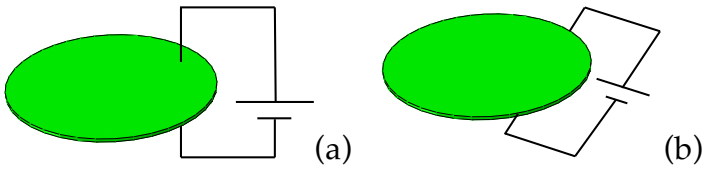

Figure 42. Electric fields are applied on matrix of the circular membrane in thickness direction and fibers of the circular membrane along the fiber orientation.

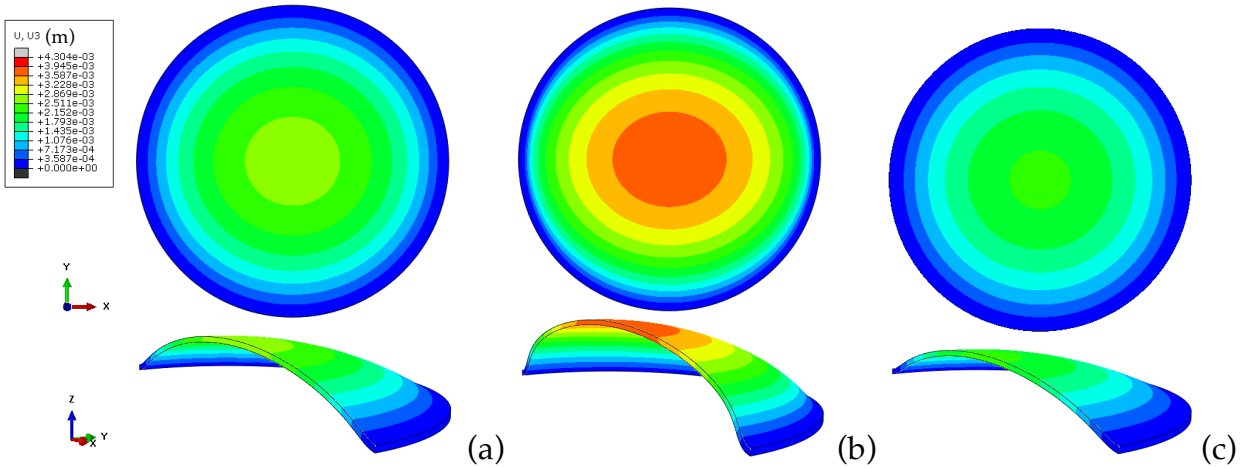

Figure 43. The deformation fields of the membrane for the three cases: (a) passive case, (b) activation in matrix with $\mathbf{E}=\begin{bmatrix} 0 & 0 & 9 \end{bmatrix}^T$ MV/m, and (c) activation in fiber with $\mathbf{E}=\begin{bmatrix} 0 & 12 & 0 \end{bmatrix}^T$ MV/m.

It is instructive to compare the deflection from matrix activation and fiber activation quantitatively and overlay the deflections of their centerlines for better assessment. Figure 44 plots the out of plane deflections of the horizontal centerlines of the pressure loaded membranes for three cases as a function of the line position as well as the deflection offset against the passive case (defined as $\Delta U_z = U_{z-total} - U_{z-passive}$). It shows that activation of the matrix increases the out of plane deflection while activation of the fibers decreases the out of plane deflection.

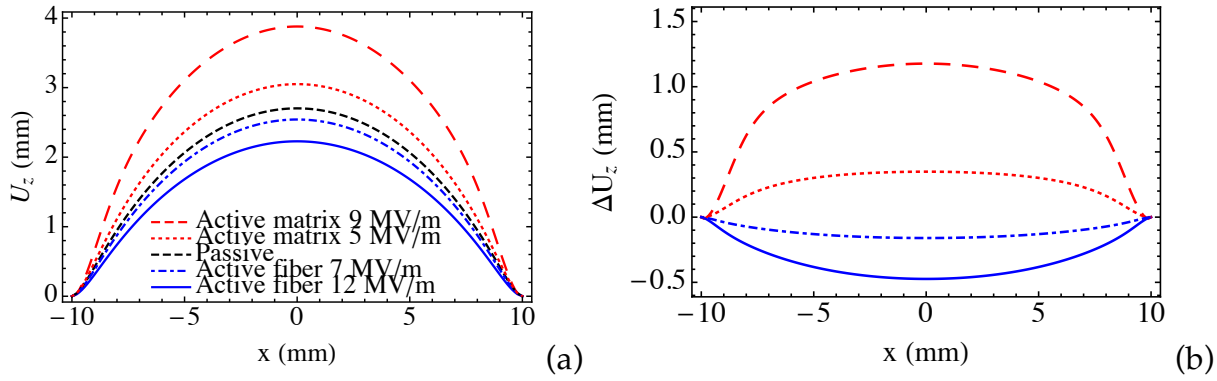

Figure 44. (a) The transverse deflection of the horizontal centerline of the membrane for passive and active cases (electric field in both matrix and fibers), and (b) the deflection offset against the passive case.

Figure 45 and Figure 46 show the logarithmic strain (true strain) and Cauchy stress fields for matrix and fiber activation, respectively. Generally, the strain fields for matrix activation (peak values are around 15%) are larger than that for fiber activation (peak values are around 5%). It reveals that fiber activation restricts the deformation. Comparing Figure 45 (c) and Figure 45 (d), it shows larger strain in the x-direction than

the y-direction due to the anisotropy of the material (the fibers are in the y-direction). Figure 46 shows that overall the stress fields (peak values are on the order of 7 kPa) are larger than those for matrix activation (peak values are on the order of 5.4 kPa). It indicates that the activated fibers stiffen the membrane and increase the membrane tension to restrict the deflection. For both activation in matrix and fibers, stresses in the y-direction are much larger than the stresses in x-direction and it indicates that the fibers carry more load and clearly reflects the anisotropy of the material.

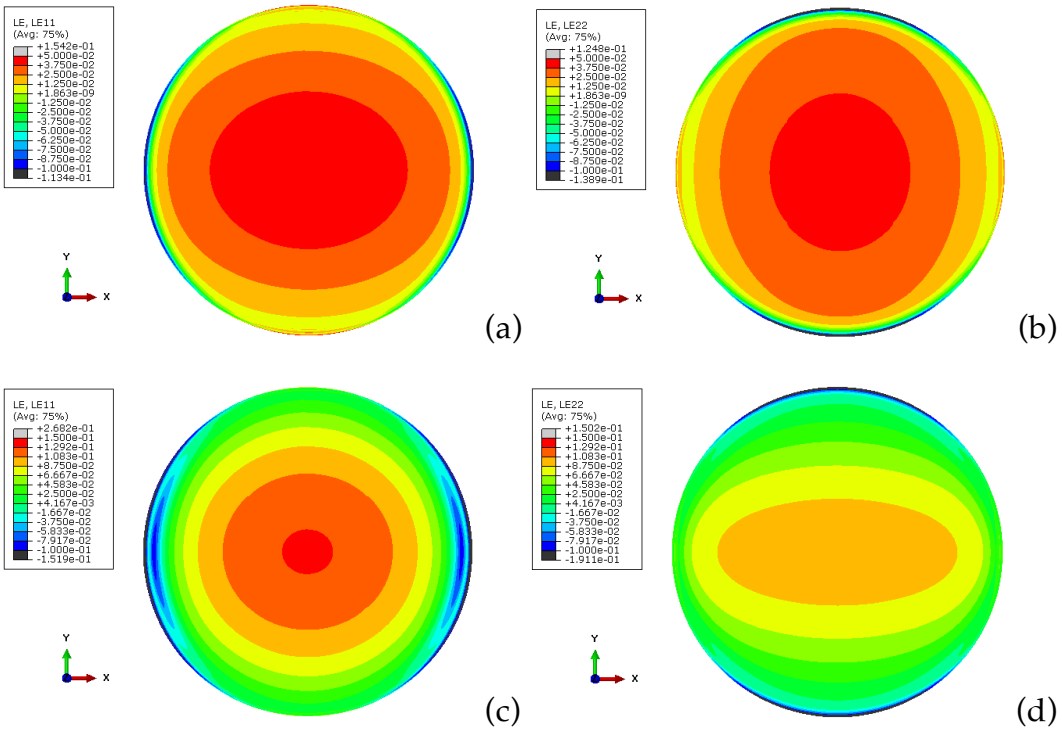

Figure 45. True strain fields of the membrane (a, c) in x-direction and (b, d) in y-direction for the composite (a~b) activated in fibers and (c~d) activated in the matrix.

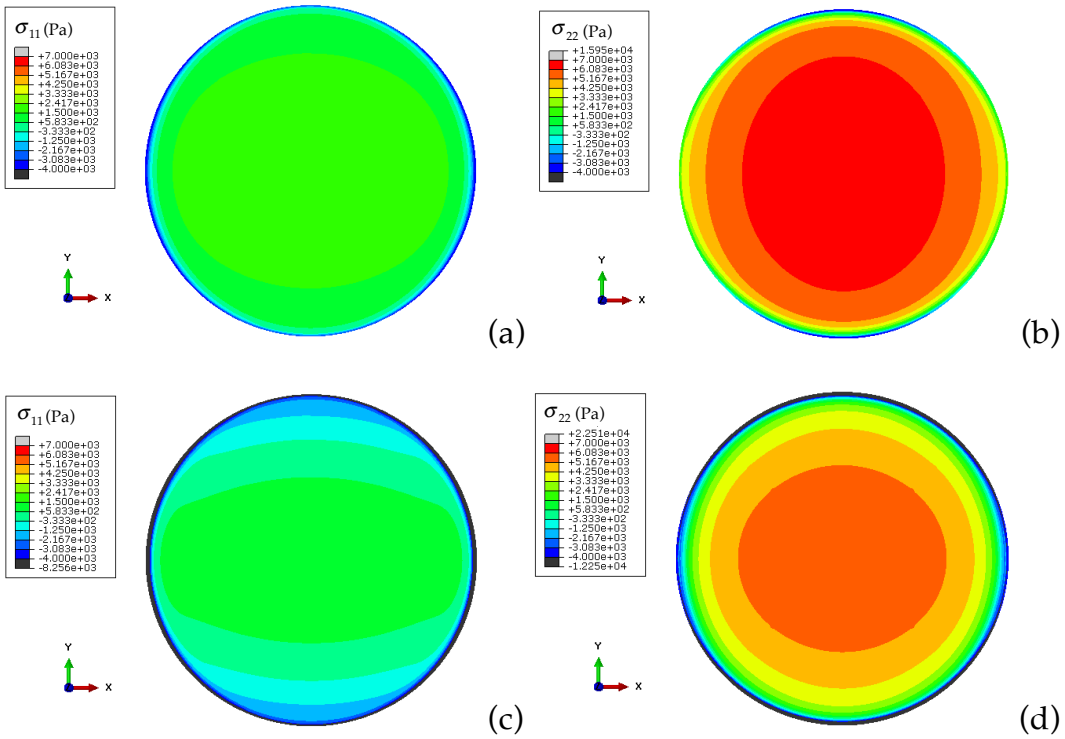

Figure 46. Cauchy stress fields of the membrane in radial (a, c) and circumferential (b, d) directions for the activation in matrix (a~b) and activation in fibers (c~d) (visualized in a cylinder coordinate system).

We define the output pressure as the resistive load that the active membrane is able to displace in an actuation work cycle. In a passive work cycle, the membrane inflates due to the bias pressure and the transverse deflection is calculated. In an actuation work cycle, the membrane is inflated under a bias pressure, activated by the electric field, and does work against an additional resistive pressure load. Figure 47 is a plot of output pressure versus peak transverse displacement for 2 activation protocols with a bias inflation pressure of 100 Pa and 200 Pa. The two protocols are: membrane activation (E = 9 MV/m) and fiber activation (E = 12 MV/m). Two grey lines are used as markers for the peak displacement when the membrane is passively inflated with 100 Pa and 200 Pa. During matrix activation, the membrane expands and inflates. The additional transverse deflection due to activation under the additional resistive load

(i.e. counter pressure on the top surface) is reported. The zero output pressure values reflect the free actuation response of the membrane with no resistive load. During fiber activation, the membrane constricts and deflates. The bias inflation pressure is increased and the additional transverse deflection due to activation is calculated. The zero output pressure value reflects the free actuation response (maximum deflection). Note that smaller transverse deflection values are consistent with membrane deflation due to in plane fiber contraction. For both actuation modes, there is a near linear relationship between output pressure and transverse deflection for the range considered here. The different slopes of the curves arise from the nonlinear stiffness of the membrane.

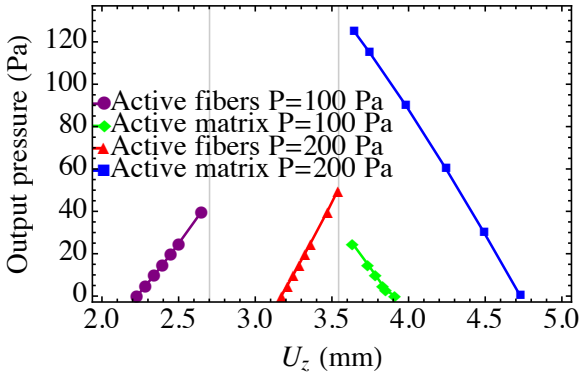

Figure 47. Output pressures of the circular membranes at various peak transverse deflections when activating the matrix or the fibers (two gray vertical lines mark the passive peak transvers deflections for pressures 100 Pa and 200 Pa).

We study the transverse peak deflections for various electric fields and pressure loadings for both types of activations and show them in Figure 48. It shows that both the electric field and pressure have a nonlinear effect on the out of plane peak deflection. Figure 48 (a) demonstrates a very small active effect for an electric field of 1 MV/m for both matrix and fiber activation, which is the minimum electric field for the given material parameters to activate the membrane. The effect of relative material

stiffness on the deformation response is shown in Figure 49. It shows i) that for an isotropic material the deflection offset relative to the passive case can reach 20% (fiber shear modulus is zero), and ii) increasing the stiffness of the fibers decreases the deflection offset (13.7% for a fiber modulus 5 times the matrix modulus). Figure 49 reveals that softer fibers induce larger transverse deflections.

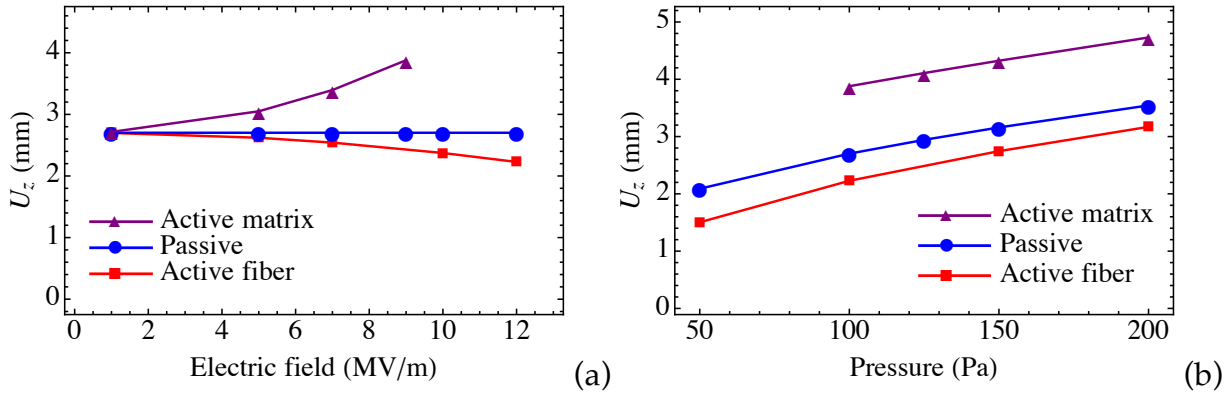

Figure 48. Transverse peak deflections (a) for various electric fields and (b) for various pressure loadings.

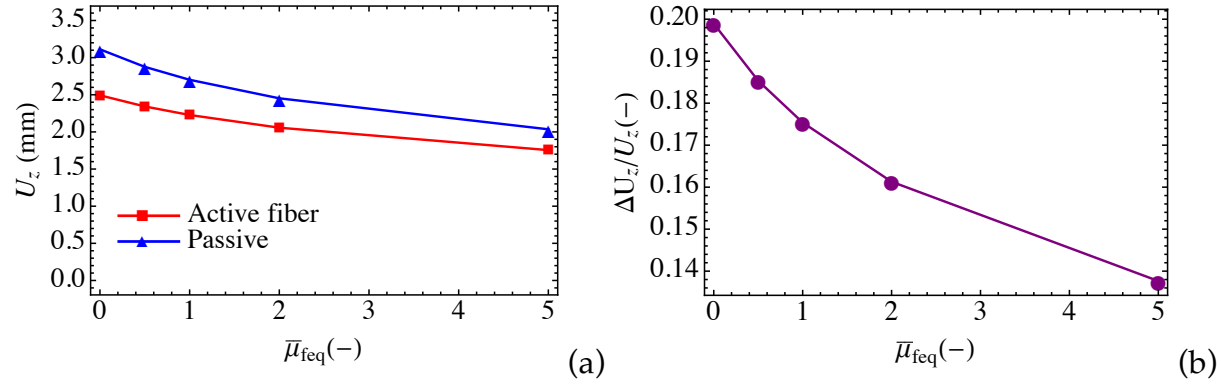

Figure 49. (a) Transverse peak deflection for various fiber over matrix modulus ratios, and (b) the out of plane peak deflection offset against passive case.

7.3 Distributed activation and fiber orientations

In this subsection, a set of simulation examples are presented to demonstrate shape changes (magnitude and slope) of thin membranes through spatial activation and as a function of fiber orientation. Consider a circular membrane in a rectangular coordinate

system with fibers oriented in the y-direction. The boundary and loading conditions are the same as in section 7.2, i.e. the circumferential edge of the circular membrane is pinned and an offset pressure of 100 Pa is applied to the bottom surface. The membrane is divided into 2 zones, which are activated according to different protocols. Figure 50 shows three activation approaches: i) zone 1 activation in the matrix and zone 2 fiber activation, ii) zone 2 fiber activation, and iii) zone 1 matrix activation. The applied electric field magnitudes for the fibers and matrix are 12 MV/m and 8 MV/m, respectively.

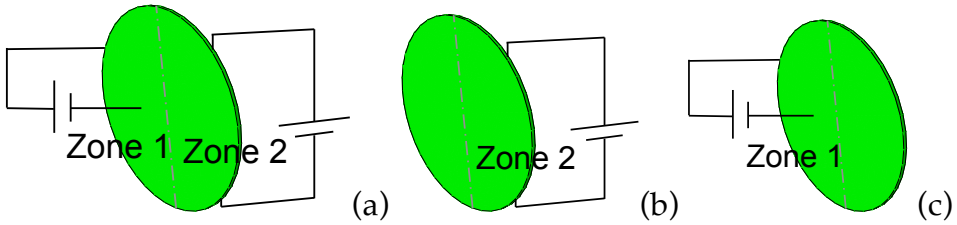

Figure 50. The schematics of the activation approaches for the first design: (a) active in both matrix in zone 1 and fibers in zone 2, (b) active only in fiber in zone 2, and (c) active only in matrix in zone 1.

Figure 51 shows the deformation fields of the three cases (active both in matrix and fiber, active only in fibers, and active only in matrix), and we plot transverse deflections for the horizontal centerlines in Figure 52 to compare and assess them quantitatively. Generally, Figure 51 shows all three activation approaches break the material symmetry and lead to asymmetric deformation fields. Matrix activation creates the largest out of plane deflection while activation in the fiber has the smallest out of plane deflection. Figure 52 (a) shows the three cases move forward the peak value positions from the center to around 40%-45% of the horizontal centerlines, which also can be seen in Figure 52 (c) at zero slope. Figure 52 (b) plots the transverse deflections offset against the passive case and shows the deflection magnitude changes of all three

cases. Matrix activation increases the deflection magnitude, for example at x=0 the deflection increment is 0.47 mm. Fiber activation decreases the deflection magnitude, e.g. at x=0 the deflection reduction is 0.29 mm. Active both in fibers and matrix have the deflection increment 0.16 mm at x=0. Figure 52 (c) shows the slopes of the centerlines for the three activation approaches. As can be seen, around the center region, the magnitudes of the slopes increases to 0.27, 0.13, and 0.1 for active in both, only active in matrix, and only active in fibers, respectively, i.e. the surfaces tilt to 15°, 7.3°, and 5.8°. It indicates that for the same material, the activation approaches affect the deformation fields of a thin membrane, including deflection magnitudes, surface slopes, and peak positions.

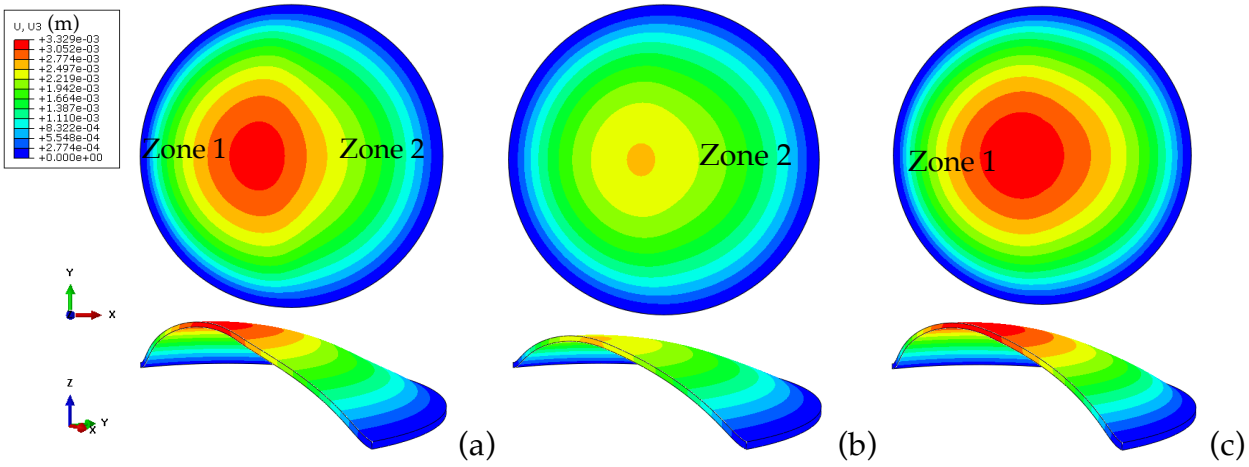

Figure 51. Deformation fields for (a) activation in matrix and fibers, (b) activation only in fibers, and (c) activation only in matrix.

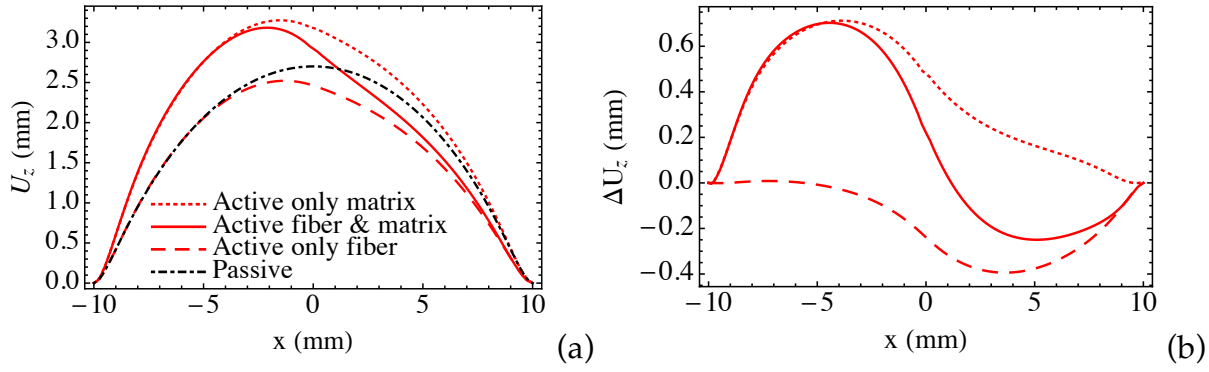

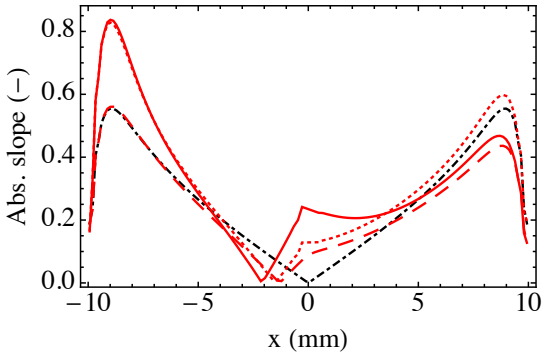

(c)

Figure 52. (a) Transverse deflection of the horizontal centerlines of the three active cases and one passive case, (b) comparison of the deflection offset for the three active cases against the passive case, and (c) the slopes of the horizontal centerlines.

Figure 53 shows the stress fields for the above three cases. Overall, the stresses in the fiber direction (y-direction) are much greater than the stresses in the x-direction due to anisotropy of the material and the activation enhancement. In the simulation, the stretch is assumed to be continuous at the boundary of the two activation zones. Since the activation in matrix and fiber soften and stiffen the material respectively, the stresses are discontinuous at the boundary of the two activation zones.

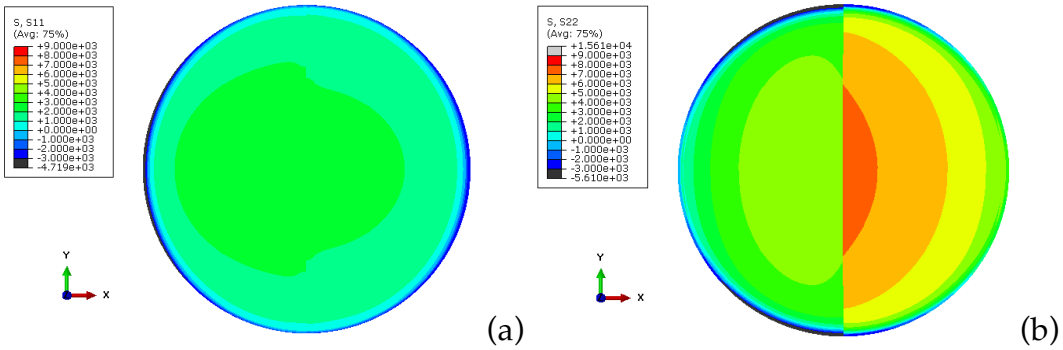

(a) (b)

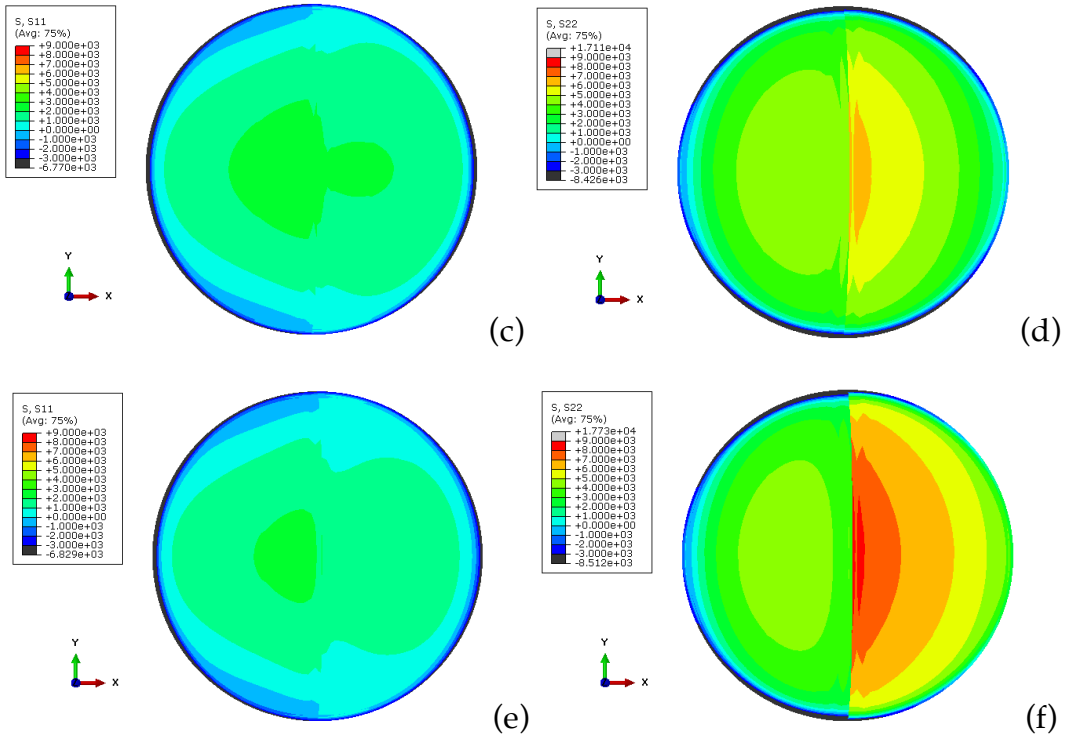

Figure 53. Stress fields for (a~b) active only in fibers, (c~d) active only in matrix, and (e~f) active both in fibers and matrix (unit: Pa).

In the second example, we investigate the effect of fiber orientation on the deformation of the DEC membrane. We consider a radial fiber distribution and a circumferential fiber distribution. The magnitudes of the electric field in the fibers are 12 MV/m for both cases. The deformation fields of the two designs are shown in Figure 54, and we plot the transverse deflections for the horizontal centerlines in Figure 55 to compare and assess them quantitatively. As can be seen, the deformation fields are axisymmetric since the material properties are axisymmetric for both cases and positions of the peak deflections stay in the center, however, they have different deformation modes and magnitudes, which is shown clearly in Figure 54 and Figure 55. Figure 55 shows that due to the embedded fiber orientations, the activation of the circular membrane with radial fibers decreases the peak transverse deflection while the

activation of the circular membrane with circumferential fibers increases the peak transverse deflection around the center region while the peripheral region has reduced transverse deflection, which leads to the slope and curvature changes of the pressure-loaded membrane surface. Figure 56 shows the curvatures for the deformed centerlines of Figure 55. As can be seen, the activation of the membrane with circumferential fibers alters the curvature of the surface in the center region significantly. While for the membrane with radial fibers, the curvatures only change slightly for passive and active cases. (It is noted that around the edge (i.e. at x=-10 and 10 mm) the large curvature is due to the circumferentially pinned edge boundary conditions i.e. the surface around the edge is curved.)

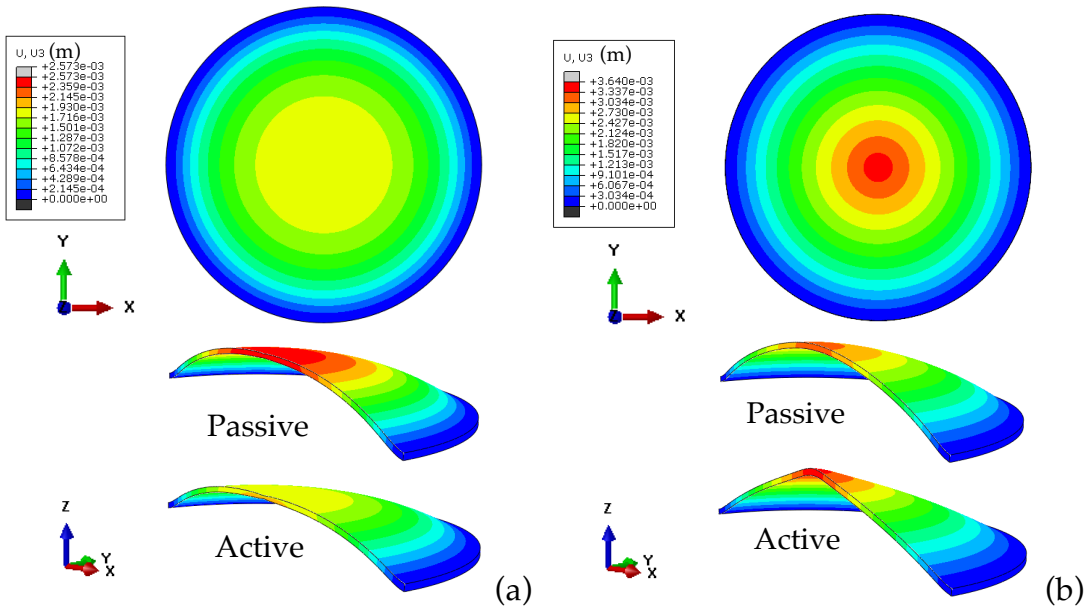

Figure 54. Deformation fields of designs with fibers in radial (a) and circumferential (b) directions.

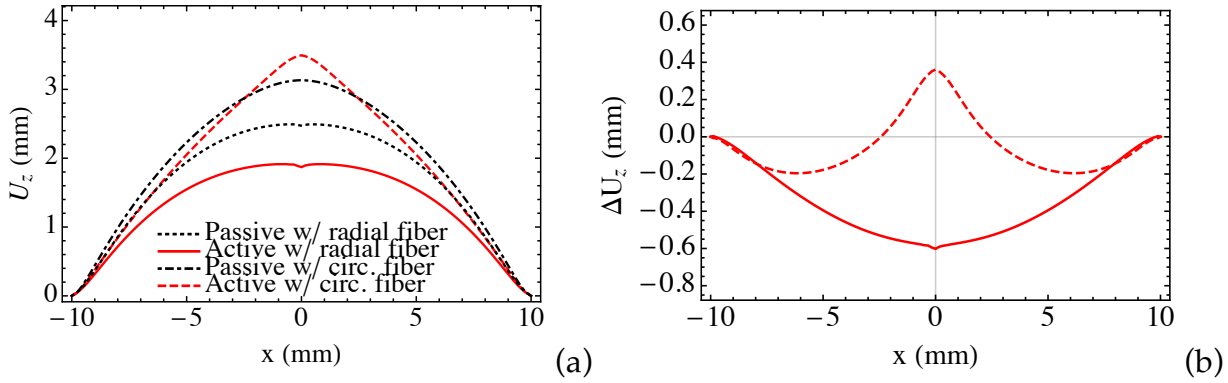

Figure 55. (a) Transverse deflection of the centerline and (b) transverse deflection offset against passive cases for pressure-loaded membranes with radial fiber distribution and circumferential fiber distribution.

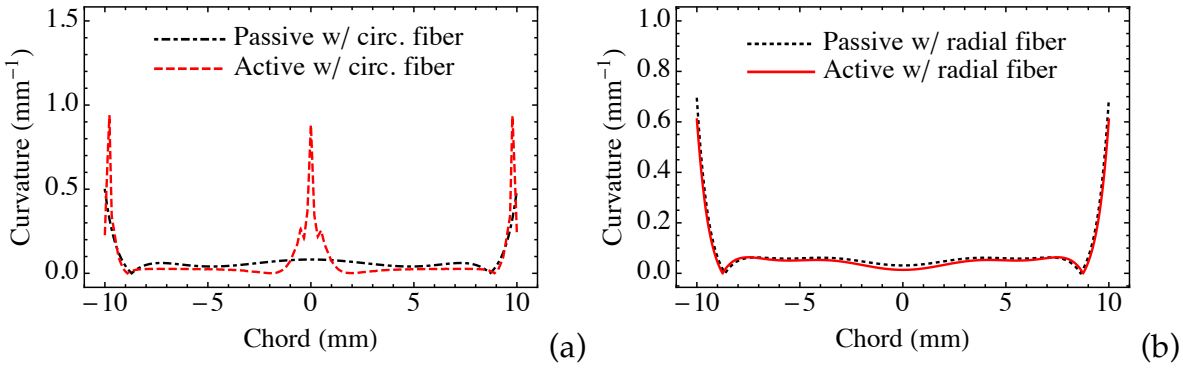

Figure 56. Curvatures of the active and passive configurations for pressure-loaded membranes with (a) radial fiber distribution and (b) circumferential fiber distribution.

Next, based on the significant change of curvature around the center region for circular membranes with circumferential fibers in the above simulations, we study the effect of activation levels on the surface configuration for circular membranes with circumferential fibers. Figure 57 shows the transverse deflections of the centerline for electric fields 10 MV/m, 12 MV/m, and 13 MV/m. Three curves interact around x=2.5 mm (marked by the arrow in Figure 57) and for higher electric fields the center region appears to form a 'second bubble'. The curvature is reversed around x=1.5~3 mm for electric fields 13 MV/m as marked in Figure 57 (b) in the circle.

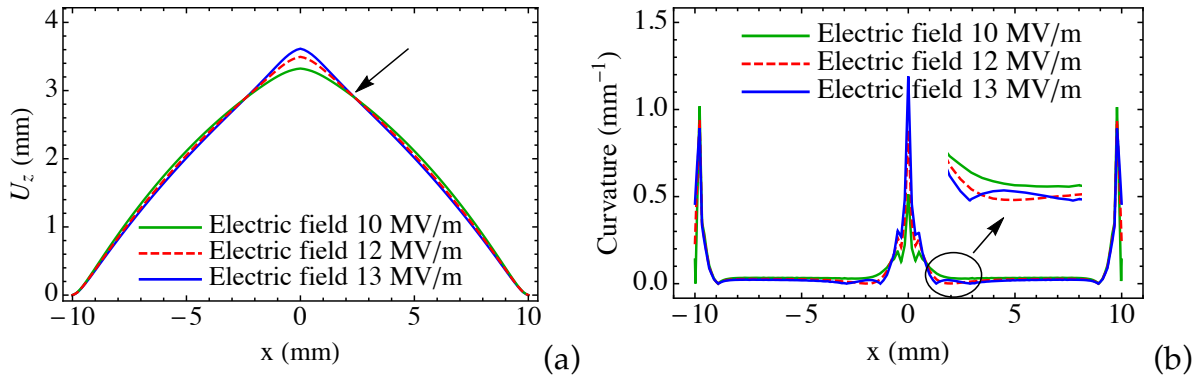

Figure 57. (a) Transverse deflections and (b) curvatures of the centerlines of the circular membranes with circumferential fibers for electric fields 10 MV/m, 12 MV/m, and 13 MV/m.

For the next subset of simulations, we assume a distribution of fibers oriented at angles 15°, 30°, 45°, 60°, and 75° from the radial direction and demonstrate surface twist because of the anisotropy of the material enhanced by fiber activation. Figure 58 shows the deformations of circular membranes for the different fiber distributions. The deformed centerline is overlaid with the contour to demonstrate the twist. Overall, passive configurations (Figure 58 left column) show slight surface twist due to the anisotropy from the embedded fibers. However, the surface twist is clearly enhanced by activation (Figure 58 right column). This twisting mode is new and in addition to the transverse deflections. Figure 59 (a) quantifies the twist angles of the horizontal centerline (only from 0~10 mm due to the symmetry) for passive and active cases. The maximum twist angles are at the center of the circular membrane and range from 14°~24° for the active case and from 5°~13° for the passive case (see Figure 59 (b)). Figure 59 (b) shows that the circular membrane with fibers oriented 30° with respect to the radial direction has the greatest twist angle for the passive case and fibers oriented at 45° has the greatest twist angle for the active case. In addition, circular membranes with fibers oriented at 15° and 75° show the smallest twist angles. While twist angles

are non-monotonic in terms of the fiber orientations, the peak deflection shows monotonicity for fiber orientations in Figure 59 (c). It is noted that for fiber angles smaller than 75° the peak deflections of the deformed active configurations are smaller than that of the deformed passive configurations.

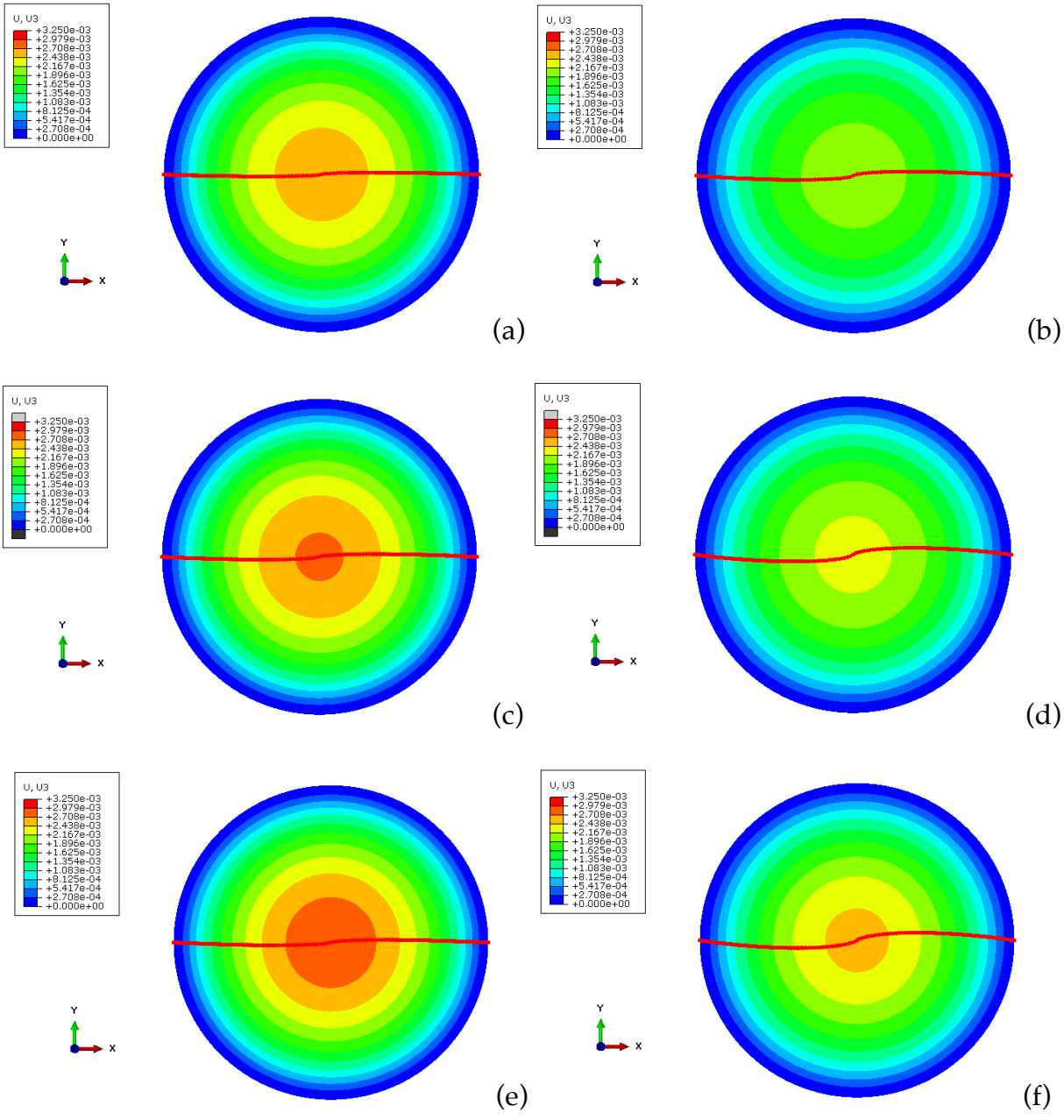

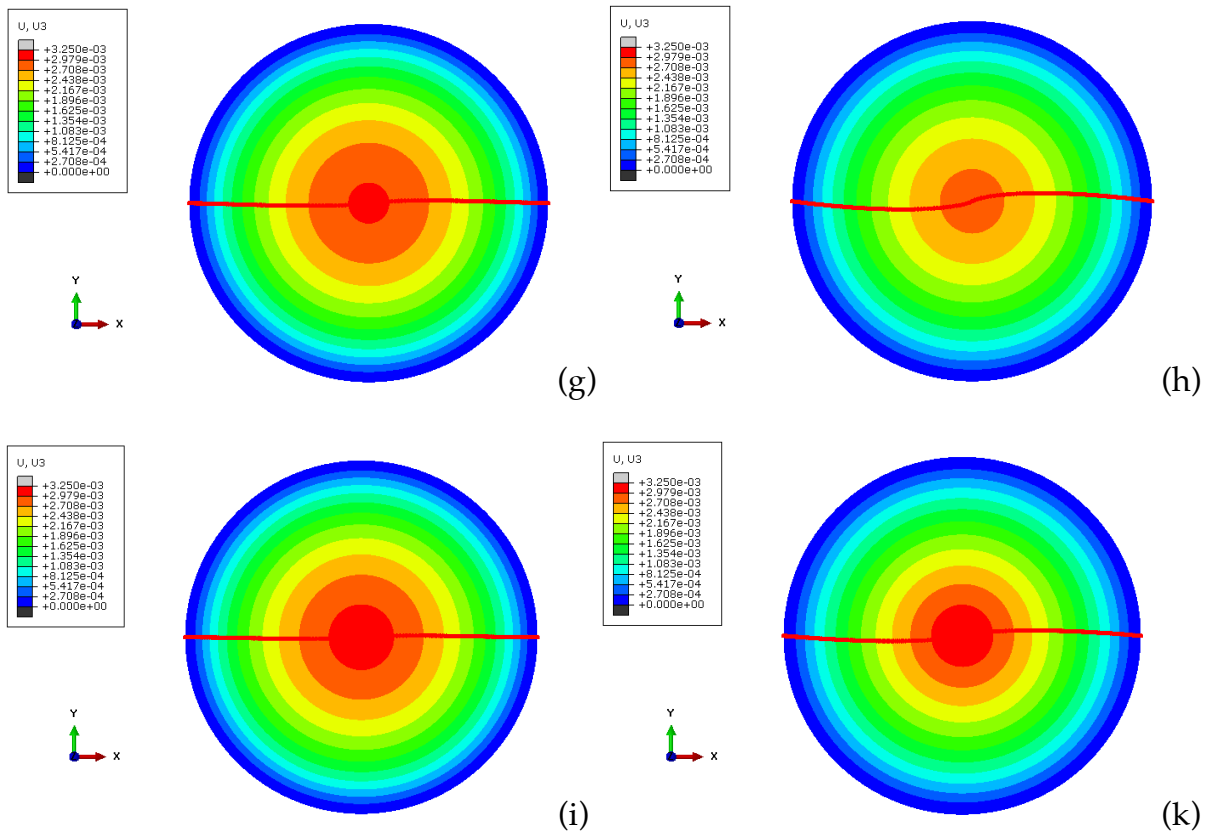

Figure 58. Deformed passive and active configurations for the circular membrane with fiber orientations: (a~b) 15°, (c~d) 30°, (e~f) 45 °, (g~h) 60°, and (i~k) 75° (unit: meter).

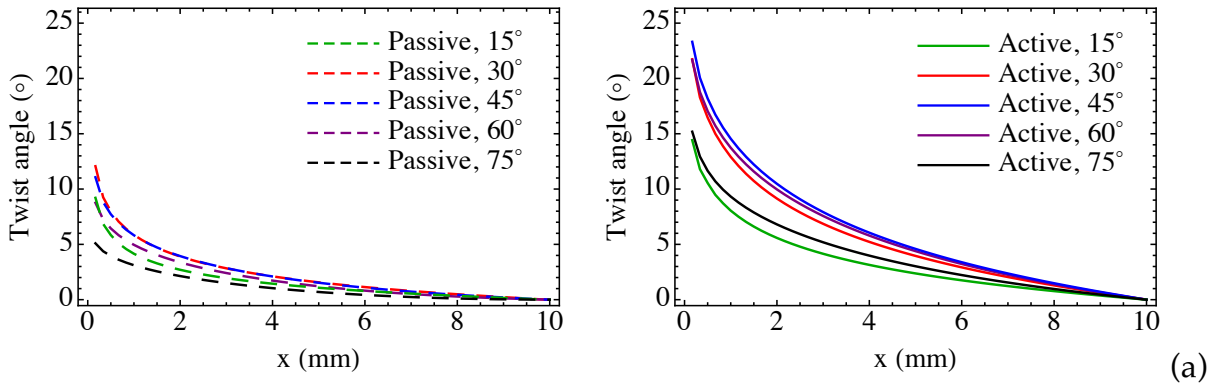

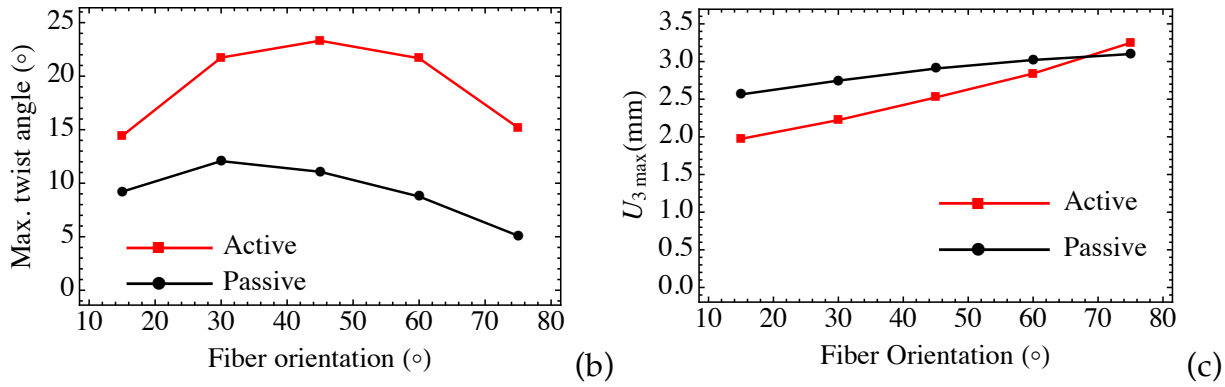

Figure 59. (a) Twist angles of the horizontal centerline, (b) peak twist angles for various fiber orientations, and (c) the magnitudes of peak deflections.

Figure 60 shows the radial, circumferential, and z-direction stress fields for the membrane with a 45° fiber family (with respect to the radial direction) as an example. As can be seen, the radial and circumferential stresses are positive for both passive and active cases. The magnitudes of the active stresses are greater than those of the passive stresses due to the electric activation. The membrane has negative stresses in the z-direction around 100 Pa.

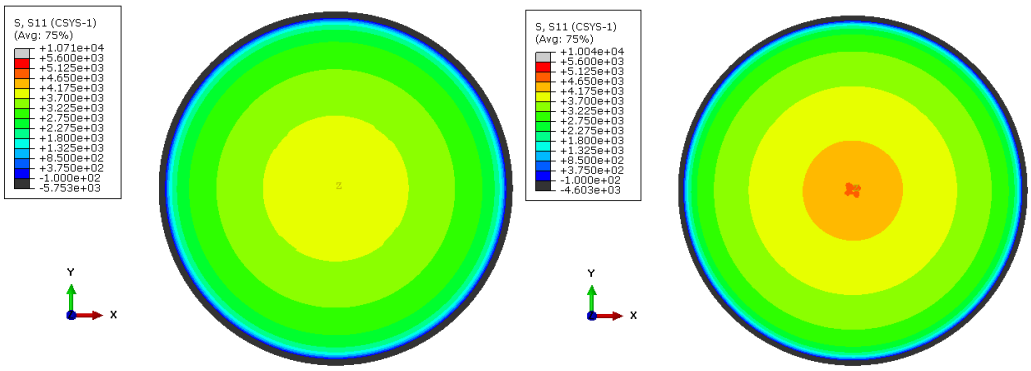

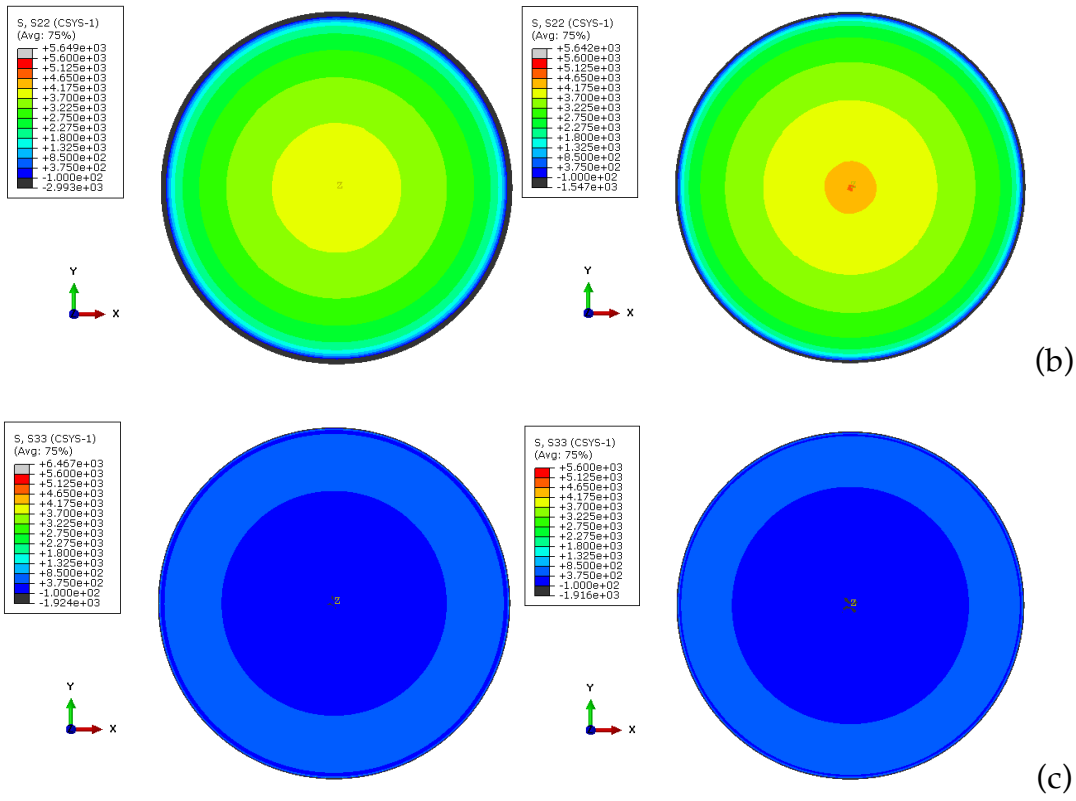

Figure 60. Radial, circumferential, and z-direction stresses in (a~c) respectively. The left column has the passive stresses and the right column has the active stresses (unit: Pa).

The above simulations focus on the surface shape (magnitudes, slopes, curvatures, and peak deflections etc.) of pressure-loaded circular membranes through spatial activation and various fiber orientations. It demonstrates how discrete activation can break the material symmetry and lead to asymmetric deformation fields. Fiber orientations can be used to change the surface curvatures through fibers contractions. In addition, the fiber orientation was shown to induce a new DE actuation mode: surface twist through fiber activation.

7.4. Electro-hydrostatic actuation in DECs

In the following, we demonstrate electro-hydrostatic simulations for two 3D geometries and a planar membrane. In Figure 61, the deformation behavior of a pressurized

spherical DEC membrane is shown. The fibers are aligned along the lines of latitude (see the schematic sketch of the fiber directions on the ball next to the legend in Figure 61 (a)). The spherical ball has inner diameter 20 mm and thickness 0.2 mm. The model parameters are from Table 12 except that $\bar{\mu}_{feq} = 0$. Figure 61 (a) shows the deformed passive configuration for an applied pressure 100 Pa on the inside surface. Figure 61 (b) shows the activated configuration which breaks the symmetry of the passive configuration. The left hemisphere of the ball is matrix activated by an electric field of 5 MV/m, and the right hemisphere is fiber activated by an electric field of 10 MV/m. Figure 61 (c) and Figure 61 (d) show the cut of the activated configuration in two different views.

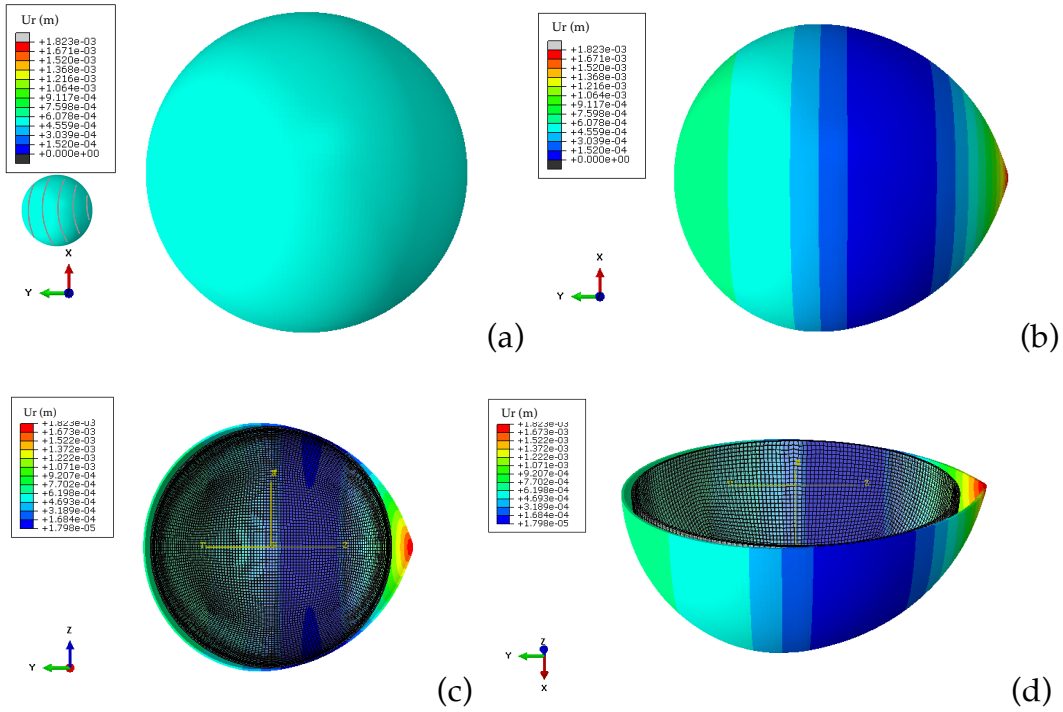

Figure 61. (a) The deformed passive configuration of a spherical ball with pressure loading, (b) the deformed active configuration of a spherical ball with pressure loading and electric fields, and (c-d) the cut of the deformed activated configuration in two different views.

As another example, Figure 62 demonstrates the basic contraction mechanism of a pressurized ring shaped actuator. The actuator has contractile fibers along the hollow tube (see the schematic sketch of the fiber directions on the ring below the legend in Figure 62 (a)) so that when the fibers contract the actuator diameter is reduced. The initial configuration of the ring actuator has centerline diameters 20 mm, tube inner diameter 2 mm and thickness 0.2 mm. The model parameters are from Table 12. Figure 62 (a) shows the deformed passive configuration for an applied pressure 100 Pa inside the tube. Figure 62 (b) is fiber activated by an electric field with magnitude 12 MV/m. Figure 62 (b) shows the activated configuration which contracts the fibers and decrease the overall diameter of the ring configuration. Figure 62 (c) and Figure 62 (d) show the overlay of the passive and active configurations. The cut of the deformed activated configuration in Figure 62 (d) clearly shows the contraction effect due to the active fibers.

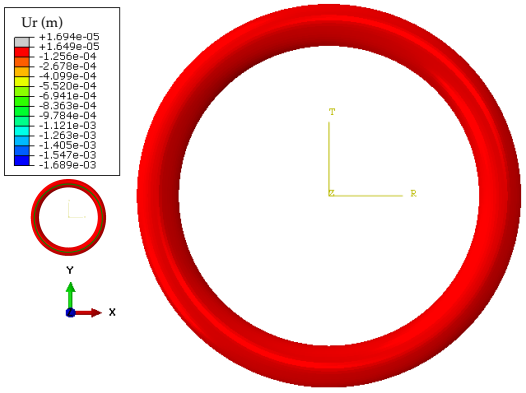

(a)

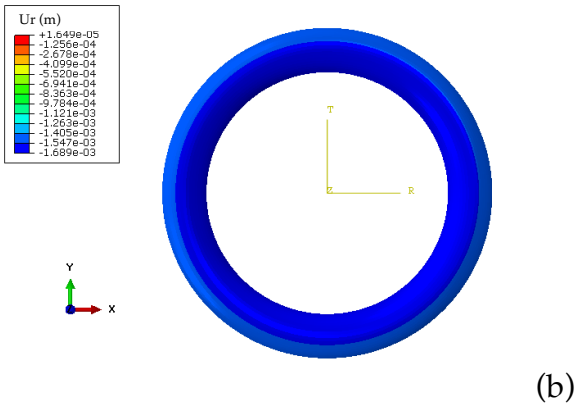

(b)

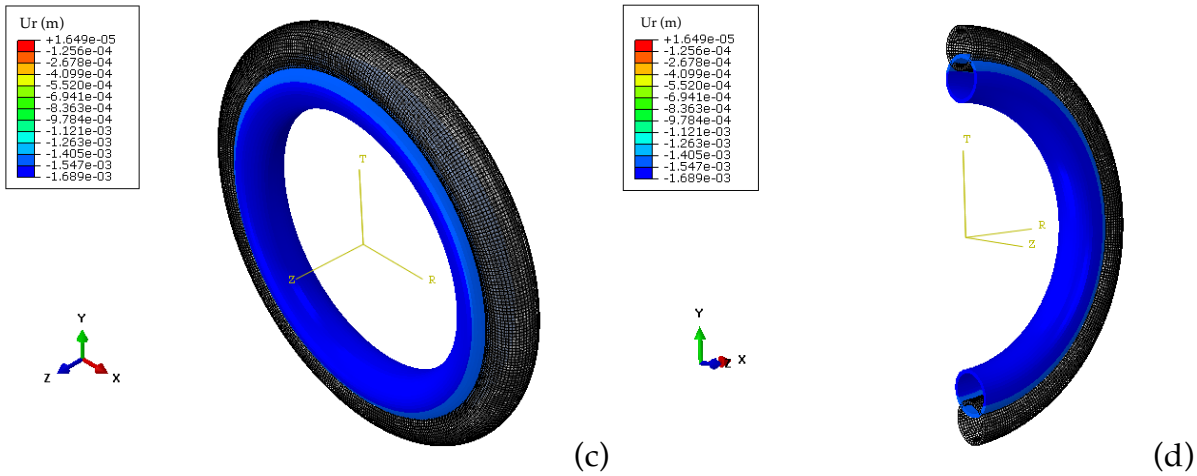

(c) (d)

Figure 62. (a) The deformed passive configuration of a swimming ring shaped actuator, (b) the deformed active configuration of a swimming ring shaped actuator, and (c-d) the overlay of the passive and active configuration in two different views.

Figure 63 demonstrates different surface conformations of a rectangular flat membrane through selective activation of the matrix and fibers. The initial configuration of the flat membrane has width 20 mm, length 30 mm, and thickness 0.5 mm. The model parameters are from Table 12. The front and rear edges are pinned and the other two edges are free. A pressure of 100 Pa is applied on the bottom surface. The flat membrane has three equal activation zones along the width (see the schematic sketch of the three zones and fiber direction in the right corner of Figure 63 (a)). Figure 63 (a) shows the deformed passive configuration. Figure 63 (b) and Figure 63 (c) show the two deformed active configurations: the first one with center zone activated in the matrix ($E_3 = 7$ MV/m) and two side zones activated in the fiber direction ($E_2 = 10$ MV/m), and the second configuration has a center zone under fiber activation ($E_2 = 10$ MV/m) with two side zones under matrix activation ($E_3 = 7$ MV/m).

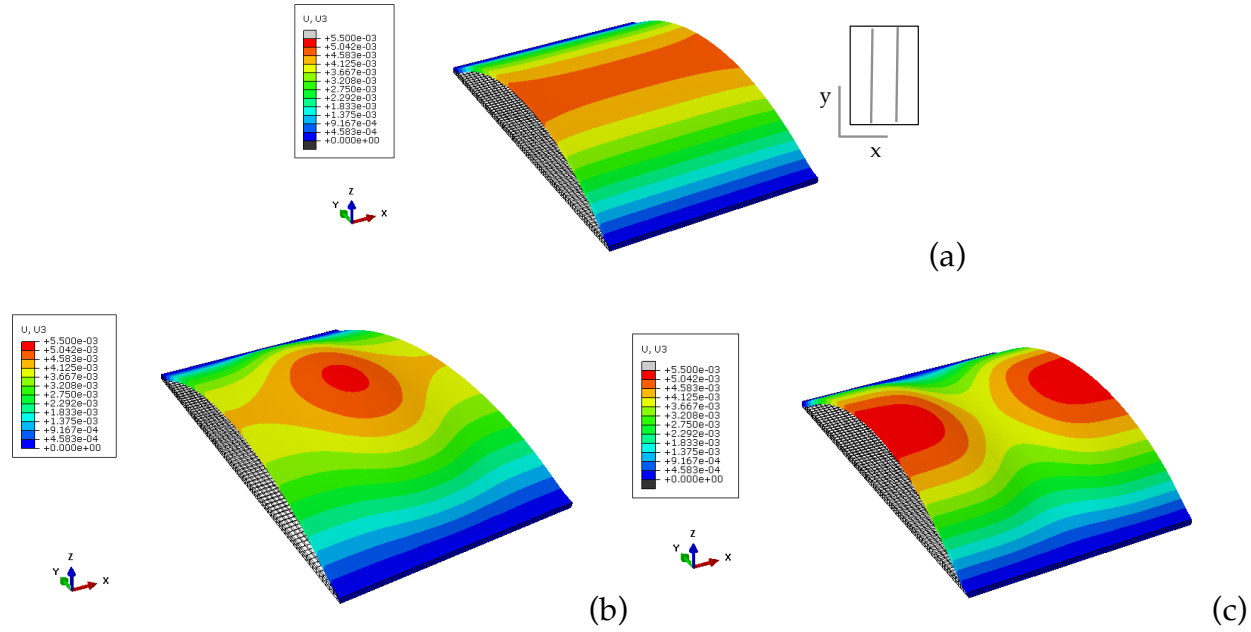

Figure 63. (a) The deformed passive configuration of a plate surface, (b~c) two deformed active configurations of the plate membrane (unit: meter).

Here, we consider patterned membranes with a combination of active and passive regions to illustrate the concept of spatially distributed activation in a more discrete sense. Three architectures are considered, each is a rectangular membrane with length 40 mm, width 30 mm, and thickness 0.5 mm. The short sides are pinned while the longer sides are free. A pressure of 50 Pa is applied on the bottom surface. The magnitudes for the electric field in the fibers are set to be 10 MV/m for all the simulations. For the first architecture, five discrete active zones (fiber activation) are defined as shown in Figure 64 with fiber oriented in the x-direction. Table 13 summarizes the activation procedures for each of the results in Figure 65. For the sequential activation of zones 1~5 (total activation time is 10 seconds), the time interval between activating any two zones is 2 seconds, i.e. at t=0 activating zone 1, and at t=2 activation zone 2, etc. For the current sequential activation procedure, each activated zone goes to steady state before the next zone is activated considering the characteristic

relaxation time of the material is 0.25 second. Figure 66 demonstrates that various wavy surfaces can be realized by different activation procedures within one design. Figure 67 (a) shows the evolution of the transverse deflections of the centerline along the y-direction (at x=0 mm) for sequentially activating zones 1~5 zones, and Figure 67 (b) shows the transient time for each activation is shorter than 1 second. Additionally, we calculate the response with the material parameter $\bar{\eta} = 2.5s$ with the same activation procedure, i.e. activating zones 1~5 (total activation time is 10 seconds) sequentially with the time interval between activating any two zones of 2 seconds. The evolution of the transverse deflections of the centerline along the y-direction (at x=0 mm) are shown in Figure 68 (a). Figure 68 (b) shows the transient time for each activation is longer than 2 seconds.

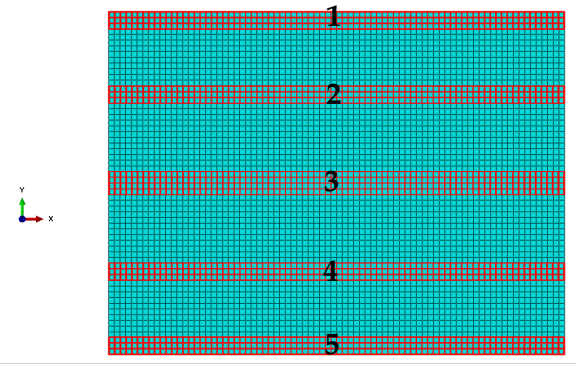

Figure 64. Five discrete activation zones with fibers oriented in the x-direction and the rest of the zones are passive.

Table 13. Activation procedures for the results in Figure 65.

Activation procedures	Results
1,2,3,4, and 5 zones activated at the same time	Figure 20 (b)
1,2,3,4, and 5 zones activated sequentially	Figure 20 (c)
Only 1,3, and 5 zones activated at the same time	Figure 20 (d)
Only 2 and 4 zones activated at the same time	Figure 20 (e)

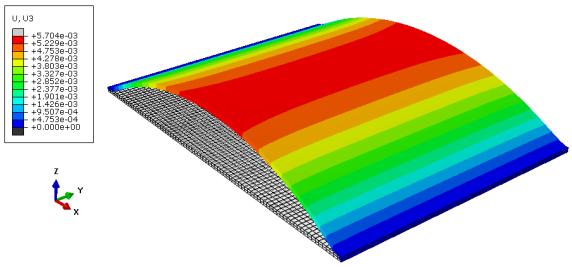
U, U3
+5.704e-03
+5.229e-03
+4.753e-03
+4.278e-03
+3.803e-03
+3.327e-03
+2.852e-03
+2.377e-03
+1.901e-03
+1.426e-03
+9.507e-04
+4.753e-04
+0.000e+00
Z
Y
X

(a)

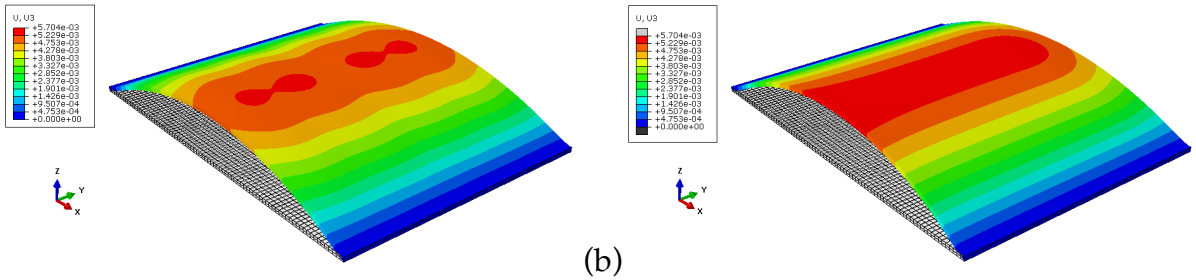
U, U3
+5.704e-03
+5.229e-03
+4.753e-03
+4.278e-03
+3.803e-03
+3.327e-03
+2.852e-03
+2.377e-03
+1.901e-03
+1.426e-03
+9.507e-04
+4.753e-04
+0.000e+00
Z
Y
X

(b)

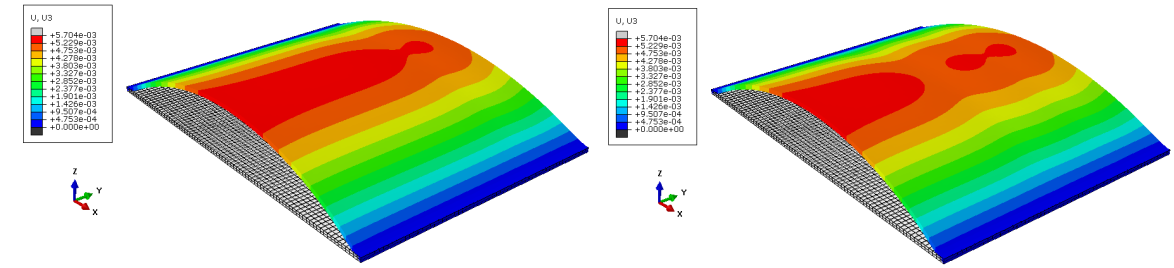
U, U3
+5.704e-03
+5.229e-03
+4.753e-03
+4.278e-03
+3.803e-03
+3.327e-03
+2.852e-03
+2.377e-03
+1.901e-03
+1.426e-03
+9.507e-04
+4.753e-04
+0.000e+00
Z
Y
X

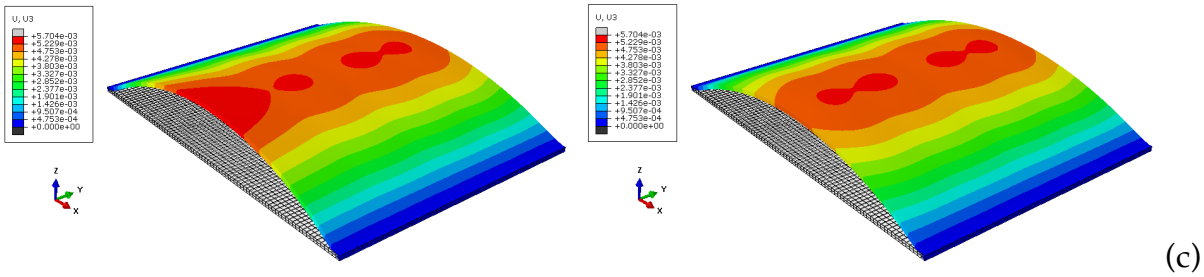
U, U3
+5.704e-03
+5.229e-03
+4.753e-03
+4.278e-03
+3.803e-03
+3.327e-03
+2.852e-03
+2.377e-03
+1.901e-03
+1.426e-03
+9.507e-04
+4.753e-04
+0.000e+00
Z
Y
X

(c)

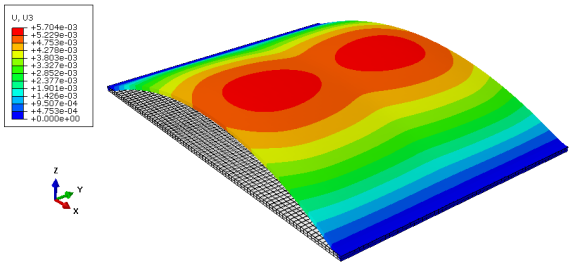
U, U3
+5.704e-03
+5.229e-03
+4.753e-03
+4.278e-03
+3.803e-03
+3.327e-03
+2.852e-03
+2.377e-03
+1.901e-03
+1.426e-03
+9.507e-04
+4.753e-04
+0.000e+00
Z
Y
X

(d)

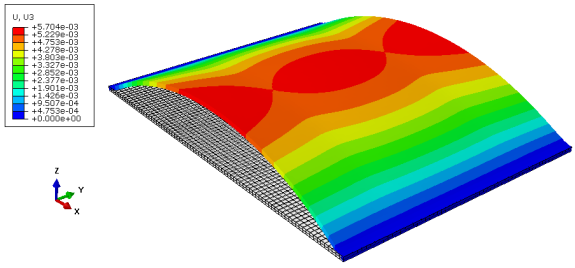
U, U3
+5.704e-03
+5.229e-03
+4.753e-03
+4.278e-03
+3.803e-03
+3.327e-03
+2.852e-03
+2.377e-03
+1.901e-03
+1.426e-03
+9.507e-04
+4.753e-04
+0.000e+00
Z
Y
X

(e)

Figure 65. Out of plane deflections of (a) the passive case and (b~e) the activation procedures listed in Table 13 (unit: meter).

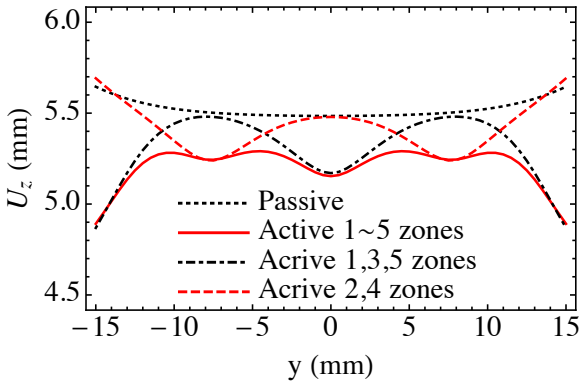

Figure 66. Transverse deflections of the centerlines along y-direction (at x=0 mm) for various activation procedures.

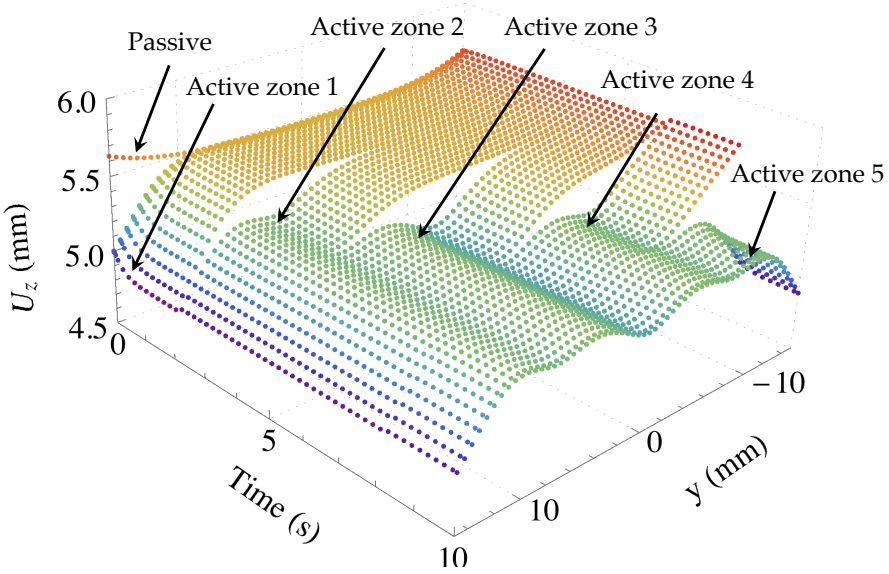

(a)

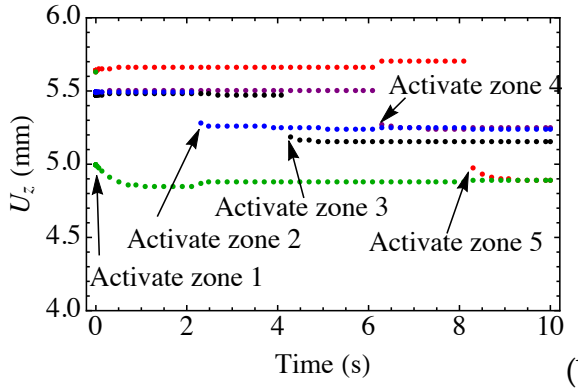

(b)

Figure 67. (a) Evolution of the transverse deflections of the centerlines along y-direction (at x=0 mm) for sequentially activating 1~5 zones, and (b) the overlay of the peak transverse deflections of 1~5 zones at x=0 mm for characteristic relaxation time 0.25 second.

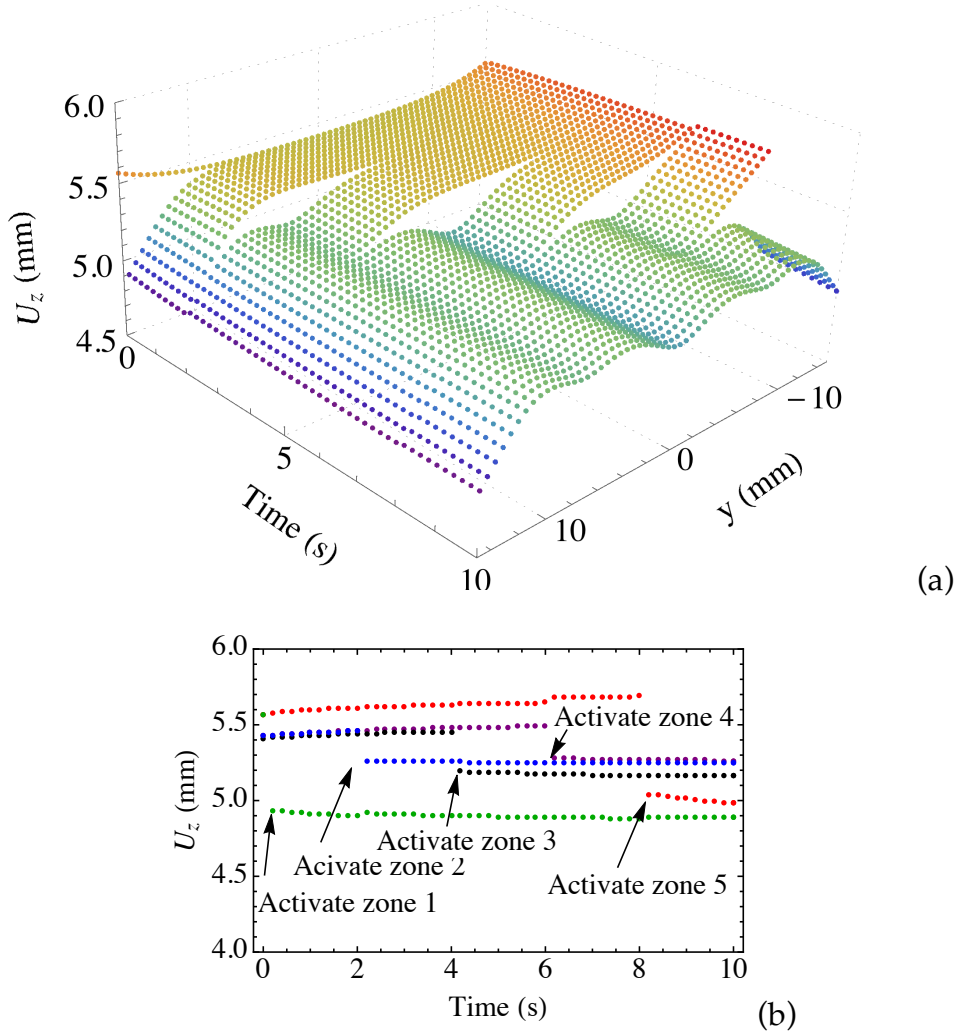

Figure 68. (a) Evolution of the transverse deflections of the centerlines along the y-direction (at x=0 mm) for sequentially activating zones 1~5 for a characteristic relaxation time of 2.5 seconds, and (b) the overlay of the peak transverse deflections of zones 1~5 at x=0 mm for a characteristic relaxation time of 2.5 seconds.

For the second architecture, six discrete fiber zones are shown in Figure 69 with fibers at zones 1~3 oriented in the y-direction and fibers at zones 4~6 oriented in the x-direction. Table 14 summarizes the activation procedures for each of the results in

Figure 70. For the sequential activation of zones 1~6 (total activation time is 10 seconds), the time interval between activating any two sets of zones is 3 seconds, i.e. at t=0 zones 1 and 4 activated, at t=4 zones 2 and 5 activated, at t=8 zones 3 and 6 activated. For the current sequential activation procedure, each activated zone goes to steady state before the next set of zones is activated considering the characteristic relaxation time of the material is 0.25 second.

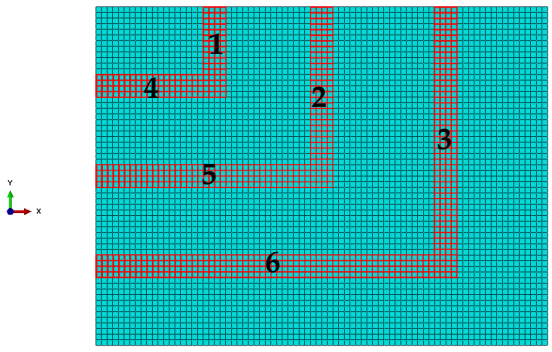

Figure 69. Six discrete activation zones with fibers at zones 1~3 oriented in the y-direction and fibers at zones 4~6 oriented in the x-direction.

Table 14. Activation procedures for the results in Figure 70.

Activation procedures	Results
Only 1, 2, and 3 zones activated at the same time	Figure 22 (b)
Only 4, 5, and 5 zones activated at the same time	Figure 22 (c)
1, 2, 3, 4, 5, and 6 zones activated at the same time	Figure 22 (d)
1, 2, 3, 4, 5, and 6 zones activated sequentially	Figure 22 (e)

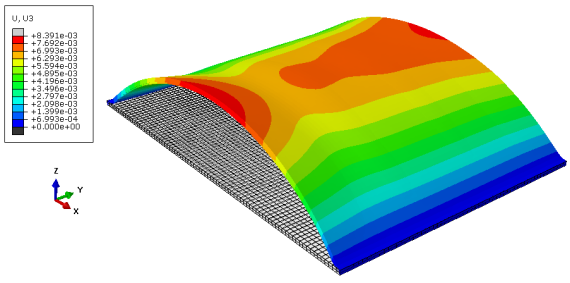

(a)

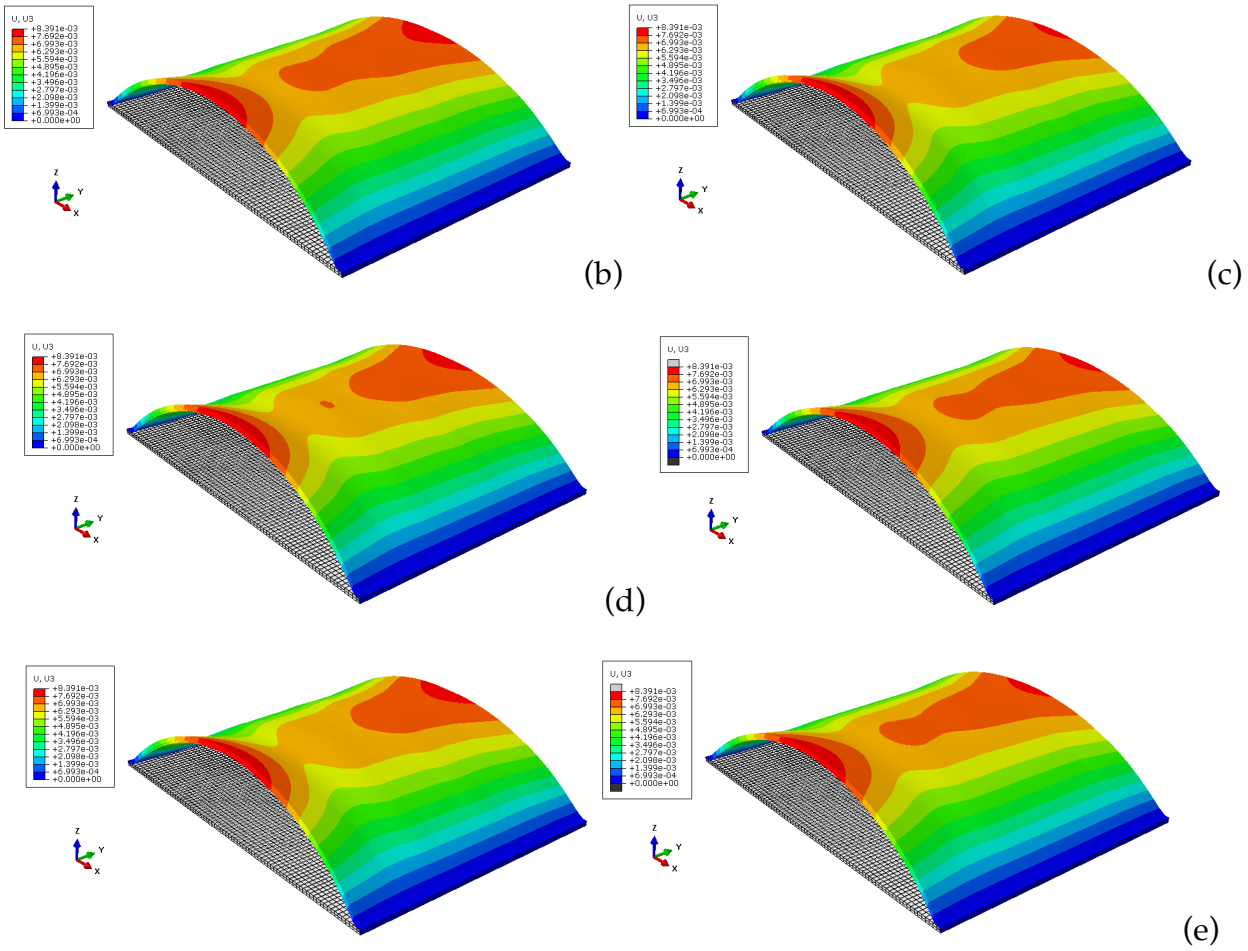

Figure 70. Out of plane deflections of (a) the passive case and (b~e) the activation procedures listed in Table 14 (unit: meter).

For the third architecture, we consider six discrete fiber zones as shown in Figure 71 with fibers oriented in the circumferential-direction. Table 15 summarizes the activation procedures for each of the results in Figure 72. For the sequential activation of zones 1~6 (total activation time is 10 seconds), the time interval between activating any two zones is 1.5 seconds, i.e. at t=0 activating zone 1, at t=1.5 activation zone 2, and at t=3 activation zone 3, etc. For the current sequential activation procedure, each activated zone goes to steady state before the next zone is activated considering the characteristic relaxation time of the material is 0.25 second.

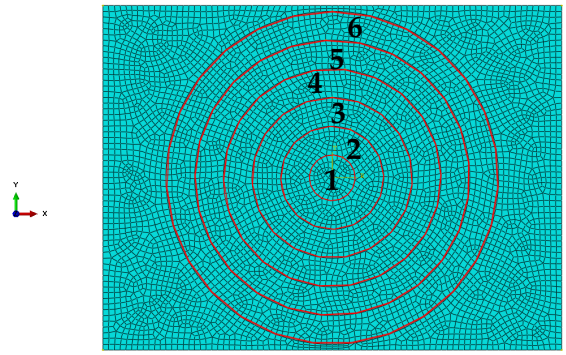

Figure 71. Six discrete activation zones with fibers oriented in circumferentially.

Table 15. Activation procedures for the results in Figure 72.

Activation procedures	Results
1, 2, 3, 4, 5, and 6 zones activated at the same time	Figure 24 (b)
Only 2, 4, and 6 zones activated at the same time	Figure 24 (c)
1, 2, 3, 4, 5, and 6 zones activated sequentially	Figure 24 (d)

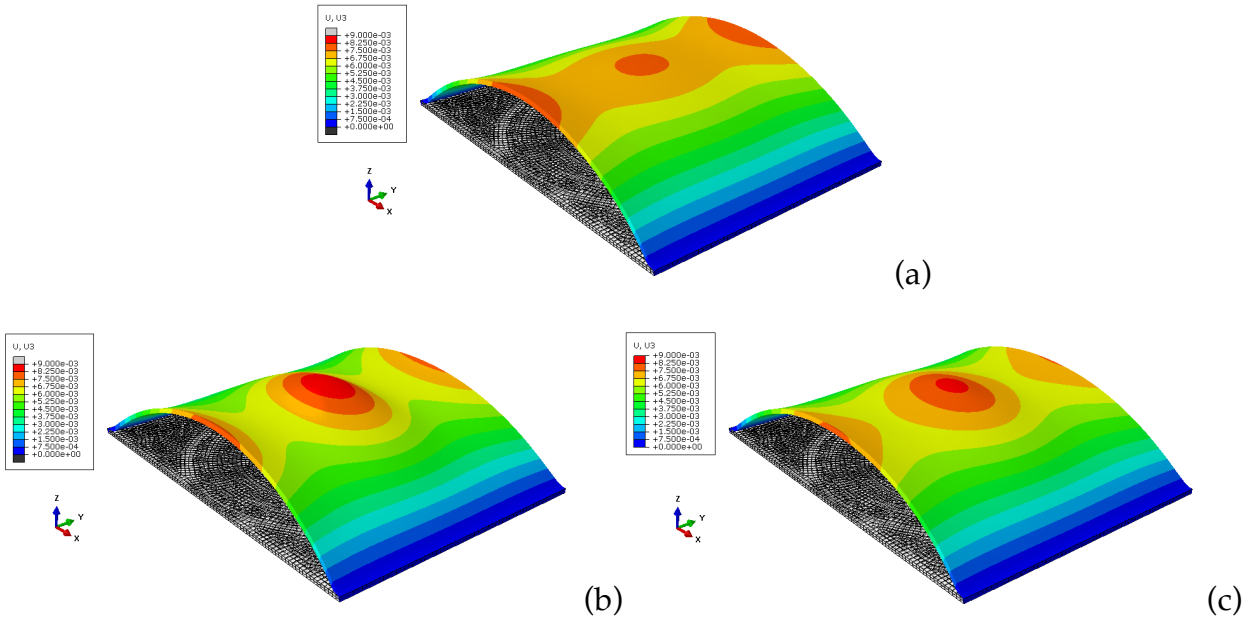

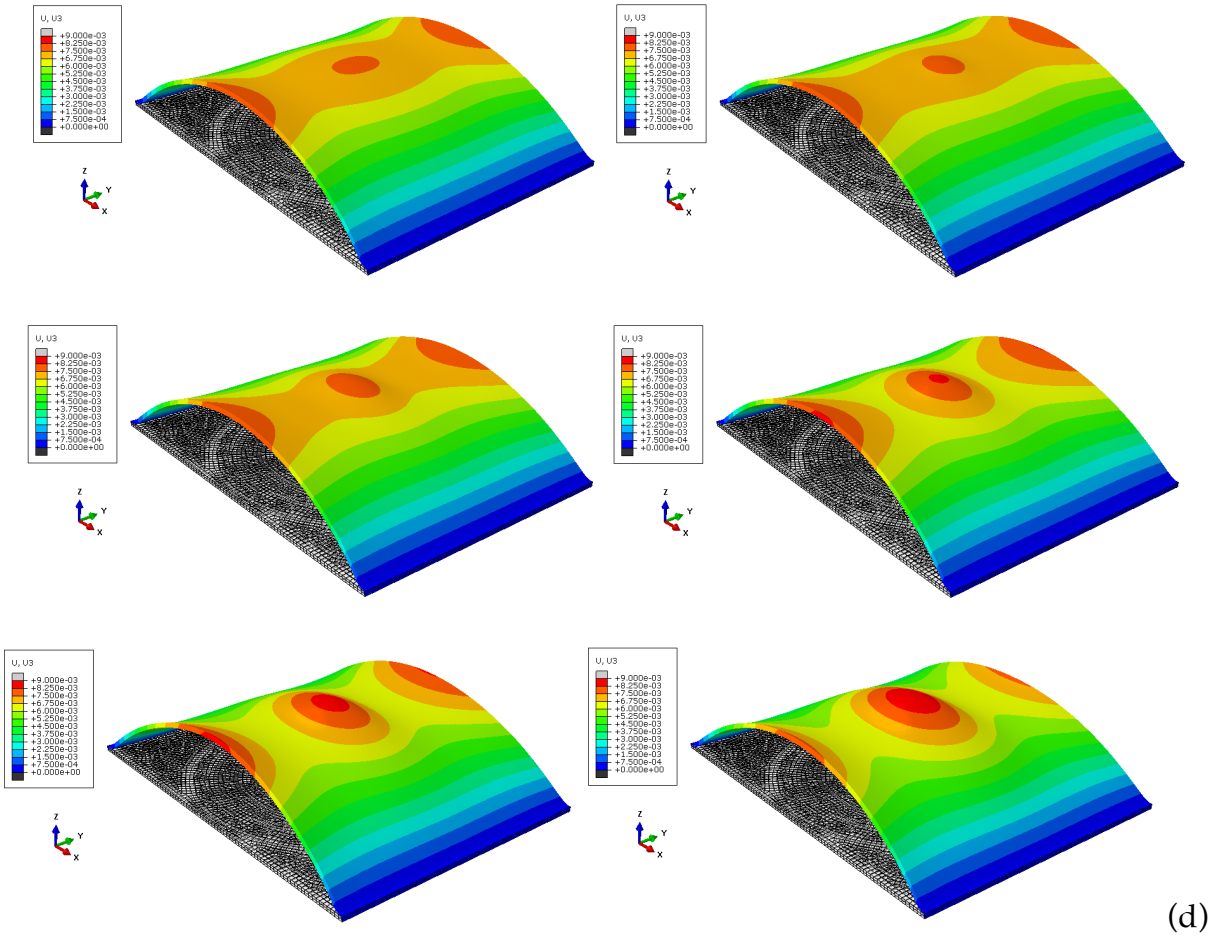

(d)

Figure 72. Out of plane deflections of (a) the passive case and (b~d) the activation procedures listed in Table 15 (unit: meter).

7.5 Summary

In this chapter, we explored the behavior of novel dielectric elastomer composites proposed in this thesis. We carried out extensive simulations using the new user subroutine developed in this research. Specifically, we explored the deformation of a pressure-loaded circular membrane through multiaxial activation, which led to dual-mode activation. Next, the concept of spatial activation as a function fiber orientation was used to demonstrate surface morphing (magnitude, slope, curvature, and peak deflection etc.). Lastly, with potential applications in mind, we considered the deformation behavior of 3D geometries due to electro-hydrostatic actuation. It was

shown how the combination of fiber and matrix activation could be used to break the shape symmetry. In a ring-shaped actuator, it was shown that we could decrease the overall diameter through the activation.

The computational formulation has been demonstrated to be a useful numerical tool to explore various actuator designs. This ultimately plays an important role in advancing the area of soft materials research.

Chapter 8. Conclusion

In summary, new constitutive formulations for active anisotropic materials undergoing finite deformations have been proposed and analyzed within a generalized continuum mechanics framework. The constitutive formulations are invariant based and focus on multiphysics coupling in materials with embedded active fibers. The constitutive equations have been developed for two material classes: i) natural biological muscle tissue and ii) synthetic electroactive polymers. Specifically, a structure-based continuum model was proposed to capture the active viscoelastic behavior of the smooth muscle tissue in Chapter 4. The constitutive model is based on the existing model framework in the literature and we propose a third order nonlinear evolution equation to describe the nonlinear behavior of smooth muscle contraction. In Chapter 5, the constitutive model for the smooth muscle tissue was applied to address one hypothesis that active viscoelastic properties of smooth muscle tissue should be considered during artery overstretch (when longer time scales are relevant). The proposed constitutive equation was employed in a thick-walled model for healthy arteries (with media and adventitia layers) and diseased arteries (with media, adventitia layers and plaque) to study the time dependent response due to overstretch. Results showed the active viscoelasticity has a non-negligible effect on artery wall stresses when longer timescales are considered. The constitutive model was implemented into finite element framework in ABAQUS as user subroutine (UANISOHYPER_INV) to provide a numerical tool for further study complex configurations with boundary loading conditions.

A novel electro-active soft polymer composite with contractile fibers was proposed. The composite can realize multiaxial activations through activating fibers and matrix. A constitutive model was proposed to model the anisotropic electro-active soft polymer composite in Chapter 6. Furthermore, the constitutive model was implemented into finite element framework in ABAQUS as user subroutine (UMAT). The finite element formulation was verified by comparing analytical solutions for uniaxial, biaxial, and simple shear tests. In Chapter 7, a series of computational simulations to highlight novel deformation modes of the proposed dielectric elastomer composite were carried out. Simulations demonstrated the proposed material can realize both lateral expansion as in traditional dielectric elastomers and fiber contraction (in the plane) similar to muscle. Several new spatial architectures were proposed and simulations demonstrated surface morphing through spatial activation and various fiber orientations. Finally, we calculated the actuation response for complex 3D geometries to open the design space. The simulations clearly pointed to the potential advancement and advantage of anisotropic dielectric elastomers for existing and future applications.

Major Research Findings and Highlights

- New constitutive formulations for active anisotropic materials undergoing finite deformations have been proposed and analyzed within a generalized continuum mechanics framework.
- Two new user subroutines have been developed and implemented in a commercial finite element code. The subroutines are amenable to modeling a range of active anisotropic materials undergoing finite viscoelastic deformations.

- Model results quantified the role of active viscoelasticity in artery mechanical response and showed a non-negligible effect on artery stresses when longer timescales are considered.
- Novel dielectric elastomer composites were proposed. The composite is capable of a new dual-mode actuation, which has not been demonstrated previously in dielectric elastomers.
- The actuation performance of dielectric elastomer membranes with different spatial architectures was explored for the first time.
- Multiaxial activation and spatially distributed activation were simulated in a dielectric elastomer membrane for the first time. Surface morphing via spatial activation has been shown to generate distinct three dimensional shapes. Fiber orientation has a strong influence on the resulting shape morphologies. The ability to morph into multiple 3 D shapes with a single design is attractive for a range of potential applications.

Appendix A. Model formulation for uniaxial tension

During experiments, the endothelial cells are removed and the adventitia layer is separated from the media layer. (Herlihy and Murphy, 1973) Considering a strip of the media excised from the artery, we establish a Cartesian coordinate system such that: the axial direction coincident with the artery tube is the 1-direction, the circumferential direction is the 2-direction, and the thickness direction is the 3-direction. In the media, the directional vector for the smooth muscle cells and collagen fibers is assumed coincident with the 2-direction and the dispersion is assumed to be zero, that is $\mathbf{V}=[0,1,0]^{\mathrm{T}}$. Components of the deformation gradient, right Cauchy Green tensor, and structure tensor for uniaxial deformation are given in matrix form as

$$\mathbf{F}_{ij}=\begin{bmatrix} 1/\sqrt{\lambda} & 0 & 0 \\ 0 & \lambda & 0 \\ 0 & 0 & 1/\sqrt{\lambda} \end{bmatrix},\mathbf{C}_{ij}=\begin{bmatrix} 1/\lambda & 0 & 0 \\ 0 & \lambda^2 & 0 \\ 0 & 0 & 1/\lambda \end{bmatrix},\mathbf{M}_{ij}=\begin{bmatrix} 0 & 0 & 0 \\ 0 & 1 & 0 \\ 0 & 0 & 0 \end{bmatrix} \tag{A.1}$$

where, $\det\mathbf{F}=1$ (the smooth muscle tissue is assumed to be incompressible). The principal Cauchy stresses are calculated from the second Piola-Kirchhoff stresses as $\sigma=\mathbf{F}\mathbf{S}\mathbf{F}^{\mathrm{T}}+p\mathbf{I}$, where p is an unknown hydrostatic pressure enforcing the incompressibility constraint. The principal components are

$$\sigma_{11}=\sigma_{33}=\mu_p\frac{1}{\lambda}+p, \tag{A.2}$$

$$\sigma_{22}=\mu_p\lambda^2+2k_1\exp\left(k_2(\lambda^2-1)^2\right)(\lambda^2-1)\lambda^2+O_{lap}(AMp+AM)\frac{\mu_f}{\left(\lambda_F^v\right)^2}\left(\frac{\lambda^2}{\left(\lambda_F^v\right)^2}-1\right)\lambda^2+p. \tag{A.3}$$

For the simple tension tests, the 1- and 3-directions are traction free, thus $\sigma_{11}=\sigma_{33}=0$, from which the hydrostatic pressure p is calculated. Substituting p into Eq. (B.3), σ_{22} is obtained

$$\sigma_{22}=\mu_p\left(\lambda^2-\frac{1}{\lambda}\right)+2k_1\exp\left(k_2(\lambda^2-1)^2\right)(\lambda^2-1)\lambda^2+O_{lap}(AMp+AM)\frac{\mu_f}{\left(\lambda_F^v\right)^2}\left(\frac{\lambda^2}{\left(\lambda_F^v\right)^2}-1\right)\lambda^2. \quad \text{(A.4)}$$

By pulling back, the first Piola-Kirchhoff stress $\mathbf{P}=\sigma\mathbf{F}^{-T}$, in the 2-direction is

$$\mathbf{P}_{22}=\mu_p\left(\lambda-\frac{1}{\lambda^2}\right)+2k_1\exp\left(k_2(\lambda^2-1)^2\right)(\lambda^2-1)\lambda+O_{lap}(AMp+AM)\frac{\mu_f}{\left(\lambda_F^v\right)^2}\left(\frac{\lambda^2}{\left(\lambda_F^v\right)^2}-1\right)\lambda. \quad \text{(A.5)}$$

The stress equation (A.5) and evolution equations provide the expressions needed to fit the uniaxial test data for the media.

In addition, we calculate and plot the stress stretch relationship for the active and passive media layer and passive adventitia layers, and three types of plaque for uniaxial tests in the circumferential direction in Figure 73.

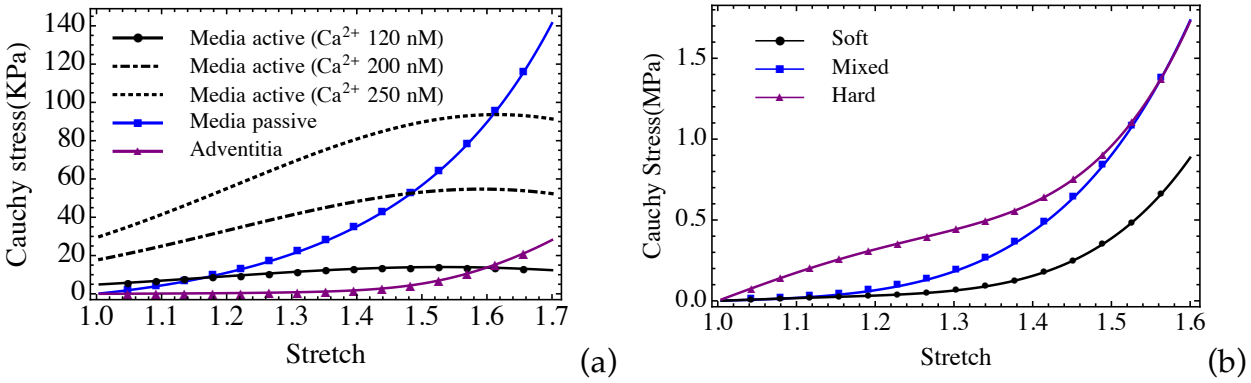

Figure 73. The stress-stretch plots for uniaxial tests in the circumferential direction for (a) artery and (b) plaque (Lawlor et al., 2011).

References

Herlihy, J. T., Murphy, R. A., 1973. Length-Tension Relationship of Smooth Muscle of the Hog Carotid Artery. Circulation Research 33, 275-283, doi:10.1161/01.RES.33.3.275.

Lawlor, M. G., O'Donnell, M. R., O'Connell, B. M., Walsh, M. T., 2011. Experimental determination of circumferential properties of fresh carotid artery plaques. Journal of Biomechanics 44, 1709-1715, doi:10.1016/j.jbiomech.2011.03.033.

Appendix B. Numerical procedures for the boundary value problem

The following is the computing procedure of Cauchy stresses in the two-layer and three-layer thick wall tube. Figure 74 shows the flow chart for the computation procedure of two-layer thick wall artery tube for a prescribed inner radius (a) and internal pressure (b) as loading conditions.

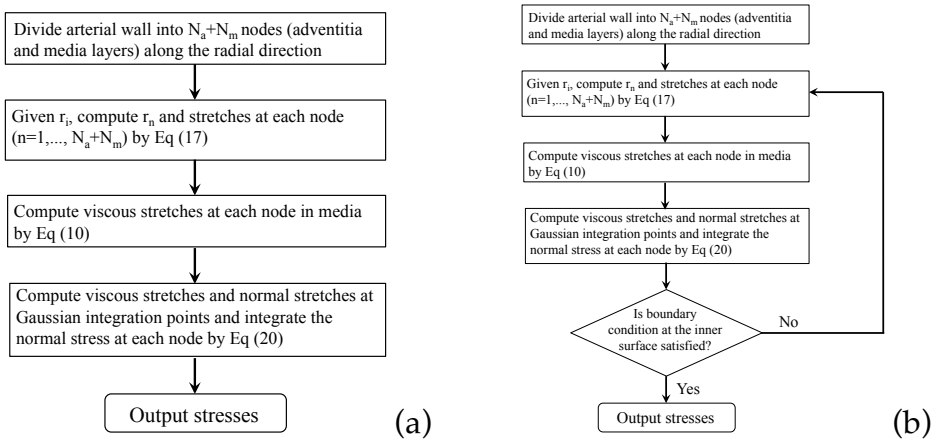

Figure 74. Flow chart for the computation procedure of two-layer thick wall artery tube for a prescribed inner radius (a) and internal pressure (b) as loading conditions.

To model diseased arteries, an axisymmetric and isotropic plaque layer of varying thickness is incorporated, thus rendering a three-layer thick-walled tube model. For the combined artery-plaque model, we use the same numerical values for the artery stretch from load free to in vivo (under mean blood pressure) as in the two-layer ring model (see Figure 75 top left and bottom left quarters). Since plaque grows on the intima in vivo, we assume that the load free configuration of plaque is the same as the

in vivo configuration, i.e. there is no pre-stretch from load free to in vivo configurations in the plaque (see top left and top right quarters). Most artery simulations assume the artery and plaque have the same stretch from load free to in vivo configurations for simplicity (see Figure 75 bottom right quarters with dashed outlines). (Buffinton and Ebenstein, 2014; Ebenstein, 2014; Gasser and Holzapfel, 2007; Holzapfel et al., 2014; Lally et al., 2005; Schmidt et al., 2015)

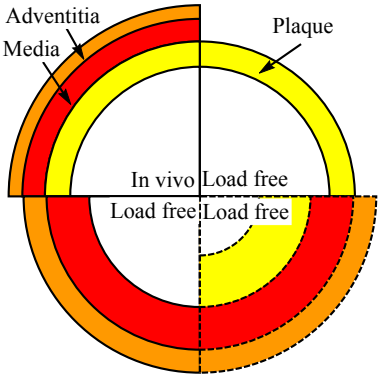

Figure 75. Schematic of load free and in vivo configurations for plaque-artery in the current work (top left and right quarters and bottom left quarter), and load free configuration used by literatures (bottom right quarter).

For diseased three-layer plaque-artery tube, the computation procedure is showing in the flow chart in Figure 76 and the results are presented in Chapter 5 section 5.3.2.

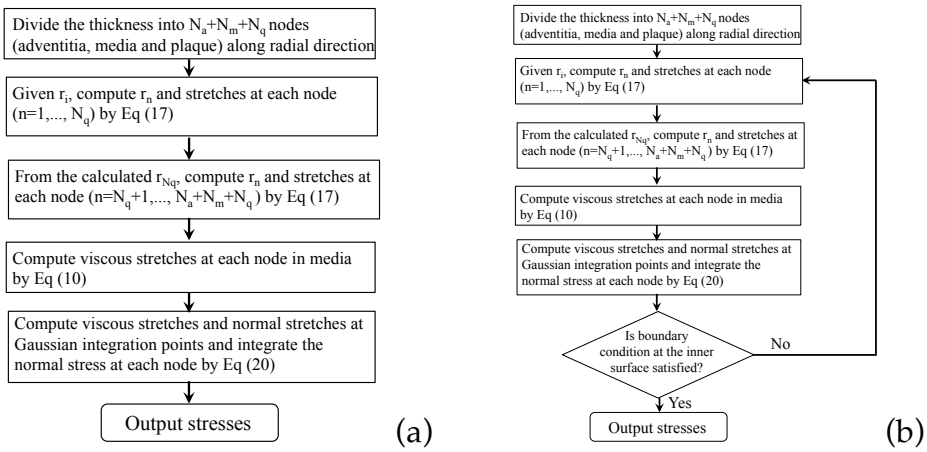

Figure 76. Flow chart for the computation procedure of three-layer thick wall plaque-artery tube for a prescribed inner radius (a) and internal pressure (b) as loading conditions.

References

Buffinton, C. M., Ebenstein, D. M., 2014. Effect of Calcification Modulus and Geometry on Stress in Models of Calcified Atherosclerotic Plaque. Cardiovascular Engineering and Technology 5, 244-260, doi:10.1007/s13239-014-0186-6.

Ebenstein, D., 2014. Effects of Calcification Modulus and Geometry on Stress in Models of Calcified Atherosclerotic Plaque. Cardiovascular Engineering and Technology, 244-260.

Gasser, T. C., Holzapfel, G. A., 2007. Modeling plaque fissuring and dissection during balloon angioplasty intervention. Annals of Biomedical Engineering 35, 711-723, doi:10.1007/s10439-007-9258-1.

Holzapfel, G. A., Mulvihill, J. J., Cunnane, E. M., Walsh, M. T., 2014. Computational approaches for analyzing the mechanics of atherosclerotic plaques: a review. Journal of Biomechanics 47, 859-869, doi:10.1016/j.jbiomech.2014.01.011.

Lally, C., Dolan, F., Prendergast, P. J., 2005. Cardiovascular stent design and vessel stresses: a finite element analysis. Journal of Biomechanics 38, 1574-1581, doi:10.1016/j.jbiomech.2004.07.022.

Schmidt, T., Pandya, D., Balzani, D., 2015. Influence of isotropic and anisotropic material models on the mechanical response in arterial walls as a result of supra-physiological loadings. Mechanics Research Communications 64, 29-37, doi:10.1016/j.mechrescom.2014.12.008.

Appendix C. UAINSIOPYHER_INV for smooth muscle tissue

```
      subroutine uanisohyper_inv (ainv, ua, zeta, nfibers, ninv,
     1     ui1, ui2, ui3, temp, noel, cmname, incmpflag, ihybflag,
     2     numstatev, statev, numfieldv, fieldv, fieldvinc,
     3     numprops, props)
C
      include 'aba_param.inc'
C
      character*80 cmname
      DIMENSION AINV(NINV), UA(2),
     2     UI1(NINV),
     3     UI2(NINV*(NINV+1)/2), UI3(NINV*(NINV+1)/2),
     4     STATEV(NUMSTATEV), FIELDV(NUMFIELDV),
     5     FIELDVINC(NUMFIELDV), PROPS(NUMPROPS)

      parameter ( half = 0.5d0,
     *            zero = 0.d0,
     *            one  = 1.d0,
     *            two  = 2.d0,
     *            three= 3.d0,
     *            four = 4.d0,
     *            five = 5.d0,
     *            six  = 6.d0)
C ---------------------------------------------------------------
C    SMOOTH MUSCLE STRAIN ENERGY FUNCTION (incompressible)
C    W=mup(I-3)/2+k1/2k2 (exp(k2 (I4-1)**2)-1)+OLAP*(AMp+AM)*muf/4*(I4/I4v-1)**2
C ---------------------------------------------------------------
C    PROPS(1) - mup
C    PROPS(2) - k1
C    PROPS(3) - K2
C    PROPS(4) - muf
C    PROPS(5) - KAPPA (COEFFICIENT IN THE DRIVING FORCE)
C ---------------------------------------------------------------
C   Read Material PROPERTIES
      PMUP=props(1)
      P =props(2)
      PP =props(3)
      PMUF=props(4)
      PK=props(5)
C           TIME INCREMENT FOR THE EVOLUTION EQUATION, AND NEED TO BE SET THE C
SAME AS INCREMENT IN ABAQUS CAE
      DT=0.1
      T=STATEV(3)+DT
```

```
C          CONSTANTS IN THE MODEL (IN EVOLUTION EQUATION)
      PLAMVOPT=1.517
      ETA=93E+6
      ALPHA=1.0E-10
      XI=one/2.3
C          CHEMICAL VARIABLES
      AMP=0.006
      AM=0.189
C
C     COMPUTEU AND 1ST AND 2ND DERIVATIVES W.R.T INVARIANTS
C     -I1
      term = ainv(1)-three
      ua(2) = PMUP/two*term
      ui1(1)= PMUP/two
      ui2(1)= zero
      ONTW=one/two
      THTW=three/two
C
C     SET UP THE INITIAL AND VALUES OF I4VTRIAL
C
      PI4V=STATEV(1)
C
C     EXPLICIT FORM TO CALCULATE I4V
C
      OLAP=STATEV(2) !Olap
      PD=-PK*OLAP*AMP !Pd
      POLAP=-OLAP*(PI4V**ONTW-PLAMVOPT)/(two*(XI**two)*(PI4V**ONTW)) !Partial Olap
      PPHI=-OLAP*(AMP+AM)*PMUF/two*(ainv(4)/PI4V-one)*ainv(4)/
     1    (PI4V**two)+POLAP*(AMP+AM)*PMUF/four*(ainv(4)/PI4V-one)**two

      RHS=PD-two*PPHI*PI4V**ONTW+ALPHA*(PD-two*PPHI*PI4V**ONTW)**three
      PI4V=(PI4V**ONTW+RHS*DT/((one+OLAP*AM)*ETA))**two
      OLAP=EXP(-(PI4V**ONTW-PLAMVOPT)**two/(two*XI**two)) !Olap
C
C     COMPUTEU AND 1ST AND 2ND DERIVATIVES W.R.T INVARIANTS
C     -I4
      AA=PP*(ainv(4)-one)**two
      ua(2) = ua(2)+P/two/PP*(exp(AA)-one)+OLAP*(AMP+AM)*PMUF/four
     1  *(ainv(4)/PI4V-one)**two
      ui1(4)=P*(exp(AA))*(ainv(4)-one)+OLAP*(AMP+AM)*PMUF/two
     1 *(ainv(4)/PI4V-one)/PI4V
      ui2(10)=two*P*EXP(AA)*AA+P*EXP(AA)
     1    +OLAP/two*(AMP+AM)*PMUF/PI4V/PI4V

      ua(1)=ua(2)

      STATEV(1)=PI4V
      STATEV(2)=OLAP
      STATEV(3)=T

      return
      end
```

Appendix D. UMAT for electro-active soft polymer composite

UMAT for activation in fibers:

```
      SUBROUTINE UMAT(STRESS,STATEV,DDSDDE,SSE,SPD,SCD,
     1 RPL,DDSDDT,DRPLDE,DRPLDT,
     2 STRAN,DSTRAN,TIME,DTIME,TEMP,DTEMP,PREDEF,DPRED,CMNAME,
     3 NDI,NSHR,NTENS,NSTATV,PROPS,NPROPS,COORDS,DROT,PNEWDT,
     4 CELENT,DFGRD0,DFGRD1,NOEL,NPT,LAYER,KSPT,KSTEP,KINC)
C
      INCLUDE 'ABA_PARAM.INC'
C
      CHARACTER*8 CMNAME
      DIMENSION STRESS(NTENS),STATEV(NSTATV),
     1 DDSDDE(NTENS,NTENS),DDSDDT(NTENS),DRPLDE(NTENS),
     2 STRAN(NTENS),DSTRAN(NTENS),TIME(2),PREDEF(1),DPRED(1),
     3 PROPS(NPROPS),COORDS(3),DROT(3,3),DFGRD0(3,3),DFGRD1(3,3),
     4 Stress_Max(6),VVE(6), VE(3),
     5 TEMP(1),DTEMP(1),DFGRDP(3),DFGRDM1(3, 3),DFGRDM0(3, 3),
     6 CBAR(3,3),DDSDDE_Max(6,6)
C
      DIMENSION BBAR(6),DISTGR(3,3), VV(6), VB(3),
     1 TTAO(NTENS), TAOBAR(NTENS), DELTA(6),DEL(3, 3)
C
      PARAMETER(ZERO=0.D0, ONE=1.D0, TWO=2.D0, THREE=3.D0, FOUR=4.D0,
     1         FIVE=5.D0, SIX=6.D0, SEVEN=7.D0, EIGHT=8.D0, NINE=9.D0,
     2         NEWTON=20, TOLER=1.0d-4)
C ----------------------------------------------------------------
C    STRAIN ENERGY FUNCTION_MECHANICAL PART
C    W=mup(I-3)/2+mufeq/2*(I4-1)**2+muf/2*(I4/I4v-1)**2+k*(J-LnJ-1)
C ----------------------------------------------------------------
C    PROPS(1) - mup
C ----------------------------------------------------------------
      PMUP=PROPS(1)
      PMUFEQ=10000
      PMUF=10000
      PKA=1E8
      V1=0
      V2=1
      V3=0
      ETA=1.E+4
      EPSILON=2.3895E-11
C
C    JACOBIAN AND DISTORTION TENSOR
```

```
C
      DET=DFGRD1(1, 1)*DFGRD1(2, 2)*DFGRD1(3, 3)
     1   -DFGRD1(1, 2)*DFGRD1(2, 1)*DFGRD1(3, 3)
      IF(NSHR.EQ.3) THEN
        DET=DET+DFGRD1(1, 2)*DFGRD1(2, 3)*DFGRD1(3, 1)
     1        +DFGRD1(1, 3)*DFGRD1(3, 2)*DFGRD1(2, 1)
     2        -DFGRD1(1, 3)*DFGRD1(3, 1)*DFGRD1(2, 2)
     3        -DFGRD1(2, 3)*DFGRD1(3, 2)*DFGRD1(1, 1)
      END IF
      SCALE=DET**(-ONE/THREE)
      DO K1=1, 3
        DO K2=1, 3
          DISTGR(K2, K1)=SCALE*DFGRD1(K2, K1)
        END DO
      END DO
C
C     3BY3 INDENTITY MATRIX AND 6BY1 IN VOIGT FORM
C
      DEL(1,1)=ONE
      DEL(2,2)=ONE
      DEL(3,3)=ONE
      DEL(1,2)=ZERO
      DEL(1,3)=ZERO
      DEL(2,3)=ZERO
      DEL(2,1)=ZERO
      DEL(3,1)=ZERO
      DEL(3,2)=ZERO

      DELTA(1)=ONE
      DELTA(2)=ONE
      DELTA(3)=ONE
      DELTA(4)=ZERO
      DELTA(5)=ZERO
      DELTA(6)=ZERO
C
C     CALCULATE LEFT CAUCHY-GREEN TENSOR (B=F.Ft)
C
      BBAR(1)=DISTGR(1, 1)**2+DISTGR(1, 2)**2+DISTGR(1, 3)**2
      BBAR(2)=DISTGR(2, 1)**2+DISTGR(2, 2)**2+DISTGR(2, 3)**2
      BBAR(3)=DISTGR(3, 3)**2+DISTGR(3, 1)**2+DISTGR(3, 2)**2
      BBAR(4)=DISTGR(1, 1)*DISTGR(2, 1)+DISTGR(1, 2)*DISTGR(2, 2)
     1      +DISTGR(1, 3)*DISTGR(2, 3)
      IF(NSHR.EQ.3) THEN
        BBAR(5)=DISTGR(1, 1)*DISTGR(3, 1)+DISTGR(1, 2)*DISTGR(3, 2)
     1        +DISTGR(1, 3)*DISTGR(3, 3)
        BBAR(6)=DISTGR(2, 1)*DISTGR(3, 1)+DISTGR(2, 2)*DISTGR(3, 2)
     1        +DISTGR(2, 3)*DISTGR(3, 3)
      END IF
C
C     CALCULATE INVARIANT I1&I4 (WITH M BEING THE UNIT VERCTOR IN CURRENT
CONFIGURATION)
C
      TRBBAR=BBAR(1)+BBAR(2)+BBAR(3)
      VB(1)=DISTGR(1,1)*V1+DISTGR(1,2)*V2+DISTGR(1,3)*V3
      VB(2)=DISTGR(2,1)*V1+DISTGR(2,2)*V2+DISTGR(2,3)*V3
      VB(3)=DISTGR(3,1)*V1+DISTGR(3,2)*V2+DISTGR(3,3)*V3
```

```
C
C   CALCULATE ORIENTATION(STRUCTURAL TENSOR m)
C
      VV(1)=VB(1)*VB(1)
      VV(2)=VB(2)*VB(2)
      VV(3)=VB(3)*VB(3)
      VV(4)=VB(1)*VB(2)
      VV(5)=VB(1)*VB(3)
      VV(6)=VB(2)*VB(3)
      TRBBARR=VV(1)+VV(2)+VV(3)
c
C    SET UP ALL THE QUANTITIES TO SOLVE EVOLUTION EQUATION BY NEWTON
ITERATION IN THE DO LOOP
C
      ONTW=ONE/TWO
      THTW=THREE/TWO
C
C    SET UP THE INITIAL AND VALUES OF I4VTRIAL
C
      PI4V=STATEV(1)
C
C    EXPLICIT FORM TO CALCULATE I4V
C
      RHS=Four*PMUF*(TRBBARR/PI4V-ONE)*TRBBARR/
     1     PI4V

      PI4V=PI4V+RHS*DTIME/ETA
C
C    CALCULATE DW/DI AND D2W/D2I
C
      WO=PMUP/TWO
      WOO=FOUR*ZERO !delta1
      WF=PMUFEQ*(TRBBARR-ONE)+PMUF*(TRBBARR/PI4V-ONE)/PI4V
      WFF=FOUR*(PMUFEQ+PMUF/PI4V/PI4V) !delta7
      WOF=FOUR*ZERO ! delat5
C
C    CALCULATE THE STRESSES AND TR(TAOBAR)
C
      TRBBART=TRBBAR/THREE
      TRBBARRT=TRBBARR/THREE
      EG=TWO/DET
      PR=TWO*PKA*(DET-ONE)
      PRBAR=TWO*PKA*(TWO*DET-ONE)
      DO K1=1,NDI
        TTAO(K1)=TWO*WO*(BBAR(K1)-TRBBART)+TWO*WF*(VV(K1)-TRBBARRT)
        TAOBAR(K1)=TWO*WO*BBAR(K1)+TWO*WF*VV(K1)
        STRESS(K1)=EG*WO*(BBAR(K1)-TRBBART)+EG*WF*(VV(K1)-TRBBARRT)
     1           +PR
      END DO
      DO K1=NDI+1,NDI+NSHR
        TTAO(K1)=TWO*WO*BBAR(K1)+TWO*WF*(VV(K1))
        TAOBAR(K1)=TWO*WO*BBAR(K1)+TWO*WF*(VV(K1))
        STRESS(K1)=EG*WO*BBAR(K1)+EG*WF*(VV(K1))
      END DO

      TRTAOBAR=TAOBAR(1)+TAOBAR(2)+TAOBAR(3)
```

```
C
C   CALCULATE THE STIFFNESS
C
      DO K2=1, 3
        DO K1=1, 3
          DDSDDE(K1, K2)=PRBAR*DELTA(K1)*DELTA(K2)
     1       -PR*TWO*DEL(K1,K2)+(WOO*BBAR(K1)*BBAR(K2)
     2       +WOF*(BBAR(K1)*VV(K2)+VV(K1)*BBAR(K2))
     3       +WFF*VV(K1)*VV(K2))/DET-((WOO*TRBBAR+WOF*TRBBARR)
     4       *(DELTA(K1)*BBAR(K2)+BBAR(K1)*DELTA(K2))+
     5       (WOF*TRBBAR+WFF*TRBBARR)*(DELTA(K1)*VV(K2)+VV(K1)
     6       *DELTA(K2)))/(THREE*DET)+(WOO*TRBBAR**TWO+
     7       TWO*WOF*TRBBAR*TRBBARR+WFF*TRBBARR**TWO)*DELTA(K1)
     8       *DELTA(K2)/(NINE*DET)+TRTAOBAR*(ONE/TWO*TWO*DEL(K1,K2)
     9       -ONE/THREE*DELTA(K1)*DELTA(K2))*TWO/(THREE*DET)-
     1       (DELTA(K1)*TTAO(K2)+TTAO(K1)*DELTA(K2))*TWO/(THREE*DET)
        END DO
      END DO

      DO K2=4, 6
        DO K1=4, 6
          DDSDDE(K1, K2)=PRBAR*DELTA(K1)*DELTA(K2)
     1       -PR*ONE*DEL(K1-THREE,K2-THREE)+(WOO*BBAR(K1)
     2       *BBAR(K2)+WOF*(BBAR(K1)*VV(K2)+VV(K1)*BBAR(K2))
     3       +WFF*VV(K1)*VV(K2))/DET-((WOO*TRBBAR+WOF*TRBBARR)
     4       *(DELTA(K1)*BBAR(K2)+BBAR(K1)*DELTA(K2))+
     5       (WOF*TRBBAR+WFF*TRBBARR)*(DELTA(K1)*VV(K2)+VV(K1)
     6       *DELTA(K2)))/(THREE*DET)+(WOO*TRBBAR**TWO+
     7       TWO*WOF*TRBBAR*TRBBARR+WFF*TRBBARR**TWO)*DELTA(K1)
     8       *DELTA(K2)/(NINE*DET)+TRTAOBAR*(ONE/TWO*ONE*
     9       DEL(K1-THREE,K2-THREE)-ONE/THREE*DELTA(K1)*DELTA(K2))
     1       *TWO/(THREE*DET)-(DELTA(K1)*TTAO(K2)+TTAO(K1)*DELTA(K2))
     2       *TWO/(THREE*DET)

        END DO
      END DO

      DO K2=4, 6
        DO K1=1, 3
          DDSDDE(K1, K2)=PRBAR*DELTA(K1)*DELTA(K2)
     1       -PR*ZERO*DEL(K1,K2-THREE)+(WOO*BBAR(K1)*BBAR(K2)
     2       +WOF*(BBAR(K1)*VV(K2)+VV(K1)*BBAR(K2))
     3       +WFF*VV(K1)*VV(K2))/DET-((WOO*TRBBAR+WOF*TRBBARR)
     4       *(DELTA(K1)*BBAR(K2)+BBAR(K1)*DELTA(K2))+
     5       (WOF*TRBBAR+WFF*TRBBARR)*(DELTA(K1)*VV(K2)+VV(K1)
     6       *DELTA(K2)))/(THREE*DET)+(WOO*TRBBAR**TWO+
     7       TWO*WOF*TRBBAR*TRBBARR+WFF*TRBBARR**TWO)*DELTA(K1)
     8       *DELTA(K2)/(NINE*DET)+TRTAOBAR*(ONE/TWO*ZERO*
     9       DEL(K1,K2-THREE)-ONE/THREE*DELTA(K1)*DELTA(K2))*TWO
     1       /(THREE*DET)-(DELTA(K1)*TTAO(K2)+TTAO(K1)*DELTA(K2))
     2       *TWO/(THREE*DET)
        END DO
      END DO

      DO K2=1, 3
        DO K1=4, 6
```

```
      DDSDDE(K1, K2)=PRBAR*DELTA(K1)*DELTA(K2)
     1       -PR*ZERO*DEL(K1-THREE,K2)+4*(WOO*BBAR(K1)*BBAR(K2)
     2       +WOF*(BBAR(K1)*VV(K2)+VV(K1)*BBAR(K2))
     3       +WFF*VV(K1)*VV(K2))/DET-4*((WOO*TRBBAR+WOF*TRBBARR)
     4       *(DELTA(K1)*BBAR(K2)+BBAR(K1)*DELTA(K2))+
     5       (WOF*TRBBAR+WFF*TRBBARR)*(DELTA(K1)*VV(K2)+VV(K1)
     6       *DELTA(K2)))/(THREE*DET)+4*(WOO*TRBBAR**TWO+
     7       TWO*WOF*TRBBAR*TRBBARR+WFF*TRBBARR**TWO)*DELTA(K1)
     8       *DELTA(K2)/(NINE*DET)+TRTAOBAR*(ONE/TWO*ZERO
     9       *DEL(K1-THREE,K2)-ONE/THREE*DELTA(K1)*DELTA(K2))*TWO
     1       /(THREE*DET)-(DELTA(K1)*TTAO(K2)+TTAO(K1)*DELTA(K2))
     2       *TWO/(THREE*DET)
        END DO
      END DO

      DDSDDE(1,1)=DDSDDE(1,1)+TWO*STRESS(1)
      DDSDDE(2,2)=DDSDDE(2,2)+TWO*STRESS(2)
      DDSDDE(3,3)=DDSDDE(3,3)+TWO*STRESS(3)
      DDSDDE(4,4)=DDSDDE(4,4)+ONTW*(STRESS(1)+STRESS(2))
      DDSDDE(5,5)=DDSDDE(5,5)+ONTW*(STRESS(1)+STRESS(3))
      DDSDDE(6,6)=DDSDDE(6,6)+ONTW*(STRESS(2)+STRESS(3))
      DDSDDE(1,4)=DDSDDE(1,4)+TWO*STRESS(4)
      DDSDDE(1,5)=DDSDDE(1,5)+TWO*STRESS(5)
      DDSDDE(2,4)=DDSDDE(2,4)+TWO*STRESS(4)
      DDSDDE(2,6)=DDSDDE(2,6)+TWO*STRESS(6)
      DDSDDE(3,5)=DDSDDE(3,5)+TWO*STRESS(5)
      DDSDDE(3,6)=DDSDDE(3,6)+TWO*STRESS(6)
      DDSDDE(4,5)=DDSDDE(4,5)+ONTW*STRESS(6)
      DDSDDE(4,6)=DDSDDE(4,6)+ONTW*STRESS(5)
      DDSDDE(5,6)=DDSDDE(5,6)+ONTW*STRESS(4)

      DO K1=1, NTENS
        DO K2=1, K1-1
          DDSDDE(K1, K2)=DDSDDE(K2, K1)
        END DO
      END DO

      En=12E6   !Electric field (MV/m)
      Enn=En**TWO
      TRBBARE=TRBBARR**TWO

      DO K1=1,NDI+NSHR
        STRESS_Max(K1)=EPSILON*Enn*VV(K1)/TRBBARE
        STRESS(K1)=STRESS(K1)+STRESS_Max(K1)
      END DO
C
C     STATE VARIABLES:
C
      STATEV(1)=PI4V

      RETURN
      END
```

UMAT for activation in matrix:

```
      SUBROUTINE UMAT(STRESS,STATEV,DDSDDE,SSE,SPD,SCD,
     1 RPL,DDSDDT,DRPLDE,DRPLDT,
     2 STRAN,DSTRAN,TIME,DTIME,TEMP,DTEMP,PREDEF,DPRED,CMNAME,
     3 NDI,NSHR,NTENS,NSTATV,PROPS,NPROPS,COORDS,DROT,PNEWDT,
     4 CELENT,DFGRD0,DFGRD1,NOEL,NPT,LAYER,KSPT,KSTEP,KINC)
C
      INCLUDE 'ABA_PARAM.INC'
C
      CHARACTER*8 CMNAME
      DIMENSION STRESS(NTENS),STATEV(NSTATV),
     1 DDSDDE(NTENS,NTENS),DDSDDT(NTENS),DRPLDE(NTENS),
     2 STRAN(NTENS),DSTRAN(NTENS),TIME(2),PREDEF(1),DPRED(1),
     3 PROPS(NPROPS),COORDS(3),DROT(3,3),DFGRD0(3,3),DFGRD1(3,3),
     4 Et(3),Stress_Max(3,3),EkEk(1),DFGRDM1_INV(3,3),En(3),
     5 TEMP(1),DTEMP(1),DFGRDP(3),DFGRDM1(3, 3),DFGRDM0(3, 3),
     6 CBAR(3,3),DDSDDE_Max(6,6)
C
      DIMENSION BBAR(6),DISTGR(3,3), VV(6), VB(3),
     1 TTAO(NTENS), TAOBAR(NTENS), DELTA(6),DEL(3, 3)
C
      PARAMETER(ZERO=0.D0, ONE=1.D0, TWO=2.D0, THREE=3.D0, FOUR=4.D0,
     1         FIVE=5.D0, SIX=6.D0, SEVEN=7.D0, EIGHT=8.D0, NINE=9.D0,
     2         NEWTON=20, TOLER=1.0d-4)
C ----------------------------------------------------------------
C    STRAIN ENERGY FUNCTION_MECHANICAL PART
C    W=mup(I-3)/2+mufeq/2*(I4-1)**2+muf/2*(I4/I4v-1)**2+k*(J-LnJ-1)
C ----------------------------------------------------------------
C    PROPS(1) - mup
C ----------------------------------------------------------------
C
      PMUP=PROPS(1)
      PMUFEQ=10000
      PMUF=10000
      PKA=1E8
      V1=0
      V2=1
      V3=0
      ETA=1.E+4
      EPSILON=4.1595E-11
C
C    JACOBIAN AND DISTORTION TENSOR
C
      DET=DFGRD1(1, 1)*DFGRD1(2, 2)*DFGRD1(3, 3)
     1   -DFGRD1(1, 2)*DFGRD1(2, 1)*DFGRD1(3, 3)
      IF(NSHR.EQ.3) THEN
        DET=DET+DFGRD1(1, 2)*DFGRD1(2, 3)*DFGRD1(3, 1)
     1         +DFGRD1(1, 3)*DFGRD1(3, 2)*DFGRD1(2, 1)
     2         -DFGRD1(1, 3)*DFGRD1(3, 1)*DFGRD1(2, 2)
     3         -DFGRD1(2, 3)*DFGRD1(3, 2)*DFGRD1(1, 1)
      END IF
      SCALE=DET**(-ONE/THREE)
      DO K1=1, 3
```

```
      DO K2=1, 3
        DISTGR(K2, K1)=SCALE*DFGRD1(K2, K1)
      END DO
    END DO
C
C   3BY3 INDENTITY MATRIX AND 6BY1 IN VOIGT FORM
C
    DEL(1,1)=ONE
    DEL(2,2)=ONE
    DEL(3,3)=ONE
    DEL(1,2)=ZERO
    DEL(1,3)=ZERO
    DEL(2,3)=ZERO
    DEL(2,1)=ZERO
    DEL(3,1)=ZERO
    DEL(3,2)=ZERO

    DELTA(1)=ONE
    DELTA(2)=ONE
    DELTA(3)=ONE
    DELTA(4)=ZERO
    DELTA(5)=ZERO
    DELTA(6)=ZERO
C
C   CALCULATE LEFT CAUCHY-GREEN TENSOR (B=F.Ft)
C
    BBAR(1)=DISTGR(1, 1)**2+DISTGR(1, 2)**2+DISTGR(1, 3)**2
    BBAR(2)=DISTGR(2, 1)**2+DISTGR(2, 2)**2+DISTGR(2, 3)**2
    BBAR(3)=DISTGR(3, 3)**2+DISTGR(3, 1)**2+DISTGR(3, 2)**2
    BBAR(4)=DISTGR(1, 1)*DISTGR(2, 1)+DISTGR(1, 2)*DISTGR(2, 2)
   1      +DISTGR(1, 3)*DISTGR(2, 3)
    IF(NSHR.EQ.3) THEN
      BBAR(5)=DISTGR(1, 1)*DISTGR(3, 1)+DISTGR(1, 2)*DISTGR(3, 2)
   1        +DISTGR(1, 3)*DISTGR(3, 3)
      BBAR(6)=DISTGR(2, 1)*DISTGR(3, 1)+DISTGR(2, 2)*DISTGR(3, 2)
   1        +DISTGR(2, 3)*DISTGR(3, 3)
    END IF
C
C   CALCULATE INVARIANT I1&I4 (WITH M BEING THE UNIT VERCTOR IN CURRENT
CONFIGURATION)
C
    TRBBAR=BBAR(1)+BBAR(2)+BBAR(3)
    VB(1)=DISTGR(1,1)*V1+DISTGR(1,2)*V2+DISTGR(1,3)*V3
    VB(2)=DISTGR(2,1)*V1+DISTGR(2,2)*V2+DISTGR(2,3)*V3
    VB(3)=DISTGR(3,1)*V1+DISTGR(3,2)*V2+DISTGR(3,3)*V3
C
C   CALCULATE ORIENTATION(STRUCTURAL TENSOR m)
C
    VV(1)=VB(1)*VB(1)
    VV(2)=VB(2)*VB(2)
    VV(3)=VB(3)*VB(3)
    VV(4)=VB(1)*VB(2)
    VV(5)=VB(1)*VB(3)
    VV(6)=VB(2)*VB(3)
    TRBBARR=VV(1)+VV(2)+VV(3)
C
```

```
C    SET UP ALL THE QUANTITIES TO SOLVE EVOLUTION EQUATION BY NEWTON
ITERATION IN THE DO LOOP
C
     ONTW=ONE/TWO
     THTW=THREE/TWO
C
C    SET UP THE INITIAL AND VALUES OF I4VTRIAL
C
     PI4V=STATEV(1)
C
C    EXPLICIT FORM TO CALCULATE I4V
C
     RHS=Four*PMUF*(TRBBARR/PI4V-ONE)*TRBBARR/
    1    PI4V

     PI4V=PI4V+RHS*DTIME/ETA
C
C    CALCULATE DW/DI AND D2W/D2I
C
     WO=PMUP/TWO
     WOO=FOUR*ZERO !delta1
     WF=PMUFEQ*(TRBBARR-ONE)+PMUF*(TRBBARR/PI4V-ONE)/PI4V
     WFF=FOUR*(PMUFEQ+PMUF/PI4V/PI4V) !delta7
     WOF=FOUR*ZERO ! delat5
C
C    CALCULATE THE STRESSES AND TR(TAOBAR)
C
     TRBBART=TRBBAR/THREE
     TRBBARRT=TRBBARR/THREE
     EG=TWO/DET
     PR=TWO*PKA*(DET-ONE)
     PRBAR=TWO*PKA*(TWO*DET-ONE)
     DO K1=1,NDI
       TTAO(K1)=TWO*WO*(BBAR(K1)-TRBBART)+TWO*WF*(VV(K1)-TRBBARRT)
       TAOBAR(K1)=TWO*WO*BBAR(K1)+TWO*WF*VV(K1)
       STRESS(K1)=EG*WO*(BBAR(K1)-TRBBART)+EG*WF*(VV(K1)-TRBBARRT)
    1          +PR
     END DO
     DO K1=NDI+1,NDI+NSHR
       TTAO(K1)=TWO*WO*BBAR(K1)+TWO*WF*(VV(K1))
       TAOBAR(K1)=TWO*WO*BBAR(K1)+TWO*WF*(VV(K1))
       STRESS(K1)=EG*WO*BBAR(K1)+EG*WF*(VV(K1))
     END DO

     TRTAOBAR=TAOBAR(1)+TAOBAR(2)+TAOBAR(3)
C
C    CALCULATE THE STIFFNESS
C
     DO K2=1, 3
       DO K1=1, 3
         DDSDDE(K1, K2)=PRBAR*DELTA(K1)*DELTA(K2)
    1        -PR*TWO*DEL(K1,K2)+(WOO*BBAR(K1)*BBAR(K2)
    2        +WOF*(BBAR(K1)*VV(K2)+VV(K1)*BBAR(K2))
    3        +WFF*VV(K1)*VV(K2))/DET-((WOO*TRBBAR+WOF*TRBBARR)
    4        *(DELTA(K1)*BBAR(K2)+BBAR(K1)*DELTA(K2))+
    5        (WOF*TRBBAR+WFF*TRBBARR)*(DELTA(K1)*VV(K2)+VV(K1)
```

```
6       *DELTA(K2)))/(THREE*DET)+(WOO*TRBBAR**TWO+
7       TWO*WOF*TRBBAR*TRBBARR+WFF*TRBBARR**TWO)*DELTA(K1)
8       *DELTA(K2)/(NINE*DET)+TRTAOBAR*(ONE/TWO*TWO*DEL(K1,K2)
9       -ONE/THREE*DELTA(K1)*DELTA(K2))*TWO/(THREE*DET)-
1       (DELTA(K1)*TTAO(K2)+TTAO(K1)*DELTA(K2))*TWO/(THREE*DET)
  END DO
 END DO

 DO K2=4, 6
  DO K1=4, 6
   DDSDDE(K1, K2)=PRBAR*DELTA(K1)*DELTA(K2)
1       -PR*ONE*DEL(K1-THREE,K2-THREE)+(WOO*BBAR(K1)
2       *BBAR(K2)+WOF*(BBAR(K1)*VV(K2)+VV(K1)*BBAR(K2))
3       +WFF*VV(K1)*VV(K2))/DET-((WOO*TRBBAR+WOF*TRBBARR)
4       *(DELTA(K1)*BBAR(K2)+BBAR(K1)*DELTA(K2))+
5       (WOF*TRBBAR+WFF*TRBBARR)*(DELTA(K1)*VV(K2)+VV(K1)
6       *DELTA(K2)))/(THREE*DET)+(WOO*TRBBAR**TWO+
7       TWO*WOF*TRBBAR*TRBBARR+WFF*TRBBARR**TWO)*DELTA(K1)
8       *DELTA(K2)/(NINE*DET)+TRTAOBAR*(ONE/TWO*ONE*
9       DEL(K1-THREE,K2-THREE)-ONE/THREE*DELTA(K1)*DELTA(K2))
1       *TWO/(THREE*DET)-(DELTA(K1)*TTAO(K2)+TTAO(K1)*DELTA(K2))
2       *TWO/(THREE*DET)

  END DO
 END DO

 DO K2=4, 6
  DO K1=1, 3
   DDSDDE(K1, K2)=PRBAR*DELTA(K1)*DELTA(K2)
1       -PR*ZERO*DEL(K1,K2-THREE)+(WOO*BBAR(K1)*BBAR(K2)
2       +WOF*(BBAR(K1)*VV(K2)+VV(K1)*BBAR(K2))
3       +WFF*VV(K1)*VV(K2))/DET-((WOO*TRBBAR+WOF*TRBBARR)
4       *(DELTA(K1)*BBAR(K2)+BBAR(K1)*DELTA(K2))+
5       (WOF*TRBBAR+WFF*TRBBARR)*(DELTA(K1)*VV(K2)+VV(K1)
6       *DELTA(K2)))/(THREE*DET)+(WOO*TRBBAR**TWO+
7       TWO*WOF*TRBBAR*TRBBARR+WFF*TRBBARR**TWO)*DELTA(K1)
8       *DELTA(K2)/(NINE*DET)+TRTAOBAR*(ONE/TWO*ZERO*
9       DEL(K1,K2-THREE)-ONE/THREE*DELTA(K1)*DELTA(K2))*TWO
1       /(THREE*DET)-(DELTA(K1)*TTAO(K2)+TTAO(K1)*DELTA(K2))
2       *TWO/(THREE*DET)
  END DO
 END DO

 DO K2=1, 3
  DO K1=4, 6
   DDSDDE(K1, K2)=PRBAR*DELTA(K1)*DELTA(K2)
1       -PR*ZERO*DEL(K1-THREE,K2)+4*(WOO*BBAR(K1)*BBAR(K2)
2       +WOF*(BBAR(K1)*VV(K2)+VV(K1)*BBAR(K2))
3       +WFF*VV(K1)*VV(K2))/DET-4*((WOO*TRBBAR+WOF*TRBBARR)
4       *(DELTA(K1)*BBAR(K2)+BBAR(K1)*DELTA(K2))+
5       (WOF*TRBBAR+WFF*TRBBARR)*(DELTA(K1)*VV(K2)+VV(K1)
6       *DELTA(K2)))/(THREE*DET)+4*(WOO*TRBBAR**TWO+
7       TWO*WOF*TRBBAR*TRBBARR+WFF*TRBBARR**TWO)*DELTA(K1)
8       *DELTA(K2)/(NINE*DET)+TRTAOBAR*(ONE/TWO*ZERO
9       *DEL(K1-THREE,K2)-ONE/THREE*DELTA(K1)*DELTA(K2))*TWO
1       /(THREE*DET)-(DELTA(K1)*TTAO(K2)+TTAO(K1)*DELTA(K2))
```

```
     2        *TWO/(THREE*DET)
       END DO
      END DO

      DDSDDE(1,1)=DDSDDE(1,1)+TWO*STRESS(1)
      DDSDDE(2,2)=DDSDDE(2,2)+TWO*STRESS(2)
      DDSDDE(3,3)=DDSDDE(3,3)+TWO*STRESS(3)
      DDSDDE(4,4)=DDSDDE(4,4)+ONTW*(STRESS(1)+STRESS(2))
      DDSDDE(5,5)=DDSDDE(5,5)+ONTW*(STRESS(1)+STRESS(3))
      DDSDDE(6,6)=DDSDDE(6,6)+ONTW*(STRESS(2)+STRESS(3))
      DDSDDE(1,4)=DDSDDE(1,4)+TWO*STRESS(4)
      DDSDDE(1,5)=DDSDDE(1,5)+TWO*STRESS(5)
      DDSDDE(2,4)=DDSDDE(2,4)+TWO*STRESS(4)
      DDSDDE(2,6)=DDSDDE(2,6)+TWO*STRESS(6)
      DDSDDE(3,5)=DDSDDE(3,5)+TWO*STRESS(5)
      DDSDDE(3,6)=DDSDDE(3,6)+TWO*STRESS(6)
      DDSDDE(4,5)=DDSDDE(4,5)+ONTW*STRESS(6)
      DDSDDE(4,6)=DDSDDE(4,6)+ONTW*STRESS(5)
      DDSDDE(5,6)=DDSDDE(5,6)+ONTW*STRESS(4)

      DO K1=1, NTENS
        DO K2=1, K1-1
          DDSDDE(K1, K2)=DDSDDE(K2, K1)
        END DO
      END DO

C     Calculate the inverse of deformation gradient
C
      DFGRDM1_INV(1,1)=DFGRD1(2,2)*DFGRD1(3,3)
     1 -DFGRD1(2,3)*DFGRD1(3,2)
      DFGRDM1_INV(1,2)=-DFGRD1(1,2)*DFGRD1(3,3)
     1 +DFGRD1(1,3)*DFGRD1(3,2)
      DFGRDM1_INV(1,3)=DFGRD1(1,2)*DFGRD1(2,3)
     1 -DFGRD1(1,3)*DFGRD1(2,2)

      DFGRDM1_INV(2,1)=-DFGRD1(2,1)*DFGRD1(3,3)
     1 +DFGRD1(2,3)*DFGRD1(3,1)
      DFGRDM1_INV(2,2)=DFGRD1(1,1)*DFGRD1(3,3)
     1 -DFGRD1(1,3)*DFGRD1(3,1)
      DFGRDM1_INV(2,3)=-DFGRD1(1,1)*DFGRD1(2,3)
     1 +DFGRD1(1,3)*DFGRD1(2,1)

      DFGRDM1_INV(3,1)=DFGRD1(2,1)*DFGRD1(3,2)
     1 -DFGRD1(2,2)*DFGRD1(3,1)
      DFGRDM1_INV(3,2)=-DFGRD1(1,1)*DFGRD1(3,2)
     1 +DFGRD1(1,2)*DFGRD1(3,1)
      DFGRDM1_INV(3,3)=DFGRD1(1,1)*DFGRD1(2,2)
     1 -DFGRD1(1,2)*DFGRD1(2,1)

      DO I=1,3
      DO J=1,3
      DFGRDM1_INV(I,J)=DFGRDM1_INV(I,J)/DET
      END DO
      END DO
C     Nominal electric field vector
      En(1)=0
```

```
      En(2)=0
      En(3)=5E6

      DO I=1,3
      Et(I)=0
      END DO

      DO I=1,3
      DO J=1,3
      Et(J)=Et(J)+En(I)*DFGRDM1_INV(I,J)
      END Do
      END Do

      EkEk=0.0D0
      DO I=1, 3
        EkEk=EkEk+Et(I)*Et(I)
      ENDDO

      DO I=1,3
       DO J=1,3
       Stress_Max(I,J)=0.0D0
       ENDDO
      ENDDO
C
C     Update the true stress due to polarization
C
      DO I=1,3
       DO J=1,3
       IF (I==J) THEN
       Stress_Max(I,J)=EPSILON*Et(I)*Et(J)-0.50D0*EPSILON*EkEk(1)
       ELSE
       Stress_Max(I,J)=EPSILON*Et(I)*Et(J)
       ENDIF
       ENDDO
      ENDDO

      STRESS(1)=STRESS(1)+Stress_Max(1,1)
      STRESS(2)=STRESS(2)+Stress_Max(2,2)
      STRESS(3)=STRESS(3)+Stress_Max(3,3)
      STRESS(4)=STRESS(4)+Stress_Max(1,2)
      STRESS(5)=STRESS(5)+Stress_Max(1,3)
      STRESS(6)=STRESS(6)+Stress_Max(2,3)
C
C     STATE VARIABLES:
C
      STATEV(1)=PI4V

      RETURN
      END
```